

Carbonation of low carbon binders

Thèse N° 9400

Présentée le 5 juillet 2019

à la Faculté des sciences et techniques de l'ingénieur
Laboratoire des matériaux de construction
Programme doctoral en science et génie des matériaux

pour l'obtention du grade de Docteur ès Sciences

par

Wioletta SOJA

Acceptée sur proposition du jury

Prof. P. Muralt, président du jury
Prof. K. Scrivener, directrice de thèse
Prof. L. Black, rapporteur
Dr P. Dangla, rapporteur
Prof. R. Flatt, rapporteur

2019

*Strength doesn't come from what you can do.
It comes from overcoming the things you once thought you couldn't.*

Rikki Rogers

Acknowledgements

This four and half years of PhD were very special for me and for sure will stay unforgettable. I would like to thank everybody who in different ways contributed to make this time such a unique experience.

At the very first I would like to express my sincere gratitude to my supervisor Prof. Karen Scrivener, the head of the Laboratory of Construction Materials at EPFL, who made this experience possible. I am grateful for the flexibility towards new ideas and for giving me the opportunity to work in this exceptional environment.

I would like to acknowledge the members of my jury for their constructive advices and valuable suggestions, Prof. Robert Flatt, Prof. Leon Black, Dr. Patrick Dangla, and Prof. Paul Muralt.

Warm thanks to the Swiss National Foundation for Research (SNF) for funding this thesis through the project no. 154062 entitled “Formulation, use, and durability of concrete with low clinker cements”, and to Lafarge-Holcim for providing the raw materials.

Big thanks to remarkable group of several generations of scientists, friends and colleagues at LMC including former and current members, for all entertaining moments, good discussions and overall help.

This dissertation would not have had been possible without the guidance, debates, criticism, corrections, and support of the postdocs, Dr. Hamed Maraghechi and Dr. Fabien Georget. I was very lucky to have them as my guides, Hamed from the beginning, and Fabien until the end of my PhD. I am very thankful for all your help. Special thanks to my dear Lili. I am happy that we could spend some great time here together, I was very lucky that at least half of my PhD here you were here. Thank you for your support, friendship, postcards!

Thanks also to: Paweł for the support at the beginning of my research path, Hadi for bringing always good mood, Arnaud for the French accent, Xuerun for help with vaterite and for German beers, Frank for contagious laughter and Haribos, Matthieu for intro to carbonation, Emmanuelle for the patience to my samples during TEM, Marcelo and his wife Gabriela for delicious Brazilian food, William for being the Microsoft Word hero, Mahsa for the extraordinary kindness, Anna for organizing amazing Europa park weekend, Khalil for all nice talks, Maya for every day optimism and for sharing all baked goodies, Alex and Julien for all game evenings, contagious “obsession” about environment, and for my first observation of the Moon’s craters and Saturn’s rings, Andrea for correcting my early stage Spanish, Franco for pisco sour, John for IT support, Silas for small German lessons, interesting discussions, and sharing the green tea, François for great guidance in Roma and for the cool France-weekends, Josh for being always a nice companion, Solène for michałki sweets.

Thanks also to the other LMC members I met here: Hui, Yan, Adrien, Aurélie, Berta, Elise, Aslam, Qiao, Yu, Alex P., Monisha, Bhagath, Diana, Gabi, Masood, Shiyu, Yosra, and Junjie.

Many thanks to all my officemates I had during all of those years: Mink, who was my officemate for almost whole duration of my PhD (thanks for sharing your great Thai food during lunches and for this whole range of cookies!), and to Sarra for nice office company for this last few months of my stay. Also thanks to my temporary officemates: Huang, Cyril, José, Anuj Anuj, Yuvaraj, Sundar, Hong, Moses, Mariana, Romain, and Kshitij.

Thanks to the temporary visitors of the lab, Vineet and Nico who were great companions. Here I also would like to include my dear Mariana (China) who unfortunately also joined the group of temporary visitors. Thank you all for your great spirit and spontaneity.

Also, a big thanks to administration team: Maude, Anne-Sandra, Marie-Alix, and Mirabelle for help during organisation our conference trips as well as for all memorable events they organised, such as lab hikes, Christmas dinners, ski seminars, and the conference to celebrate the centennial of LMC and Karen's 60th birthday. Thanks also to the technician team, Lionel, Jean, Antonio, Paul, Nathan for helping me with setting up my new experimental equipment.

Thanks to BioRob team for all those nice activities I could be part of, including GoKards, Laser Tag, cinemas with all kind of superheroes, canyoning, rope park, treasure hunts, coffee breaks, Christmas dinners, and for all other food-related events.

Warm acknowledgments to all industrial and academic partners involved in the project, including Lafarge-Holcim, Sika, and ETHZ who contributed to the improvement of the work through the regular progress meetings. Thanks also to Federica and Matteo for having so kind cooperation during those years in WP1. Thanks to Roman Loser from EMPA and to Dr. Hong Wong from Imperial College for sharing their experience on gas diffusion. Big thanks go also to Dr. Bruno Huet and PhD student Mouna from LafargeHolcim for sharing their diffusion set-up which made the gas diffusion experiments possible. Thanks to the cement plants in Siggenthal and in Ecléplens for caring on the accelerated carbonation test. Thanks to ENAC lab for lending the CO₂ detector and to CIME lab for the access to the slow speed saw which was crucial for my experiments.

Thanks also to my closest friends, Justynka and Wanda, and to friends and colleagues I met in Switzerland, for all of those good times and adventures we could share.

Deep thanks to the whole Hauser family, especially to Heidi and Theo, for big support and for all good times we had together. *Ein herzliches Dankeschön an die ganze Familie Hauser, vor allem an Heidi und Theo, für die große Unterstützung und für die guten zeiten, die wir gemeinsam verbringen durften.*

An enormous thank you goes to my family for their support and giving me courage. *Ogromne podziękowania kieruję do mojej rodziny, za ich wsparcie i dodawanie mi odwagi.*

I would like to address special thanks to a special person and a great companion for discovering the World, to a person who greatly supported me, always motivates me, and gives me courage to do more. Simon, thank you for e v e r y t h i n g. I am so grateful and enjoyed a lot that we could go through our PhDs unique adventure together. We made it! \ (*^_ ^*) / \ (^~^) ☺

A big part of this manuscript was written down in Oberried am Brienersee, the place which I own the acknowledgements for the inspiration, and for making the time of the thesis writing such a nice experience.

*Wioletta Soja
Oberried am Brienersee & Lausanne, 2019*

Abstract

To reduce the impact of the embodied energy and of the carbon dioxide emissions of concrete, the use of supplementary cementitious materials (SCMs) in the cement industry has become a common practice. However, the practical experience on such cements is limited due to the lower strength at early ages and the concern about long term performance, especially potentially higher carbonation rates due to a lower capacity to bind CO₂. To increase the protection of the steel in the concrete where carbonation might be a risk, the full understanding of the microstructure changes due to carbonation is necessary.

The main goal of this thesis is to characterise and to quantify the correlation between transport properties and modification of the microstructure in the carbonated concrete. We propose a new approach to obtain a representative specimen of “fully carbonated” material in relatively short time. The innovative idea of using a thin cement paste sample allowed the characterization of the gas diffusion properties in naturally carbonated cement paste. This, together with the measured changes in phase assemblage and pore structure, can be used to better understand the reactive transport model. The adaptation to natural exposure conditions ensures obtaining representative results.

Investigating the governing parameters of carbonation and emphasizing the influence of the non-carbonated reference advanced the understanding of the carbonation mechanism, especially in the low carbon binders. This study sheds a new light at the problem of overestimating the effect of carbonation on the microstructure of the cementitious material. In particular, it shows the importance of subtracting the effect of the drying taking place during carbonation, to diminish the risk of attributing the changes in porosity only to carbonation.

The monitoring of the changes in the phase assemblage and the assessment of the carbonation coefficient during exposure to carbonation showed a promising performance of the new ternary blend with 50 % clinker replacement by burnt oil shale, slag, and limestone.

The obtained results on characterisation of the carbonating binders can be used to improve carbonation models, that are essential to predict the resistance of new types of cements. That could help to assess the balance between the benefits of using alternative materials, and the potential danger of low resistance against carbonation. The profit will be to make cement and concrete even more sustainable and a more environmentally friendly construction material.

Keywords: carbonation, reactive transport, diffusion coefficient, pore size distribution, natural carbonation, phase assemblage, supplementary cementitious materials

Résumé

Afin de réduire l'impact de l'énergie intrinsèque et des émissions de dioxyde de carbone du béton, l'utilisation de matériaux de substitution du ciment (SCM) est devenue une pratique courante. Cependant, l'expérience pratique sur de tels ciments est limitée en raison de la résistance plus faible au jeune âge et des performances à long terme, en particulier des taux de carbonatation potentiellement plus élevés due à une capacité plus faible de fixation du CO₂. Pour accroître la protection de l'acier dans le béton lorsque la carbonatation peut constituer un risque, il est nécessaire de bien comprendre les modifications de la microstructure dues à la carbonatation.

L'objectif principal de cette thèse est de caractériser, et de quantifier la corrélation entre les propriétés de transport et la modification de la microstructure dans le béton carbonaté. Nous proposons une nouvelle approche pour obtenir un échantillon représentatif de matériau «entièrement carbonaté» en un temps relativement court. L'idée novatrice d'utiliser un échantillon de pâte de ciment mince a permis de caractériser les propriétés de diffusion du gaz dans une pâte de ciment naturellement carbonatée. Les changements mesurés dans l'assemblage de phase et dans la structure des pores, peuvent être utilisés pour mieux comprendre les modèles de transport réactif. L'adaptation des conditions d'exposition naturelles permet d'obtenir des résultats représentatifs.

L'étude des paramètres qui régissent la carbonatation et la mise en évidence de l'influence de la référence non carbonatée ont permis de mieux comprendre le mécanisme de la carbonatation, en particulier dans les liants à faible teneur en carbone. Cette étude met en avant le problème de la surestimation de l'effet de la carbonatation sur la microstructure du matériau. En particulier, il montre l'importance de soustraire l'effet du séchage ayant lieu pendant la carbonatation, afin de diminuer le risque d'attribuer les changements de porosité uniquement à la carbonatation.

L'analyse des modifications de l'assemblage des phases et l'évaluation du coefficient de carbonatation au cours de l'exposition à la carbonatation ont montré des résultats prometteurs pour le nouveau mélange ternaire avec un remplacement de 50 % du clinker par du schiste bitumineux calciné, du laitier et du calcaire.

Les résultats obtenus sur la caractérisation des liants carbonatés peuvent être utilisés pour améliorer les modèles de carbonatation, indispensables pour prédire la résistance de nouveaux types de ciments. Cela pourrait aider à évaluer l'équilibre entre les avantages de l'utilisation de matériaux de remplacement et le danger potentiel d'une faible résistance à la carbonatation. Le profit sera de rendre le ciment et le béton encore plus durables et un matériau de construction plus respectueux de l'environnement.

Mots-clés: carbonatation, transport réactif, coefficient de diffusion, distribution de taille de pore, carbonatation naturelle, assemblage de phase, matériaux de substitution au ciment

Zusammenfassung

Die Zementindustrie verwendet bereits heutzutage supplementäre zementartige Materialien (SCMs), um den Kohlenstoff-Dioxid (CO_2) Ausstoss von Beton zu vermindern. Die praktische Erfahrung mit solchem Zement ist allerdings eingeschränkt. Einerseits ist solcher Zement zu Anfang etwas schwächer. Andererseits gibt es Bedenken über das Langzeitverhalten, besonders wegen einer potentiell höheren Karbonisierungsrate aufgrund einer niedrigeren CO_2 Bindungskapazität. Um den Schutz des Stahls in Beton zu erhöhen, ist es nötig, die Änderungen in der Mikrostruktur durch Karbonisierung besser zu verstehen.

Das Ziel dieser These ist es, die Korrelation zwischen Transporteigenschaften und die Änderungen der Mikrostruktur in karbonisiertem Zement zu charakterisieren und quantifizieren. Wir schlagen eine neue Methode vor, um ein repräsentatives Probestück von "vollständig karbonisiertem" Material in relativ kurzer Zeit zu erzeugen. Die neuartige Idee, ein dünnes Zementpaste-Musterstück zu verwenden, erlaubte es, die Gasdiffusionseigenschaften in natürlich karbonisierter Zementpaste zu charakterisieren. Dies, zusammen mit den gemessenen Änderungen in der Phasenzusammensetzung und Porenstruktur, kann verwendet werden, um das reaktive Transportmodell besser zu verstehen. Die Adaption zu natürlichen Expositionsbedingungen garantiert repräsentative Resultate.

Die Untersuchung der Hauptparameter der Karbonisierung in Zusammenhang mit der nicht-karbonisierten Referenz förderte das Verständnis der Karbonisierungsmechanismen, vor allem für Grundstoffe mit niedrigerer Kohlenstoff-Bindungskapazität. Diese These erlaubt eine erneute Betrachtung des Problems der Überschätzung der Karbonisierung in der Mikrostruktur von zementartigen Materialien. Speziell wird aufgezeigt, wie wichtig es ist, den Effekt der Trocknung während der Karbonisierung zu subtrahieren, um das Risiko zu vermindern, die Änderungen in der Porosität nur der Karbonisierung zuzuschreiben.

Die Überwachung dieser Hauptparameter zeigte ein vielversprechendes Verhalten für den neuen ternären Mix, in dem 50 % des Klinkers durch gebrannten Ölschiefer, Schlacke und Kalkstein ersetzt ist.

Die Resultate der Charakterisierung der Karbonisierungsbinder können Karbonisierungsmodelle verbessern, welche essentiell für die Voraussagung der Resistenz von neuen Zementarten sind. Dies kann zur Verwendung von neuen, alternativen Materialien führen und die potentielle Gefahr gegen niedrige Karbonisierungsresistenz vermindern. Im Endeffekt kann dies Zement und Beton zu nachhaltigeren und umweltfreundlicheren Materialien machen.

Stichwörter: Karbonisierung, reaktiver Transport, Diffusionskoeffizient, Verteilung der Porengrösse, natürliche Karbonisierung, Phasenzusammensetzung, supplementäre zementartige Materialien

Streszczenie

Aby zmniejszyć wpływ emisji dwutlenku węgla z produkcji betonu, stosowanie dodatków mineralnych do cementów w przemyśle cementowym stało się powszechną praktyką. Doświadczenie w takich cementach jest jednak ograniczone ze względu na niższą wytrzymałość wczesną i obawy dotyczące długoterminowej wydajności, zwłaszcza potencjalnie wyższego współczynnika karbonatyzacji ze względu na mniejszą zdolność do wiązania CO₂. Aby zwiększyć ochronę stali w betonie, gdzie karbonatyzacja może stanowić zagrożenie, konieczne jest pełne zrozumienie zmian mikrostruktury spowodowanych karbonatyzacją.

Głównym celem tej pracy jest scharakteryzowanie i określenie ilościowe zależności pomiędzy właściwościami transportowymi a modyfikacją mikrostruktury w skarbonatyzowanym betonie. Proponujemy nowe podejście do uzyskania reprezentatywnego materiału „całkowicie skarbonatyzowanego” w stosunkowo krótkim czasie. Innowacyjne użycie cienkiej próbki z pasty cementowej pozwoliło na scharakteryzowanie właściwości dyfuzji gazu w naturalnie skarbonatyzowanej paście cementowej. To, wraz ze zmierzonymi zmianami składu fazowego i struktury porów, może być wykorzystane do lepszego zrozumienia modelu reaktywnego transportu. Dostosowanie do naturalnych warunków ekspozycji zapewnia uzyskanie reprezentatywnych wyników.

Badanie regulujących parametrów karbonatyzacji i podkreślenie wpływu niesarbonatyzowanego odnośnika przyczyniło się do lepszego zrozumienia mechanizmu karbonatyzacji, zwłaszcza w przypadku spoiw o niskiej zawartości węgla. Niniejsza praca rzuca nowe światło na problem przeszacowania wpływu karbonatyzacji na mikrostrukturę materiałów cementowych. W szczególności pokazuje to, jak ważne jest rozróżnienie efektu wysuszenia zachodzącego podczas karbonatyzacji, by zmniejszyć ryzyko przypisywania wszelkich zmian jedynie karbonatyzacji.

Monitorowanie zmian w składzie fazowym oraz ocena współczynnika karbonatyzacji podczas ekspozycji na karbonatyzację wykazały obiecujące wyniki dla nowej mieszanki trójskładnikowej z 50 % zastąpieniem klinkieru przez spalony łupek olejowy, żużel i kamień wapienny.

Uzyskane wyniki charakteryzacji skarbonatyzowanych spoiw można wykorzystać do ulepszenia modeli karbonatyzacji, które są niezbędne do przewidywania odporności nowych cementów. Może to pomóc w ocenie równowagi między korzyściami płynącymi z użycia dodatków mineralnych a potencjalnym niebezpieczeństwem niskiej odporności na karbonatyzację. Zyskiem będzie uczynienie cementu i betonu jeszcze bardziej zrównoważonym i bardziej przyjaznym dla środowiska materiałem budowlanym.

Słowa kluczowe: karbonatyzacja, transport reaktywny, współczynnik dyfuzji, rozkład wielkości porów, karbonatyzacja naturalna, skład fazowy, dodatki mineralne

Contents

Acknowledgements	v
Abstract	vii
Résumé	ix
Zusammenfassung	xi
Streszczenie	xiii
List of Figures	xvii
List of Tables	xxiii
Chapter 1 Introduction	1
1.1 Overview	1
1.2 Statement of the problem	2
1.3 Research objectives	3
1.4 Thesis structure and main contributions	4
Chapter 2 State of the art	7
2.1 Mechanism of carbonation	7
2.2 Effect of carbonation on porosity	12
2.3 Change in diffusion properties in concrete	13
2.4 Effect of relative humidity	14
2.5 Accelerated vs natural carbonation	15
2.6 About available carbonation models	16
Chapter 3 Materials and methods	19
3.1 Characterization of raw materials	20
3.1.1 Physical properties	20
3.1.2 Chemical and mineralogical composition	20
3.2 Sample preparation and exposure conditions	24
3.2.1 Cement paste	24
3.2.2 Microconcrete and concrete	25
3.3 Experimental methods	28
3.3.1 X-ray powder diffraction (XRD)	28
3.3.2 Thermogravimetric analysis (TGA)	29
3.3.3 High-resolution microscope	30
3.3.4 Scanning electron microscopy (SEM-EDS)	30
3.3.5 Mercury intrusion porosimetry (MIP)	31
3.3.6 Water dynamic vapour sorption (DVS)	32
3.3.7 Non-steady state gas diffusion	33
3.3.8 Carbonation depth	35

Chapter 4	Carbonation rates.....	37
4.1	Effect of the binder composition, curing time and relative humidity on carbonation rate	38
4.2	Further study on the influence of curing time and w/c on selected blends	41
4.3	Meaning of w/CaO _{reactive} and its effect on carbonation rate	43
4.4	Natural vs accelerated carbonation	46
Chapter 5	Microstructural characteristics of the cement paste and its changes due to drying.....	49
5.1	Porosity evolution due to drying	50
5.1.1	Porosity evolution studied by MIP	50
5.1.2	Microstructure investigation using backscatter-electron images (BSE).....	56
5.1.3	Morphology investigation using high-resolution microscopy	59
5.2	Phase assemblage	63
5.2.1	XRD-Rietveld quantification	63
5.2.2	Differential thermogravimetry analysis	66
5.2.3	C-S-H composition studied by SEM-EDX	66
5.3	Impact of reimmersion on porosity	67
Chapter 6	Microstructural changes of the cement paste due to carbonation.....	69
6.1	Changes in phase assemblage during carbonation.....	70
6.1.1	Qualitative and quantitative analysis using XRD-Rietveld and TGA/DTG	70
6.1.2	Determination of the total CaCO ₃ and degree of carbonation	84
6.2	Microstructure investigation using microscopy.....	91
6.2.1	Backscatter-electron images of the surface of the exposed samples	91
6.2.2	BSE images and EDS mapping of the cross section of the exposed samples	94
6.2.3	Composition of C-S-H studied by SEM-EDS.....	100
6.2.4	Morphology investigation using high-resolution microscopy	105
Chapter 7	Changes of the pore structure and diffusivity due to carbonation.....	107
7.1	Changes of the pore structure during carbonation	108
7.2	Gas diffusion	124
7.3	Dynamic vapor sorption (DVS)	132
7.4	Comparing the porosity changes with existing literature	134
Chapter 8	Conclusions and perspectives.....	137
Appendix A	Composition of C-S-H	141
Appendix B	XRD diffractograms during exposure to carbonation	145
Appendix C	Porosity characteristics during exposure to carbonation	149
Appendix D	Code for obtaining the diffusion coefficient	151
References		155
Curriculum Vitae		161

List of Figures

Figure 1-1. Correlation between different factors controlling carbonation reactive transport model; Scope of this research includes “Microstructure characterization” and “Transport properties”..... 4

Figure 2-1. The main chemical species involved in carbonation phenomena [15]. 8

Figure 2-2. pH values of dissolution of individual hydrates [30]...... 10

Figure 2-3. Thermodynamic predictions of phase assemblage of the cement paste during carbonation [30][41]. 11

Figure 2-4. The Cement/Concrete carbon cycle, “chemical” CO₂ emitted during production from limestone breakdown is proportional to CO₂ reabsorption capacity during carbonation [3]...... 11

Figure 2-5. Oxygen diffusion coefficient for carbonated and non-carbonated cement pastes [50]. 14

*Figure 2-6. Comparison of corrosion rate as a function of relative humidity and for different concretes [58].*15

Figure 2-7. Pore size distribution by mercury intrusion porosimetry (MIP) as a function of CO₂ concentration during carbonation for Portland cement (left) and slag cement (right) [60]. 16

Figure 2-8. Depth of carbonation as a function of the upscaling parameters m, h and μ [64]...... 17

Figure 3-1. Clinker and SCMs substitution levels for studied binders...... 20

Figure 3-2. Isothermal calorimetry at an early age (left) and the cumulative curve at later ages (right) for the investigated cement pastes. 22

*Figure 3-3. Polished section of burn oil shale; heterogenous distribution of elements observed by SEM-EDS.*23

Figure 3-4. Ternary plot of BOS showing the composition of the amorphous phase. 24

Figure 3-5. Procedure of paste samples preparation. 25

Figure 3-6. Schematic illustration of the sample dimensions. 25

Figure 3-7. Example of exposure condition during natural carbonation. 26

Figure 3-8. Compressive strength development of microconcrete made with OPC and blended cements at w/c=0.50. 28

Figure 3-9. Sample preparation for XRD-Rietveld analysis. 29

Figure 3-10. Illustration of the sample preparation for TGA. 29

Figure 3-11. Sample preparation for the high-resolution microscope...... 30

Figure 3-12. Determination of C-S-H composition from atomic scatter plots [70]...... 31

Figure 3-13. Sample preparation for SEM. 31

Figure 3-14. The way of determining total porosity, critical pore radius and threshold pore entry radius from MIP curves [71]. 32

Figure 3-15. Illustration of the sample preparation for MIP analysis. 32

Figure 3-16. Sample preparation for DVS...... 33

Figure 3-17. Oxygen diffusion cell sketch ([11]) 34

Figure 3-18. Sample preparation for diffusion test...... 34

Figure 3-19. Microconcrete cube (4cm) broken with the use of hydraulic press (left picture) and sprayed with thymolphthalein (blue) and phenolphthalein(pink) pH indicators to measure the carbonation depth (right picture)...... 35

<i>Figure 4-1. Research scope: carbonation rates.</i>	37
<i>Figure 4-2. Clinker and SCMs substitution levels for studied binders.</i>	38
<i>Figure 4-3. Carbonation depth as a function of cement type and curing time (w/c=0.50, natural CO₂ concentration, 22°C and 55% RH).</i>	39
<i>Figure 4-4. Dependence of relative humidity on carbonation rate for microconcretes made with different binder compositions, with w/c=0.50, cured for 28 days.</i>	40
<i>Figure 4-5. Influence of curing time and w/c for CEM II/B-M and CEM I undergoing natural carbonation in 55% RH for 3 years.</i>	41
<i>Figure 4-6. Influence of decreasing of the w/c on carbonation rate for CEM II/B-M blend cured for 1, 3 and 28 days before exposure to carbonation.</i>	42
<i>Figure 4-7. Influence of decreasing of the w/c on carbonation rate for CEM I cured for 3 and 28 days before exposure to carbonation.</i>	43
<i>Figure 4-8. Carbonation coefficient as a function of CaO_{reactive} at 3 different relative humidity conditions, A): 55 % RH, B): 70 % RH and C): 86 % RH).</i>	45
<i>Figure 4-9. Natural carbonation compared to accelerated test.</i>	46
<i>Figure 5-1. Research scope: characterisation of the cement paste microstructure.</i>	50
<i>Figure 5-2. Impact of drying on pore size distribution for OPC and blended cements paste, cured for 3 days at RH > 95 %, followed by exposure at 70 % RH in a CO₂-free atmosphere. For all cements, except MixSL, w/c=0.40.</i>	53
<i>Figure 5-3. Impact of drying on pore size distribution for OPC and blended cements paste cured for 28 days at RH > 95 %, followed by exposure at 70 % RH in a CO₂-free atmosphere. For all cements, except one of the MixSL, w/c=0.40.</i>	54
<i>Figure 5-4. Critical entry pore size for OPC and blended cement pastes after curing for 3 and 28 days, followed by exposure at 70 % RH in CO₂-free atmosphere.</i>	55
<i>Figure 5-5. Total porosity quantification of OPC and blended cement pastes after curing for 3 and 28 days, followed by exposure at 70 % RH in CO₂-free atmosphere.</i>	55
<i>Figure 5-6. Consequence of the exposure at different relative humidities on the coarsening effect.</i>	56
<i>Figure 5-7. BSE for CEM I cured for 28 days (A) and then exposed at 70 % RH in CO₂-free atmosphere for 1 month (B).</i>	57
<i>Figure 5-8. BSE for CEM II/B-M cured for 28 days (A) and then exposed at 70 % RH in CO₂-free atmosphere for 1 month (B) and 2 months (C).</i>	58
<i>Figure 5-9. BSE for CEM II/B-M cured for 3 days (A) and then exposed at 70 % RH in CO₂-free atmosphere for 1 month (B).</i>	58
<i>Figure 5-10. Schematic morphologies of C-S-H during hydration (divergent C-S-H) and after exposure into drying in CO₂-free environment (convergent C-S-H) in decreased RH.</i>	59
<i>Figure 5-11. Micrographs of CEM I at 3 days of curing (on the left) vs additional 12 months of drying at 70 % RH (on the right).</i>	60
<i>Figure 5-12. Micrographs of CEM II/B-LL at 3 days of curing (on the left) vs additional 12 months of drying at 70 % RH (on the right).</i>	61
<i>Figure 5-13. Micrographs of CEM II/B-M at 3 days of curing (on the left) vs additional 12 months of drying at 70 % RH (on the right), illustrating the usage of the ImageJ, measuring the radius of 50 pores per picture.</i>	62
<i>Figure 5-14. Comparison of the pore radius obtained from MIP vs semi-quantitative image analysis method measuring the pore radius from SFEG micrographs.</i>	62

<i>Figure 5-15. Portlandite (Ca(OH)₂) and calcium carbonate (CaCO₃) content as a function of exposure time in CO₂-free atmosphere and 70 % RH, for several mixes and curing times. For all cements, except one of the MixSL, w/c=0.40.</i>	64
<i>Figure 5-16. Changes in unreacted clinker content as a function of exposure time in CO₂-free atmosphere and 70 % RH, for several mixes and curing times.</i>	65
<i>Figure 5-17. DTG graph during exposure at 70 % RH and CO₂-free atmosphere, for the ternary blend with limestone and burnt oil shale after 28 days of curing.</i>	66
<i>Figure 5-18. Changes of the critical pore radius due to after-curing in the pore solution.</i>	68
<i>Figure 5-19. Total porosity changes due to after curing in the pore solution.</i>	68
<i>Figure 6-1. Research scope: changes in the phase assemblage due to carbonation.</i>	70
<i>Figure 6-2. XRD diffractograms of CEM II/B-M during 2 years of exposure to natural carbonation, after 28 days of curing; E-ettringite, Hc-hemicarboaluminate, Mc-monocarboaluminate, P-portlandite, A-Aragonite, V-vaterite, C-calcite.</i>	71
<i>Figure 6-3. XRD-Rietveld quantification of the crystalline hydrated phases (portlandite, ettringite, and unreacted clinker) during exposure to carbonation at 70 % RH (CEM I, 3 and 28 days of curing).</i>	71
<i>Figure 6-4. XRD-Rietveld quantification of the crystalline hydrated phases content (portlandite, ettringite, and unreacted clinker) during exposure to carbonation at 70 % RH (CEM II/B-M, 3 and 28 days of curing).</i>	72
<i>Figure 6-5. XRD-Rietveld quantification of the crystalline hydrated phases content (portlandite, ettringite, and unreacted clinker) during exposure to carbonation at 70 % RH (CEM II/B-LL, 3 and 28 days of curing).</i>	72
<i>Figure 6-6. XRD-Rietveld quantification of the crystalline hydrated phases content (portlandite, ettringite, and unreacted clinker) during exposure to carbonation at 70 % RH (CEM III/A, 3 and 28 days of curing).</i>	73
<i>Figure 6-7. XRD-Rietveld quantification of the crystalline hydrated phases content (portlandite, ettringite, and unreacted clinker) during exposure to carbonation at 70 % RH (MixSL, 3 and 28 days of curing).</i>	73
<i>Figure 6-8. XRD-Rietveld quantification of the crystalline hydrated phases content (portlandite, ettringite, and unreacted clinker) during exposure to carbonation at 70 % RH (MixSL with w/c=0.35, 3 and 28 days of curing).</i>	73
<i>Figure 6-9. Changes in ettringite content after exposure to carbonation at 70 % RH and to CO₂-free atmosphere at 70 % RH (left figure) and changes in amorphous content for the same samples at CO₂-free atmosphere at 70 % (right figure); CEM I, 3 and 28 days of curing.</i>	75
<i>Figure 6-10. DTG curves for CEM I cured for 28 days and exposed to CO₂-free atmosphere at 70% RH.</i>	75
<i>Figure 6-11. Carbonation depth measured with phenolphthalein and thymolphthalein pH indicator, for different mixes. All cements were cured for 28 days before exposure to carbonation. Carbonation depths for mixes A-D were measured after 24 months of carbonation, while mixes E and F, after 18 months of exposure to carbonation at 70 % RH.</i>	76
<i>Figure 6-12. XRD-Rietveld quantification of the calcium carbonate content in the carbonating samples (3 and 28 days of curing, carbonation at 70 % RH).</i>	77
<i>Figure 6-13. Illustration of thermodynamic limitations for calcite precipitation (figure used with the permission of F. Georget).</i>	78
<i>Figure 6-14. TGA curves of the carbonating cement mixes.</i>	80
<i>Figure 6-15. DTG curves of the carbonating cement mixes.</i>	81
<i>Figure 6-16. TGA and DTG plots for CEM II/B-LL, indicating the temperature range chosen for the calculation of the total CaCO₃, which was used in further calculations for estimating the degree of carbonation.</i>	83
<i>Figure 6-17. Degree of carbonation.</i>	86
<i>Figure 6-18. Carbonation depth as a function of cement type (w/c=0.50, natural CO₂ concentration, 22°C, and 55% RH) for microconcrete samples (see chapter 4 for the details).</i>	87

Figure 6-19. The relation between the DoC measured in cement paste, and the carbonation coefficient measured in microconcrete.	87
Figure 6-20. Average of the CaCO ₃ origin (portlandite, ettringite, or C-S-H and other hydrates) during carbonation, coming from carbonated, non-carbonated, and reaction front regions in 1mm thin disk, during 18 or 24 months of natural carbonation at 70 & RH.	89
Figure 6-21. Carbonation degree of portlandite, during 2 years of exposure to carbonation at 70 % RH.	90
Figure 6-22. Amount of amorphous CaCO ₃ for various cement mixes cured for 28 days and exposed to carbonation at RH 70% (total CaCO ₃ content from TGA decreased by subtracting the crystalline CaCO ₃ obtained from XRD-Rietveld).	91
Figure 6-23. SEM-BSE images of CEM I cured for 28 days and exposed at RH 70%, A): for 1 month at CO ₂ -free atmosphere, B): for 1 month at 400 ppm of CO ₂ , C): for 2 months at 400 ppm of CO ₂	92
Figure 6-24. SEM-BSE images of CEM II/B-M cured for 28 days and exposed at RH 70%, A): for 1 month at CO ₂ -free atmosphere, B): for 1 months at 400 ppm of CO ₂ , C): for 2 months at 400 ppm of CO ₂	93
Figure 6-25. SEM-BSE images of CEM II/B-M cured for 3 days and exposed at RH 70%, A): for 1 month at CO ₂ -free atmosphere, B): for 1 months at 400 ppm of CO ₂	93
Figure 6-26. Cross section of the hydrated disk exposed to CO ₂ -free atmosphere (A) and to carbonation (B), at 70 % RH; CEM II/B-M cured for 28 days before exposure.	94
Figure 6-27. Composite map of sulphur (S) and sodium (Na) of CEM I exposed to CO ₂ -free atmosphere (top) and to carbonation (down), at 70 % RH.	95
Figure 6-28. S/Ca ratio (top) and Na/Ca ratio(down) in hydrates, as a function of depth; CEM I exposed to CO ₂ -free atmosphere, and to carbonation at 70 % RH.	96
Figure 6-29. Cross section of the hydrated disk, exposed to CO ₂ -free atmosphere (A) and to carbonation (B), at 70 % RH; CEM II/B-M cured for 28 days before exposure.	97
Figure 6-30. Composite map of sulphur (S) and sodium (Na) of CEM II/B-M exposed to CO ₂ -free atmosphere (top) and to carbonation (down), at 70 % RH.	98
Figure 6-31. S/Ca ratio (top) and Na/Ca ratio(down) in hydrates, as a function of depth; CEM II/B-M exposed to CO ₂ -free atmosphere and to carbonation, at 70 % RH.	99
Figure 6-32. Solid phases profiles for the reference solution at 30 days [8].	100
Figure 6-33. Example of selected points of inner and outer C-S-H for calculating the chemical composition of C-S-H; (CEM II/B-M, 28d curing (left) and 28d curing + 2 months of carbonation (right)).	101
Figure 6-34. EDS point analysis of CEM I, cured for 28 days and exposed at RH 70 %, A): for 1 month at CO ₂ -free atmosphere, B): for 1 month at 400 ppm of CO ₂ , C): for 2 months at 400 ppm of CO ₂	102
Figure 6-35. EDS point analysis of CEM II/B-M cured for 28 days and exposed at RH 70 %, A): for 1 month at CO ₂ -free atmosphere, B): for 1 month at 400 ppm of CO ₂ , C): for 2 months at 400 ppm of CO ₂	103
Figure 6-36. EDS point analysis of CEM II/B-M cured for 3 days and exposed at RH 70% A) for 1 month at CO ₂ -free atmosphere, B) for 1 month at 400 ppm of CO ₂	104
Figure 6-37. Images of CEM II/B-M cured for 3 days and exposed at 70 % RH for 12 months at CO ₂ -free atmosphere (left), and for 12 months at 400 ppm of CO ₂ (right).	105
Figure 7-1. Research scope: Pore size distribution and transport properties during carbonation.	107
Figure 7-2. Impact of carbonation on the pore size distribution and on the total porosity for CEM I cured for 3 and 28 days, followed by exposure at 70 % RH with atmospheric CO ₂ concentration.	109
Figure 7-3. Impact of carbonation on the pore size distribution and on the total porosity for CEM II/B-M cured for 3 and 28 days, followed by exposure at 70 % RH with atmospheric CO ₂ concentration.	110
Figure 7-4. Impact of carbonation on the pore size distribution and on the total porosity for CEM II/B-LL cured for 3 and 28 days, followed by exposure at 70 % RH with atmospheric CO ₂ concentration.	111

Figure 7-5. Impact of carbonation on the pore size distribution and on the total porosity for CEM III/A cured for 3 and 28 days, followed by exposure at 70 % RH with atmospheric CO ₂ concentration.	112
Figure 7-6. Impact of carbonation on the pore size distribution and on the total porosity for MixSL cured for 28 days, followed by exposure at 70 % RH with atmospheric CO ₂ concentration.	112
Figure 7-7. Impact of carbonation on the pore size distribution and on the total porosity for MixSL (w/c=0.35), cured for 3 and 28 days, followed by exposure at 70 % RH with atmospheric CO ₂ concentration.	113
Figure 7-8. Total porosity quantification of OPC and blended cement pastes after curing for 3 and 28 days, followed by exposure to carbonation at 70 % RH.	114
Figure 7-9. Critical pore radius quantification of OPC and blended cement pastes after curing for 3 and 28 days, followed by exposure to carbonation at 70 % RH.	114
Figure 7-10. Porosity analysis of CEM I exposed to carbonation and to CO ₂ -free atmosphere at 70 % RH; 3- and 28-days curing time before exposure (t ₀).	115
Figure 7-11. Porosity analysis of CEM II/B-M exposed to carbonation and to CO ₂ -free atmosphere at 70 % RH; 3- and 28-days curing time before exposure (t ₀).	116
Figure 7-12. Porosity analysis of CEM II/B-LL exposed to carbonation and to CO ₂ -free atmosphere at 70 % RH; 3- and 28-days curing time before exposure (t ₀).	117
Figure 7-13. Porosity analysis of CEM III/A exposed to carbonation and to CO ₂ -free atmosphere at 70 % RH; 3- and 28-days curing time before exposure (t ₀).	118
Figure 7-14. Porosity analysis of MixSL exposed to carbonation and to CO ₂ -free atmosphere at 70 % RH; 28-days curing time before exposure (t ₀).	118
Figure 7-15. Porosity analysis of MixSL (w/c=0.35) exposed to carbonation and to CO ₂ -free atmosphere at 70 % RH; 3- and 28-days curing time before exposure (t ₀).	119
Figure 7-16. Total porosity, critical pore radius, and entry pore radius changes after carbonation in compare with two references: before exposure and exposure at CO ₂ -free atmosphere; CEM I cured for 3 and 28 days before exposure.	120
Figure 7-17. Total porosity, critical pore radius, and entry pore radius changes after carbonation in compare with two references: before exposure and exposure at CO ₂ -free atmosphere; CEM II/B-M cured for 3 and 28 days before exposure.	120
Figure 7-18. Total porosity, critical pore radius, and entry pore radius changes after carbonation in compare with two references: before exposure and exposure at CO ₂ -free atmosphere; CEM II/B-LL cured for 3 and 28 days before exposure.	121
Figure 7-19. Total porosity, critical pore radius, and entry pore radius changes after carbonation in compare with two references: before exposure and exposure at CO ₂ -free atmosphere; CEM III/A cured for 3 and 28 days before exposure.	121
Figure 7-20. Total porosity, critical pore radius, and entry pore radius changes after carbonation in compare with two references: before exposure and exposure at CO ₂ -free atmosphere; MixSL cured for 28 days before exposure.	122
Figure 7-21. Total porosity, critical pore radius, and entry pore radius changes after carbonation in compare with two references: before exposure and exposure at CO ₂ -free atmosphere; MixSL, w/c=0.35, cured for 3 and 28 days before exposure.	122
Figure 7-22. Porosity distribution after carbonation vs before exposure vs elongated curing (90 days) vs exposure at CO ₂ -free atmosphere vs non-carbonated zone of a cylinder exposed to carbonation.	124
Figure 7-23. Correlation of the total porosity, the critical pore radius, and the entry pore radius with diffusion coefficient for carbonated and non-carbonated samples cured for 3 days before carbonation.	127
Figure 7-24. Correlation of the total porosity, the critical pore radius, and the entry pore radius with diffusion coefficient for carbonated and non-carbonated samples cured for 28 days before carbonation.	128

<i>Figure 7-25. Correlation of the diffusion coefficient with the total porosity obtained from MIP; A): linear scale, $R^2=0.51$, B): logarithmic scale.</i>	129
<i>Figure 7-26. Correlation of the diffusion coefficient with the critical pore radius obtained from MIP; A): linear scale, $R^2=0.82$, B): logarithmic scale.</i>	130
<i>Figure 7-27. Correlation of the diffusion coefficient with the entry pore size obtained from MIP; A): linear scale, $R^2=0.85$, B): logarithmic scale.</i>	131
<i>Figure 7-28. DVS of the CEM II/B-M, exposed to CO₂-free atmosphere (left) and to carbonation (right), at 70 % RH for 30 months after 28 days of curing.</i>	132
<i>Figure 7-29. DVS of the CEM III/A, exposed to CO₂-free atmosphere (left) and to carbonation (right), at 70 % RH for 30 months after 28 days of curing.</i>	133
<i>Figure 7-30. Mass dependence during 6 months exposure at 70 % RH in CO₂-free atmosphere for all studied cements.</i>	135
<i>Figure A-8-1. C-S-H composition studied by SEM-EDS for CEM I cured for 28 days (A) and then exposed at 70 % RH in CO₂-free atmosphere for 1 month (B).</i>	141
<i>Figure A-8-2. C-S-H composition studied by SEM-EDS for CEM II/B-M cured for 28 days (A) and then exposed at 70 % RH in CO₂-free atmosphere for 1 month (B) and 2 months (C).</i>	142
<i>Figure A-8-3. C-S-H composition studied by SEM-EDS for CEM II/B-M cured for 3 days (A) and then exposed at 70 % RH in CO₂-free atmosphere for 1 month (B).</i>	143

List of Tables

<i>Table 2-1. Properties of the minerals which can be involved in the carbonation process (adapted from [45][21])</i>	12
<i>Table 3-1. Physical properties of the cements and of the raw materials.</i>	20
<i>Table 3-2. Oxide composition of the cements and the raw materials.</i>	21
<i>Table 3-3. Mineralogical composition of cements and raw materials.</i>	21
<i>Table 3-4. Oxide composition from XRF compared with oxide composition obtained from SEM-EDS mapping.</i>	23
<i>Table 3-5. Summary of the sample preparation and exposure conditions of the microconcrete and concrete exposed to carbonation.</i>	26
<i>Table 3-6. Microconcrete mixture proportions.</i>	27
<i>Table 4-7. Carbonation coefficients changes after increasing curing time before exposure to carbonation (data from Figure 4-3).</i>	40
<i>Table 4-8. Content of reactive CaO for various binders with different w/c.</i>	44
<i>Table 4-9. Comparison of the sample preparation, curing and exposure conditions for natural and accelerated carbonation tests.</i>	47
<i>Table 5-1. Critical pore radius changes for all cement types after the increase of the curing time from 3 days to 28 days.</i>	51
<i>Table 5-2. Total porosity changes for all cement types after the increase of the curing time from 3 days to 28 days.</i>	51
<i>Table 5-3. Ca/Si ratios of the C-S-H composition (average of inner and outer C-S-H) for different cement types.</i>	67
<i>Table 6-1. Verification of the amount of CaCO₃ amount vs decomposition of CaCO₃, in different temperature ranges present in the literature [37].</i>	83
<i>Table 6-2. Capacity of CO₂ binding in the different cements.</i>	84
<i>Table 6-3. Total amount CaCO₃ originated by carbonation, and degree of carbonation.</i>	85
<i>Table 6-4. Ca/Si ratios of the C-S-H composition (average of inner and outer C-S-H) for different cement types before exposure to carbonation.</i>	104
<i>Table 7-1. Different types of reference samples compared with carbonated sample.</i>	123
<i>Table 7-2. Diffusion coefficient as a function of cement type, curing time and exposure conditions.</i>	125
<i>Table 7-3. Example of repeatability of the test; standard deviation evaluated after testing 3 different samples of the same system.</i>	126
<i>Table C-1. Total porosity, critical pore radius and entry pore radius changes due to exposure to carbonation in a function of cement type and curing time.</i>	149



Chapter 1 Introduction

1.1	Overview.....	1
1.2	Statement of the problem.....	2
1.3	Research objectives.....	3
1.4	Thesis structure and main contributions	4

1.1 Overview

Concrete is a cheap, durable, and environmentally friendly material with very low emission of CO₂ and energy. However, due to the growing needs to satisfy the demand for construction using enormous volumes of this material, concrete accounts for 5 to 10 % of man-made CO₂ emission worldwide [1]. This is an essential material for infrastructure to build houses, roads, and bridges so we cannot replace it with another material but we have to make it better to reach the goals of sustainable development. Lowering the clinker content in concrete, which is the most produced material in the world, can significantly contribute to the decrease of the embodied energy and of the carbon dioxide emission of concrete. To reduce this impact, the use of supplementary cementitious materials (SCMs) in the cement industry has become a common practice. Increasing and widespread use of such composite cements is advantageous in both, environmental and engineering aspects. Utilizing SCMs can also lead to improvements in durability through enhancement of the cement microstructure. Typical replacement levels for CEM II/B are presently between 21-35 % [2] but the objective is to move to a higher replacement level. However, the practical experience on such cements is limited. Two of the major reasons blocking this uptake are the limited strength at early ages and the concern about long term performance/durability, especially higher carbonation rates due to a lower capacity to bind CO₂ [3].

Concrete is responsible for protecting the steel in reinforced concrete structures. However, concrete structures are continuously exposed to a certain amount of carbon dioxide in the atmosphere (approximately 400ppm in the air). This CO₂ can penetrate into concrete through the pores, dissolve in pore solution, and react with the hydrated phases to form carbonated phases. The process leads to the lowering of the pH of the pore solution from about above 13 to around 9 [4]. This causes the dissolution of the protective surface oxide layer of the

steel bars and their depassivation, and the corrosion of the steel reinforcement [5]. To increase the protection of the steel in the concrete full understanding of the microstructure changes is necessary.

1.2 Statement of the problem

The carbonation rate is sensitive to many parameters (Figure 1-1). The formulation of the binder and the design of the concrete, together with the curing time and the exposure conditions, all have an influence on the hydrated solid phases and the corresponding pore structure. Transport properties affect back this microstructure. Due to the alteration of the microstructure occurring during carbonation, the diffusion parameters of the carbonated layer also change. Many data published on diffusion properties, enquired in the laboratory, were focused on avoiding interaction with carbon dioxide. All those results are important but they become less relevant for durability assessment, due to disregarding the fact that concrete structures are exposed to carbonation, and change the microstructure attributed to the presence of carbon dioxide in the atmosphere.

Diffusion of carbon dioxide towards the non-carbonated layer occurs through the carbonated zone. Understanding and quantifying the correlation between transport properties and microstructure in carbonated concrete would help to fill the gap of missing data needed to obtain a good carbonation model [6][7][8]. The lack of the required data causes difficulties in simulating the long-term durability issues, such as carbonation, especially for concrete made with supplementary cementitious materials. Investigating the changes of the solid phase assemblage, which modifies the microstructure, and thus the transport properties, could bring forward the field of carbonation modeling.

Moreover, the carbonation of concrete is a slow phenomenon and in laboratory studies special treatments are often used to accelerate the carbonation rate, and corrosion of the steel. The accelerated carbonation tests are the most widely used approaches to assess the performance of new materials because of their relatively short duration (few months). Unfortunately, such tests change the mechanisms of carbonation, taking place in the natural environment. For example, different calcium carbonate polymorphs are formed during accelerated carbonation, where CO_2 concentration is increased [9]. Although accelerated tests have advantages in terms of time scale, they can provide too conservative results for blended cement systems. Furthermore, there is no consensus among researchers or civil engineers on the procedure that should be followed to carry out accelerated carbonation tests. In Europe, there is a wide range of carbon dioxide level (between 1 and 50% of CO_2 concentration), preconditioning, and duration time for accelerated carbonation tests [10]. In general, studies on carbonation should be focused on better understanding the phases that are formed upon natural carbonation. That could help to decide the compatible accelerated tests, allowing extrapolation to natural conditions.

1.3 Research objectives

The main goal of this thesis is to understand, and to quantify the correlation between transport properties and modification of the microstructure in the carbonated concrete. This should advance the field of carbonation modeling, which in a global perspective will contribute to the prediction of the service life of real concrete structures. We adopted the following guidelines for the study:

- Focus the study on natural carbonation to avoid the risk of distorting the results of microstructure changes, which could take place in accelerated conditions.
- Deconvolution of the mechanism of carbonation from that of drying, to better identify the relative impact of individual parameters.
- Perform experiments on cement pastes to obtain precise quantitative results of the microstructure and transport properties. Furthermore, the use of thin paste samples allows to monitor the progress of carbonation over time and to accelerate the time to obtain a “fully carbonated” system in a relatively short time, while a parallel work on microconcrete samples allows to upscale the results to the concrete level.

Apart from traditional techniques to characterize the carbonated microstructure, a gas diffusion set-up [11] was adapted to use thin cement paste samples. This set-up is used to characterize the diffusion properties after carbonation and to compare them with non-carbonated microstructure. This process provides a new type of data, which brings us a step closer towards predicting carbonation rates of new cements types with reduced clinker content. In addition to commercially available blended cements, a new mix is tested in term of carbonation resistance. This mix, designed at ETHZ, uses limestone, slag, and burnt oil shale (BOS) and substitutes 50 % of the clinker content. Among different supplementary cementitious materials, BOS (available in Switzerland) has gained attention as one of the main potential substitution material, allowing a higher replacing of the clinker [12]. Figure 1-1 shows a schematic overview of the relationship between the objectives addressed in this thesis.

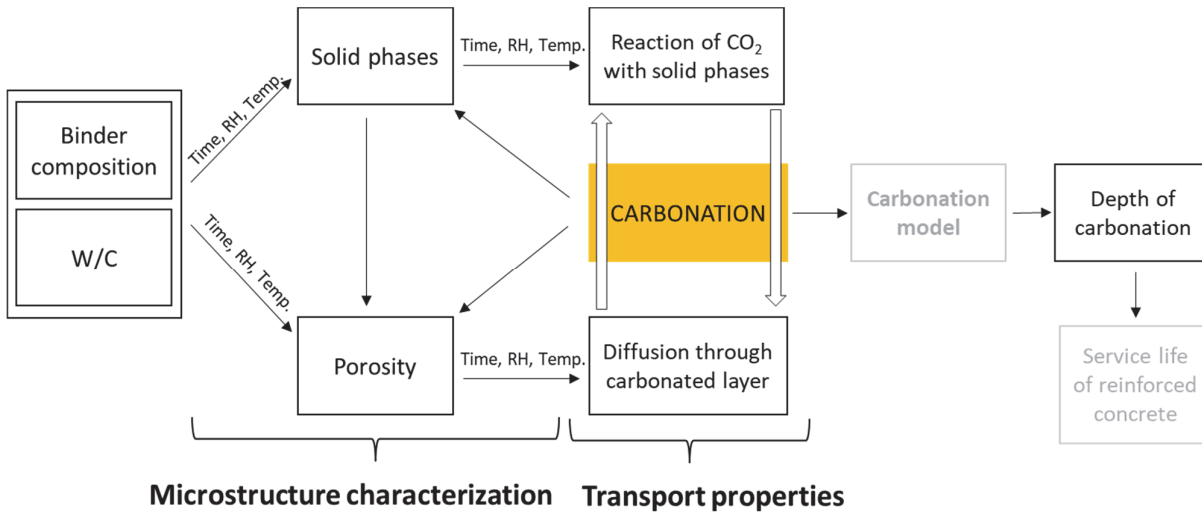


Figure 1-1. Correlation between different factors controlling carbonation reactive transport model; Scope of this research includes “Microstructure characterization” and “Transport properties”.

To better understand carbonation mechanism of low clinker binders, this work is linked with the studies carried on at ETHZ, dealing with developing new robust mixes with decreased clinker content, and with corrosion propagation in carbonated concrete [13]. This work is under the scope of the joint project “Low energy concrete” found by the National Research Programme.

1.4 Thesis structure and main contributions

The chapters are divided as follow:

Chapter 2 review of the current state of the art.

Chapter 3 materials and techniques used in this work.

Chapter 4 looks at how various parameters affect the carbonation rate. The focus is on the effect of the binder composition, curing time, relative humidity and water to cement ratio. Characteristics of carbonation coefficient, obtained in natural naturally carbonated microconcrete were also compared with accelerated carbonation method.

Chapter 5 describes the microstructural characteristics of hydrated cement paste and its changes due to drying during exposure at lower relative humidity (70 %) in the absence of CO₂. Understanding the porosity changes taking place during this drying, is important in the context of carbonation.

Chapter 6 discusses the influence of carbonation on the phase assemblage of the samples made with different cement formulations, characterized by different CO₂ binding capacities.

Chapter 7 focuses on the correlation of pore structure changes in carbonated cement paste with the diffusion coefficient of carbonated samples.

Finally, chapter 8 summarises the work, presents the main conclusions obtained from this work and it gives perspectives for further research in the carbonation field.

Main contributions:

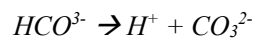
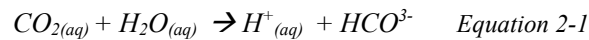
- Gas transport properties and microstructural changes during carbonation are characterized and a comprehensive set of data of the reactive transport phenomenon of CO₂ was obtained, that can be used in service-life models.
- The understanding of the carbonation mechanism is advanced by investigating governing parameters, and by emphasizing the influence of the non-carbonated reference.
- A new approach to measure gas diffusion is used to obtain the gas transport properties of “fully carbonated” cement paste specimens.
- A new approach is proposed to obtain a representative specimen of “fully carbonated” material in relatively short time. This carbonated material is needed to characterize its transport properties, without the risk of changing the microstructure due to increased CO₂ concentration.

Chapter 2 State of the art

2.1	Mechanism of carbonation.....	7
2.2	Effect of carbonation on porosity.....	12
2.3	Change in diffusion properties in concrete	13
2.4	Effect of relative humidity	14
2.5	Accelerated vs natural carbonation	15
2.6	About thermodynamics and available carbonation models	16

2.1 Mechanism of carbonation

CO₂ inherent in the air in the presence of moisture reacts with hydrated cement paste. In fact, the reacting species is carbonic acid from the dissolution of gaseous CO₂. As a weak acid, the carbonic acid H₂CO₃ dissociates into HCO₃⁻ and CO₃²⁻ ions [14] according to Eq. 2-1:



This dissolution, under equilibrium conditions, follows Henry's law illustrated by Eq. 2-2:

$$CO_{2(aq)} = K_h P_{CO_2} \quad \text{Equation 2-2}$$

Where CO_{2(aq)} is the activity of the dissolved CO_{2(aq)}, K_h is Henry's constant for the dissolution of CO_{2(g)} in water and P_{CO₂} is the atmospheric partial pressure of CO_{2(g)}.

Dissociated ions of carbonic acid penetrate into concrete through the pores from regions of high CO₂ concentration (the environment) to those of low. And they neutralize the basic compounds of hydrated cement, thereby modifying the chemical balances between the solution and the hydrates.

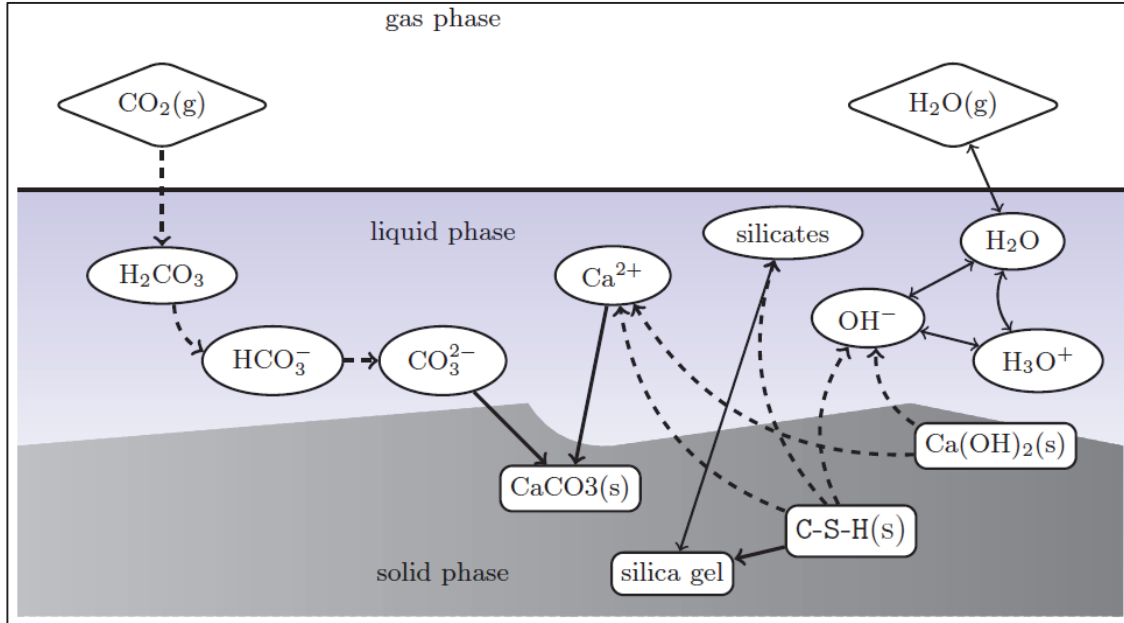


Figure 2-1. The main chemical species involved in carbonation phenomena [15].

Aqueous carbon dioxide reacts with cement paste phases to form carbonates [16]. The main cement hydrates, i.e. calcium silicate hydrate, calcium hydroxide, and various calcium aluminate or ferro-aluminate hydrates react to produce calcium carbonate, silica gel, hydrated aluminum, and iron oxides, while the sulphate originally present in the cement reverts to gypsum after complete carbonation. The concrete pore solution is an alkaline solution, which contains essentially sodium and potassium hydroxides. The presence of them reduces the solubility of calcium hydroxide [17]. Soluble Na_2CO_3 and K_2CO_3 form readily, as shown in Eq. 2-3. Reactions presented in Eq. 2-4 and Eq. 2-5 release hydroxyl ions which can again react with CO_2 as presented in Eq. 2-3. The process will be continued until portlandite and C-S-H are available [18].

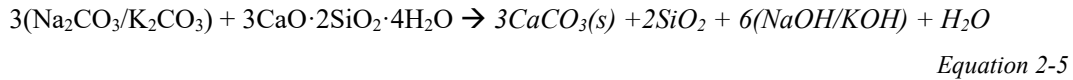
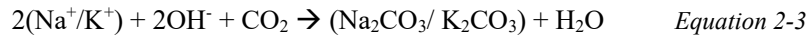
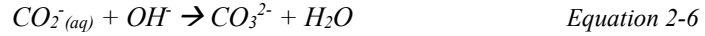
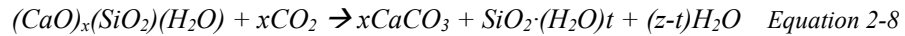


Figure 2-1 summarizes different chemical species involved in the carbonation of a cement paste containing CH and C-S-H in presence of water. In conventional Portland cements the concentration of calcium hydroxide is significant and the reaction of carbon dioxide with portlandite prevails. Calcium hydroxide buffers the alkaline pH of the pore structure. When solid calcium hydroxide dissolves, it releases calcium and hydroxyl ions which diffuse from regions of high alkalinity to those of low [4]. Eq. 2-6 and Eq. 2-7 present the precipitation of CaCO_3 [19][20]. The reaction releases hydroxyl ions and can proceed as long as calcium hydroxide is available. Consumption of calcium hydroxide consequently reduces the pH of the pore solution [21].



In contrast to Portland cements, in pozzolanic cements part of calcium hydroxide is consumed by pozzolanic or additionally synergetic reactions [22], and only the remaining quantity is available for carbonation. It has been shown that carbonation depth is greater when the content of $Ca(OH)_2$ is lower [23]. However, in the same cement type, another effect was also observed, namely during the reaction between silica and $Ca(OH)_2$ the microstructure of cement paste becomes denser. This causes a decrease of CO_2 diffusion rate and in consequence, limits the rate of carbonation. In the systems where $Ca(OH)_2$ has been depleted or was absent from the beginning, carbonation proceeds further by the consumption of C-S-H or any calcium-bearing hydrate present in the system and in equilibrium with the pore solution. Carbonation products of C-S-H can be described by Eq. 2-8:



Carbonation of C-S-H depends on its initial Ca/Si ratio [24][25][26]. Well known low-density (outer product) and high-density (inner product) C-S-H carbonate differently. The outer product carbonates [27], and both products become a silica-gel [24]. It was also shown, that carbonation of C-S-H lowers the Ca/Si ratio and leads to the formation of silica gel and less stable forms of $CaCO_3$ such as vaterite and aragonite [28]. Sauman [29] found that vaterite is the first reaction product formed, and is gradually converted to the stable modification – calcite.

Decomposition of the different hydrates takes place in different pH, as shown in Figure 2-2 [30]. Ettringite, similarly to C-S-H, decomposes below pH of around 10.4 [31]. It was shown in the literature that AFt decomposes to calcium carbonate, gypsum and alumina gel [32][33][34]. The decomposition process is illustrated in the following reaction (Eq. 2-9):



Some study showed that unhydrated cement grains also can dissolve due to the reaction with CO_2 [27][35].

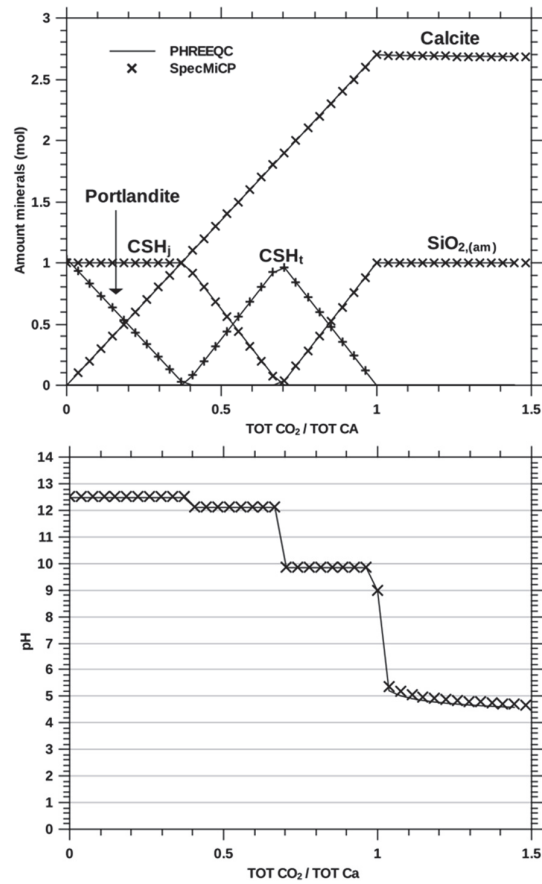


Figure 2-2. pH values of dissolution of individual hydrates [30].

It was shown that portlandite does not always deplete completely during carbonation. Some researchers explain, that as carbonation progress, the rate of portlandite dissolution decreases due to the formation of a relatively dense microcrystalline calcium carbonate layer around partially dissolved the CH crystals [36][37][38][39]. It is a proposed explanation to the common observation that after a period of relatively rapid consumption of portlandite, its carbonation rate is significantly reduced [40], and other hydrates, such as C-S-H or ettringite starts to carbonate in spite portlandite is still in the system. From the other hand, thermodynamic modeling shows that portlandite is the first phase to carbonate (Figure 2-3), followed by carbonation of other phases i.e. C-S-H or ettringite after the complete depletion of CH [30][41].

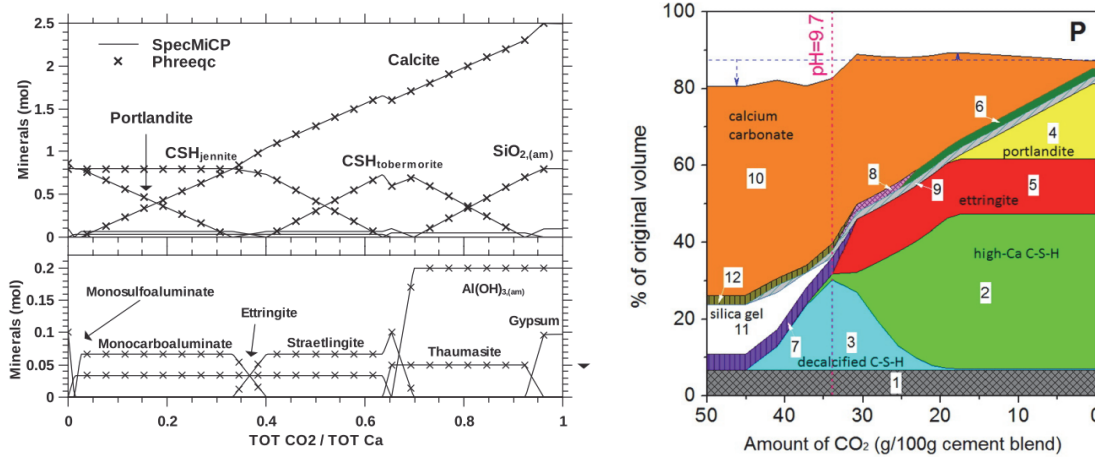


Figure 2-3. Thermodynamic predictions of phase assemblage of the cement paste during carbonation [30][41].

In general, all calcium-bearing hydrates, as well as unreacted clinker grains, can carbonate and contribute to the formation of calcium carbonate. Researchers agree that the amount of CaCO_3 formed significantly exceed the CaCO_3 amount that could result in the complete dissolution of $\text{Ca}(\text{OH})_2$ [37][39][42][35].

The capacity of how much CO_2 can be bound into the hydrated cement paste is directly related to the reactive CaO which after the reaction with CO_2 can precipitate as CaCO_3 . It is related to the carbon cycle, presented in Figure 2-4 [3]. It basically shows that the same amount of CO_2 which is emitted during limestone decomposition ($\text{CaCO}_3 \rightarrow \text{CaO} + \text{CO}_2$) when producing cement, can react with hydration products and precipitate as calcium carbonate.

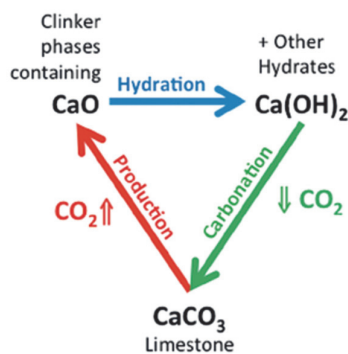


Figure 2-4. The Cement/Concrete carbon cycle, “chemical” CO_2 emitted during production from limestone breakdown is proportional to CO_2 reabsorption capacity during carbonation [3].

Carbonation rate of the concrete made with different cement types is largely governed by the CO_2 binding capacity[43][44]. The higher the content of reactive CaO , the more CO_2 can be bound by the hydrated cement paste, resulting in higher buffer capacity against carbonation. Researchers proposed that the binding capacity

per volume of paste is a decisive parameter for predicting resistance against carbonation, and can be expressed by the ratio between water and $\text{CaO}_{\text{reactive}}$ known as $w/\text{CaO}_{\text{reactive}}$ [43][44].

2.2 Effect of carbonation on porosity

Apart from the pH drop, causing the dissolution of the protective oxide layer around the steel rebars, one of the most notable changes of carbonation is the porosity. It is attributed to the dissolution of cement phases and precipitation of calcium carbonate in the pore network.

Table 2-1. Properties of the minerals which can be involved in the carbonation process (adapted from [45][21])

Mineral	Density (g/cm ³)	Molar volume (cm ³ /mol)	Variation of volume (%)
Portlandite	2.25	33.10	-
Calcite	2.71	36.90	11.5
Aragonite	2.93	34.48	4.2
Vaterite	2.66	37.59	13.6

Changes of the porosity and pore size distribution caused by carbonation are still not well understood. Coarsening of the pore structure and increase of porosity due to carbonation has been reported in the blended cements [46][41]. From the other hand, some researchers have observed a reduction of the porosity and refinement of pore structure after carbonation for OPC and cements containing SCMs, while other experimental results showed an increase of the critical pore radius and reduction of the total porosity for OPC.

Reduced porosity for CEM I upon carbonation was proven in many studies [47][48]. The formation of calcium carbonate in replacement of portlandite reduces the porosity of the material induced by increasing the volume. Depending if the formed crystal is aragonite, calcite or vaterite the volume increases respectively 4.2, 11.5 or 13.6 % (see Table 2-1). Calcite, which is the most stable form under normal temperature and pressure, is the main calcium carbonate polymorphs forming by carbonation. Higher molar volume of calcite occupies a greater volume than $\text{Ca}(\text{OH})_2$ [21].

It was shown on 20 year old concrete samples, that carbonation leads to coarsening of the pore structure of the concrete made with blended cement whereas for OPC pores become finer [49]. Some blended cements have much less amount of CH than traditional OPC. That often leads to formation of calcite in replacement of C-A-S-H, ettringite (AFt) or monosulphate hydrates (AFm) phases, and to increase the porosity of the material, since calcite has a lower molar volume in comparison to C-A-S-H, AFt and AFm phases (molar volume respectively 111.11 cm³/mol, 1000 cm³/mol and 250 cm³/mol) [45]. Due to differences in the molar volumes of the parent hydrates and solid products a decrease of the solid volume is expected to effect in increased porosity, and in the formation of silica gel due to C-S-H decomposition [50].

2.3 Change in diffusion properties in concrete

Diffusion is a process by which molecules can pass through the gas or liquid phase of the concrete down a concentration gradient [51]. Gas diffusion through the porous system is usually defined as the Fick's first law [52] for CO₂ and usually is expressed in a unit of cm²/s. The diffusion coefficient for CO₂-diffusion in concrete is described by Nilsson [53] as the flux of gaseous CO₂ through an infinitesimal layer of concrete (Eq.2-10):

$$J_{CO_2} = -D_{CO_2} \frac{\partial c}{\partial x} \quad \text{Equation 2-10}$$

Where D_{CO_2} is the diffusion coefficient, x refers to the depth and the cross-section of concrete, c is the CO₂ concentration given as an amount in a unit volume of air.

Carbonation rate depends on carbon dioxide migration through the porous structure of concrete. It is important to emphasize that the CO₂ diffusion coefficient in water is much smaller than in air, and this is a decisive factor in the process of carbonation [17]. In reality, diffusion processes in capillaries of porous media are complex and we can classify them into at least three independent transport mechanisms [54]:

- Molecular or ordinary diffusion, which takes place in larger pores where the mean free path of the gas molecules is smaller than pore diameter and molecule-molecule collisions dominate over the collisions between gas molecules and the pore walls.
- Knudsen diffusion or free molecule flow, which takes place if the pore dimensions are smaller than the mean free path of the gas molecules so that molecule-wall collisions dominate over molecule-molecule collisions.
- Surface diffusion or surface flow, which occurs when there is significant adsorption of the gas molecules on the pore walls and the gas molecules move in the adsorbed layer. It can occur at the same time in addition to the two above mentioned mechanisms but in very big pores surface diffusion becomes negligible.

The larger molar volume of calcium carbonate which precipitates during carbonation contributes to porosity clogging [55][56]. Ngala and Page [50] showed that carbonation had a large impact on oxygen diffusion resistance of hardened cement paste, with a larger effect on blended mixes than OPC. Houst and Wittman [48] noted that carbonation causes a decrease of the water absorption in comparison to non-carbonated sample. They also showed that the effective diffusion coefficient strongly depends on the porosity and, it is approximately an exponential function of the porosity. It was found that a complex microscopic mechanism of diffusion does not depend on the pore diameter for big pores of diameter bigger than 450 nm, where capillary condensation and adsorption can occur. In this network water content strongly influence diffusion [17]. Diffusivity depends on relative humidity which has an influence on free volume for gaseous diffusion.

The diffusion coefficient in concrete will change as the carbonation process changes the porous microstructure which is one of the driving factors of diffusion. It was observed that carbonation has a larger effect on transport properties in blended cements, such as the diffusion coefficient after carbonation increased by one order of magnitude [50] (Figure 2-5).

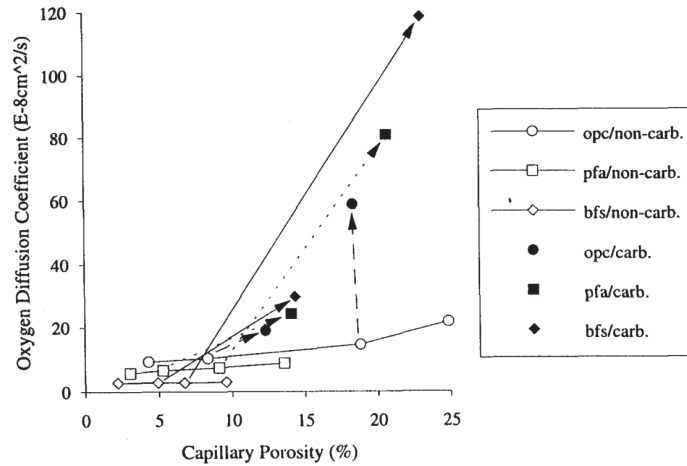


Figure 2-5. Oxygen diffusion coefficient for carbonated and non-carbonated cement pastes [50].

Dissolution and precipitation of phases, taking place during carbonation, change the microstructure of the porous medium. This transformation affects transport properties such as diffusion coefficient. It is commonly assumed that diffusion of CO_2 takes place through the carbonated zone, resulting in the carbonation front. That is why characterization of the diffusion properties of the carbonated zone is very important, especially for carbonation modeling. However, due to missing data, this parameter is often chosen arbitrarily, and it is assumed to be constant over the entire sample.

2.4 Effect of relative humidity

Carbonation rate is significantly affected by the moisture content of the environment. CO_2 molecules penetrate the porous system of the cement matrix in the gaseous state and dissolve in the concrete pore solution. Diffusion in the liquid in comparison to air is approximately 10 000 times slower [57]. Even though the diffusivity of CO_2 is significantly higher in gas-filled pores, compared to pores completely saturated with water, the presence of moisture is essential for gaseous CO_2 to react with hydrated phases [41]. The degree of pore saturation is a controlling factor for carbonation, as water blocks the pores and reduces the diffusion of CO_2 . Hence, it is evident, that in a very fine network of capillaries CO_2 diffusion is influenced by RH. Figure 2-6 shows that the optimal conditions for carbonation are different than for steel corrosion in terms of relative humidity. In practice, it means that even if carbonation risk has to be considered, there are relatively few situations in which it is a danger for concrete integrity. However, carbonation leads to release of the additional water into the

system, as shown in the carbonation equations. That water might contribute to the increase of the pores saturation, and in fact, to higher RH inside the sample than in the surrounding atmosphere.

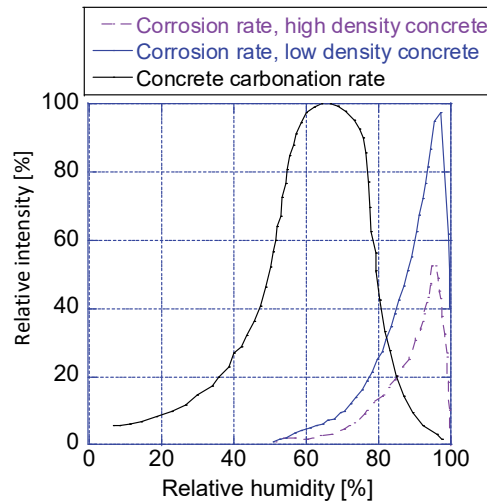


Figure 2-6. Comparison of corrosion rate as a function of relative humidity and for different concretes [58].

Dry concrete, and also concrete exposed to very high RH are very unlikely to suffer corrosion due to carbonation. The easiest conditions for carbonation to occur are when a layer of water is present on the surface of the capillary pores in which quickly diffusing carbon dioxide dissolves and reacts with calcium ions [57]. The maximum carbonation rate occurs in the range of relative humidity between 40 and 80%, in equilibrium with the moisture of concrete [57]. Experimental results of Papadakis [59] show that carbonation is maximum at RH around 50%. He also investigated the shape of the carbonation front and he deduced that for RH above 50% the front is sharp but below this value, no sharp front is formed and the kinetics of the carbonation reactions become important.

2.5 Accelerated vs natural carbonation

The accelerated carbonation tests are the most widely used approaches to assess the performance of new materials because of their relatively short duration. The most recent results comparing accelerated with natural carbonation show that accelerated tests cause a change in carbonated phases [9]. The main difference is the formation aragonite which is a calcium carbonate polymorph with lower molar volume compare to calcite and vaterite. This causes changes in microstructure and results in higher porosity than natural carbonation. Therefore, the pore structure will be coarser than in natural carbonation conditions in the case of blended cements.

Changes in microstructure depending on CO₂ concentration was shown already earlier by Bier & Kropp [60]. Two types of carbonation are compared between Portland and slag cement as a function of pore size distribution (Figure 2-7) which authors explained by forming different calcium carbonate polymorphs.

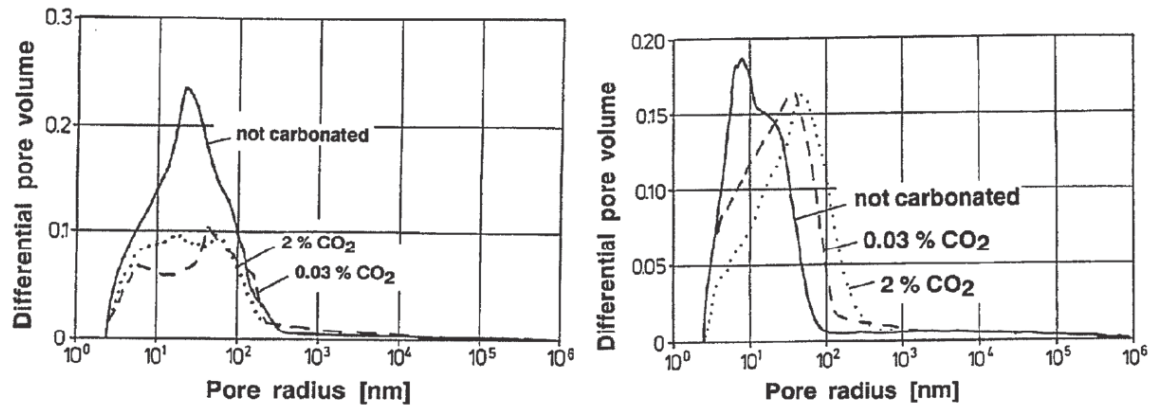


Figure 2-7. Pore size distribution by mercury intrusion porosimetry (MIP) as a function of CO₂ concentration during carbonation for Portland cement (left) and slag cement (right) [60].

Preliminary results on carbonation performed at LMC [9] show that accelerated carbonation in an environment with 4 % of carbon dioxide does not describe properly the actual carbonation rate of the blends. It can be explained by the formation of different calcium carbonate polymorphs in the blends for accelerated conditions that are not representative of the reality in natural carbonation.

Moreover, there is no general agreement on the procedure that should be followed to carry out carbonation tests with increased CO₂ concentration. There is a wide range of carbon dioxide level (between 1 and 50 % or even 100 % of CO₂ concentration), preconditioning, and duration time for accelerated carbonation tests [10].

2.6 About available carbonation models

Durability design, emphasizing carbonation, which can lead to reinforcement corrosion, should get more attention. Updating the quantitative models which can predict the initiation time of carbonation-induced corrosion would have great value to better design the formulation. At the moment we mostly rely on empirical approaches which means that every time we change a parameter in the formulation of the concrete, we have to test it again. Moving to a model approach can be a key to enable extrapolation of different kind of parameters.

In the last decades many different carbonation models were created using diffusion-based equation [16][61][62][63]. Some include diffusion as a function of the local water content. Some approaches also include the effect of the temperature on gas transport. Most of the available carbonation models include the amount of calcium only, making it not enough sensitive to the composition of the different binders. Most of them focus on the classical OPC formulation, neglecting the alternative binders. As the demand for using supplementary cementitious materials increases, a robust model should be able to reproduce the impact of them on the durability issues.

Moreover, many assumptions on macroscopic transport properties are made. For example, gas diffusion coefficient characteristics are chosen arbitrarily and are considered to be constant over the entire sample, without including the macrostructure changes caused by carbonation. Figure 2-8 present how the simulated depth of carbonation depends on m , h and μ (parameters for constitutive equations of capillary pressure and diffusion coefficient) which are chosen arbitrarily. The simulation ([64]) shows, that these parameters have a large impact while predicting carbonation depth.

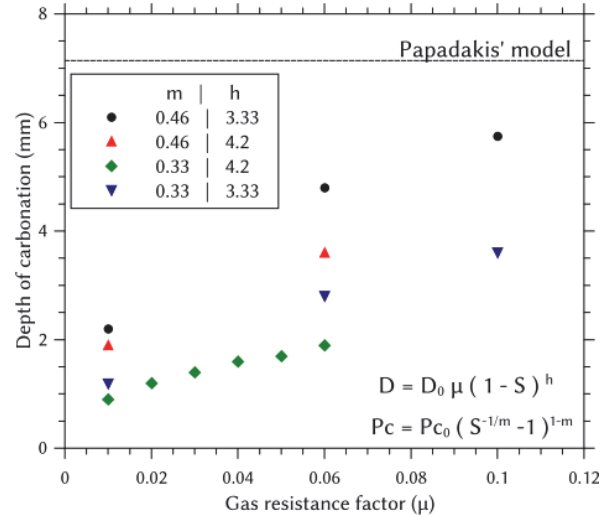


Figure 2-8. Depth of carbonation as a function of the upscaling parameters m , h and μ [64].

In the work of Georget et. al [65][64][30][66] a new reactive transport simulator was developed to be able to implement complex models of durability issues for cement paste. It was shown that saturation parameters, such as capillary pressure and gas diffusion coefficient, are very important since the competition between the ingress of CO_2 and the drying govern the kinetics of carbonation.

However, modeling does not mean the end of experimental science. A large set of consistent experimental data is necessary because the best results can be often achieved when combining targeted experiments with modeling. This way predictions can be calibrated and validated to give the confidence in using the models, especially if they are going to be used to predict the long-term durability of daily used concrete structures.

Chapter 3 Materials and methods

3.1	Characterization of raw materials	20
3.1.1	Physical properties.....	20
3.1.2	Chemical properties.....	20
3.2	Sample preparation and exposure conditions.....	24
3.2.1	Cement paste.....	24
3.2.2	Microconcrete and concrete.....	25
3.3	Experimental methods	28
3.3.1	X-ray powder diffraction (XRD)	28
3.3.2	Thermogravimetric analysis (TGA)	29
3.3.3	High-resolution microscope.....	30
3.3.4	Scanning electron microscopy (SEM-EDS)	30
3.3.5	Mercury intrusion porosimetry (MIP)	31
3.3.6	Water dynamic vapour sorption (DVS).....	32
3.3.7	Non-steady state gas diffusion.....	33
3.3.8	Carbonation depth.....	35

Experiments were carried out on cement pastes, micro-concretes, and concrete specimens. The aim of this chapter is to characterize the raw materials and to describe the experimental procedures and parameters that led to the results presented in the next chapters. Cement types, which are used in this work (Figure 3-1), are commercially available cements provided by Lafarge-Holcim from the Siggenthal, Untervaz and Höver cement plants. In addition, a parallel group at ETHZ designed a new low clinker cement “MixSL”, which was also implemented into the scope of this study.

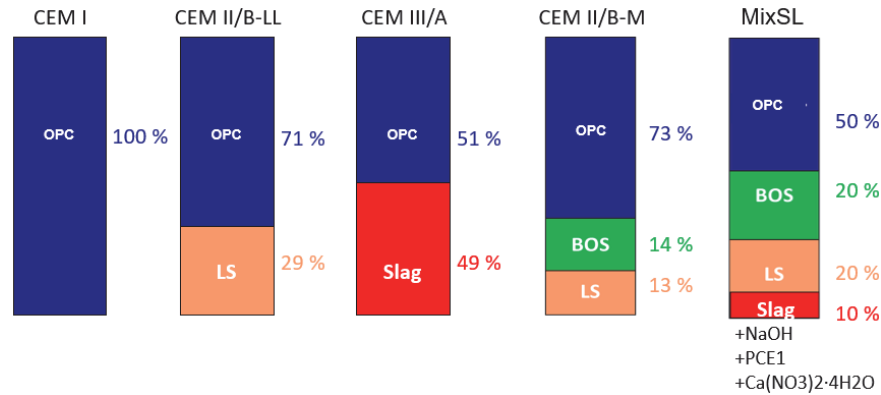


Figure 3-1. Clinker and SCMs substitution levels for studied binders.

3.1 Characterization of raw materials

3.1.1 Physical properties

The particle size distribution (PSD), specific surface area (SSA) and density of the binders were measured and are presented in Table 3-1. Those parameters have an influence on the workability, on the hydration, and on the mechanical properties, and therefore in the long term on durability properties.

Table 3-1. Physical properties of the cements and of the raw materials.

Analysis conditions	Materials								
	Raw materials				Cements				
	Burnt oil shale	Limestone 0-90	Fly ash	Slag	CEM I	CEM II/B-M	CEM II/B-LL	CEM III/A	MixSL
Specific surface area (m ² /g)	6.53 ± 0.08	2.19 ± 0.01	1.50 ± 0.01	0.72 ± 0.00	1.01 ± 0.00	1.83 ± 0.02	1.45 ± 0.02	n/a	n/a
D ₅₀ (μm)	6.07	7.39	14.40	14.95	11.68	9.85	15.27	n/a	n/a
Density (g/cm ³)	2.79	n/a	2.34	n/a	3.16	3.03	2.99	3.02	2.93

3.1.2 Chemical and mineralogical composition

The oxide composition data of the powders were provided by Lafarge-Holcim, and it is presented in Table 3-2. In addition, the mineralogical composition of the powders, measured by XRD and quantified by the Rietveld analysis, is presented in Table 3-3. Figure 3-2 shows the results of the isothermal calorimetry for studied cement types at early and later ages.

Table 3-2. Oxide composition of the cements and the raw materials.

	Cements					Raw materials			
	CEM I	CEM II/B-M	CEM II/B-LL	CEM III/A	MixSL	BOS	Fly ash	Limestone	Slag
CaO	62.8	59.5	64.7	53.5	52.11	29.65	3.2	52.5	40.2
SiO ₂	20.2	21.3	11.9	28.1	20.78	33.53	51.3	1.12	39.7
Al ₂ O ₃	4.7	5.5	3.2	7.7	2.97	10.05	24.1	0.58	11.6
Fe ₂ O ₃	3.1	3.5	2.2	1.3	2.97	6.1	14.7	0.44	-
MgO	2.1	1.8	1.6	2.7	2.43	1.82	1.9	0.3	4.37
P ₂ O ₅	0.19	0.22	0.33	n.d.	0.31	0.30	0.33	0.01	-
K ₂ O	1.03	1.14	0.65	0.76	0.90	2.02	2.79	0.04	0.83
Na ₂ O	0.22	0.20	0.18	0.37	0.24	0.30	0.97	0.01	0.37
SO ₃	3.5	3.2	2.7	2.7	n/a	9.8	0.3	0.01	n/a
LOI	1.4	6.7	14.3	14.3	9.87	5.38	2.6	n/a	n/a

Table 3-3. Mineralogical composition of cements and raw materials.

	Cements					Raw materials			
	CEM I	CEM II/B-M	CEM II/B-LL	CEM III/A	MixSL	BOS	Fly ash	Limestone	Slag
C ₃ S	67.6	47.5	40.0	27.8	-	-	-	-	-
C ₂ S	6.4	7.0	7.3	6.6	-	-	-	-	-
C ₃ A	4.6	4.5	4.2	5.1	-	-	-	-	-
C ₄ AF	8.7	5.6	4.3	1.8	-	-	-	-	-
Lime	0.4	0.5	-	-	-	6.5	-	-	-
Calcite	1.1	12.9	28.0	1.1	-	15.8	-	93.75	-
Quartz	-	2.8	-	-	-	20.8	10.6	-	-
Gypsum	4.6	3.2	4.7	0.1	-	-	-	-	-
Bassanite	-	2.2	2.6	4.7	-	-	-	-	-
Anhydrite	-	2.7	0.1	3.9	-	22.7	-	-	-
Hematite	-	-	-	-	-	2.8	2.4	-	-
Mullite	-	-	-	-	-	-	16.2	-	-
Magnetite	-	-	-	-	-	-	1.5	-	-
Amorphous	6.6	11.2	8.8	49.1	-	32.5	69.2	-	-

Isothermal calorimetry was used to evaluate the reactivity of the different binders. The measurements at $20 \pm 0.1^\circ\text{C}$ were performed on most of the mixtures with w/c of 0.40, and 0.35 on MixSL with a TAM Air calorimeter. The calorimeter was placed in a room with controlled temperature to enhance the stability of the baseline. After mixing, approximately 10 g of paste was placed in a glass ampoule with a diameter of 25 mm. For the normalization purpose, the exact weight of each sample was precisely measured. After gentle taping, samples

were sealed with airtight caps and inserted into the calorimeter. Measurement in most of the cases lasted for 28 days, except MixSL, which was measured for 7 days. The obtained data were normalized per gram of anhydrous.

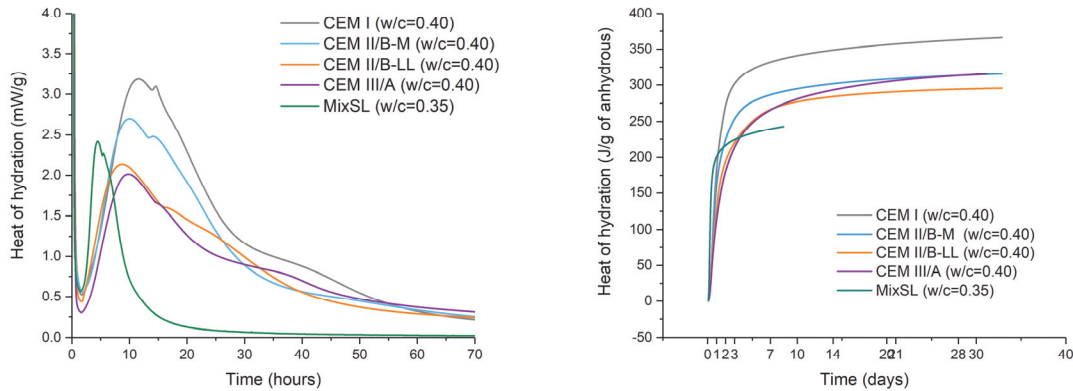


Figure 3-2. Isothermal calorimetry at an early age (left) and the cumulative curve at later ages (right) for the investigated cement pastes.

Among the different SCMs, burnt oil shale (BOS) gained additional attention as one of the main potential material allowing higher substitution of the clinker in the cement. Burnt oil shale used in this study is obtained from in Dotternhausen, south-west Germany. In the 1930s, it was found there, that it is possible to burn the oil shale in the way that it develops hydraulic or cementitious properties [12]. The heat of this burning process is used to simultaneously produce electricity. Hydraulic burnt oil shale is mainly used together with clinker to make Portland-Burnt Shale Cement (CEM II/B-T), according to European standard EN 197-1 [2]. The consequence of this finding was the development of a process that integrates the utilization of oil shale into operation for cement manufacturing. This process makes use of all the oil shale energy as well as its minerals. This blend and its resistance against carbonation is studied here as “CEM II/B-M”. The MixSL also contains BOS, which together with limestone and slag substitutes 50 % of the clinker content.

To see the composition of the BOS, pressed pellets of the powder was impregnated, polished, and observed with SEM. From the obtained maps on a polished section of BOS, we could perform EDS analysis and compare the oxide content calculated from the maps with XRF data (Table 3-4). Calculated values correspond well.

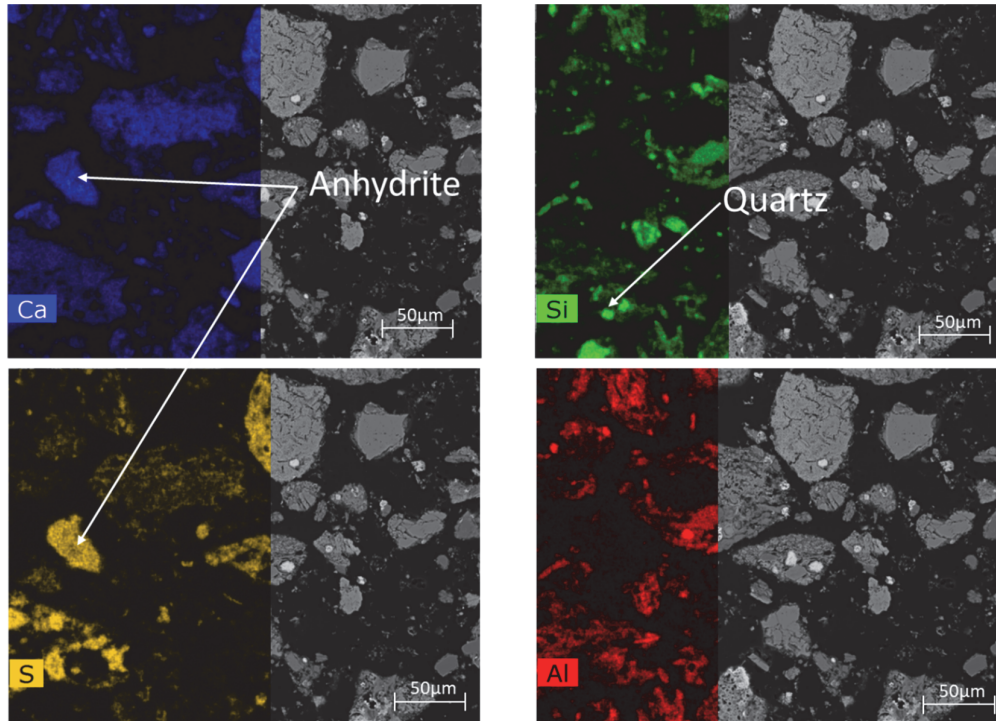


Figure 3-3. Polished section of burn oil shale; heterogenous distribution of elements observed by SEM-EDS.

Presence of calcium and sulfur in the same particle/agglomeration (Figure 3-3) indicates the presence of anhydrite detected in XRD analyses. Silicon-rich particles confirm the presence of quartz crystals, also detected by XRD technique. Minor aluminum content in crystal phases was found only in illite, the rest should be present in the amorphous part.

Table 3-4. Oxide composition from XRF compared with oxide composition obtained from SEM-EDS mapping.

Oxides	XRF of BOS (%)	BOS- quantification by SEM mapping (%)
CaO	29.65	31.18 (\pm 5,43)
SiO ₂	33.53	34.55 (\pm 4,03)
Al ₂ O ₃	10.05	10.81 (\pm 1,41)
Fe ₂ O ₃	6.10	6.25 (\pm 0,43)
MgO	1,82	1.82 (\pm 0,14)
P ₂ O ₅	0,30	1.17 (\pm 0,23)
K ₂ O	2,02	2.73 (\pm 0,28)
Na ₂ O	0,30	0.91 (\pm 0,09)
SO ₃	9.80	10.58 (\pm 0,92)

Three major elements were chosen to show Ca-Al-Si ternary frequency plot ([67]) and to locate the crystals found by XRD analysis (Figure 3-4). It gives also information about the composition of the amorphous phase of the BOS.

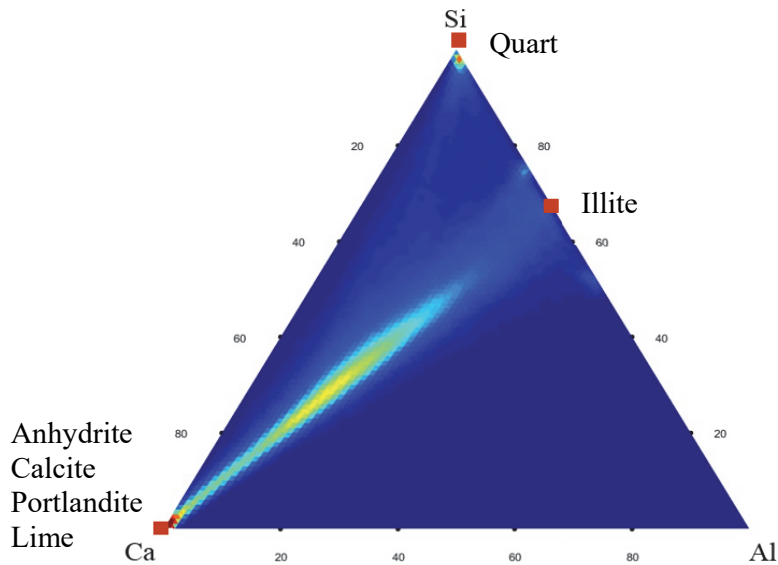


Figure 3-4. Ternary plot of BOS showing the composition of the amorphous phase.

3.2 Sample preparation and exposure conditions

3.2.1 Cement paste

Paste mixtures were prepared with $w/b = 0.4$, using a vacuum mixer and cast in plastic cylindrical moulds of diameter 32 mm and height 70 mm. After one day of sealed curing, the pastes were demoulded and exposed at the relative humidity of 95 %. Curing was continued up to 3 and 28 days. Cylinders were cut with a slow speed saw (Figure 3-6) allowing to obtain thin slices with a thickness of 1.00 mm ($\pm 5\%$). The slices (Figure 3-6) were exposed to natural carbonation environment at 400 ppm of CO_2 and 70% RH. Moreover, reference samples were exposed to CO_2 -free atmosphere to decouple the effect of ongoing hydration and drying from that of carbonation. The CO_2 -free conditions had the same relative humidity and temperature as the ones where samples were carbonating. The samples were stored in the glovebox sealed from the atmosphere, in which CO_2 concentration was always below 50 ppm. The CO_2 free atmosphere was maintained by using soda lime, capturing the CO_2 . RH was controlled by using a saturated salt solution (55 %, 70 %, and 86 % were controlled by using saturated solutions of magnesium nitrate, potassium iodide, and potassium chloride, respectively). In addition to the thin disk samples, some paste cylinders were also exposed to carbonation.

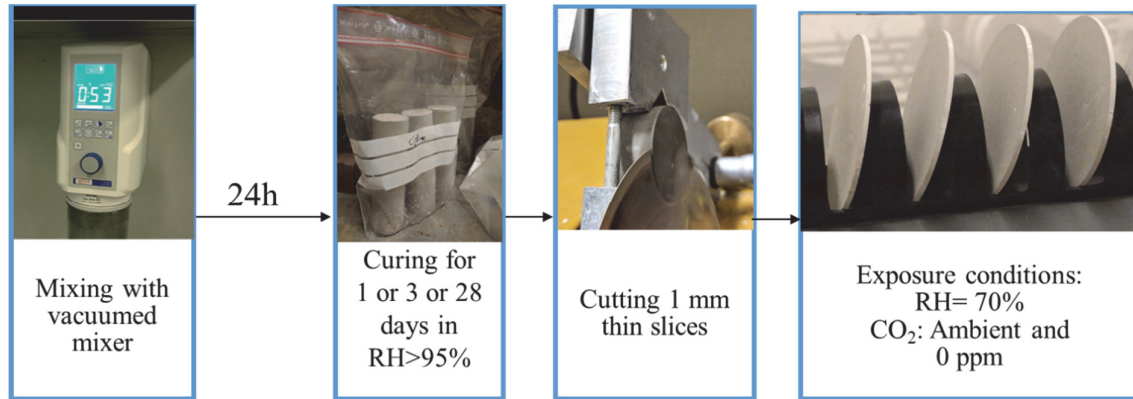


Figure 3-5. Procedure of paste samples preparation.

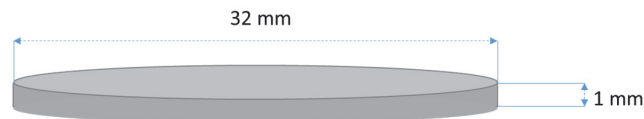


Figure 3-6. Schematic illustration of the sample dimensions.

3.2.2 Microconcrete and concrete

Micro-concrete samples were prepared in parallel, using the maximum aggregate size of 8 mm (55 % of granulate 0/3, 45 % of granulate 3/8). Five types of binders were studied. Different w/c were used, according to Table 3-6. After 1 day of curing in the moist room and in sealed moulds (4x4x16 cm), the specimens were demoulded and cut into cubes of 4 cm. Some of the samples were directly exposed to natural carbonation, some were cured further up to 3 days, and the last was cured for 28 days in a humidity-controlled chamber at 22°C and RH>95 %. After curing, concrete specimens were exposed into natural carbonation without additional preconditioning. To maintain constant RH of the surrounding atmosphere samples were stored in glove boxes with a controlled RH, using saturated salt solution (for RH 56 % with magnesium nitrate salt and 86 % with potassium chloride salt), or in a room with a controlled RH (i.e., RH=70 %). For the samples stored in gloveboxes (Figure 3-7), ambient air was constantly pumped into the chambers to maintain the CO₂ as close as possible to a natural concentration of 400 ppm. Figure 3-8 presents the strength development during hydration between 1 and 90 days for the studied mixes.

In addition to microconcrete samples, some concrete specimens were cast in the Lafarge-Holcim laboratory to be exposed to accelerated carbonation conditions. The sample preparation and the exposure conditions are summarized in Table 3-5.

Table 3-5. Summary of the sample preparation and exposure conditions of the microconcrete and concrete exposed to carbonation.

	Accelerated carbonation on concrete (Lafarge-Holcim)	Natural carbonation on microconcrete (EPFL)
Curing time before exposure	28 day, underwater	28 days, a moist room at 95 % RH
CO ₂ concentration	4 %	0.04 %
Relative humidity	57 % ±3 %	55 % ±5 %
Temperature	20°C	20°C±3°C
Sample size	12x12x36 cm	4x4x4 cm
Max. aggregate size	32 mm (wet)	8 mm (dry)

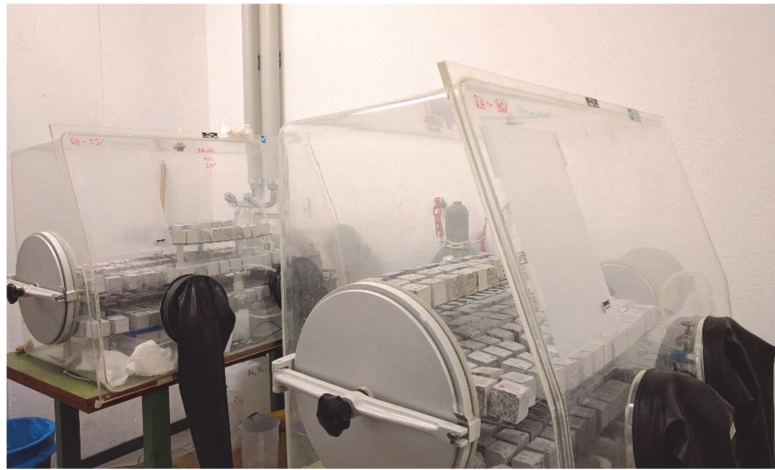


Figure 3-7. Example of exposure condition during natural carbonation.

Table 3-6. Microconcrete mixture proportions.

Concrete	Cement type	Concrete proportioning details			Curing before exposure (days) and RH of the exposure chamber (%)
		W/C	Cement: kg/m ³	Aggregate: kg/m ³	
1	CEM I	0.6	360	1738	1 (56%, 70%, 86%), 3 (56%, 70%, 86%), 28 (56%, 70%, 86%),
2		0.5	404	1741	1 (56%, 70%, 86%), 3 (56%, 70%, 86%), 28 (56%, 70%, 86%),
3		0.4	460	1747	1 (86%), 3 (56%), 28 (56%, 70%, 86%),
4	CEM II/B-M	0.6	355	1738	1 (56%, 70%, 86%), 3 (56%, 70%, 86%), 28 (56%, 70%, 86%),
5		0.5	398	1741	1 (56%, 70%, 86%), 3 (56%, 70%, 86%), 28 (56%, 70%, 86%),
6		0.4	452	1747	1 (56%, 86%), 3 (56%, 86%), 28 (56%, 70%, 86%),
7	CEM II/B-LL	0.6	353	1738	1 (86%), 3 (56%, 70%, 86%), 28 (56%, 70%, 86%),
8		0.5	395	1741	1 (56%, 70%), 3 (56%, 70%), 28 (56%, 70%, 86%),
9	CEM III/A	0.6	354.5	1738	3 (70%), 28 (70%),
10		0.5	397	1741	1 (56%, 70%), 3 (56%, 70%), 28 (56%, 70%, 86%),
11	MixSL	0.5	392.6	1741	3 (56%, 70%, 86%), 28 (56%, 70%, 86%),

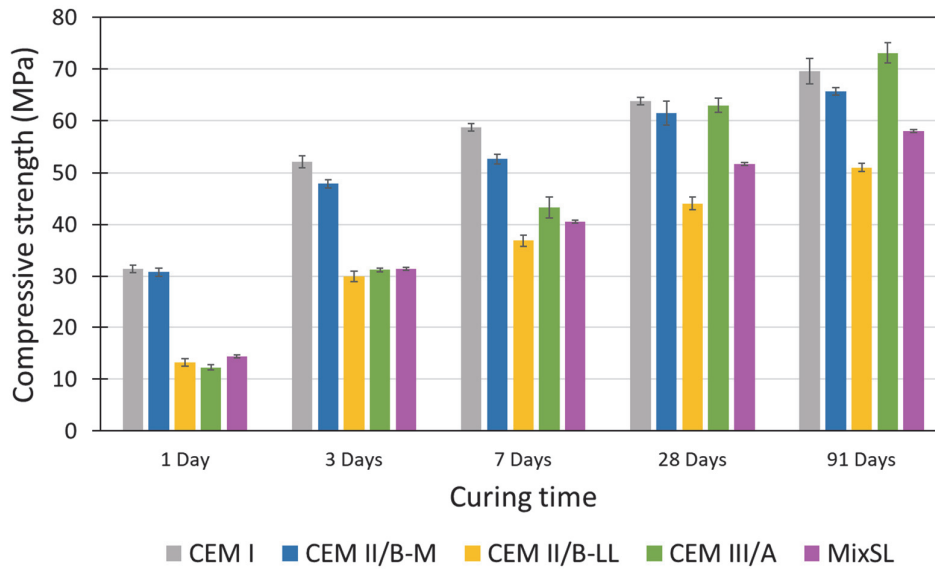


Figure 3-8. Compressive strength development of microconcrete made with OPC and blended cements at $w/c=0.50$.

3.3 Experimental methods

3.3.1 X-ray powder diffraction (XRD)

To quantify the crystalline phases in hydrated cement pastes before and during exposure to carbonation, X-ray powder diffraction together with Rietveld analysis was used. For the reference, samples before exposure were investigated. In addition, uncarbonated samples were measured as a reference for carbonating samples to deconvolute the effect of carbonation from eventual further hydration and consequence of drying. Thin disk samples were removed from the conditioning chambers at different exposure times, and ground into powder using a mortar and pestle prior to the analysis, as demonstrated in Figure 3-9. Attempts were made to do the grinding as fast as possible, to avoid carbonation in the samples during preparation. The mineralogical evolution was studied using PANalytical X'Pert Pro MPD diffractometer in Bragg-Brentano geometry [68]. The X-ray generator was operated at 45 kV and 40 mA. Scans were taken from 5° to 70° 2θ angles using a fixed divergence slit of 0.5° , a step size of 0.017° and a time per step 60 ms. The sample was rotating during the measurement to improve statistics. One measurement lasted about 15 minutes. Crystalline phases were quantified by Rietveld refinement using X'Pert High Score Plus software with rutile as an external standard.

The results of the external standard quantification are expressed per 100g of the anhydrous binder (there is 140 g of paste per 100 g of anhydrous).

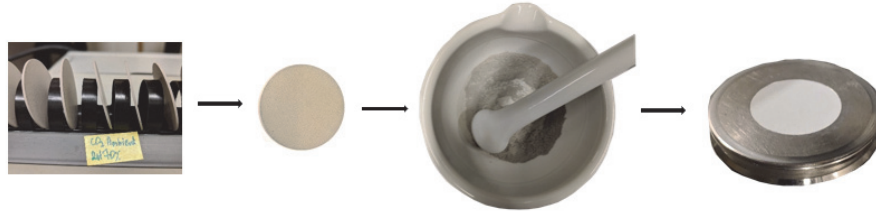


Figure 3-9. Sample preparation for XRD-Rietveld analysis.

3.3.2 Thermogravimetric analysis (TGA)

In the TGA, samples are subjected to high-temperature heating. Characterization of the material can be based on the decomposition pattern due to the mass loss. For thermogravimetric analysis, samples were dried using a solvent exchange method with isopropanol, followed by 7 days in a desiccator prior to performing the experiment. In such dried samples, the mass loss until 550°C corresponds to the amount of bound water in the hydrate samples. Dried samples were ground and 50 mg was used for each test (Figure 3-10). A Mettler Toledo TGA/SDTA851 used for TGA. Approximately 50 mg of ground cement paste was placed in 150 μ L alumina crucibles covered by aluminum lids to reduce carbonation before analysis. The temperature ranged from 30 to 1000 °C with a heating rate of 10/min under a nitrogen atmosphere to prevent carbonation. The mass loss as a function of the temperature was obtained. After derivation, the DTG curve was plotted to show various peaks that correspond to the mass loss due to H₂O release (dehydration, dihydroxylation) and due to CO₂ release (decarbonation).

TGA allows identifying the phases as different phases decompose within specific temperature ranges. A derivative of TG curve (called DTG) allows for easier identification of the different phases. To quantify the amount of a phase, the relative mass loss due to water or carbon dioxide recorded by TGA is compared to the mass fraction of the water or carbon dioxide in the pure phase. Typically, only portlandite and calcite can be quantified with satisfactory confidence.

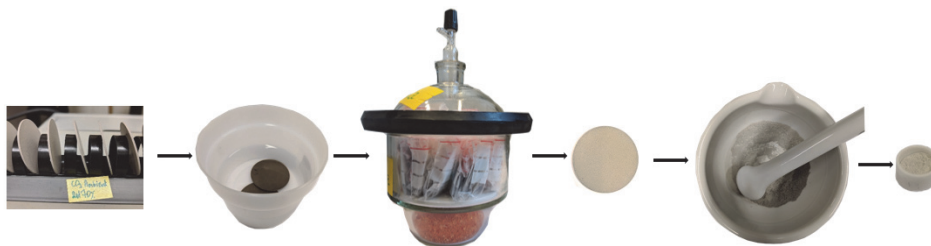


Figure 3-10. Illustration of the sample preparation for TGA.

3.3.3 High-resolution microscope

FEI XLF-30 SFEG-SEM [69] was used to study the morphological variation of the dried samples. The source of the beam is a field emission gun. Operating voltage was set on 2 kV. Samples were crushed prior to the experiment into small pieces, dispersed on an adhesive carbon tab and coated with an iridium layer of 4 nm layer (Figure 3-11). The microscope parameters are shown on the micrographs.

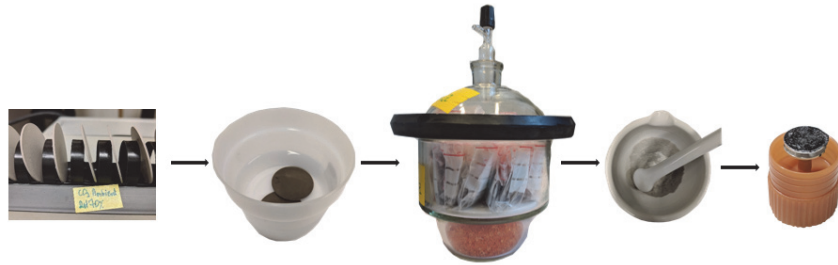


Figure 3-11. Sample preparation for the high-resolution microscope.

3.3.4 Scanning electron microscopy (SEM-EDS)

Electron dispersive spectroscopy (EDS) is widely used in hydrated cement to determine the composition of the C-S-H from atomic ratio scatter plots [70]. C-S-H has a variable chemical composition and EDS provides information on the stoichiometry of the components. Because the influence of the neighbor phases cannot be avoided, the composition of C-S-H has to be found graphically. Si/Ca ratios are plotted versus Al/Ca and a cloud of points appears as a characteristic of the intermixing of between different phases (C-S-H, Aft, AFm, and CH). The composition of pure C-S-H can be found at the extreme right-hand side of the cloud. Figure 3-12 is an example of a typical atomic scatter plot of Al/Ca versus Si/Ca. The cloud obtained from the measurements represents the variability of the C-S-H composition in the sample.

The pieces of thin disks were impregnated, using a low-viscosity epoxy resin, and polished using successive diamond abrasives down to 1 μm size. After desiccator drying, the surface of the samples was coated with a conductive carbon layer prior to testing (Figure 3-13).

FEI Quanta 200 electron microscope was used for SEM-EDS investigation. The working distance of 12.5 mm and an operating voltage of 15 kV were set. C-S-H composition was determined using EDS point analysis. The EDS microanalyses were carried out on inner and outer products of C-S-H to obtain the composition of the C-S-H. For statistical accuracy, about 100 points were acquired for inner C-S-H and 100 points for outer C-S-H.

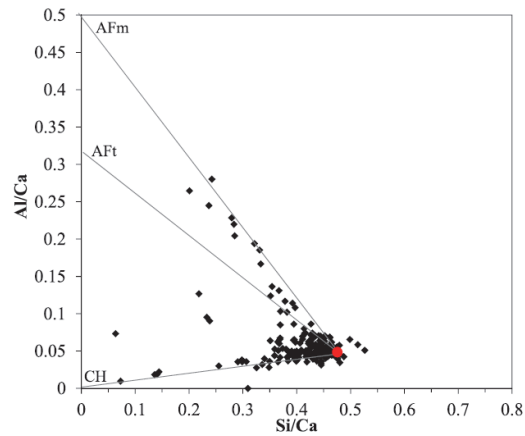


Figure 3-12. Determination of C-S-H composition from atomic scatter plots [70].



Figure 3-13. Sample preparation for SEM.

3.3.5 Mercury intrusion porosimetry (MIP)

MIP was used to study the porosity evolution. A porosimeter equipped with two devices was used: Pascal 140 and 440, POROTEC, with a maximum pressure of 150 kPa and 400 MPa in the low pressure and high-pressure chambers, respectively [71]. The first one introduces the mercury into the sample and measures macroporosity. The second one measures the micro- and nano-porosity. To interpret the data, the Washburn equation was used (Eq. 3-1). The contact angle of mercury on the cement paste was assumed to be $\theta=140^\circ$ [72], and the surface tension of mercury was assumed to be $\gamma_{\text{Hg}}=0.48$ N/M.

$$d = \frac{-4\gamma\cos(\theta)}{P} \quad \text{Equation 3-1}$$

Figure 3-14 illustrates how the total porosity, critical pore radius and threshold pore entry radius were determined.

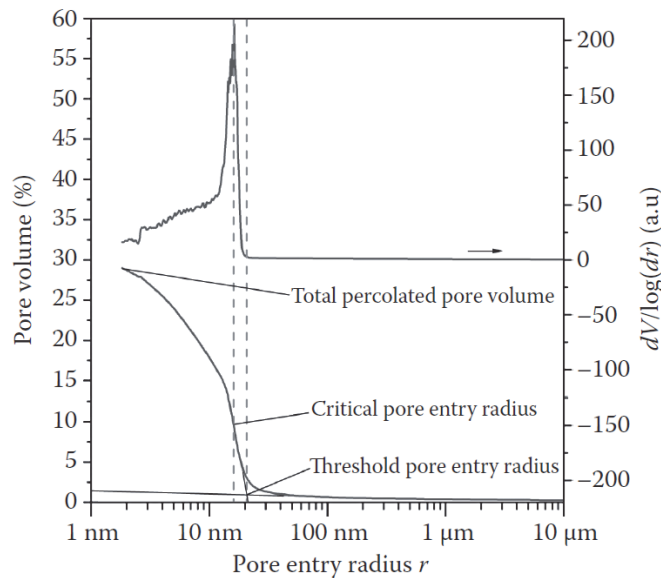


Figure 3-14. The way of determining total porosity, critical pore radius and threshold pore entry radius from MIP curves [71].

Hydration and carbonation were stopped prior to MIP analysis by solvent exchange method using isopropanol. After 7 days of solvent exchange samples were moved to desiccator to dry it. For all pastes, half of the dried disk was broken into 8 pieces (Figure 3-15). The total weight of each sample was around 0.7 g. The pieces were inserted into the dilatometer followed by the MIP measurements.

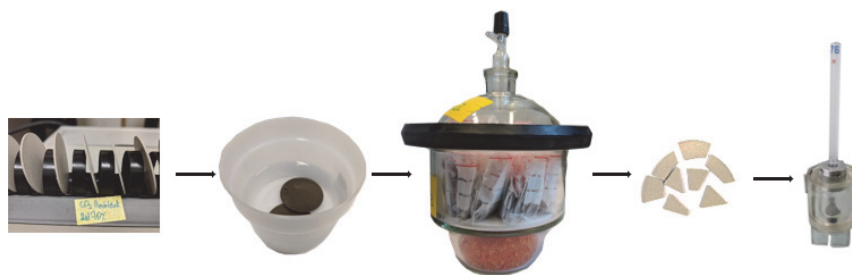


Figure 3-15. Illustration of the sample preparation for MIP analysis.

3.3.6 Water dynamic vapour sorption (DVS)

The sorption isotherm experiment is one of the methods to study the pore structure. It is obtained by measuring the mass variation of a sample exposed to a gas at a target relative humidity. The experiment is done at constant temperature (25°C). The shape of the isotherm depends on the microstructure, mainly on the pore size distribution. The result of the analysis is the water content of the sample as a function of relative humidity.

At a given carbonation time or exposure into CO₂-free environment, at 70% RH, the sample was crushed in a mortar. Around 40 mg of powder was deposited in the sample holder in the DVS chamber (Figure 3-16). Three successive isotherms were recorded: absorption from 70 % to 100 % RH, desorption from 100 to 0% RH, and finally absorption from 0 to 100 % RH. For all steps, a mass change criterion of $dm/dt=0.001$ mg/min was applied according to the sensitivity of the DVS analyzer. The total measurement time was about 2 weeks.

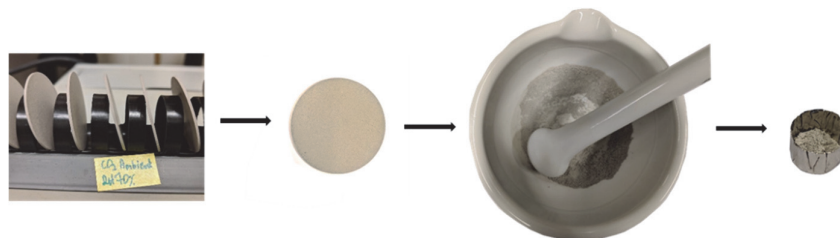


Figure 3-16. Sample preparation for DVS.

3.3.7 Non-steady state gas diffusion

A non-steady state oxygen diffusion cell was used to measure the changes in the diffusion coefficient of carbonated materials when compared to noncarbonated ones. The design of the cell, presented in Figure 3-17, was based on the diffusion cell from Boumazaa et al. [11]. The accumulation of oxygen from ambient into the cell was measured until reaching equilibrium, i.e. until O₂ concentration reaches a typical ambient concentration of ~21%. The high-density polyethylene material makes the cell airtight. The only way for O₂ to diffuse is through the porosity of the sample. Silicon joint, which is between the sample and the screw, ensure the good sealing during tightening. In addition, before the test, the samples were glued with a silicon glue into a metal ring to avoid any pressure which might cause cracks in the sample during tightening (Figure 3-18). Design of the outlet and inlet avoid any overpressure in the cell. The geometry of the cell was determined to enable the sufficient reliability of the test. A smaller volume of the cell compared to the previous study [11] allows for a reduction in the duration of the experiment.

The experiment starts with purging the pure nitrogen into the diffusion chamber through the inlet of the cell for around 30 seconds until reaching a value of around 30 ppm of O₂ inside the chamber. Reaching lower O₂ concentration in the cell prior diffusion is possible, however in the range below 30 ppm, a decrease of O₂ concentration has a lower rate, therefore reaching 0 ppm could cause the risk of drying the sample. The cell is placed into a climate box pre-equilibrated at the 70 % relative humidity (the same as for the sample exposure). Sample mass was checked before and after each experiment and the changes were found to be negligible. It means that no significant drying is taking place during the purging of the nitrogen.

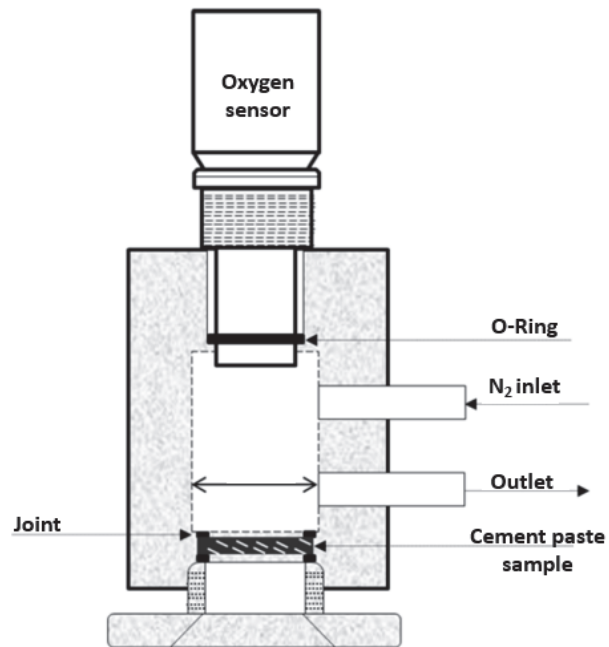


Figure 3-17. Oxygen diffusion cell sketch ([11])

Experiments were performed under constant temperature and pressure ($20^{\circ}\text{C}\pm 2^{\circ}\text{C}$, 1 atm). Oxygen concentration inside the cell diffusing through the sample was measured constantly by use of the O_2 gas sensor from Vernier, placed on the top of the cell. The sensor measures the oxygen level in the range between 0 to 21 % with an accuracy of 1 %. The gas diffusion coefficient was back-calculated using a simple Fick's law equation for the diffusion equation. The code used to obtain the diffusion coefficient is presented in Appendix D, as well as its online version under the link:

<https://bitbucket.org/specmicp/nonsteadydiffusion-cell/src/964fdae47b714f176be7a2a87c6274dac3fcb683?at=master>

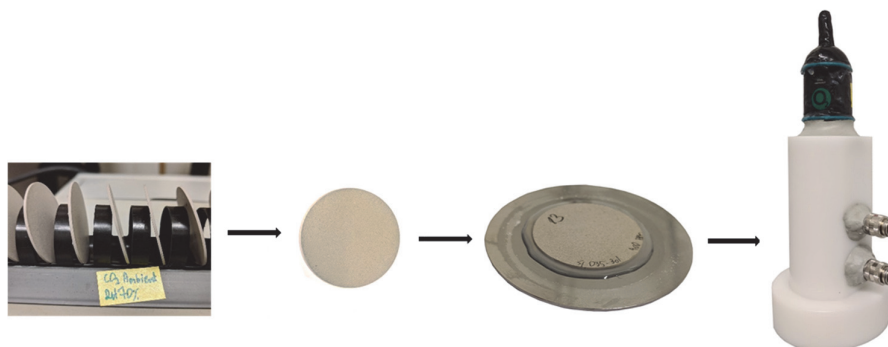


Figure 3-18. Sample preparation for diffusion test.

3.3.8 Carbonation depth

To observe the extent of the CO₂ ingress in concrete, carbonation depth was measured on microconcrete cubes obtained from cutting 16x4x4 cm prism. At certain times of exposure to carbonation, cube samples were taken from the climate chambers to be tested on the freshly broken surface, as presented in Figure 3-19. Carbonation depth was measured using phenolphthalein and thymolphthalein pH indicators with a pH threshold value of about 9 and 10, respectively. After 10 minutes after spraying, pictures were taken with constant light conditions. The depth of carbonation was calculated in ImageJ. Reported carbonation depths are the average values of carbonation depth measured on 10 lines around the uncoloured rim on the outer edge of the sample representing the carbonated zone, where the pH drops below the threshold. The coloured areas are the regions where carbonation did not occur and alkalinity is still high enough. No difference in carbonation was noted between cut and cast surfaces. The method is simple, fast, and easy to use, however, during spraying with the phenolphthalein special precaution (as wearing protective respiratory tract mask) has to be taken due to its cancerogenic potential. The carbonation depth was measured between 3 and 30 months of exposure to natural carbonation as a function of the binder composition, curing time, water to cement ratio, and relative humidity. To compare the natural exposure with accelerated conditions, an accelerated test following the protocol of the Swiss norm, SIA 262-1, was carried out in the Lafarge-Holcim laboratory on the concrete made with chosen binders.

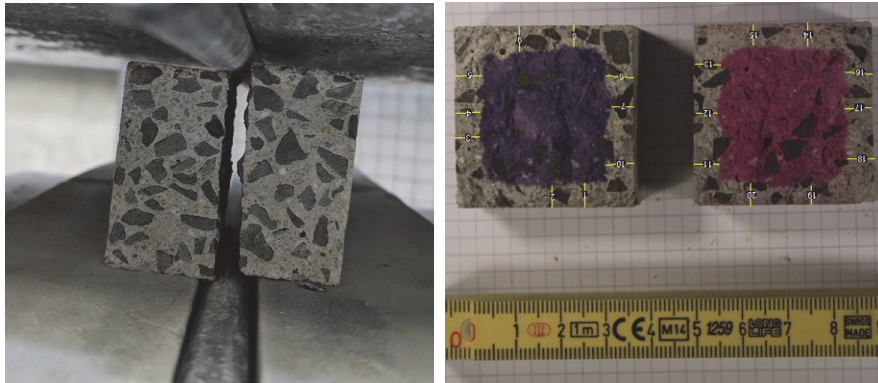


Figure 3-19. Microconcrete cube (4cm) broken with the use of hydraulic press (left picture) and sprayed with thymolphthalein (blue) and phenolphthalein (pink) pH indicators to measure the carbonation depth (right picture).

Chapter 4 Carbonation rates

- 4.1 Effect of the binder composition, curing time and relative humidity on carbonation rate 38
- 4.2 Further study on the influence of curing time and w/c on selected blends 41
- 4.3 Meaning of w/CaO_{reactive} and its effect on carbonation rate 43
- 4.4 Natural vs accelerated carbonation 46

In this chapter, the influence of various parameters on carbonation depth during natural carbonation is presented. Portland cement is a reference for the blends containing diverse supplementary cementitious materials, such as burnt oil shale, limestone, or slag. Following subchapters focus on the effect of the binder composition, curing time, relative humidity and water to cement ratio (Figure 4-1). A determination of carbonation coefficient is also presented. Finally, for chosen mixes, natural carbonation is compared with the accelerated test. To analyse the influence of individual parameters, first, the depth of carbonation had to be measured.

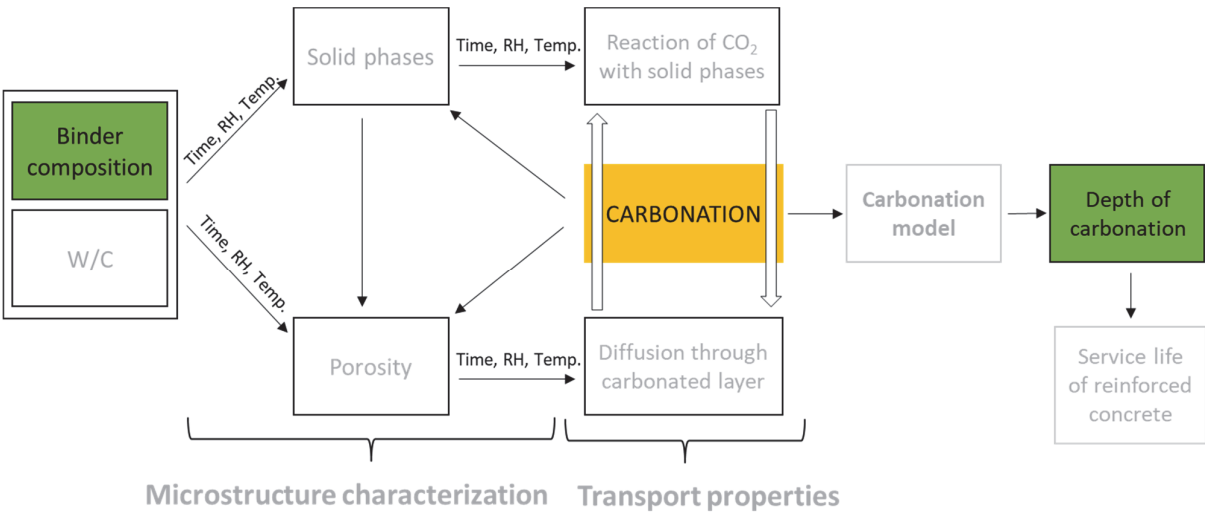


Figure 4-1. Research scope: carbonation rates.

4.1 Effect of the binder composition, curing time and relative humidity on carbonation rate

With increasing exposure time, carbonation depth decreases. The carbonation depth is usually presented as a function of the square root of time [73][43]. The carbonation coefficient is calculated as the slope of the regression of the carbonation depth, as presented in Figure 4-3.

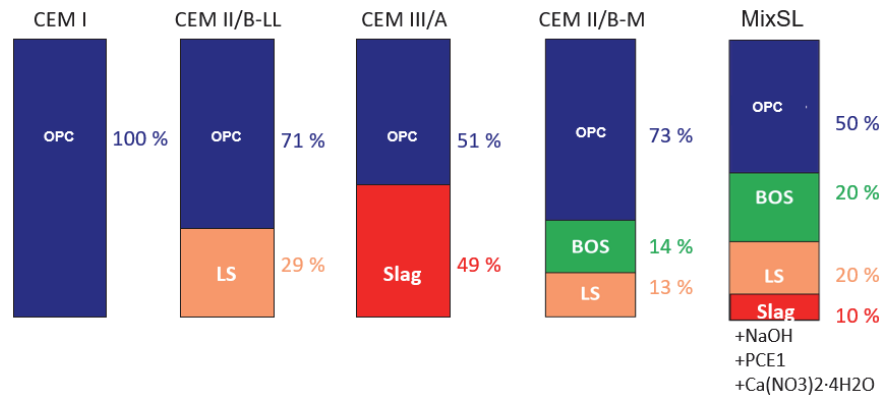


Figure 4-2. Clinker and SCMs substitution levels for studied binders.

It can be seen that curing time is one of the major factors influencing carbonation rate. By increasing curing from 3 days to 28 days carbonation depth decreases significantly. Results presented in Figure 4-3 and in Table 4-7 show how influential curing is for carbonation, especially for the binders including supplementary cementitious materials (SCMs). Figure 4-2 reminds about the substitution level of the clinker in the blends.

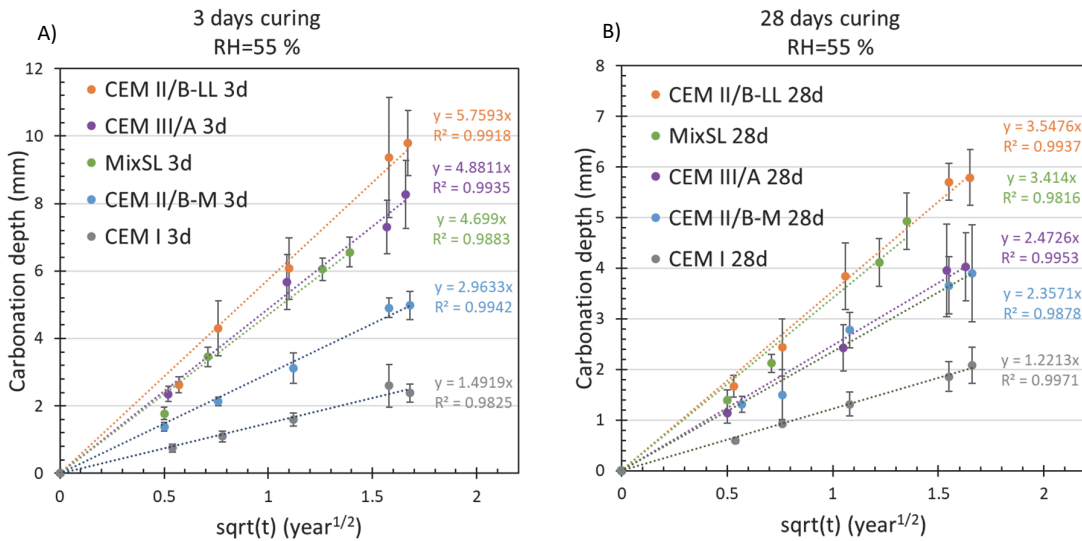


Figure 4-3. Carbonation depth as a function of cement type and curing time ($w/c=0.50$, natural CO_2 concentration, $22^\circ C$ and 55% RH).

All mixes decrease the carbonation rate after the increase of the curing time (Figure 4-3). However, the most significant decrease was noted for CEM III/A where the carbonation coefficient decreased from 4.88 at 3 days of curing to 2.47 at 28 days of curing. In general, cement mixes containing supplementary cementitious materials have lower resistance against carbonation than Portland cement. This finding was also reported by Papadakis et al. [74]. For the cement types with lower initial carbonation coefficients K , the decrease of K after additional curing is less significant. Independently of curing time, Portland cement is the most resistance cement against carbonation. Both, for short curing of 3 days or longer curing of 28 days before exposure to carbonation, the carbonation coefficient is the lowest for CEM I.

Interestingly, the new mix, MixSL with 50 % of clinker replacement by SCMs, behave relatively good against carbonation when compared to the other blends. Although the replacement level is much higher than for CEM II/B-LL, the carbonation rate for both systems cured for 28 days is similar. Another example of the similarity in the carbonation rate is between CEM II/B-M and CEM III/A, although they contain a different proportion of clinker. MixSL and slag blend have the same clinker substitution level of 50 %. The carbonation coefficient for those mixes after 3 days of curing is nearly the same. However, if exposure to carbonation was started after 28 days of curing, then the decrease in carbonation rate is much higher for CEM III/A. It might be due to a slow reaction of the slag, therefore a significantly lower degree of hydration after 3 days of curing compared to 28 days of curing. Another couple of mixes with the same substitution level by SCMs but different resistance against carbonation is CEM II/B-M together with CEM II/B-LL. For both mixes, the replacement level reaches 30 %. However, for CEM II/B-LL all substitution level is complete by limestone which is mostly nonreactive SCM [74]. That is why in compare to CEM II/B-M, where clinker is partly replaced by limestone and partially by burnt oil shale, the CEM II/B-LL is not as resistant blend against carbonation as CEM II/B-M. Studying the buffer capacity of this mixes in the subchapters 4.3 “Meaning of $CaO_{reactive}$ and its effect on carbonation

rate”, and the microstructure development in further chapters should partially explain the behavior of the mixes against carbonation.

Table 4-7. Carbonation coefficients changes after increasing curing time before exposure to carbonation (data from Figure 4-3).

	Carbonation coefficient K (mm/year ^{1/2})		Reduction of K	Reduction of K (percentage)
	3 days of curing before exposure	28 days of curing before exposure		
CEM I	1.49	1.22	-0.27	-18 %
CEM II/B-M	2.96	2.36	-0.60	-20 %
CEM II/B-LL	5.76	3.55	-2.21	-38 %
CEM III/A	4.88	2.47	-2.41	-49 %
MixSL	4.70	3.41	-1.29	-27 %

Apart from the binder composition and curing time, the relative humidity of the exposure environment is also a significant factor that governs the diffusion of carbon dioxide in concrete. The results of the carbonation rate presented so far were processed on samples exposed in relative humidity of 55 %, where the carbonation rate is known to be the highest [75], [76]. At the relative humidity ranges above 50 % carbonation rate decreases with increasing RH [75]. This is also well presented in Figure 4-4. It shows microconcrete mixes exposed to relative humidity of 55 %, 70 %, and 86 %. It can be seen that the carbonation rate is not always dependent on the substitution level by SCMs. That aspect is discussed further in this chapter in part 4.3.

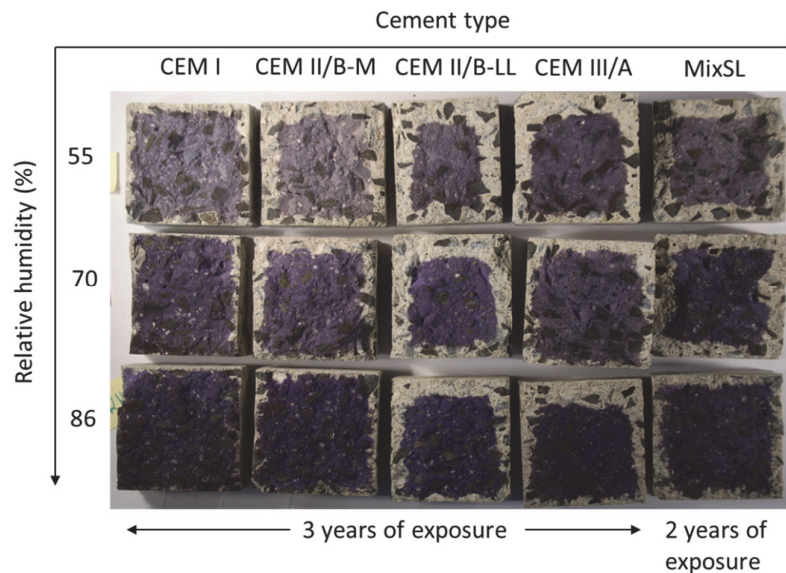


Figure 4-4. Dependence of relative humidity on carbonation rate for microconcretes made with different binder compositions, with $w/c=0.50$, cured for 28 days.

4.2 Further study on the influence of curing time and w/c on selected blends

In addition to 3 and 28 days of curing, presented in Figure 4-3, the effect of shortening of the curing to only 1 day is presented in Figure 4-5. Picture B illustrates CEM I while picture A focuses on the blend CEM II/B-M. For both mixes, the curing for only 1 day before exposure shows much less resistance against carbonation than the longer curing times, 3 days or 28 days. After 3 years of natural carbonation, the blended system carbonated completely so the measurement of the depth is impossible on the cube with a dimension of 4 cm, where CO₂ can ingress in all directions. The picture also gives an indication that increasing curing from 1 to 3 days is very important and has a much bigger impact than further curing up to 28 days.

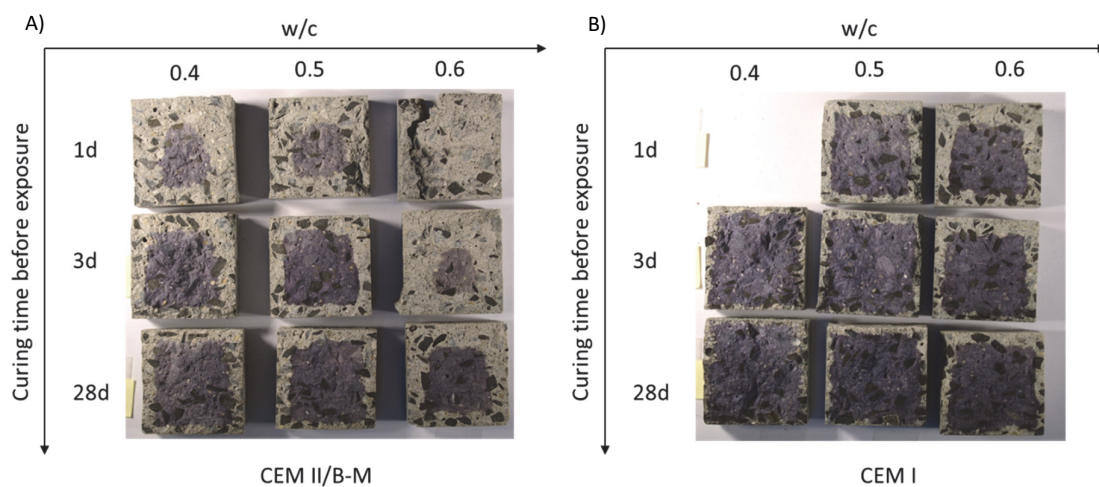


Figure 4-5. Influence of curing time and w/c for CEM II/B-M and CEM I undergoing natural carbonation in 55% RH for 3 years.

In addition to the impact of curing time, Figure 4-5 gives also a good indication of the importance of w/c while designing a mix robust against carbonation. Namely, it can be seen that for both cement types, a decrease of w/c from 0.60 to 0.50 lower the carbonation depth. However, further decrease of the w/c from 0.50 to 0.40 does not anymore have a significant influence on carbonation depth for the blend, however, carbonation coefficient of PC still decreases. To look at this phenomenon more quantitatively, changes in carbonation coefficient are presented in Figure 4-6 and Figure 4-7. For microconcretes made with blended cement the decrease of w/c from 0.60 to 0.50 causes reduction of carbonation coefficient by the factor of 2 on average. Further decrease of w/c causes only a minor decrease in the carbonation rate. For PC microconcrete, a decrease of w/c from 0.60 to 0.50 causes almost the same reduction level in carbonation coefficient as further decrease w/c from 0.50 to 0.40. In [77] is shown that it is not the case for the fly ash cement with the clinker substitution up to 50 %, where the decrease of the w/c from 0.50 to 0.40 leads to further decrease of carbonation coefficient. In general, more study is needed to examine, if this effect of w/c reduction on carbonation rate is also characteristic for other blended cements.

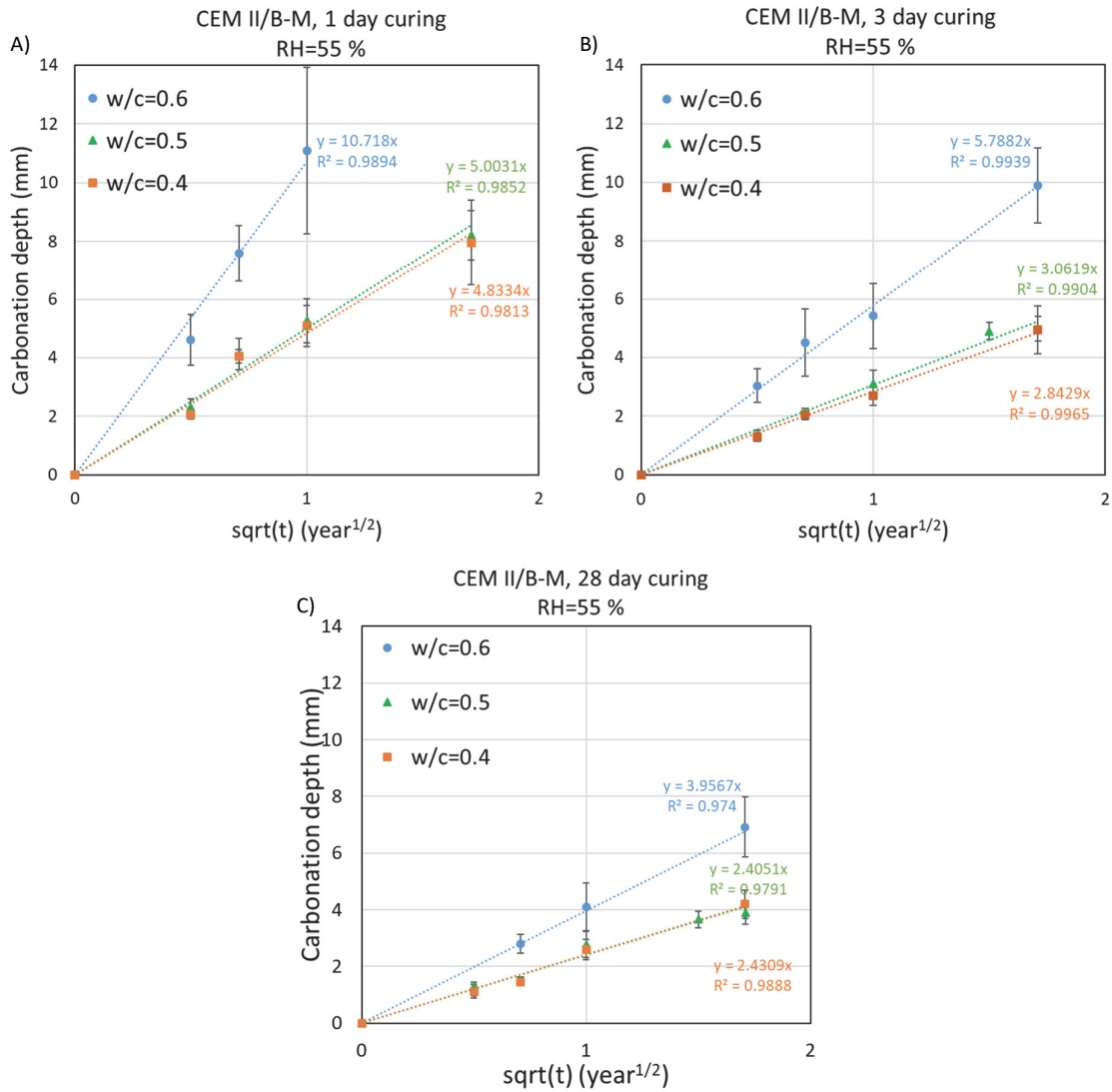


Figure 4-6. Influence of decreasing of the w/c on carbonation rate for CEM II/B-M blend cured for 1, 3 and 28 days before exposure to carbonation.

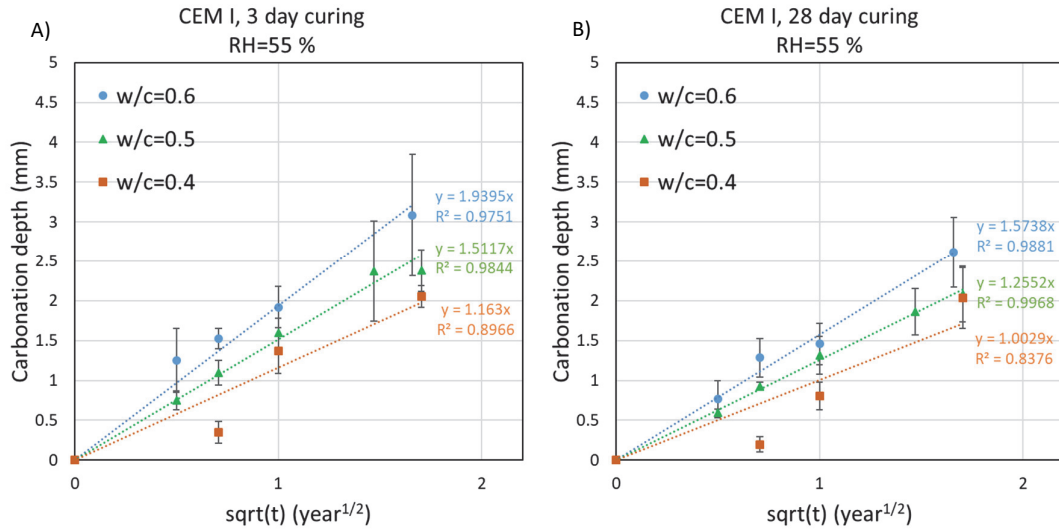


Figure 4-7. Influence of decreasing of the w/c on carbonation rate for CEM I cured for 3 and 28 days before exposure to carbonation.

4.3 Meaning of w/CaO_{reactive} and its effect on carbonation rate

Carbonation rate of the concrete made with different cement types is largely governed by the CO_2 binding capacity [43][44]. The higher the content of reactive CaO , the more CO_2 can be bound by the hydrated cement paste, resulting in higher buffer capacity against carbonation. Reactive CaO , which is present in the hydrates, can be transferred into $CaCO_3$ during the carbonation process. The binding capacity per volume of paste can be expressed by the ratio between water and CaO_{reactive} , known as w/CaO_{reactive} .

To calculate the amount of CaO_{reactive} , first, the amount of CaO obtained from a chemical analysis is needed. The standard procedure to obtain CaO content is X-ray fluorescence, known as XRF. The amount of unreactive CaO which is mostly originated by the presence of limestone was subtracted from the total CaO content. For CEM II/B-M, CEM II/B-LL and MixSL 13 %, 29 % and 20 % of the total CaO were subtracted, as that was the amount of limestone in individual blends, respectively. Carbon dioxide can react only with CaO present in the hydrates [43][44], so ideally the degree of hydration of examined microconcretes should be implemented. However, due to difficulties in examining the degree of hydration in concrete in general, the degree of hydration in the microconcrete was not known for this study. To simplify the calculations and to make the comparison possible, the entire CaO_{reactive} in the binders was taken into calculation, assuming full hydration.

Table 4-8. Content of reactive CaO for various binders with different w/c.

Cement type	w/c	CaO _{reactive} (kg/m ³)
CEM I	0.60	228.1
	0.50	253.7
	0.40	288.9
CEM II/B-M	0.60	184.8
	0.50	207.2
	0.40	235.3
CEM II/B-LL	0.60	162.8
	0.50	182.2
CEM III/A	0.60	189.7
	0.50	212.4
MixSL	0.50	163.7

All mixes were cured for 28 days and then were exposed to natural carbonation at controlled relative humidity environments, without additional preconditioning. Carbonation depth was measured every few months, to obtain the value of the carbonation coefficient for individual mixes. Figure 4-8 shows the influence of the $w/\text{CaO}_{\text{reactive}}$ on the carbonation coefficient. The $w/\text{CaO}_{\text{reactive}}$ was compared with the determined carbonation coefficients. A clear correlation can be observed between $w/\text{CaO}_{\text{reactive}}$ and the carbonation coefficient determined at natural carbonation. That indicates, that the CO_2 buffer capacity acts to be an important parameter for estimating the carbonation resistance in concrete. Correlation of the $w/\text{CaO}_{\text{reactive}}$ worsens in the 86 % RH exposure ($R^2=0.83$, 0.84 and 0.69 for 55 % RH, 70 % RH and 86 % RH respectively). Increased moisture increases inaccuracy in the correlation between $w/\text{CaO}_{\text{reactive}}$. That is due to the increased amount of pores filled with water by capillary condensation at higher relative humidity, which reduces the porosity available for gas diffusion [44]. The diffusion coefficient is dependent on the moisture content in the porosity of the concrete. The effect is fairly constant in relative humidity ranges of about 70-80 %, while above this range the diffusion coefficient falls with the decrease in moisture content [78]. Understanding the pore size distribution and its impact on transport is thus more important at high relative humidity.

Although the $w/\text{CaO}_{\text{reactive}}$ correlates relatively well with the carbonation coefficient, the more realistic would be to correlate it with $w/\text{CaO}_{\text{reacted}}$. Although all mixes were cured for 28 days in moist conditions, the hydration likely did not reach 100 % and it was progressing further during exposure [79][80]. The degree of hydration can evolve with time, depending on the exposure conditions, especially in the higher relative humidity [81]. Moreover, while exposure to carbonation, concrete simultaneously is also subjected to drying, this is why the degree of hydration can be a function of the depth in the concrete. Assessing the degree of hydration is especially difficult when more hydraulic supplementary cementitious materials, like slag and burnt oil shale with specific hydration kinetic, are present.

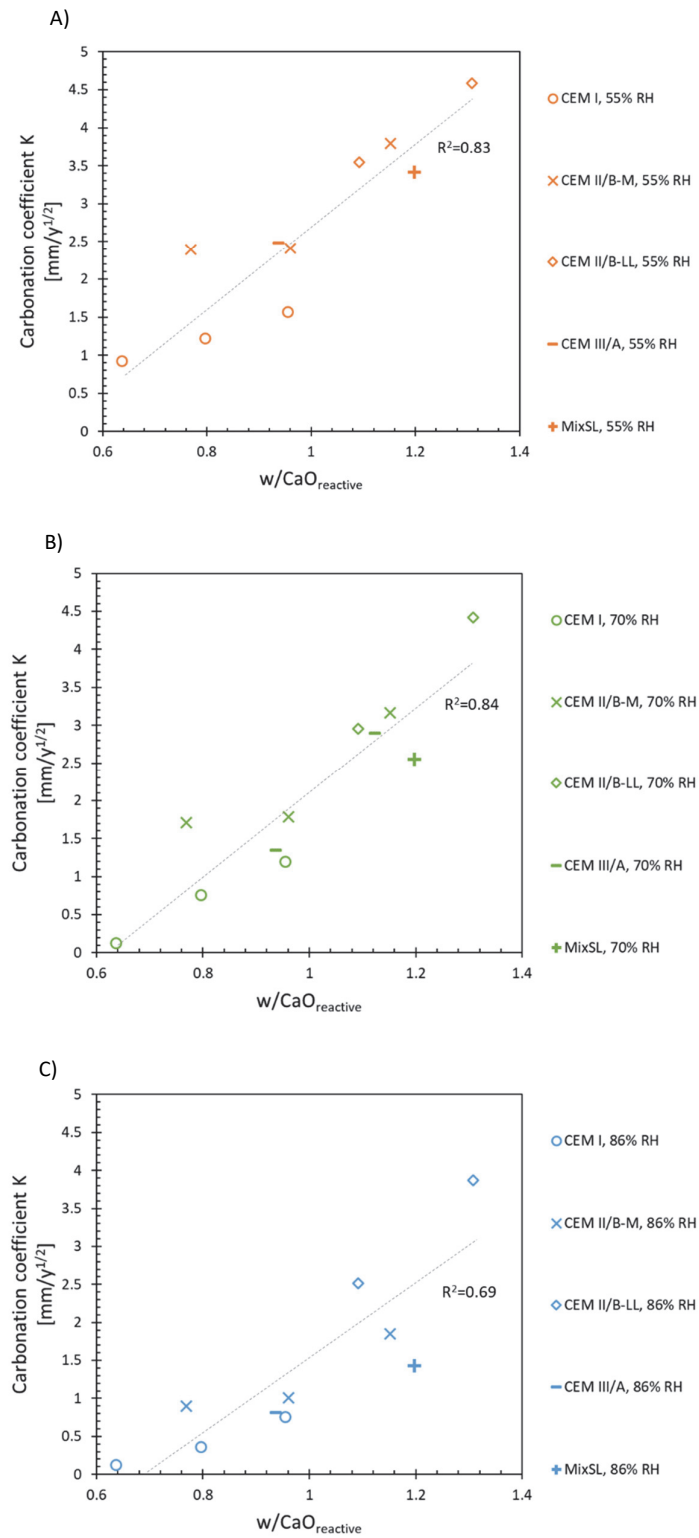


Figure 4-8. Carbonation coefficient as a function of $CaO_{reactive}$ at 3 different relative humidity conditions, A): 55 % RH, B): 70 % RH and C): 86 % RH).

4.4 Natural vs accelerated carbonation

Figure 4-9 presents five cement types, of which sample preparation, curing type, and exposure conditions are detailed in Table 4-7. The purpose is to compare natural carbonation to an accelerated test following the protocol of the Swiss norm, SIA 262-1. According to the norm, the carbonation coefficient in the natural condition is converted from the accelerated test using the formula from Eq. 4-1.

$$K_N = a \cdot b \cdot c \cdot K_A = 2.6 \cdot K_A \quad \text{Equation 4-1}$$

K_N - carbonation coefficient at natural carbonation (in years)

K_A - carbonation coefficient at 4% Vol.-% CO_2 (in days)

a - conversion from 1 day to 1 year: $\sqrt{(365/1)} = 19.10$

b - conversion from 4% to 0.04% Vol.-% CO_2 : $\sqrt{(0.04/4.0)} = 0.10$

c - correction for accelerated carbonation: 1.36

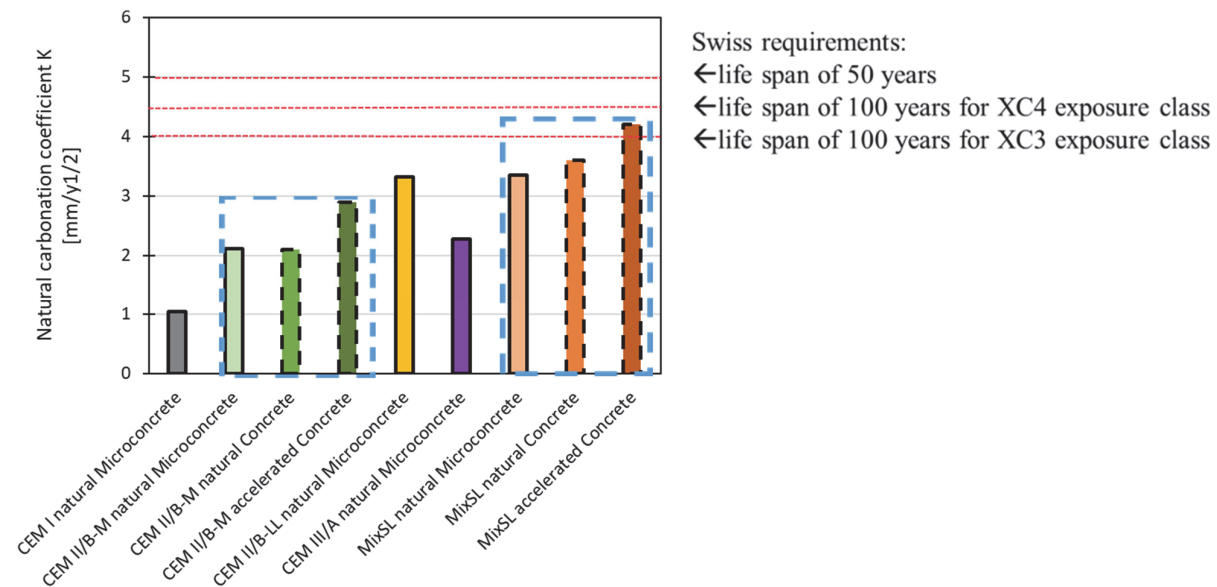


Figure 4-9. Natural carbonation compared to accelerated test.

The solid-line pillars present the carbonation coefficient of the microconcretes exposed to natural carbonation. From all cement types two blends, CEM II/B-M, and MixSL were chosen to compare the accelerated test with the natural carbonation. Types of cements and exposures are indicated on the x-axis. Interestingly, although all blends are less resistant against carbonation than the Portland cement, all of them pass the requirements of

the life span of 50 years and of 100 years for XC4 exposure class. Even though blends do not match the resistance of the PC, they are still in many cases good enough.

For both blends, the accelerated test overestimates the value of the carbonation coefficient measured in natural carbonation conditions. This is in agreement with a previous study [9]. It means that the formula provided in the norms is not representative of all blended systems. It is too conservative. This cannot be fixed by changing the conversion coefficient as the ratio of accelerated versus natural carbonation is not constant (as can be seen from Figure 4-9), what is due to the fact that in accelerated carbonation tests there is a constant competition between carbonation and drying. This has strong implications for the development of new sustainable formulations, which are classified too harshly of being unsafe with respect to carbonation. Use of the cements with high substitution level is still a big question in terms of predicting the carbonation behavior, especially for new cements. More reliable accelerated test has to be found, which do not unjustifiably discourage the use of more environmentally friendly materials.

Use of accelerated test is necessary to decrease the time of experiment which in natural conditions takes very long due to the slow process of carbonation. However, norms regarding accelerated tests need to be better optimised for the blended cements. That would enable to convert the carbonation coefficient obtained during the accelerated test to the realistic exposure conditions. Decreasing the duration of the experiment is important, but the reliability of the test should be on the first place.

Although the accelerated test was performed on concrete samples, while the natural carbonation on microconcrete (max aggregate size 8 mm), it seems that the volume of paste does not influence the carbonation rate. That is in the agreement with [82] where the authors show, that the carbonation depth does not depend on the paste volume in the mix. Basically, it means that carbonation depth for paste, mortar, microconcrete or concrete made with the same w/c for chosen cement type does not vary. That is very relevant information while comparing the carbonation rate for samples made with different paste volumes, as it is the case in this study.

Table 4-9. Comparison of the sample preparation, curing and exposure conditions for natural and accelerated carbonation tests.

	Accelerated carbonation on concrete (Lafarge-Holcim)	Natural carbonation on microconcrete (EPFL)	Natural carbonation on concrete cast at Lafarge-Holcim exposed at EPFL
Curing time before exposure	28 day, underwater	28 days, a moist room at 95 % RH	28 day, underwater
CO ₂ concentration	4 %	0.04 %	0.04 %
RH	57 % ±3 %	55 % ±5 %	55 % ±5 %
T	20°C	20°C±3°C	20°C±3°C
Sample size	12x12x36 cm	4x4x4 cm	12x12x36 cm
Max. aggregate size	32 mm (wet)	8 mm (dry)	32 mm (wet)

This chapter shows how carbonation resistance is influenced by the design of the concrete, including binder composition, water to cement ratio, curing time before exposure to carbonation and exposure conditions itself, where especially relative humidity plays a big role. Carbonation rate is also dependent on carbon dioxide migration through the porous structure of concrete. The diffusion coefficient, which is characteristic for individual concretes, will change as the carbonation process changes the porous microstructure, which is one of the driving factors of diffusion. That is why the following chapters will examine the microstructure (including phase assemblage and porosity) changes due to carbonation and its correlation with diffusion coefficient.

Further work will focus on the paste study, as this is where the principle changes occur in different materials. Moreover, natural exposure conditions will avoid the danger of a too pessimistic outlook for the blended cement systems.

Chapter 5 Microstructural characteristics of the cement paste and its changes due to drying

5.1	Porosity evolution due to drying.....	50
5.1.1	Porosity evolution studied by MIP	50
5.1.2	Microstructure investigation using a backscatter-electron images (BSE)	56
5.1.3	Morphology investigation using high-resolution microscopy	59
5.2	Phase assemblage.....	63
5.2.1	XRD-Rietveld quantification.....	63
5.2.2	Differential thermogravimetry analysis.....	66
5.2.3	C-S-H composition studied by SEM-EDX.....	66
5.3	Impact of reimmersion on porosity.....	67

Prolonged curing of hydraulic cementitious materials in high relative humidity (RH) leads to an increase in cement hydration that is necessary for the further improvement of concrete quality [83]. It is reported that when the RH drops below 80 %, hydration of clinker ceases [84][85]. However, it does not mean that the porosity remains unchanged. The microstructure of hydrated cement paste is sensitive to environmental drying [81]. It is significant since changes to the microstructure are associated with the changes to the diffusion properties of the concrete that is responsible for protecting the reinforcing steel [86]. It was shown that exposure of ordinary Portland cement (OPC) to environmental drying modifies the porosity [81][86][87][88][89][90][50]. Understanding these changes in the pore size distribution is important in the context of carbonation. Variation of microstructure and porosity of cement binders due to carbonation can interfere with parallel changes of the microstructure, arising from a simultaneous variation of relative humidity. In the literature, most of the focus was on OPC systems. As the demand for low clinker cements increases, there is increased emphasis on blended cements [91]. In addition to OPC, blends with limestone, slag, and burnt oil shale are studied here to investigate if the drying has a similar effect on those blends. In this chapter, the hydration and porosity evolution as a function of exposure time, at 70 % RH in the absence of carbon dioxide, are examined (Figure 5-1). It is intended to provide a better understanding of the properties of the cement paste made with diverse SCMs mixes

subjected to environmental drying. The specimens were exposed in the same conditions as during carbonation but in the absence of carbon dioxide. Deconvolution of the drying from carbonation will help to provide a relevant reference for carbonated systems, presented in the next chapters. In addition to the study on phase assemblage and on porosity evolution, high-resolution microscopy was used to investigate differences in morphology of the hydrates.

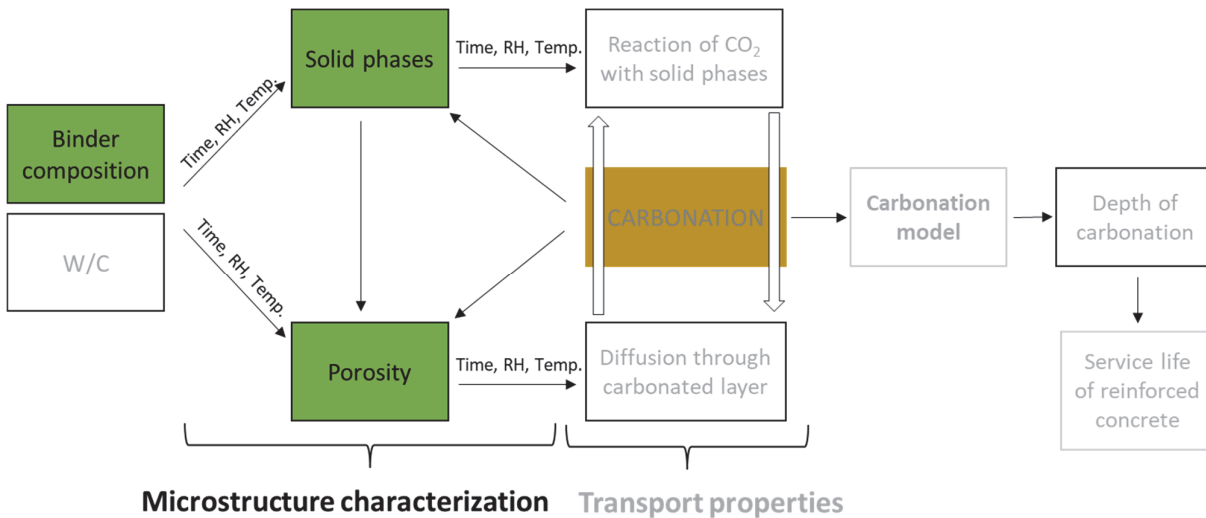


Figure 5-1. Research scope: characterisation of the cement paste microstructure.

5.1 Porosity evolution due to drying

5.1.1 Porosity evolution studied by MIP

Effect of initial curing at t_0

The pore entry size distributions at different times of exposure, for the five different cement compositions, are presented in Figure 5-2 (3 days curing) and Figure 5-3 (28 days curing). MIP curves were obtained after curing, and then, at chosen times, up to 19 months of exposure. Prior to the experiment, investigated samples were dried using a solvent exchange method. For all mixes, the same water to cement ratio of 0.40 was used. The only exception was the MixSL, for which additionally $w/c=0.35$ was used to see the full effect of the additives and superplasticizer with which the new mix was designed. Due to the progress of hydration between 3 and 28 days of curing, all types of cement show a decrease in capillary pore volume and a shift of the curve towards smaller pore radii (Table 5-1). The most significant decrease of the critical pore radius (a maximum peak in the derivative of the mercury intrusion curve) after increasing curing time from 3 to 28 days, was for the CEM II/B-LL. The critical pore radius for this blend is decreased by 22.87 nm, which constitutes 65 % of the initial critical pore radius after 3 days of curing. It is also worth mentioning that this cement has the highest critical

pore radius after 3 days of curing among all of the studied cements. Interestingly, after 28 days of curing, all studied cements had a critical pore radius of around 11 nm (± 2 nm).

Table 5-1. Critical pore radius changes for all cement types after the increase of the curing time from 3 days to 28 days.

	Critical pore radius R_c (nm)		Reduction of the radius ($R_{c_{28d}} - R_{c_{3d}}$) (in nm)	Reduction of the radius ($R_{c_{28d}} - R_{c_{3d}}$) (in %)
	3 days of curing before exposure $R_{c_{3d}}$	28 days of curing before exposure $R_{c_{28d}}$		
CEM I	13.14	11.29	-1.85	-14
CEM II/B-M	18.82	12.85	-5.97	-32
CEM II/B-LL	35.27	12.40	-22.87	-65
CEM III/A	23.90	11.38	-12.52	-52
MixSL	-	9.84	-	-
MixSL, w/c=0.35	14.97	7.47	-7.50	-50

In Table 5-2 values of total porosity after 3 days and 28 days of curing are presented. Prolonged curing from 3 up to 28 days decreases the pore volume. After 3 days of curing all blended cement have higher total porosity than OPC. The only exception is noticed for MixSL with w/c=0.35. This mix reaches basically the same value as Portland cement. After additional curing up to 28 days, the decrease in the total porosity varies between 4 and 9 % (Table 5-2).

Table 5-2. Total porosity changes for all cement types after the increase of the curing time from 3 days to 28 days.

	Total porosity (%)		Reduction of the total porosity ($P_{28d} - P_{3d}$)
	3 days of curing before exposure P_{3d}	28 days of curing before exposure P_{28d}	
CEM I	24.56	19.66	-4.90
CEM II/B-M	27.48	23.45	-4.03
CEM II/B-LL	33.51	26.42	-7.09
CEM III/A	32.44	23.77	-8.67
MixSL	-	22.96	-
MixSL, w/c=0.35	24.28	19.16	-5.12

Porosity evolution in time

Interestingly, for the specimens kept at constant RH without CO₂, the porosity becomes coarser and the microstructure of the samples alters. Already after 1 month of exposure at 70 % RH, the pore entry size distribution changes significantly. The evolution (coarsening) continues with further exposure for all five systems. This effect is enhanced when the curing time is decreased from 28 to only 3 days.

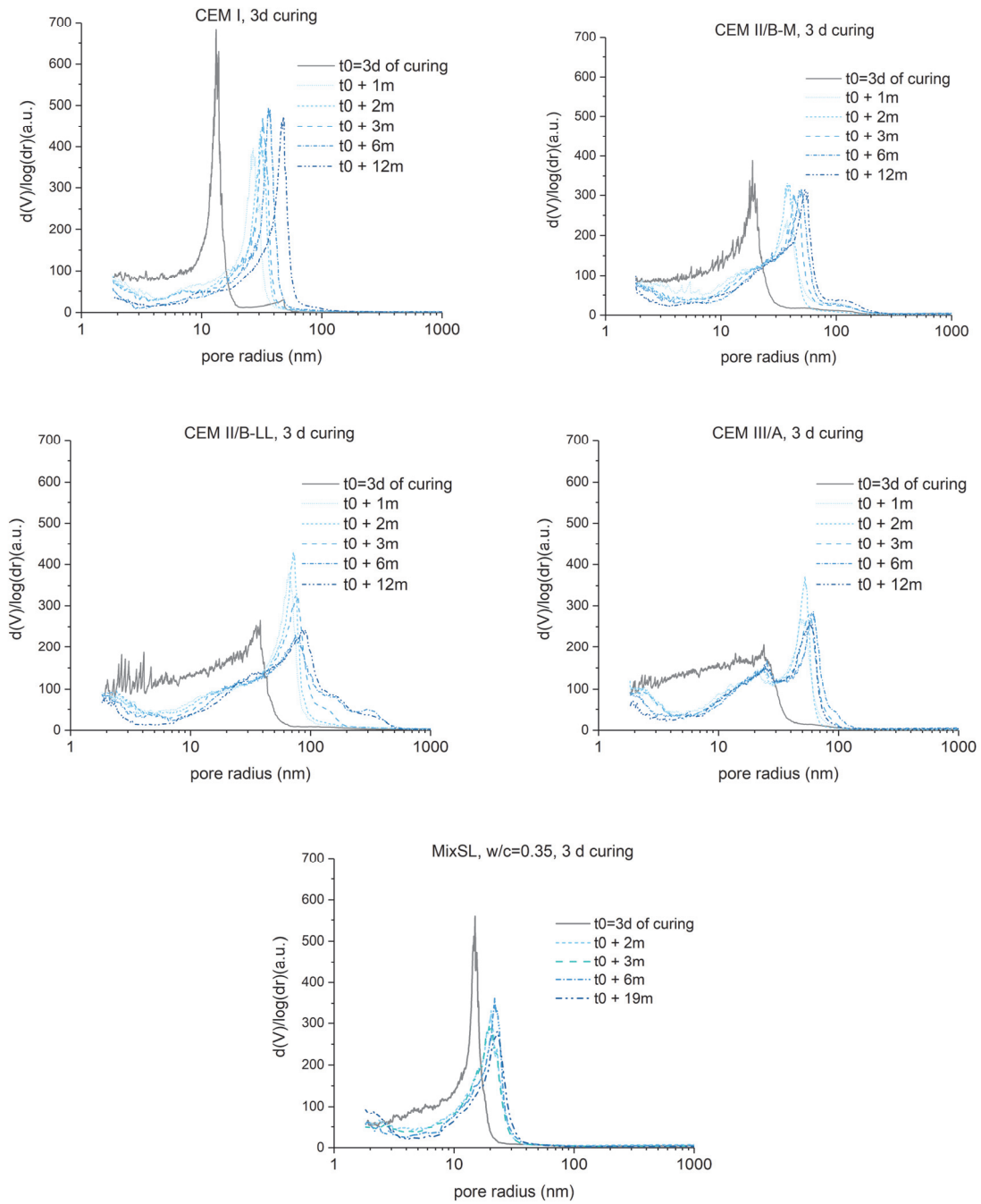


Figure 5-2. Impact of drying on pore size distribution for OPC and blended cements paste, cured for 3 days at RH > 95 %, followed by exposure at 70 % RH in a CO₂-free atmosphere. For all cements, except MixSL, w/c=0.40.

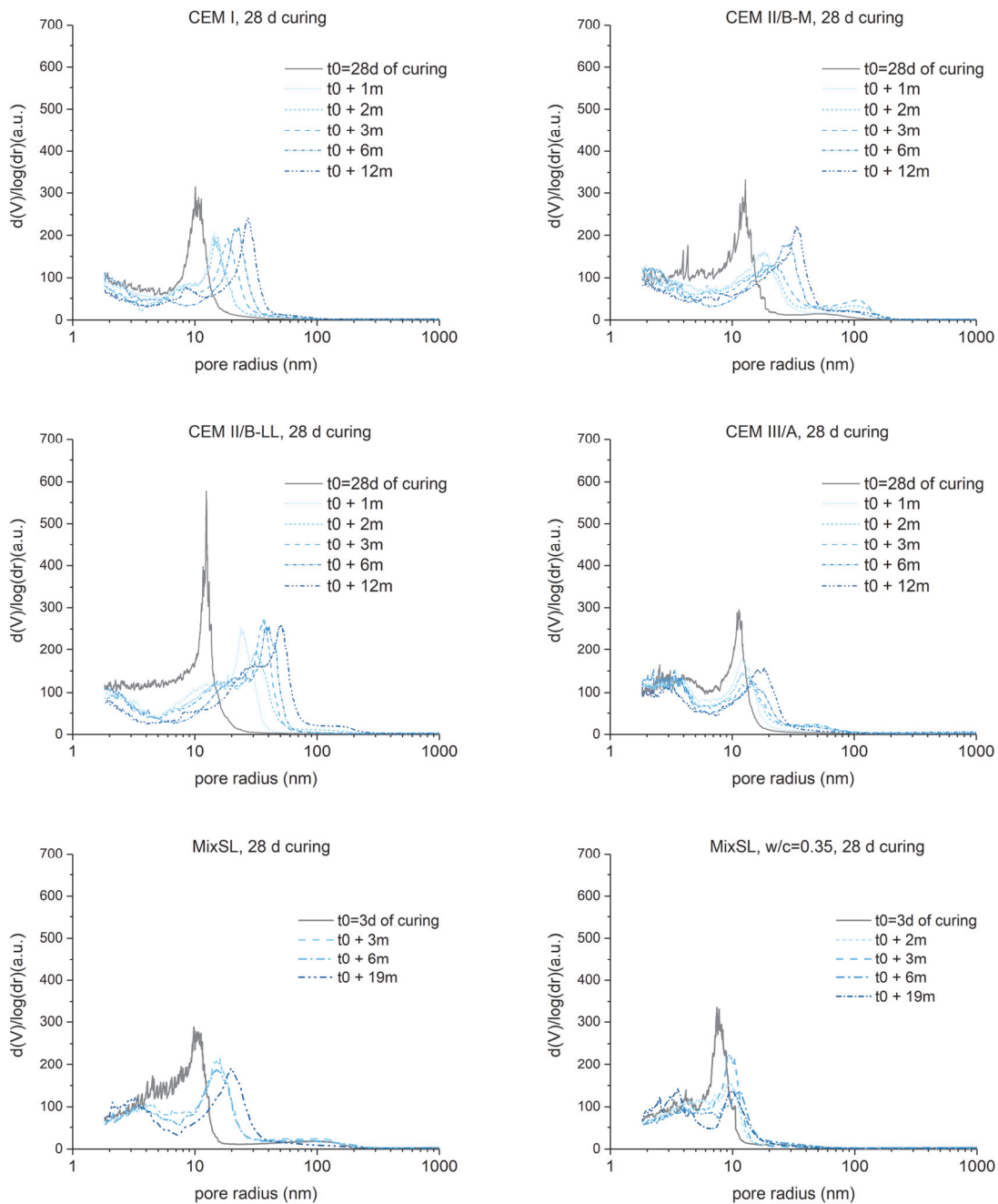


Figure 5-3. Impact of drying on pore size distribution for OPC and blended cements paste cured for 28 days at RH > 95 %, followed by exposure at 70 % RH in a CO₂-free atmosphere. For all cements, except one of the MixSL, w/c=0.40.

Such changes in porosity on drying have previously been reported in the literature for OPC [86][87][88][89][90][50] or on blends with slag or fly ash [88][50]. The coarsening effect is also observed in this work, performed on the commercially available blends with limestone, slag, ternary blend with limestone and burnt oil shale, and on the new MixSL with burnt oil shale, slag, limestone, and additives. Figure 5-4 and Figure 5-5 summarise the results of evolution in porosity distribution and total porosity. Differences in the

critical pore radius between different binders at 3 days of hydration are an effect of different compositions and finesses, affecting the reaction rate. Surprisingly, at 28 days of curing, the effect of different binders does not have influence anymore on the critical pore size, which is nearly the same for all five types of cement. We can see in Figure 5-4 and in Table 5-1 that all systems cured for 28 days have very comparable initial critical pore radius, of $11 \text{ nm} \pm 2 \text{ nm}$ at $t=0$ (means before exposure). Despite the same starting critical pore radius values, (after 28 days of curing) the ends values (at 12 or 19 months of exposure) are different for all systems. The pore volume, as measured by MIP, is higher for blended cements than for OPC paste. Contrary to critical pore size, the total porosity shows almost no variation (max $\pm 3 \%$) between the initial values and the porosity after 12 months of exposure.

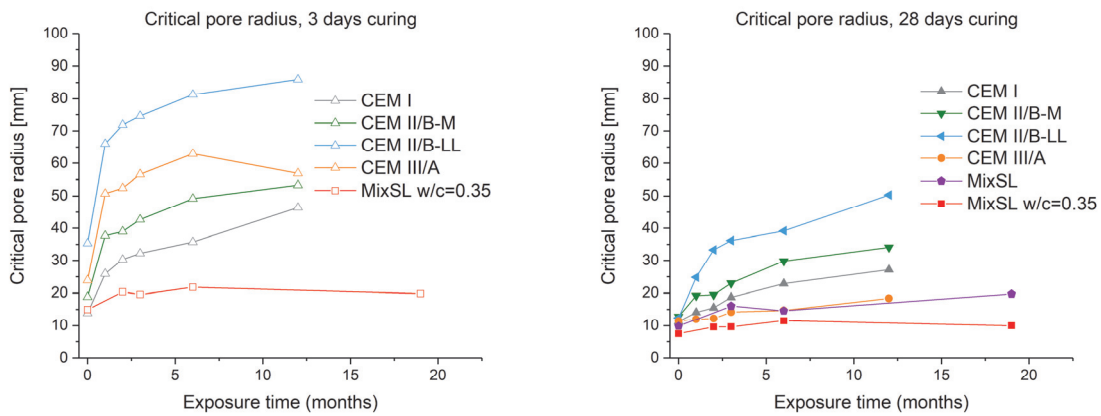


Figure 5-4. Critical entry pore size for OPC and blended cement pastes after curing for 3 and 28 days, followed by exposure at 70 % RH in CO_2 -free atmosphere.

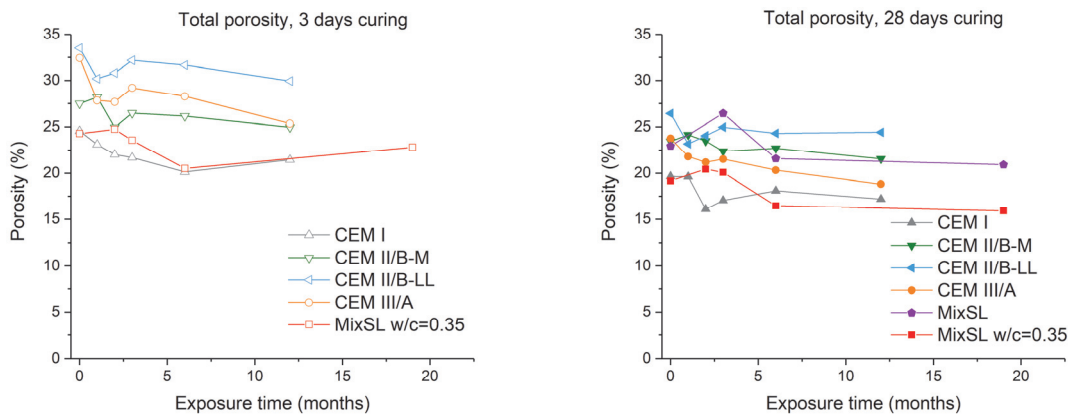


Figure 5-5. Total porosity quantification of OPC and blended cement pastes after curing for 3 and 28 days, followed by exposure at 70 % RH in CO_2 -free atmosphere.

Effect of different relative humidity

We know what happens to the porosity distribution while exposing samples to the relative humidity of 70 %. To ensure that it does not occur only in these conditions, the cement paste was cast again for one of the blends and the effect of the relative humidity of 55 % on the porosity redistribution was studied. The solid lines in Figure 5-6 show the same type of cement, cast with one year of a break in between. Although the cement was stored in the sealed conditions, some hydration of the raw material could have occurred during storage. That could explain the minor differences in porosity after 28 days of curing (grey solid line) versus the new cast (orange solid line). Similar to the 70 % RH conditions, the 55 % RH does not cause major changes in total porosity, as the initial porosity is 20 % and the one after 3 months of exposure in RH of 55 % equals 21 %. However, the critical pore radius increases from 17 nm up to 46 nm, that accounts for 170 % of the increase in critical pore radius value, while at RH 70 % this increase is 86 % (also after 3 months of exposure, and continue the increase up to 200 % after 2 years of exposure).

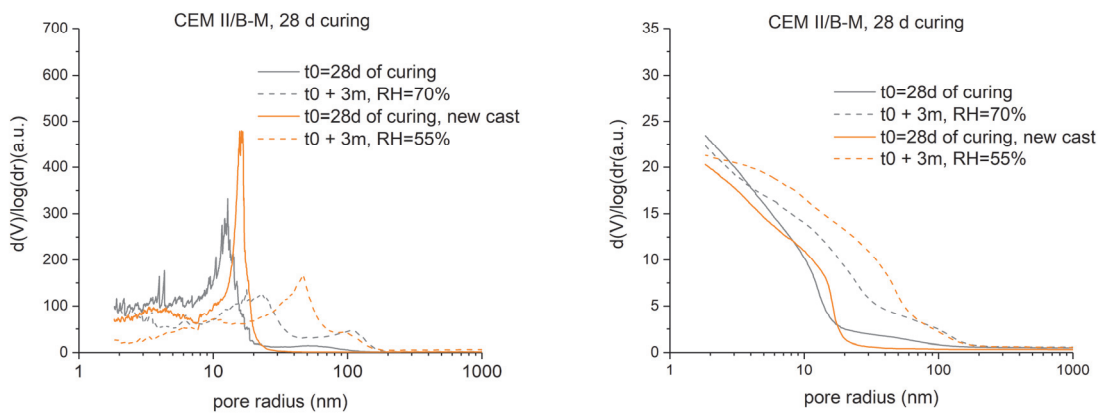


Figure 5-6. Consequence of the exposure at different relative humidities on the coarsening effect.

It is believed that the coarsening of the porosity is happening due to a partial collapse in the small pores, that is induced by the surface tension forces arising during drying [88][90]. The phenomenon takes place at both studied relative humidities. It seems, that lower RH has a higher impact on porosity redistribution. That might be crucial while investigating the carbonation effect on microstructural changes. To explore the behavior of the porosity redistribution, the microstructure was further investigated as explained in the following sections.

5.1.2 Microstructure investigation using backscatter-electron images (BSE)

Backscatter-electron imaging was used to qualitatively assess the matrix in 3 or 28 days cured paste versus paste additionally exposed into drying at 70 % RH without the presence of CO₂. The results presented in this section come from the PC and the blended cement CEM II/B-M with limestone and burnt oil shale. The images

were collected at 500x magnification, with the field of view 1024 x 768 pixels. The results obtained are presented in micrographs from Figure 5-7 to Figure 5-9.

In Figure 5-7 can be seen that microstructures between the two studied cases do not change significantly. Micrograph A presents the microstructure after 28 of curing, while micrograph B represents the microstructure after 1 month of additional exposure into 70 % RH without CO₂. The images demonstrate that there is no major difference in the microstructure after exposure. The number of anhydrous seems to stay on a similar level. Also, space-filling does not change significantly. An additional purpose of taking the BSE images was to investigate if any cracks, which could be caused by drying, can be observed. On the studied samples no cracks were noticed, however, a possibility of cracking occurring on a finer scale, which can not be detected by BSE images, is not excluded.

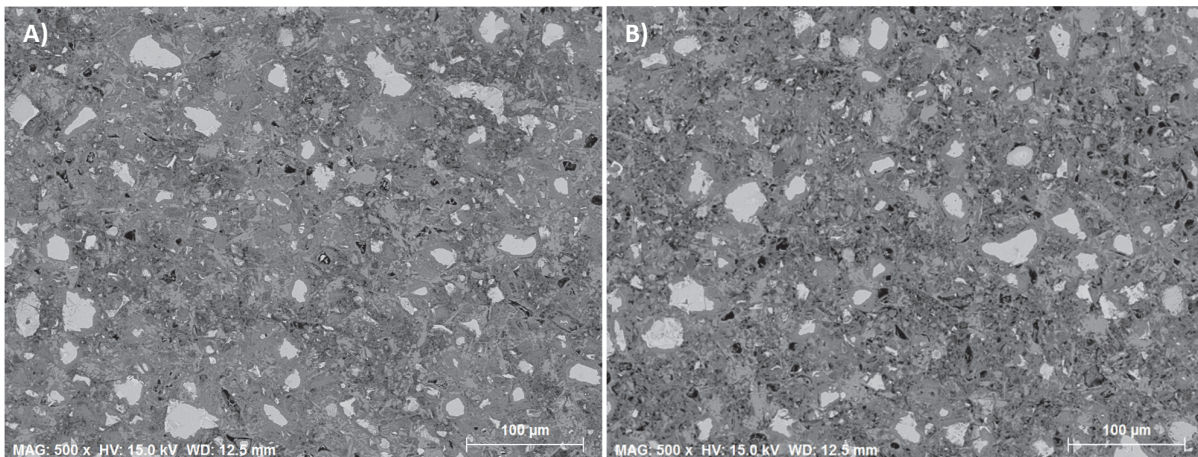


Figure 5-7. BSE for CEM I cured for 28 days (A) and then exposed at 70 % RH in CO₂-free atmosphere for 1 month (B).

In addition to exposure for 1 month at 70 % RH in CO₂-free atmosphere for CEM II/B-M cured for 28 days, observation after 2 months of exposure was also performed. Although MIP curves show a difference between those ages the micrographs do not help to find an answer for the questions regarding the coarsening due to drying. A similar conclusion is drawn after looking on the microstructure of the blend after only 3 days of curing (Figure 5-9). From Figure 5-4 it can be seen that the critical pore radius gets coarser more significantly for the systems cured for 3 days before exposure than in the ones cured for 28 days. Despite that, the changes in microstructure provided by BSE are only minor.

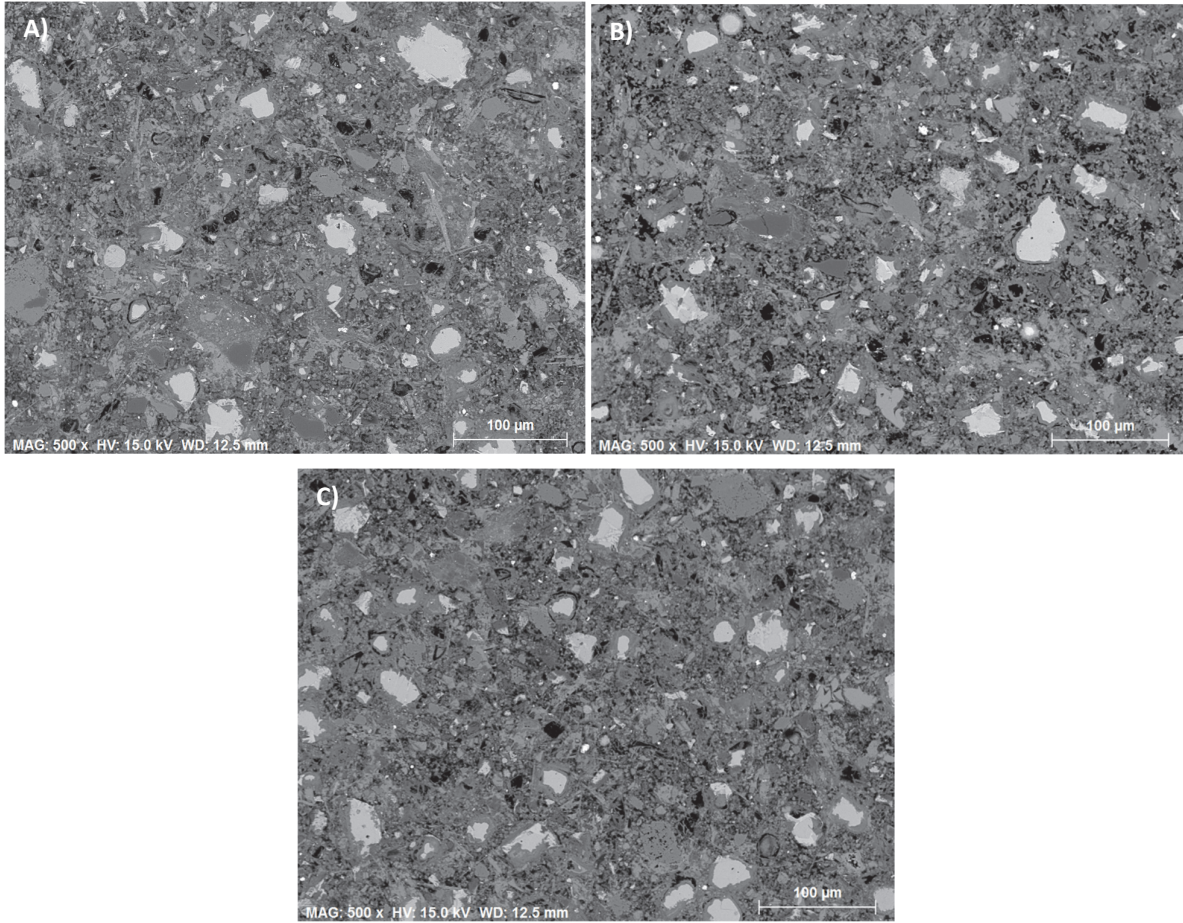


Figure 5-8. BSE for CEM II/B-M cured for 28 days (A) and then exposed at 70 % RH in CO_2 -free atmosphere for 1 month (B) and 2 months (C).

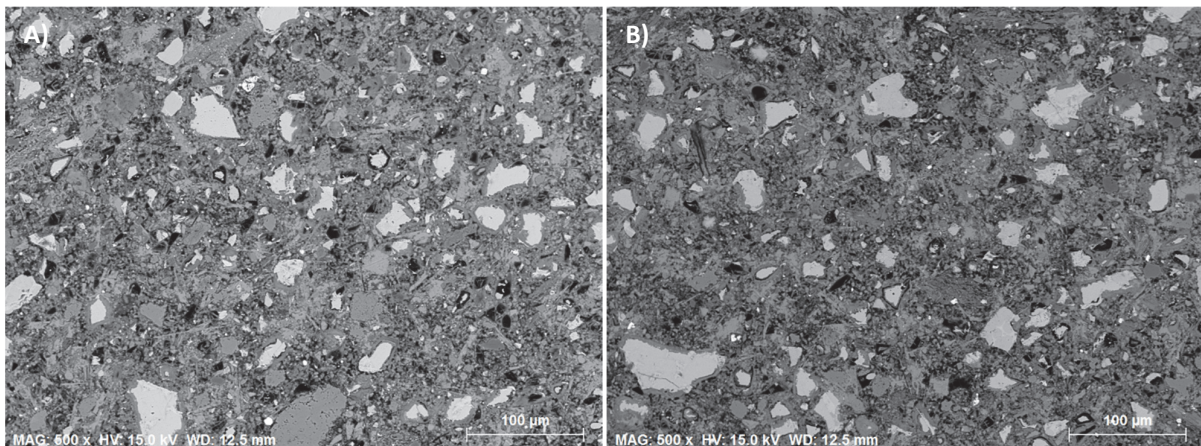


Figure 5-9. BSE for CEM II/B-M cured for 3 days (A) and then exposed at 70 % RH in CO_2 -free atmosphere for 1 month (B).

The micrographs obtained from BSE give an overview about the microstructure and exclude the probability of the presence of cracks in the studied samples, however, the magnification which can be used in BSE images does not allow to find the answer for the question about the coarsening, raised after MIP experiments. For further digging to find the reason for coarsening, the high-resolution microscope was used. It provides some information about the morphology of the hydrates on the nanometres scale, that potentially could provide an explanation of the trends observed in the MIP curves.

5.1.3 Morphology investigation using high-resolution microscopy

It is known that C-S-H grows as clusters of needles termed “fibrillary morphology” [92]. The porosity in the mature paste is dominated by the spaces between these needles [92]. One of the hypotheses of this study is that during the conservation at 70 % RH the needles are converging together. Instead of having very small gaps between them, much larger gaps are observed, as shown schematically in Figure 5-10.

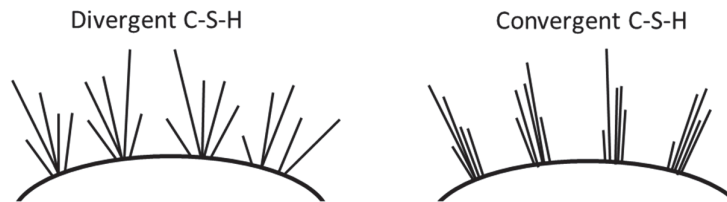


Figure 5-10. Schematic morphologies of C-S-H during hydration (divergent C-S-H) and after exposure into drying in CO₂-free environment (convergent C-S-H) in decreased RH.

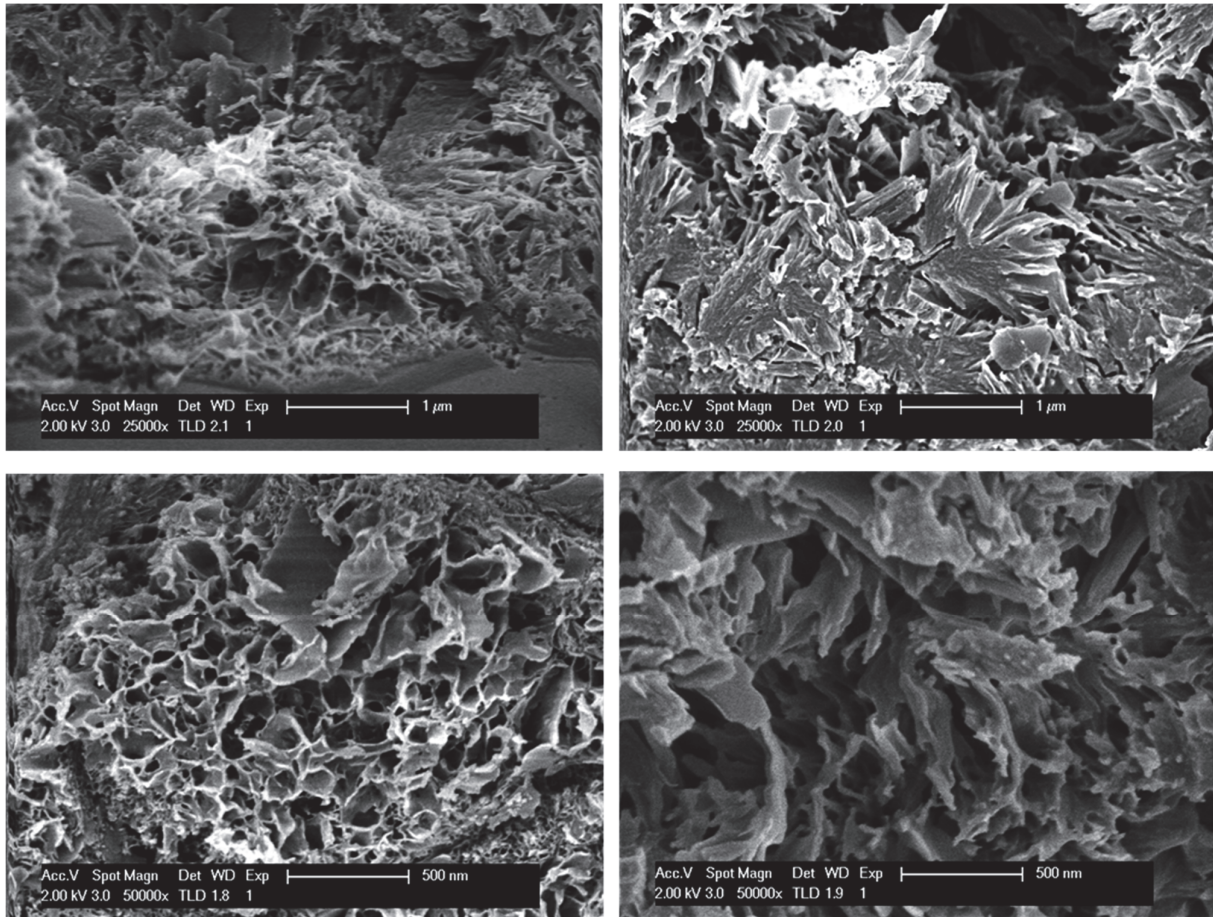


Figure 5-11. Micrographs of CEM I at 3 days of curing (on the left) vs additional 12 months of drying at 70 % RH (on the right).

Unlike for BSE images, where the cement paste had to be prepared by polishing a section immersed into an epoxy, for the high-resolution microscope, the sample was broken into small pieces. This allows the morphology to be observed. Small pieces from the samples (before exposure and after 12 months of exposure at CO_2 -free atmosphere and 70 % RH) were coated with iridium. Specimens made with CEM I and CEM II/B-LL cured for 3 days were chosen for topology observations with the use of the high-resolution microscope. Figure 5-11 and Figure 5-12 show micrographs of the specimens at 3 days of curing, and after additional exposure for 12 months at CO_2 -free atmosphere at 70 % RH. Both figures show characteristic C-S-H morphology [92]. The main difference between the samples obtained directly after curing (on the left side of the figure) and the samples followed by exposure at 70 % RH (on the right side of the figure) is the reduction of small pores in the morphology of the C-S-H. That, in consequence, changes the microstructure of the samples exposed to drying at lower RH. We can notice that the samples studied directly after curing have more of the “beehive” like structure, while the ones exposed to drying, form more isolated, converged peaks of C-S-H.

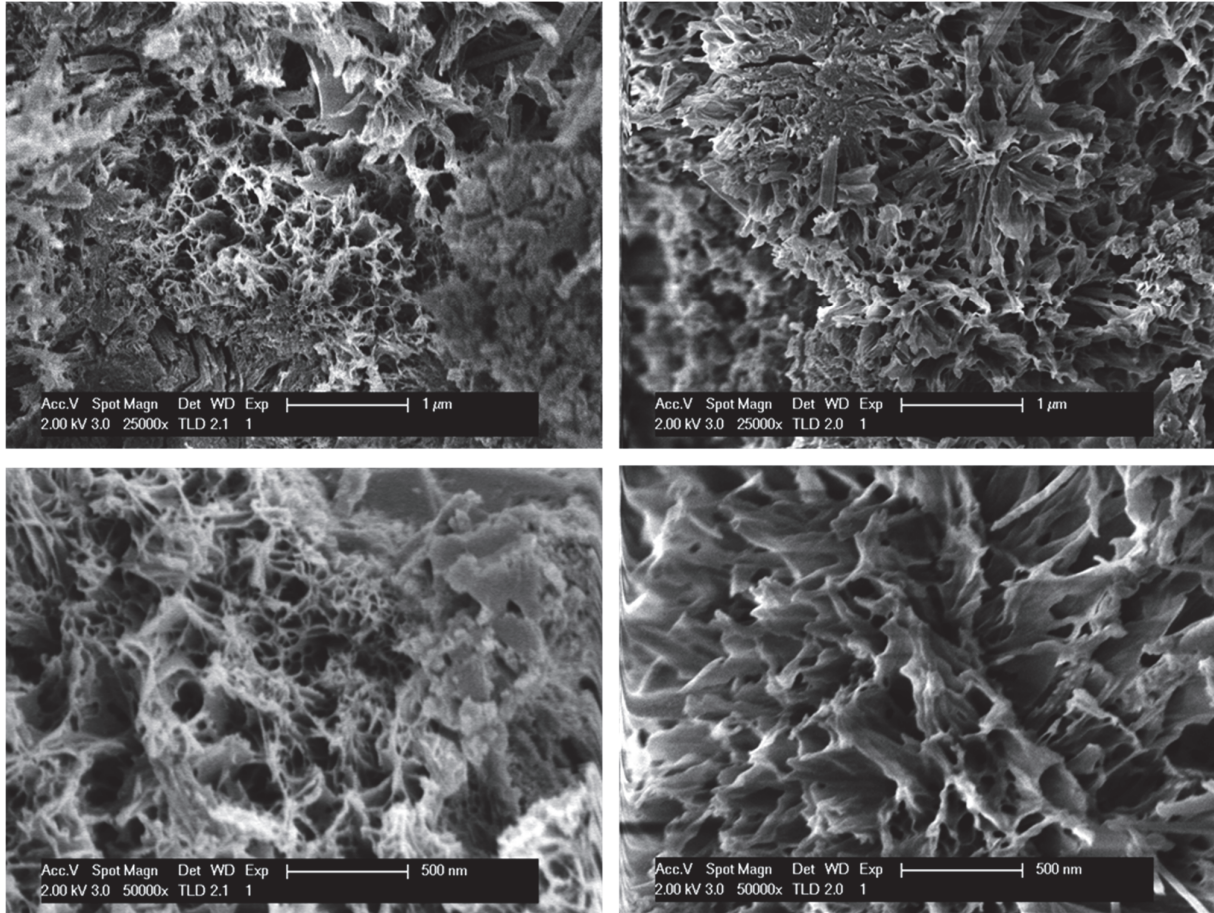


Figure 5-12. Micrographs of CEM II/B-LL at 3 days of curing (on the left) vs additional 12 months of drying at 70 % RH (on the right).

To find out if the magnification is sufficient to be comparable with the MIP results, one of the systems was chosen to perform a semi-quantitative analysis. For this purpose, it was easier to work with the CEM II/B-LL because of the more open structure due to the limestone addition. That allows easier observation of the C-S-H morphology. Before comparing with MIP curves, five pictures for PC and five for blends were chosen. For each picture 50 pore diameters were measured. Figure 5-13 presents the same micrographs as Figure 5-12, but additionally, it indicates the pores which were measured in ImageJ. The yellow lines designate the pore diameter. To make it comparable with MIP results the diameters were converted to the radius. The average pore diameter was calculated for samples cured for 3 days and for samples additionally exposed for 12 months of drying at 70 % RH in CO₂-free atmosphere. Results of this analysis are presented in Figure 5-14.

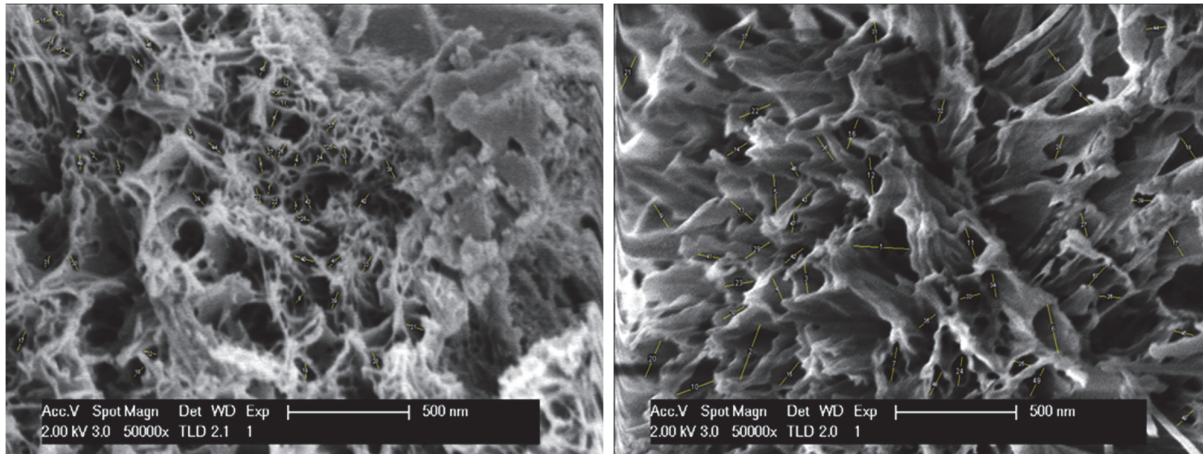


Figure 5-13. Micrographs of CEM II/B-M at 3 days of curing (on the left) vs additional 12 months of drying at 70 % RH (on the right), illustrating the usage of the ImageJ, measuring the radius of 50 pores per picture.

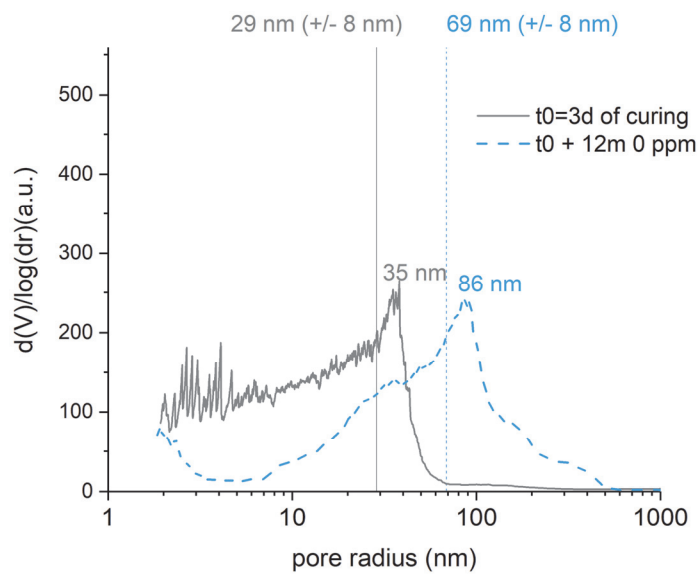


Figure 5-14. Comparison of the pore radius obtained from MIP vs semi-quantitative image analysis method measuring the pore radius from SFEG micrographs.

We can see that the average pore diameter, measured by image analysis on the micrographs taken by the high-resolution microscope, fell slightly below the critical pore radius obtained by MIP, but considering the semi-quantitative nature of the SEM measurements, the agreement is remarkable. This indicates that the MIP results are reliable and despite the reported limitations of this technique [93][94], we can trust the results obtained concerning the porosity redistribution. That means that the coarsening observed in the MIP curves reflect the real phenomena happening in the samples due to drying in lower RH.

5.2 Phase assemblage

5.2.1 XRD-Rietveld quantification

Figure 5-15 presents the portlandite and calcium carbonate content as a function of exposure time. The presence of calcium carbonate in CEM II/B-M and CEM II/B-LL is due to the limestone in the original mixes. It can be seen that the contents of both portlandite and calcium carbonate, do not change significantly during the exposure. The constant value of calcium hydroxide at 70 % RH is consistent with the OPC hydration data published in [90], showing additional portlandite formation only above 70 % RH.

The constant values for portlandite and calcium carbonate content in the current work (Figure 5-15) confirm that there was no carbonation occurring during the exposure time.

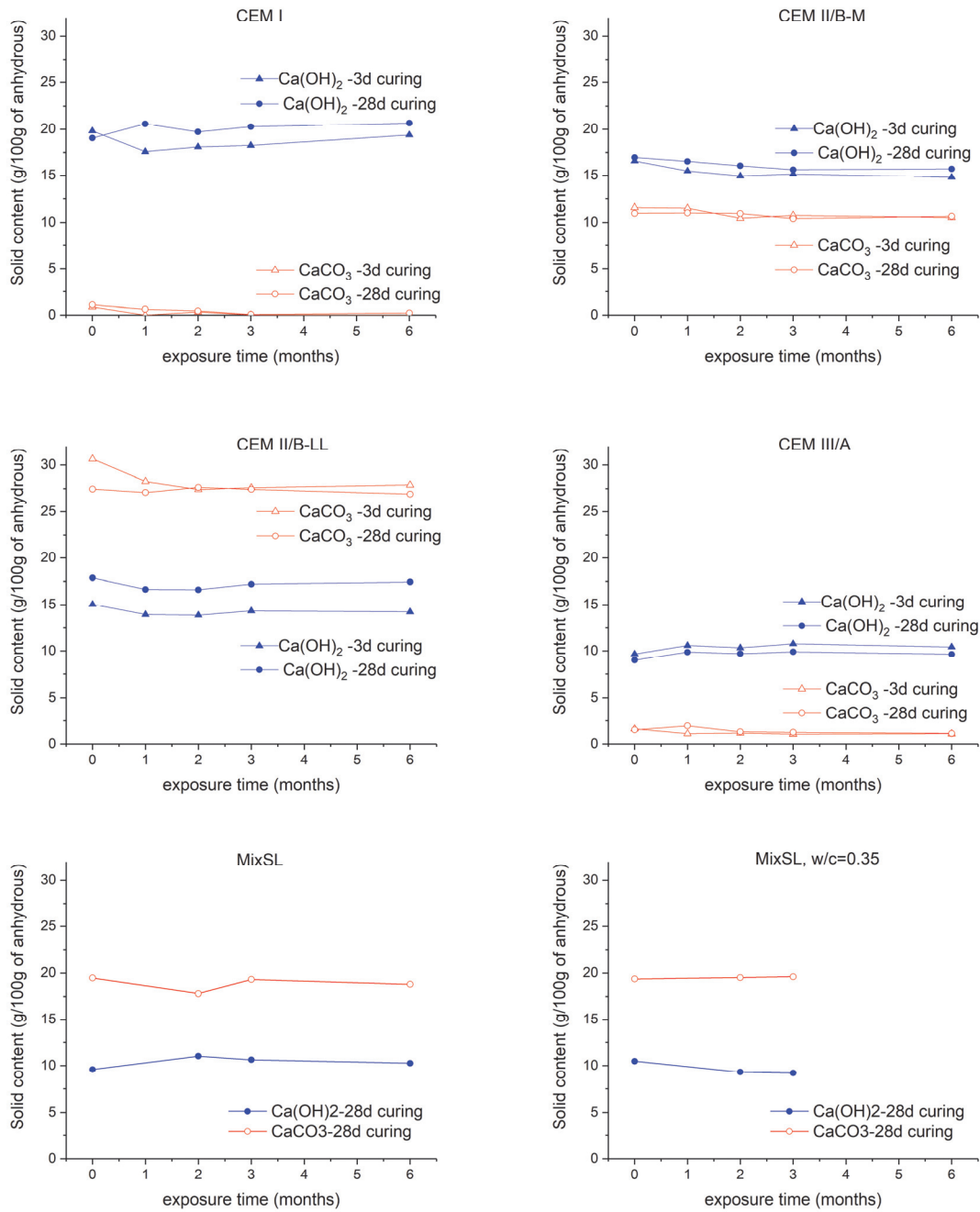


Figure 5-15. Portlandite ($\text{Ca}(\text{OH})_2$) and calcium carbonate (CaCO_3) content as a function of exposure time in CO_2 -free atmosphere and 70 % RH, for several mixes and curing times. For all cements, except one of the MixSL, $w/c=0.40$

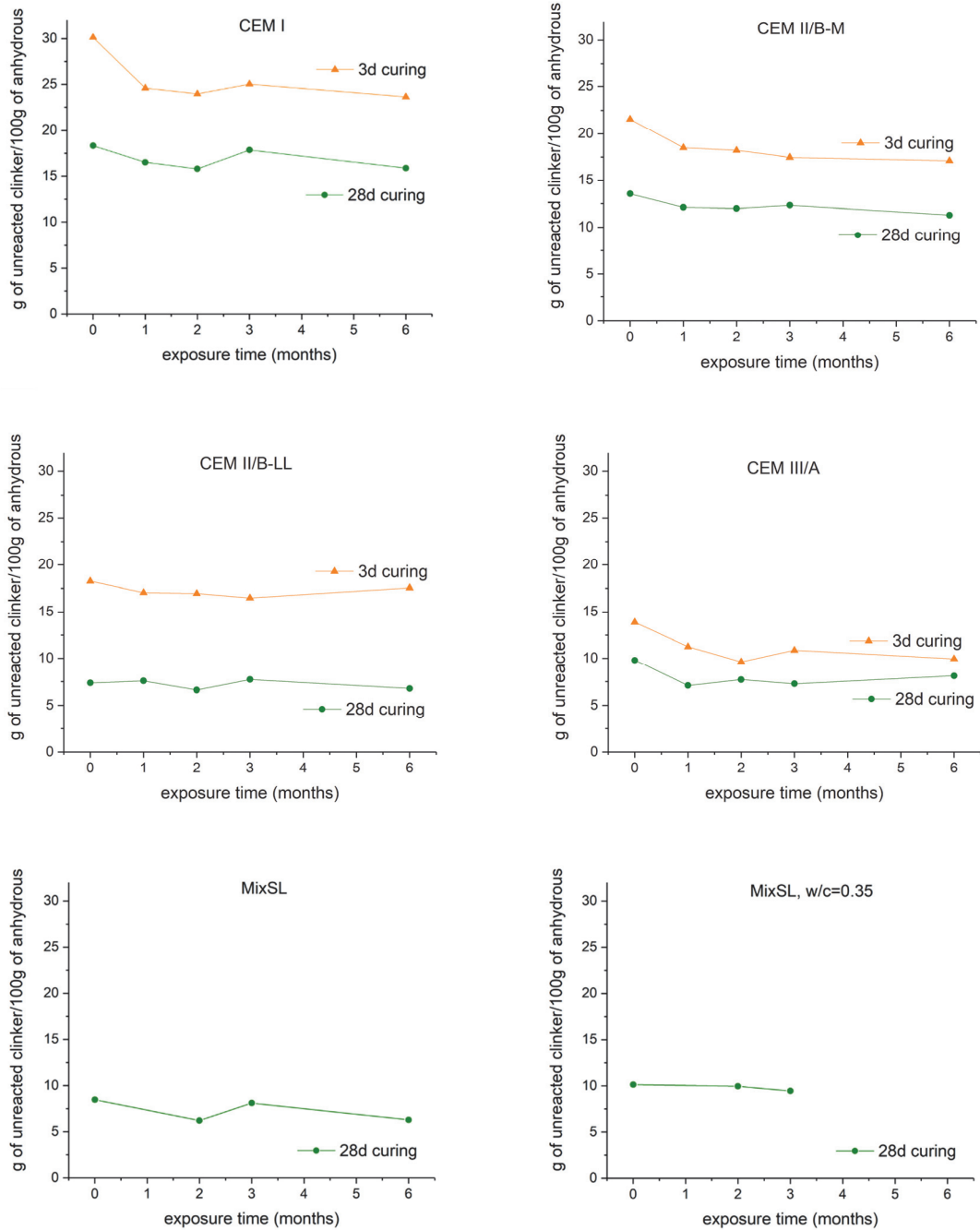


Figure 5-16. Changes in unreacted clinker content as a function of exposure time in CO₂-free atmosphere and 70 % RH, for several mixes and curing times.

Figure 5-16 shows that the content of unreacted clinker phases changes only slightly in samples, which were kept in the environment without CO₂ and at RH 70 %. There is a lower degree of reaction for the samples with the shorter curing time (3 days) compared to those cured for 28 days. It can be seen that exposure of the samples

at 70 % RH substantially slows down the hydration or even stops it completely. It has been reported by several authors that hydration slow down significantly at relative humidities below 80% [84][90].

5.2.2 Differential thermogravimetry analysis

Figure 5-17 presents the results of DTA for CEM II/B-M. They are in agreement with the XRD results presented in section 5.2.1. It is shown that the content of the portlandite (with the peak around 460°C) and calcium carbonate (between 600 °C and 800°C) does not change significantly during exposure at lower RH in the CO₂-free atmosphere. The two other blends and OPC show the same trend, both for 3 and 28 days of curing (not presented here). This confirms that there is no carbonation occurring during CO₂-free exposure conditions and phase assemblage does not change either. Monitoring was continued up to 6 months of exposure.

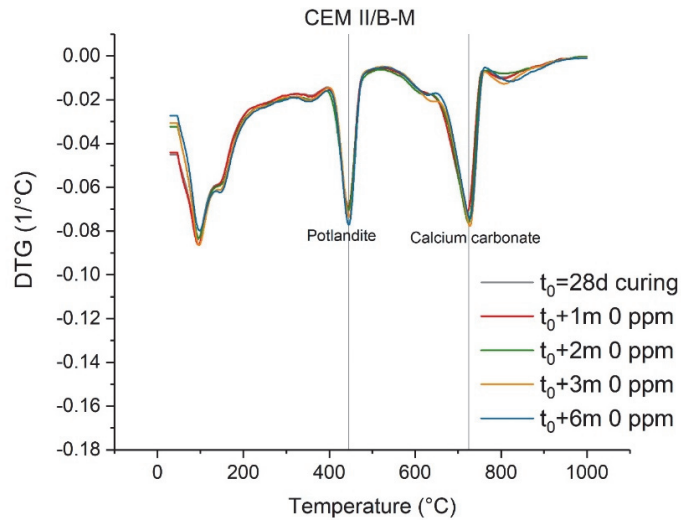


Figure 5-17. DTG graph during exposure at 70 % RH and CO₂-free atmosphere, for the ternary blend with limestone and burnt oil shale after 28 days of curing.

5.2.3 C-S-H composition studied by SEM-EDX

Systems cured for 28 days were chosen to study the C-S-H composition of the different mixes. For comparison, one system cured only for 3 days was also studied.

The point analysis was performed on inner and outer C-S-H. Appendix A presents the analysis for OPC and CEM II/B-M cured for 3 or 28 days, and C-S-H composition of the same systems exposed additionally to the relative humidity of 70 % in CO₂-free atmosphere, in constant temperature conditions. The results are summarized in Table 5-3.

Table 5-3. Ca/Si ratios of the C-S-H composition (average of inner and outer C-S-H) for different cement types.

	Before exposure	After 1 month of exposure
Cement type	Ca/Si	Ca/Si
CEM I 28d curing	1.96	1.96
CEM II/B-M 28d curing	1.89	1.89
CEM II/B-M 3d curing	1.96	1.96
CEM II/B-LL 28d curing	1.85	1.85
CEM III/A 28d curing	1.72	1.72

It seems that there is no difference in C-S-H composition between paste samples before exposure and after 1 month of additional exposure at CO₂-free atmosphere.

5.3 Impact of reimmersion on porosity

We know that the porosity of hardened paste samples, independently of cement type or curing time, gets coarser when moved from high RH (> 95 %) into relative humidity of 70 % or 55% (relative humidity where the hydration does not progress any more). However, what happens to porosity when the samples are reimmersed in pore solution? This section is dedicated to finding the answer.

The OPC system was chosen to study changes happening after submerging into a pore solution. For that purpose, a fresh paste of CEM I was cast and pore solution of the mix was subtracted right after casting by using a centrifuge Hermle Z 206 A for 1 hour. The obtained pore solution was used to immerse CEM I paste cured for 28 days, which was exposed for 1 month and 6 months and at 70 % RH in CO₂-free environment. Samples with different exposure times were chosen to see the effect of different porosity distribution on the results of reimmersion.

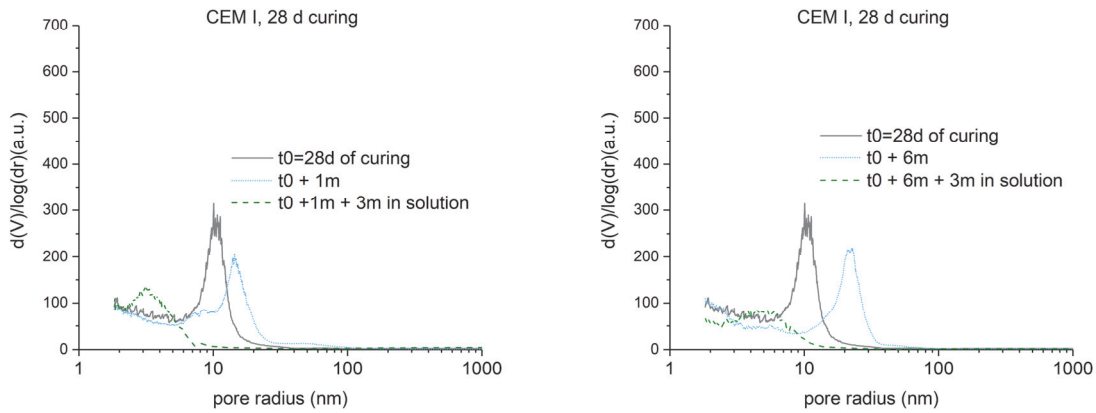


Figure 5-18. Changes of the critical pore radius due to after-curing in the pore solution.

The green dash lines on the figures represent the porosity distribution (Figure 5-18) and total porosity (Figure 5-19) after immersing the hardened cements paste for 3 months in the pore solution. The critical pore radius of the samples exposed for one month before immersion decreased to 3.15 nm, while the radius of the sample exposed for 6 months decreased to 5.26 nm. Both radii decreased dramatically. All measurable porosity is now below 10 nm. The range of the critical entry-pore size is on the border of the MIP detection limit, which is 2 nm.

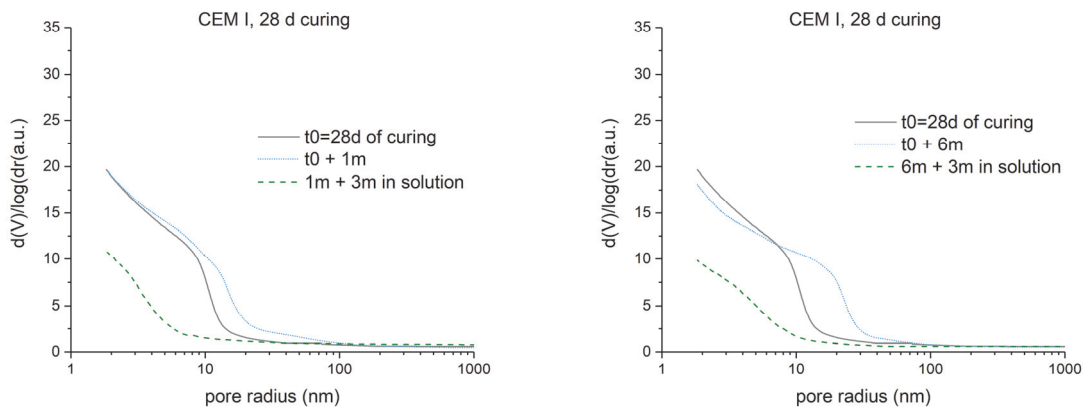


Figure 5-19. Total porosity changes due to after curing in the pore solution.

As the shift in pore size, the total porosity is also dramatically affected by immersion experiment (Figure 5-19). For both cases, the total porosity decreased to around 10 %. It is clear, that reimmersion dramatically affects the dried C-S-H, but the exact nature of these changes is not yet clear.

Chapter 6 Microstructural changes of the cement paste due to carbonation

6.1	Changes in phase assemblage during carbonation	70
6.1.1	Qualitative and quantitative analysis using XRD-Rietveld and TGA/DTG	70
6.1.2	Determination of the total CaCO ₃ and degree of carbonation	84
6.2	Microstructure investigation using microscopy	91
6.2.1	Backscatter-electron images of the surface of the exposed samples	91
6.2.2	BSE images and EDS mapping of the cross section of the exposed samples.....	94
6.2.3	Composition of C-S-H studied by SEM-EDS	100
6.2.4	Morphology investigation using high-resolution microscopy	105

This chapter discusses the influence of carbonation on the microstructure of the samples, cast using different cement types (Figure 6-1). To evaluate the changes of the phase assemblage due to carbonation, different techniques, such as XRD-Rietveld, TGA/DTG, and SEM-EDS were used. Additionally, results obtained from high-resolution microscope and BSE illustrate changes in the morphology of the carbonated cement paste.

All studied mixes were cured before exposure to carbonation for 3 or 28 days. Then, 1 mm thin disc samples were exposed into natural carbonation at controlled RH of 70 %, for 2 years.

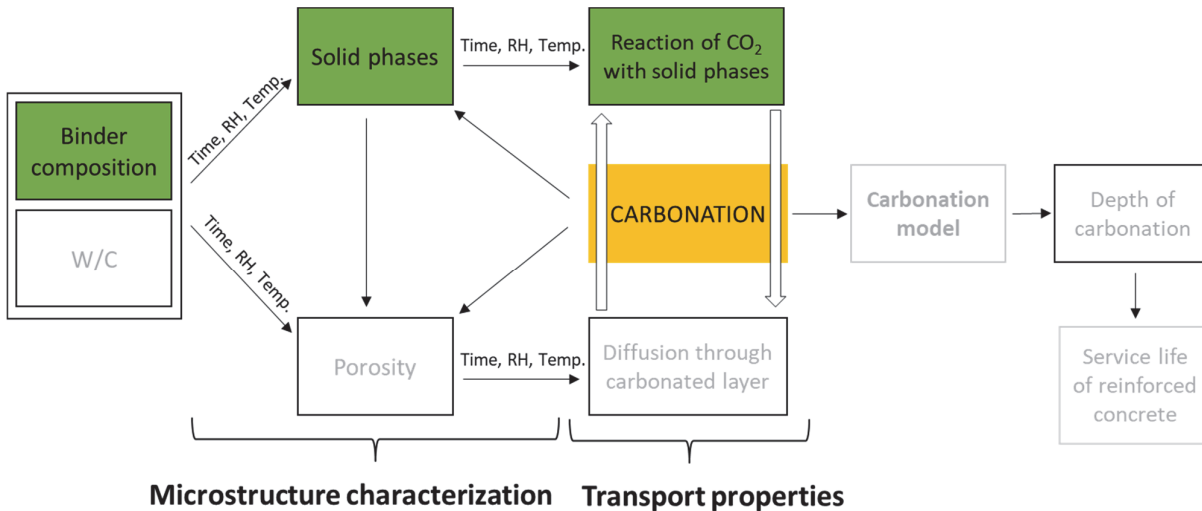


Figure 6-1. Research scope: changes in the phase assemblage due to carbonation.

6.1 Changes in phase assemblage during carbonation

6.1.1 Qualitative and quantitative analysis using XRD-Rietveld and TGA/DTG

Figure 6-2 demonstrates an example of the qualitative analysis of XRD scans. The XRD patterns of all studied binder are available in Appendix B. It should be emphasized that reported values are the averages obtained from one disk samples. Details of the sample preparation are described in chapter 3 “Materials and methods”. Figure 6-2 shows the XRD spectrums at 28 days of curing and at different times of exposure to carbonation. Portlandite and ettringite are the major crystalline hydrates for all the cements before exposure to carbonation. A minor amount of monocarboaluminate and hemicarboaluminate are also present. A calcite peak present in CEM II/B-M, CEM II/B-LL, and MixSL cements is attributed to the initial limestone addition in the mixes. CEM I and CEM III/A XRD diffractograms also have a small amount of calcite in the initial hydrated cement paste. During exposure to carbonation, the hydrate peaks decrease or disappear for all mixes. Among the calcium carbonate polymorphs, calcite is by far the major phase formed. Aragonite does not appear. Some vaterite can be seen in the blend with slag (CEM III/A). For the other cements, only minor peaks of this polymorph are detected. Based on the XRD diffractograms, the quantitative analysis was acquired using XRD-Rietveld [95]. Decomposition of the main hydrates (portlandite and ettringite) and the unreacted clinker phases during exposure to carbonation are presented from Figure 6-3 to Figure 6-8, while precipitation of the carbonate phases is presented in Figure 6-12.

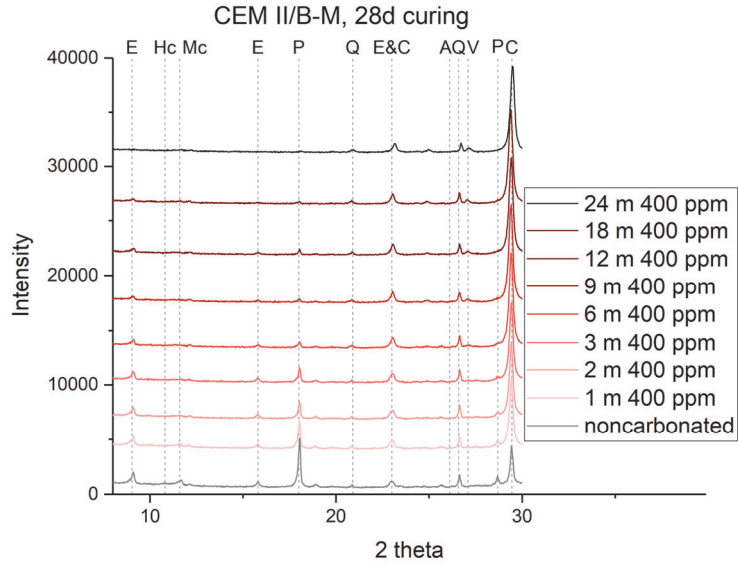


Figure 6-2. XRD diffractograms of CEM II/B-M during 2 years of exposure to natural carbonation, after 28 days of curing; E-ettringite, Hc-hemicarboaluminate, Mc-monocarboaluminate, P-portlandite, A-Aragonite, V-vaterite, C-calcite.

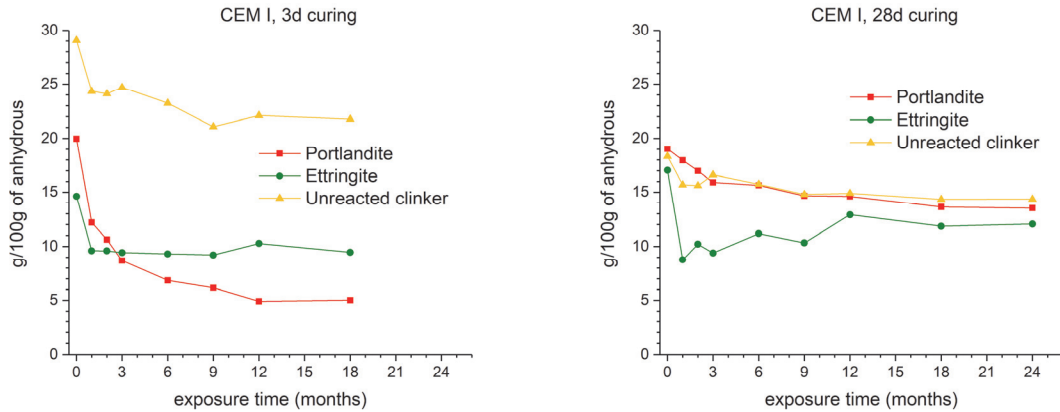


Figure 6-3. XRD-Rietveld quantification of the crystalline hydrated phases (portlandite, ettringite, and unreacted clinker) during exposure to carbonation at 70 % RH (CEM I, 3 and 28 days of curing).

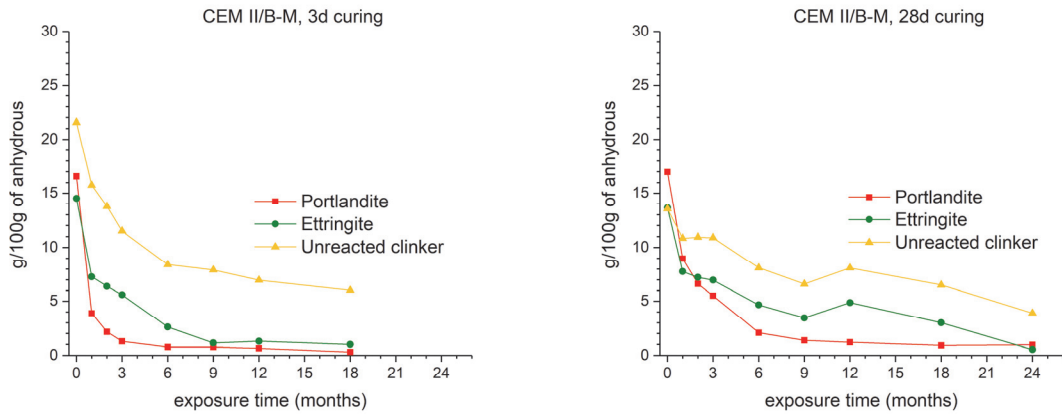


Figure 6-4. XRD-Rietveld quantification of the crystalline hydrated phases content (portlandite, ettringite, and unreacted clinker) during exposure to carbonation at 70 % RH (CEM II/B-M, 3 and 28 days of curing).

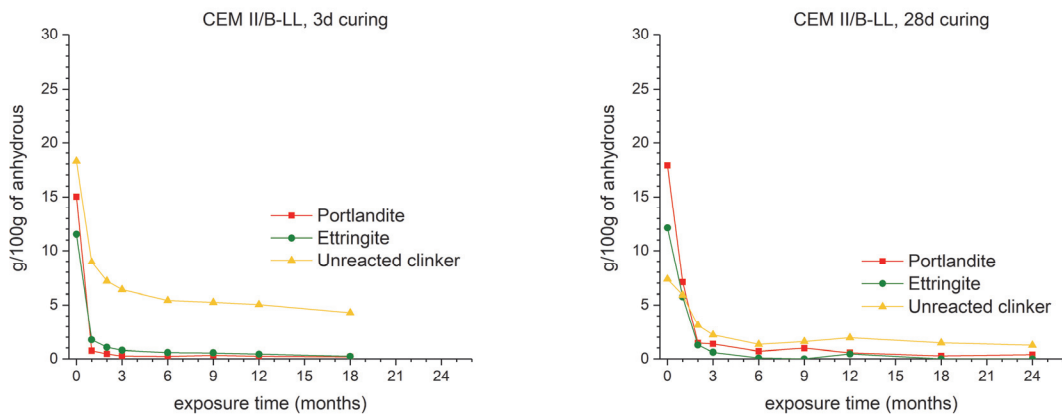


Figure 6-5. XRD-Rietveld quantification of the crystalline hydrated phases content (portlandite, ettringite, and unreacted clinker) during exposure to carbonation at 70 % RH (CEM II/B-LL, 3 and 28 days of curing).

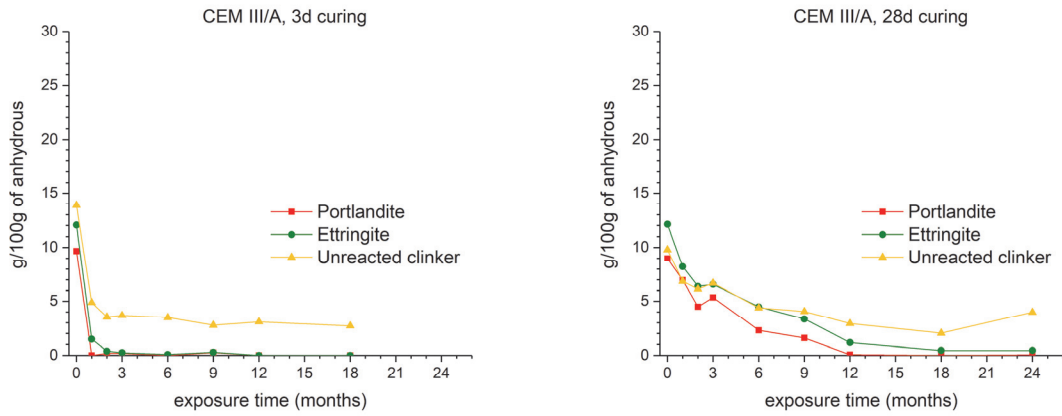


Figure 6-6. XRD-Rietveld quantification of the crystalline hydrated phases content (portlandite, ettringite, and unreacted clinker) during exposure to carbonation at 70 % RH (CEM III//A, 3 and 28 days of curing).

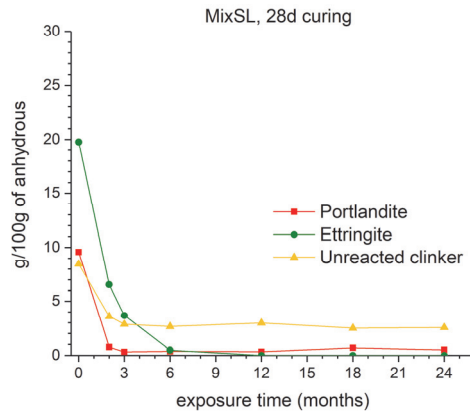


Figure 6-7. XRD-Rietveld quantification of the crystalline hydrated phases content (portlandite, ettringite, and unreacted clinker) during exposure to carbonation at 70 % RH (MixSL, 3 and 28 days of curing).

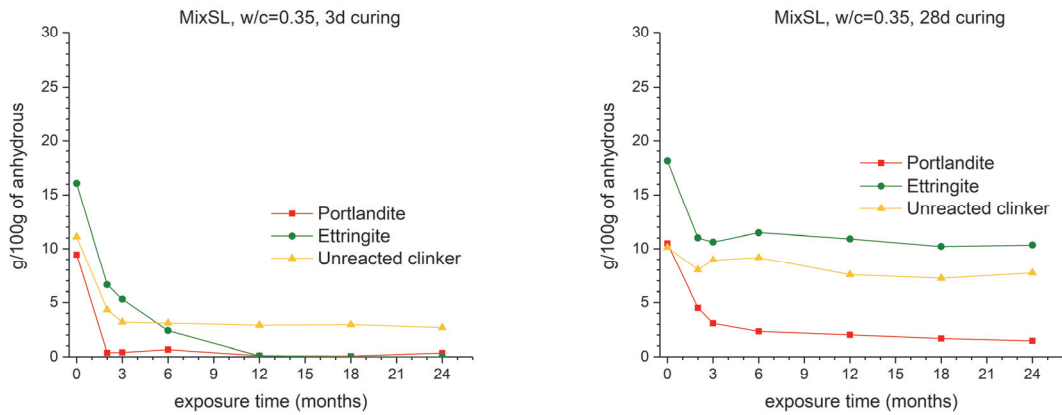


Figure 6-8. XRD-Rietveld quantification of the crystalline hydrated phases content (portlandite, ettringite, and unreacted clinker) during exposure to carbonation at 70 % RH (MixSL with w/c=0.35, 3 and 28 days of curing).

Obtained results show how the amount of crystalline phases decrease during carbonation, in the 1 mm thin cement paste samples, as a function of different cement types and curing times (3 and 28 days). The exposure “t=0” corresponds to the time after curing.

Portlandite for most of the mixes completely disappears. The time of total depletion varies between different binder compositions and curing time. The mix, where the Ca(OH)_2 remains in appreciable amount, even after 2 years of exposure to carbonation, is CEM I. The drop in portlandite seems to stabilise after a few months of carbonation. This is also the case for the MixSL blend with $w/c=0.35$. The quantification results are calculated for the overall Ca(OH)_2 content in the 1 mm thin disk, so the results show the average amount in the carbonating disk. The drop in CH content, observed after the few first months of carbonation, most probably corresponds only to a carbonated layer on the surfaces of the sample. The inhibition of the portlandite dissolution does not occur for the blended cements (at $w/c=0.4$) in this study. Figure 6-11 (from B to F) shows that for all blends, the carbonation depth was sufficient to carbonate a few mm deep, such that the studied 1 mm thin disk was colourless after spaying the pH indicator, demonstrating a drop of pH below 9. The total CH depletion happens much quicker when the sample was cured only for 3 days before exposure to carbonation instead of 28 days. For most of the cases, the difference of the initial Ca(OH)_2 content between 3 and 28 days of curing is negligible. Despite that, the carbonation rate for samples with shorter curing times is higher.

Ettringite also carbonates according to the reaction:



XRD-Rietveld analysis show how the amount of ettringite changes during exposure to carbonation for the different binder compositions, cured for 3 and 28 days. Interestingly, for CEM I and MixSL with $w/c=0.35$ ettringite content decreases only during the first few months of carbonation and then the decrease is inhibited. For CEM I ettringite even starts to slightly increase during the exposure. The initial decrease of the ettringite content is not the consequence of the carbonation. Samples exposed to the same environments, but without CO_2 , show the same trend in ettringite decrease (Figure 6-9, left). The initial drop could be caused by exposure into 70 % RH, where the drying environment could cause partial damage to the crystal structure [96]. The increase of the amorphous content after exposure in a CO_2 -free environment support this hypothesis (Figure 6-9, right). Moreover, the TGA/DTG curves performed on the samples after curing and the samples exposed to CO_2 -free atmosphere does not show major changes for the peak present in the temperature of around 100°C , where the decomposition peak of portlandite is taking place (Figure 6-10).

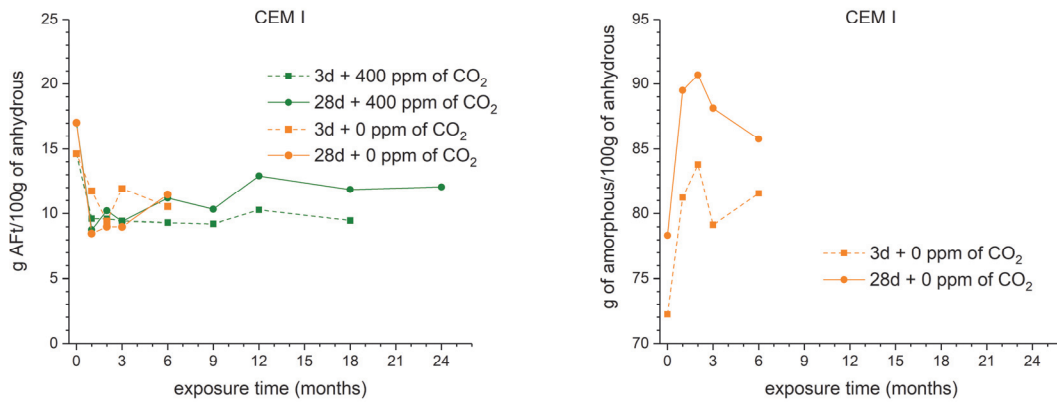


Figure 6-9. Changes in ettringite content after exposure to carbonation at 70 % RH and to CO₂-free atmosphere at 70 % RH (left figure) and changes in amorphous content for the same samples at CO₂-free atmosphere at 70 % (right figure); CEM I, 3 and 28 days of curing.

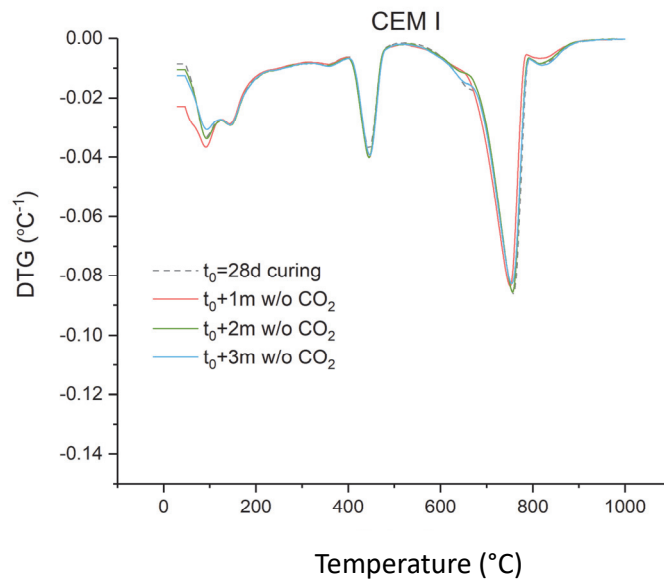


Figure 6-10. DTG curves for CEM I cured for 28 days and exposed to CO₂-free atmosphere at 70% RH.

It seems, that as long as portlandite is present in the system, ettringite does not carbonate. The stable presence of ettringite would indicate that the pH is still controlled by the portlandite, meaning that this is not a diffusion-barrier controlled dissolution, but rather a thermodynamically controlled mechanism, caused by either a low diffusivity in the carbonated area stopping the reaction in the timescale of the experiment, or a lack of space for calcite precipitation. The only exception is at the beginning of the exposure when the surface of the freshly cut sample is available to carbonation and all exposed phases carbonates simultaneously.

The sum of the unreacted clinker phases, C₃S, C₂S, C₃A, and C₄AF, during exposure to carbonation is also presented. When comparing the pastes cured for 3 days we can see, that CEM I has the highest amount of the

unreacted clinker phases. Increase of the curing time results in a decrease in the number of unreacted clinker grains as the effect of further hydration. The decrease of the clinker phases can be observed for all cement types. The decrease of the clinker phases during carbonation is more rapid for 3 days cured pastes than for the ones cured for 28 days, as it is more porous. XRD-Rietveld quantifications, discussed in the section 5.2.1 of chapter 5 show that there is no decrease happening in the exposure in CO₂-free atmosphere. However, the possibility of restarted hydration due to the water supply released during carbonation, cannot be excluded. Another explanation could be the pH-controlled dissolution of these phases, which is also facilitated by the dilution of the pore solution by the water from carbonation. Dissolution of the calcium from the anhydrous grain is not happening when the portlandite is still controlling the pH and calcium content of the pore solution (observed in the examples of MixSL with w/c=0.35 and CEM I cured for 28 days).

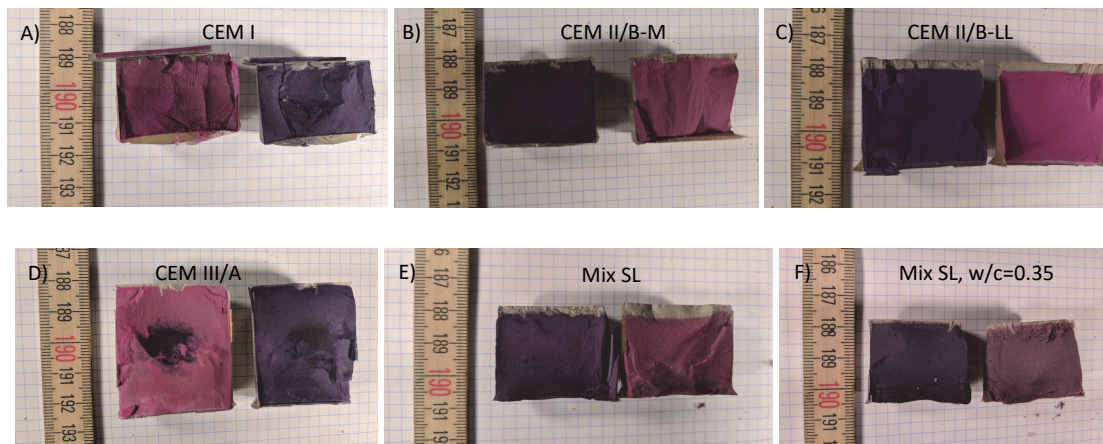


Figure 6-11. Carbonation depth measured with phenolphthalein and thymolphthalein pH indicator, for different mixes. All cements were cured for 28 days before exposure to carbonation. Carbonation depths for mixes A-D were measured after 24 months of carbonation, while mixes E and F, after 18 months of exposure to carbonation at 70 % RH.

Figure 6-11 shows that the depth of carbonation for MixSL with w/c=0.35 reached further than 1 mm, despite the presence of portlandite in the carbonating disk is still reported by XRD. Although literature data [97][98][37] show that the Ca(OH)₂ carbonation does not exhibit a sharp reaction front, the results might be explained by preferential diffusion paths in the samples, or kinetic factors.

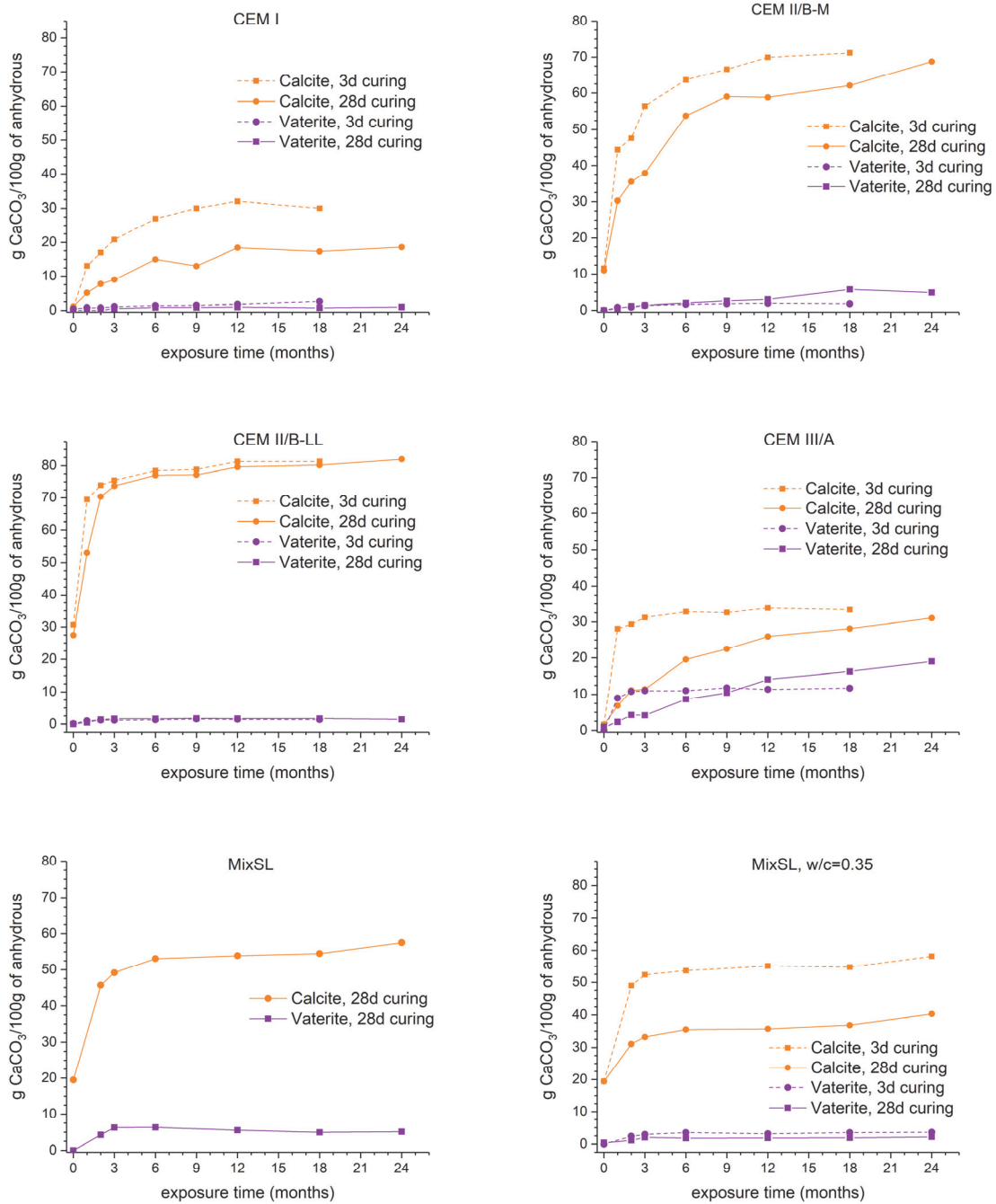


Figure 6-12. XRD-Rietveld quantification of the calcium carbonate content in the carbonating samples (3 and 28 days of curing, carbonation at 70 % RH).

Some literature reports that the hindered precipitation of CaCO₃ can be explained by the diffusion theory. It basically tells that a dense coating around partially reacted Ca(OH)₂ limits accessibility to portlandite [37][36][99][46]. That is why after a period of relatively rapid consumption of portlandite its carbonation rate is significantly reduced [40]. Our results are an argument against that theory.

For portlandite to exist, the calcium concentration and the pH of the pore solution have to be high enough, otherwise, it dissolves as predicted by thermodynamic [41][8][100]. In normal carbonation conditions, calcite precipitates due to supersaturation i.e. high content in calcium and carbonates in the pore solution. Transformation of portlandite into calcite takes place because in these conditions calcite is more stable.

Significantly decreased or almost inhibited rate of dissolution of portlandite, ettringite, and clinker phases decrease is observed for CEM I and MixSL with $w/c=0.35$ (28 days cured). This suggests that not the diffusion barrier but thermodynamic controlled mechanism governs the portlandite dissolution in pore solution, and carbonation is inhibited.

Three possible scenarios could explain the stability of portlandite in our carbonated materials: (i) lack of space for calcite to precipitate, (ii) not enough CO_2 had diffused to the reaction front, or (iii) preferential diffusion paths, leading to inhomogeneous carbonation.

The lack of space theory can be explained by the refinement of the porosity during carbonation. When the pore structure gets refined, the calcium concentration required for calcite precipitation becomes higher and higher. It means that at some point portlandite becomes more stable than the calcite, and the carbonation is effectively stopped. When the portlandite is stable then the other hydrates (i.e. ettringite) will also be stable. These thermodynamic limitations are summarised in Figure 6-13.

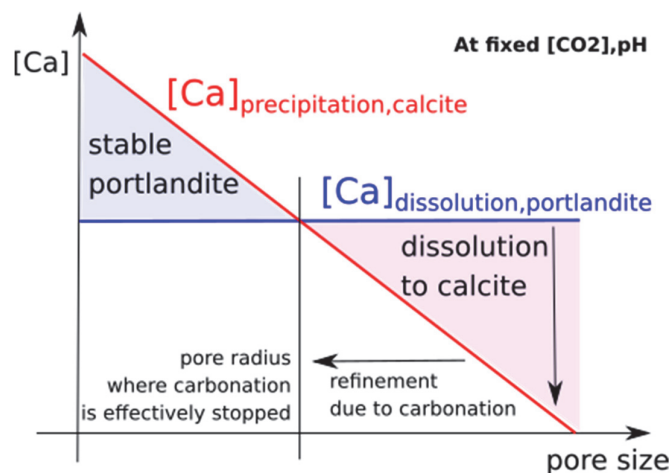


Figure 6-13. Illustration of thermodynamic limitations for calcite precipitation (figure used with the permission of F. Georget).

The fact that the local equilibrium during carbonation [100] seems to be respected is quite important for the carbonation models:

- Most of portlandite needs to be consumed before further changes can happen.
- No diffusion-barrier mechanism (caused by forming a dense layer around portlandite grains prohibiting its dissolution) takes place if portlandite is still present, which will control pH and calcium of the pore solution.
- Dissolution of ettringite and unreacted clinker phase is possible but after portlandite depletion.
- Including CaO from unreacted clinker in $\text{CaO}_{\text{reactive}}$ is the correct approach, since it will participate in the carbonation reaction.
- If the lack of space theory is correct, then the thermodynamic models need to be linked to the evolution of the pore size distribution.

The total amount of crystalline calcium carbonate underestimates the total carbon dioxide coming from carbonated phases [101]. Inconsistency between chemical analysis and X-ray diffraction in quantification the amount of CaCO_3 is evidence that amorphous calcium carbonate also forms during carbonation [37]. To estimate the total amount of CO_2 bound in carbonating cement paste TGA/DTA was used.

TGA was carried out on the samples exposed to natural carbonation, where the CO_2 concentration was around 400 ppm. The temperature was constant at around 22°C and relative humidity was maintained at 70 %. First samples were analysed after 28 days of curing, in order to obtain the references for carbonating samples. Figure 6-14 shows the TGA mass loss curves of studied cements. Before exposure to carbonation, the amount of calcium carbonate in individual samples was also quantified by TGA/DTG analysis and cross-checked with the XRD-Rietveld quantification. It confirmed the amount of initial CaCO_3 , originated from the presence of limestone in the mix. XRD-Rietveld also allowed quantification of minor amounts of CaCO_3 for mixes where limestone was not added into the original mix. This initial amount of limestone was subtracted from the total CaCO_3 examined by TGA/DTG, to calculate the CaCO_3 formed by the carbonation reaction. The experiments on carbonating samples were carried at different ages between 1 and 24 months of exposure to atmospheric carbon dioxide concentration. It is visible that the total weight loss occurred on decomposition due to heating, increases with the increase of the exposure time. It implies continuous carbonation of hydrated phases.

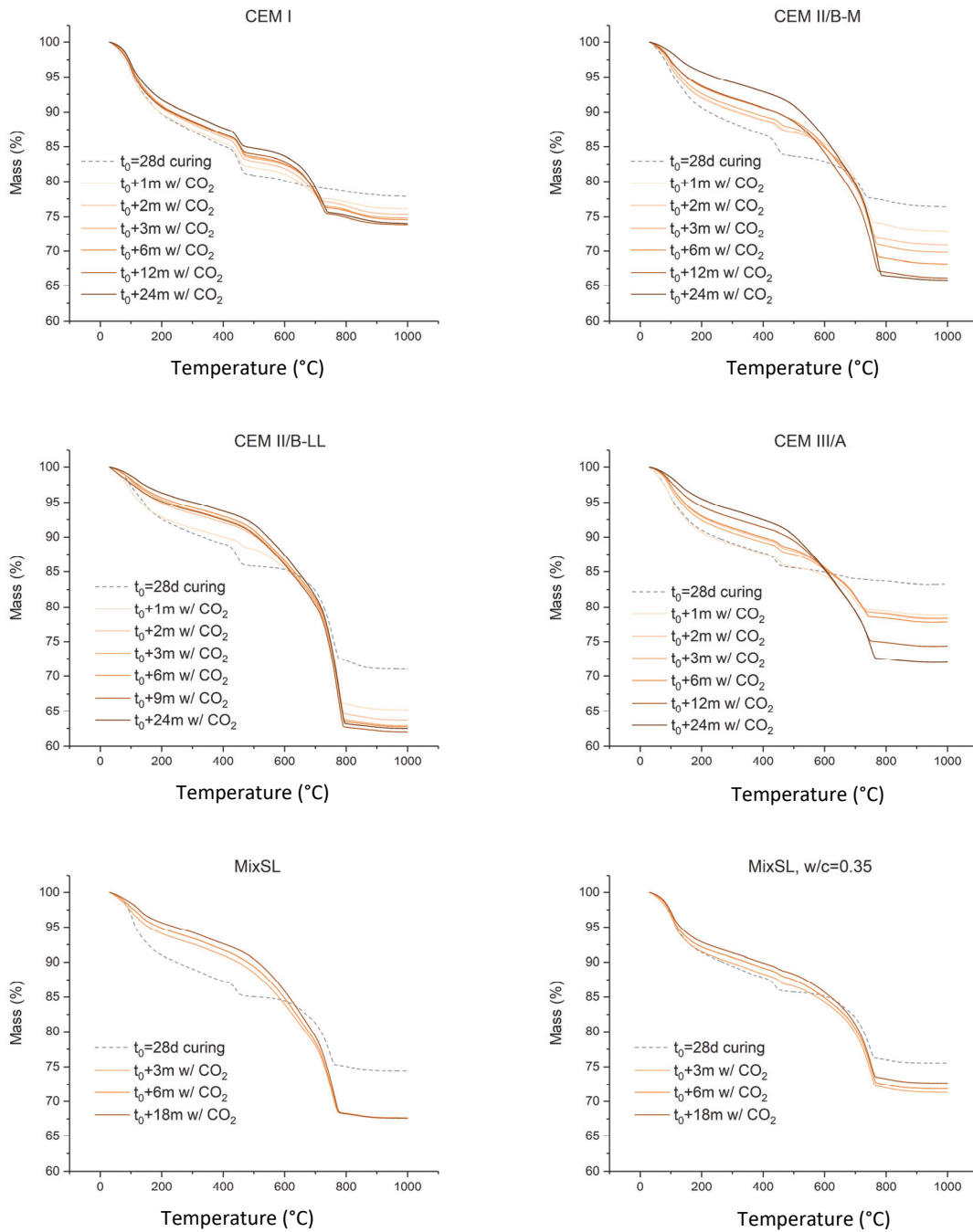


Figure 6-14. TGA curves of the carbonating cement mixes.

Figure 6-15 shows the DTG curves of the cement mixes. DTG peaks can be resolved in three temperature ranges (Figure 6-15). Mass loss in the temperature range 30-300°C corresponds to C-S-H, Aft and AFm decomposition, in the temperature 400-500°C decomposition of portlandite takes place, while the decomposition of calcium carbonate has a main peak at around 750°C [41]. The presence or absence of portlandite and calcite during exposure, seen from the DTG curves is consistent with XRD diffractograms.

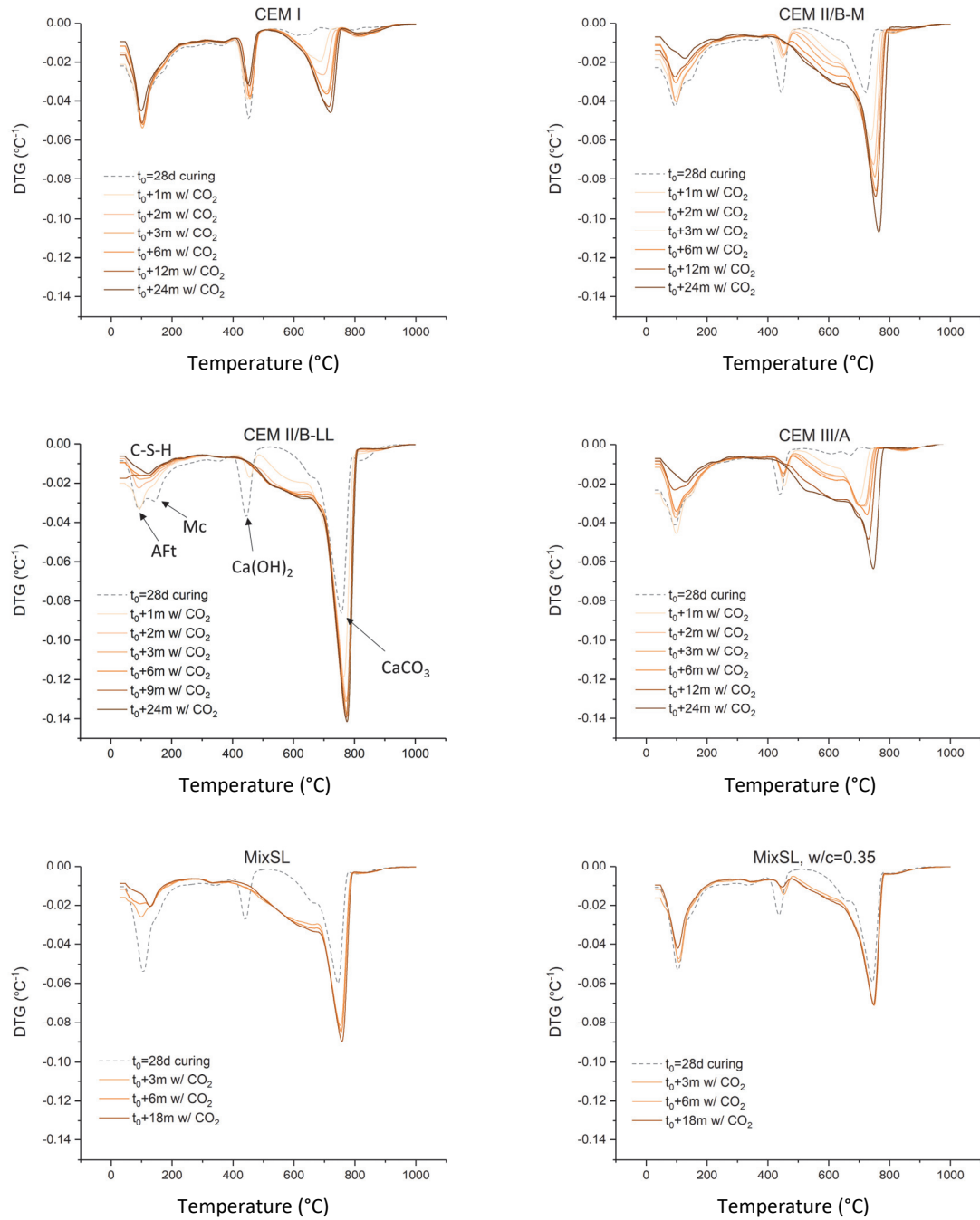


Figure 6-15. DTG curves of the carbonating cement mixes.

The major weight loss in samples exposed to carbonation is due to the decomposition of calcium carbonate. From DTG curves of carbonating mixes (Figure 6-15), it can be seen that there is no clear temperature where the decomposition of calcium carbonate starts. Besides the strong peak at around 750°C all mixes have a characteristic hump. It starts to appear right after the temperature of the portlandite decomposition (around 500°C) and the hump becomes more visible for the blends.

The method to calculate the total amount of CaCO_3 from TGA/DTG curves is not so obvious, and there is some debate among researchers. There are many different ranges of CaCO_3 decomposition associated with decomposition of calcium carbonate reported in the literature. Shi [41] reported the presence of CaCO_3 on DTG curve in the temperature range between 300°C and 850°C . To compute the amount of calcium carbonate, summarizing the amount of calcite, vaterite and aragonite phases, Kocaba [102] used the step method of the weight loss occurring in the temperature range from 500°C to 800°C . Villain et al. [28] shows that the CO_2 mass loss due to carbonation occurs from 530°C to 950°C and to clarify the diverging opinions about the interpretation of the mass loss between 520°C and 650°C , a mass spectroscopy experiment was performed [28]. That confirmed that the mass loss in the temperature range above 520°C corresponds mainly to CO_2 emission. Herterich [103] performed FTIR on carbonated cement paste containing 30 % of slag. The results showed that mass loss above 450°C is clearly a consequence of carbonate species. According to Thiery et al. [37] decomposition of CaCO_3 can be divided for 3 modes: mode I ($780 - 990^\circ\text{C}$), mode II ($680 - 780^\circ\text{C}$) and mode III ($550 - 680^\circ\text{C}$). Modes I and II are attributed to crystalline phases of CaCO_3 polymorphs (calcite, vaterite, and aragonite). According to Sauman [104], the mass loss in the mode I is associated with calcite decomposition, which is well crystalline polymorph of calcium carbonate. Other polymorphs of CaCO_3 , such as vaterite and aragonite cannot be distinguished by DTG due to the allotropic transformation into calcite when heated to $440-470^\circ\text{C}$. The calcite produced from transformation of those phases is less stable and decomposes in the temperature of the mode II [104]. Thiery et al. claim that the mode III could be associated with amorphous calcium carbonate. The amorphous calcium carbonate has been characterized in [105]. Amorphous calcium carbonate cannot be detected by XRD analysis. This is why TGA analysis is so crucial to obtain the total calcium carbonate produced during carbonation. Results of mass spectroscopy, coupled with the thermogravimetric analyser, confirmed the CO_2 emission in the temperature range of the mode III [37][42]. The temperature ranges of those 3 modes overlap, which makes it difficult to deconvolute them. However, the mode I, II and III together provides a relatively reliable total amount of calcium carbonate present in the sample.

The total amount of CaCO_3 was calculated by TGA/DTG from the mass loss between 500°C and 990°C . The total CaCO_3 formed during exposure to carbonation was calculated by subtracting the unreactive CaCO_3 originated by the presence of the limestone. The temperature where CaCO_3 starts to decompose is in agreement with Morandea et al. where authors confirmed the beginning of the CO_2 emission of carbonated OPC paste in that temperature by mass spectroscopy [42]. Figure 6-16 shows that choosing the end temperature of $\text{Ca}(\text{OH})_2$ dehydration as a beginning temperature of CaCO_3 decarbonation was the most suitable for studied here cements.

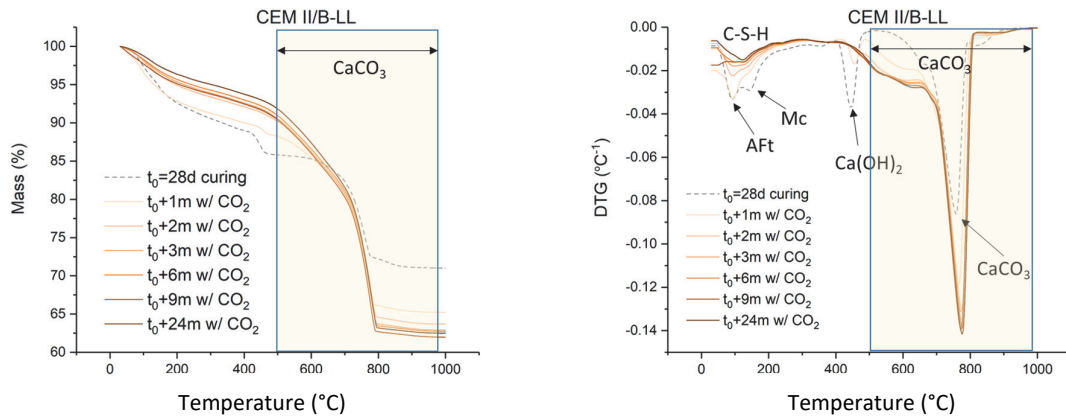


Figure 6-16. TGA and DTG plots for CEM II/B-LL, indicating the temperature range chosen for the calculation of the total CaCO_3 , which was used in further calculations for estimating the degree of carbonation.

Table 6-1. Verification of the amount of CaCO_3 amount vs decomposition of CaCO_3 , in different temperature ranges present in the literature [37].

	Time of exposure to carbonation	CaCO ₃ from Ca(OH) ₂ carbonation	Calcite from carbonation (XRD)	Mode I (780-990°C) [37][104]	Total crystalline phases (from XRD)	Mode I + II (680-990°C) [37]
		g / 100 g of anhydrous				
CEM I	24 months	7.46	17.47	4.00	18.44	18.80
CEM II/B-M		21.62	57.77	4.36	62.63	38.10
CEM II/B-LL		23.61	54.53	14.08	55.96	35.76
CEM III/A		12.07	29.56	1.55	48.57	25.71
MixSL	18 months	11.89	35.03	2.35	39.42	20.22
MixSL, w/c=0.35		11.98	17.45	2.17	19.33	7.76

According to Sauman [104], mode I (780-990°C) is associated with the carbonation of portlandite which leads to the formation of the most stable polymorph of calcium carbonate, namely calcite. The calculation made in this work only partly can agree with that statement. Amount of CaCO_3 associated with decomposition in the mode I could originate from the presence of calcite, however, this polymorph would have to be located also in other temperature range since the amount of calcite (“calcite from carbonation”) exceed the amount of CaCO_3 in the mode I (780-990°C). Moreover, from Figure 6-15, it can be seen that the sharp peak which is associated with calcite decomposition is shifted toward slightly lower temperature than reported in [104] and [37]. It could explain the underestimation the CaCO_3 present in the temperature range of the mode I of this study. In [37] the mass loss, taking place in the temperature range of the mode I+II corresponds to the amount of the total crystalline phases formed during carbonation. The current study agrees with that statement, however only

for the Portland cement. The assumption does not seem to be accurate for the cements with supplementary cementitious materials.

6.1.2 Determination of the total CaCO_3 and degree of carbonation

The degree of carbonation was calculated by following the methodology proposed in [106] and [107]. To determine the total amount of CO_2 bonded in the carbonated materials, the authors performed TGA/DTG and the heating weight loss for calcium carbonate was calculated between 600°C and 800°C . In the current study the same methodology was applied, however, the total amount of CaCO_3 was calculated by TGA/DTG from the mass loss between 500°C and 990°C as explained in the previous section.

The amount of the initial CaCO_3 was subtracted from the total CaCO_3 obtained from the mass loss between 500 and 990°C , to calculate the amount of the CaCO_3 formed by the carbonation reaction. Then, the capacity of CO_2 binding was estimated. The amount of $\text{CaO}_{\text{reactive}}$ was calculated by subtracting the CaO content originated by initial limestone in the mix from the CaO content of the raw cement powder (obtained by XRF). The CO_2 binding capacity was calculated from the maximum CaCO_3 , which can be formed if the total $\text{CaO}_{\text{reactive}}$ would carbonate. All values for individual cement mixes are presented in Table 6-2.

Table 6-2. Capacity of CO_2 binding in the different cements.

	$\text{CaO}_{\text{total}}$ (from XRF)	$\text{LS}_{\text{initial}}$ (amount of initial limestone, from XRD)	$\text{CaO}_{\text{reactive}}$ ($\text{CaO}_{\text{total}} - \% \text{ of } \text{LS}_{\text{initial}} \cdot \text{CaO}_{\text{in LS}}$)	Capacity of CO_2 binding ($\text{CaCO}_3_{\text{max}}$) ($\text{CaO}_{\text{reactive}} \cdot M_{\text{CaCO}_3} / M_{\text{CaO}}$)
	g in 100 g of anhydrous			
CEM I	62.8	1.1	62.1	110.9
CEM II/B-M	59.5	11.0	53.76	96.0
CEM II/B-LL	64.7	27.5	50.25	89.73
CEM III/A	53.5	1.5	52.71	94.13
MixSL	52.1	19.5	41.86	74.75
MixSL, w/c=0.35	52.1	19.5	41.86	74.75

Finally, the degree of carbonation was calculated by comparing the total CaCO_3 formed during carbonation, obtained from TGA analysis, with the $\text{CaCO}_3_{\text{max}}$. Table 6-3 presents the CaCO_3 resulted from carbonation for the cement mixes at a different time of exposure to carbonation, followed by the degree of carbonation.

Table 6-3. Total amount CaCO_3 originated by carbonation, and degree of carbonation.

Cement type	Time of exposure to carbonation ($t_0=28$ days of curing)	CaCO_3 from carbonation (TGA) (g / 100 g of anhydrous)	DoC (degree of carbonation in %)
CEM I	t_0	0	0
	$t_0 + 1$ month	16.2	14.6
	$t_0 + 2$ months	21.2	19.1
	$t_0 + 3$ months	24.3	21.9
	$t_0 + 6$ months	25.7	23.2
	$t_0 + 9$ months	28.8	26.0
	$t_0 + 12$ months	29.3	26.4
	$t_0 + 24$ months	31.3	28.2
CEM II/B-M	t_0	0	0
	$t_0 + 1$ month	29.7	31.4
	$t_0 + 2$ months	37.3	39.4
	$t_0 + 3$ months	42.9	45.3
	$t_0 + 6$ months	52.9	56.0
	$t_0 + 9$ months	57.7	61.0
	$t_0 + 12$ months	60.7	64.2
	$t_0 + 24$ months	69.4	73.4
CEM II/B-LL	t_0	0	0
	$t_0 + 1$ month	40.9	48.8
	$t_0 + 2$ months	53.1	63.3
	$t_0 + 3$ months	57.6	68.7
	$t_0 + 6$ months	59.6	71.1
	$t_0 + 9$ months	61.3	73.1
	$t_0 + 12$ months	62.4	74.4
	$t_0 + 24$ months	63.4	75.6
CEM III/A	t_0	0	0
	$t_0 + 1$ month	17.9	19.0
	$t_0 + 2$ months	26.1	27.7
	$t_0 + 3$ months	24.4	26.0
	$t_0 + 6$ months	28.4	30.2
	$t_0 + 9$ months	48.2	51.2
	$t_0 + 12$ months	44.1	46.8
	$t_0 + 24$ months	55.1	58.5
MixSL	t_0	0	0
	$t_0 + 3$ months	43.7	58.4
	$t_0 + 6$ months	46.3	61.8
	$t_0 + 18$ months	49.8	66.5
MixSL, w/c=0.35	t_0	0	0
	$t_0 + 3$ months	24.4	32.6
	$t_0 + 6$ months	25.2	33.6
	$t_0 + 18$ months	24.6	32.9

Figure 6-17 shows how the degree of carbonation advances in time. For CEM I, CEM II/B-LL, and MixSL with $w/c=0.35$, it seems like the carbonation degree reaches a plateau after a few months of exposure. CEM II/B-LL reaches this equilibrium after complete depletion of $\text{Ca}(\text{OH})_2$. Interestingly, for the two other mixes (CEM I and MixSL with $w/c=0.35$) this leveling off appears despite significant amounts of $\text{Ca}(\text{OH})_2$ still being present in the mixes. The highest DoC was obtained for CEM II/B-LL, which reached 76 % after 2 years of natural carbonation. Almost the same degree, 74 %, was reached by CEM II/B-M, however, the rate of car-

bonation of the blend with burnt oil shale and limestone was much slower. CEM II/B-M has higher CO₂ binding capacity than limestone blend. That can explain the fact that the DoC of CEM II/B-M seems to have the potential to increase further. MixSL with w/c=0.35 is much more resistant against carbonation than the one with w/c=0.40. In spite their binding capacities are equal, the DoC of the one with lower w/c is only half as high in comparison to the one with w/c=0.40. MixSL with w/c=0.35 has not only lower water content than the rest of the studied mixes, but it includes also admixtures (NaOH and Ca(NO₃)₂·4H₂O) and a customised superplasticiser. The mix was designed by a parallel group of the project at ETHZ, with a special focus on the improvement of the early mechanical properties of the blends with high substitution of the clinker by SCMs.

To compare the DoC studied on cement paste with the carbonation coefficient studied on microconcrete specimens, the graph presented earlier (in chapter 4) is again presented in Figure 6-18. All microconcrete mixes were prepared with constant w/c=0.50 and the graph shows similar carbonation coefficients for MixSL and CEM II/B-LL.

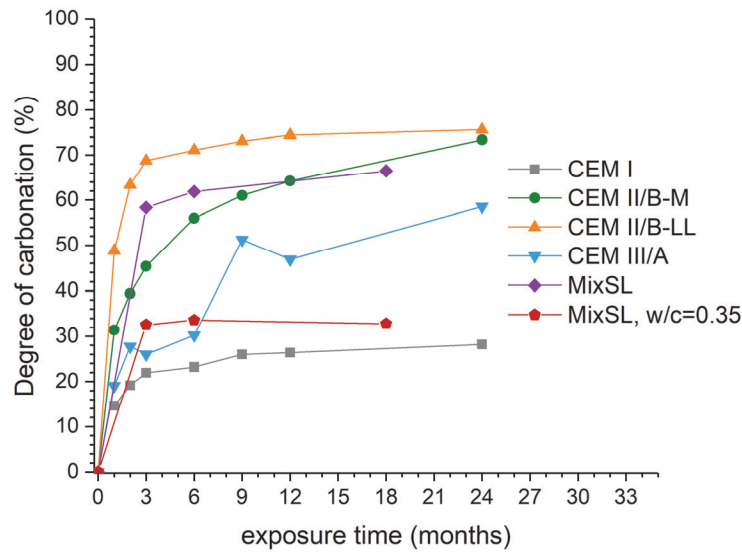


Figure 6-17. Degree of carbonation.

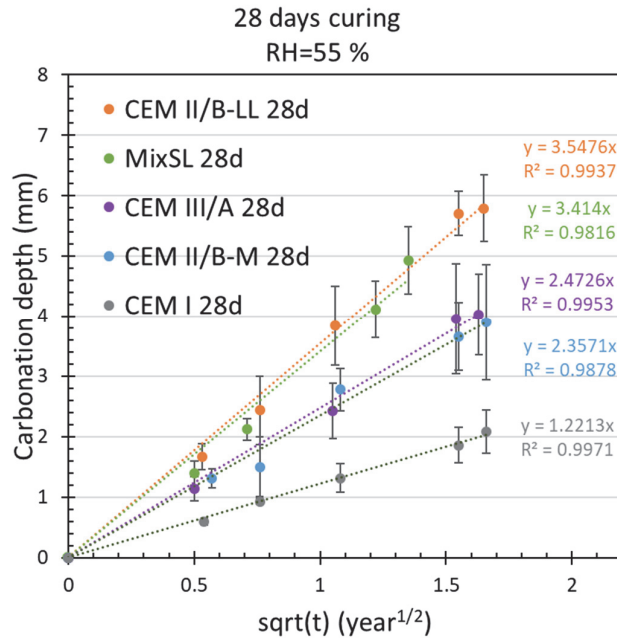


Figure 6-18. Carbonation depth as a function of cement type ($w/c=0.50$, natural CO_2 concentration, $22^\circ C$, and 55% RH) for microconcrete samples (see chapter 4 for the details).

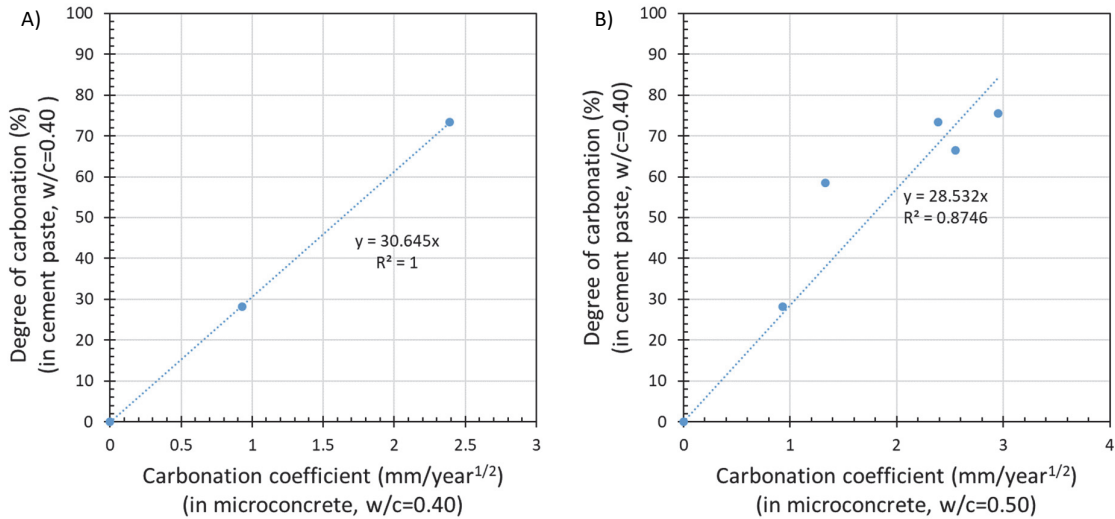


Figure 6-19. The relation between the DoC measured in cement paste, and the carbonation coefficient measured in microconcrete.

Figure 6-19 illustrates how the degree of carbonation (DoC), measured after 18 months of exposure of both MixSL blends and after 24 months of exposure for remaining mixes, correlates with the carbonation coefficient of the microconcretes obtained during 2.5 years of exposure. Both, cement paste and microconcrete were exposed to natural carbonation at 70 % RH. All cement pastes were cast with $w/c=0.40$ while only two types of microconcrete were cast on $w/c=0.40$ (CEM I and CEM II/B-LL). Full matrix of microconcretes was cast for

w/c=0.50. Due to the fact that only 2 cement types can be compared with cement paste on the same w/c (graph A in Figure 6-19), the carbonation coefficient of the microconcretes with w/c=0.50 is also presented to provide a comparison for all cement types. We can see that the DoC in cement paste and carbonation coefficient in the microconcrete is well correlated. The better correlation is observed while comparing systems with the same water to cement ratios. However, the correlation between concrete with higher w/c=0.50 and cement paste with w/c=0.40 is also relatively good ($R^2=0.87$), and approximate the relation for the mixes between the same w/c ratios. This confirms, that studying the behavior of the concrete on the cement paste estimates well the behavior of the concrete, as shown in [82]. Moreover, results of DoC obtained from cement paste specimens suggest, that we could improve the resistance against carbonation of the microconcrete/concrete made with MixSL quite significantly by decreasing w/c.

It is known that not only Ca(OH)_2 undergoes carbonation but also other hydrates containing calcium [28] can react with CO_2 , as shown also in section 6.1.1. Further analysis, implementing the amount of CaCO_3 originated from portlandite (Equation 3) and ettringite (Equation 4), allow to estimate the amount of the CaCO_3 which was originated by the carbonation of the C-S-H and other hydrate phases.

CaCO_3 originated from the calcium hydroxide carbonation ($\text{CaCO}_3_{[\text{Ca(OH)}_2]}$) can be calculated according to the stoichiometry of the Eq. 6-2, followed by Eq. 6-3:



$$\text{CaCO}_3_{[\text{Ca(OH)}_2]} = \text{Ca(OH)}_{2[\text{carbonated}]} \cdot M_{\text{CaCO}_3} / M_{\text{Ca(OH)}_2} \quad \text{Equation 6-3}$$

The carbonation of ettringite was shown in part 6.1.1. Amount calcium carbonate originated from the ettringite carbonation ($\text{CaCO}_3_{[\text{AFt}]}$) can be calculated, according to Eq.6-4:

$$\text{CaCO}_3_{[\text{AFt}]} = \text{AFt}_{\text{carbonated}} \cdot 3M_{\text{CaCO}_3} / M_{\text{AFt}} \quad \text{Equation 6-4}$$

Figure 6-20 presents how different hydrates contribute to CaCO_3 production due to carbonation. The graphs show the average properties of the 1 mm thin sample over carbonated, non-carbonated and reaction front regions. The reaction layers are not isolated in this analysis. It makes the interpretation more complicated. For example, portlandite might still exist in the core, while C-S-H gets carbonated at the surface. However, it can be concluded that among carbonating hydrates, the main contribution into the DoC comes from carbonation of “C-S-H and other hydrates”, where C-S-H is the main phase.

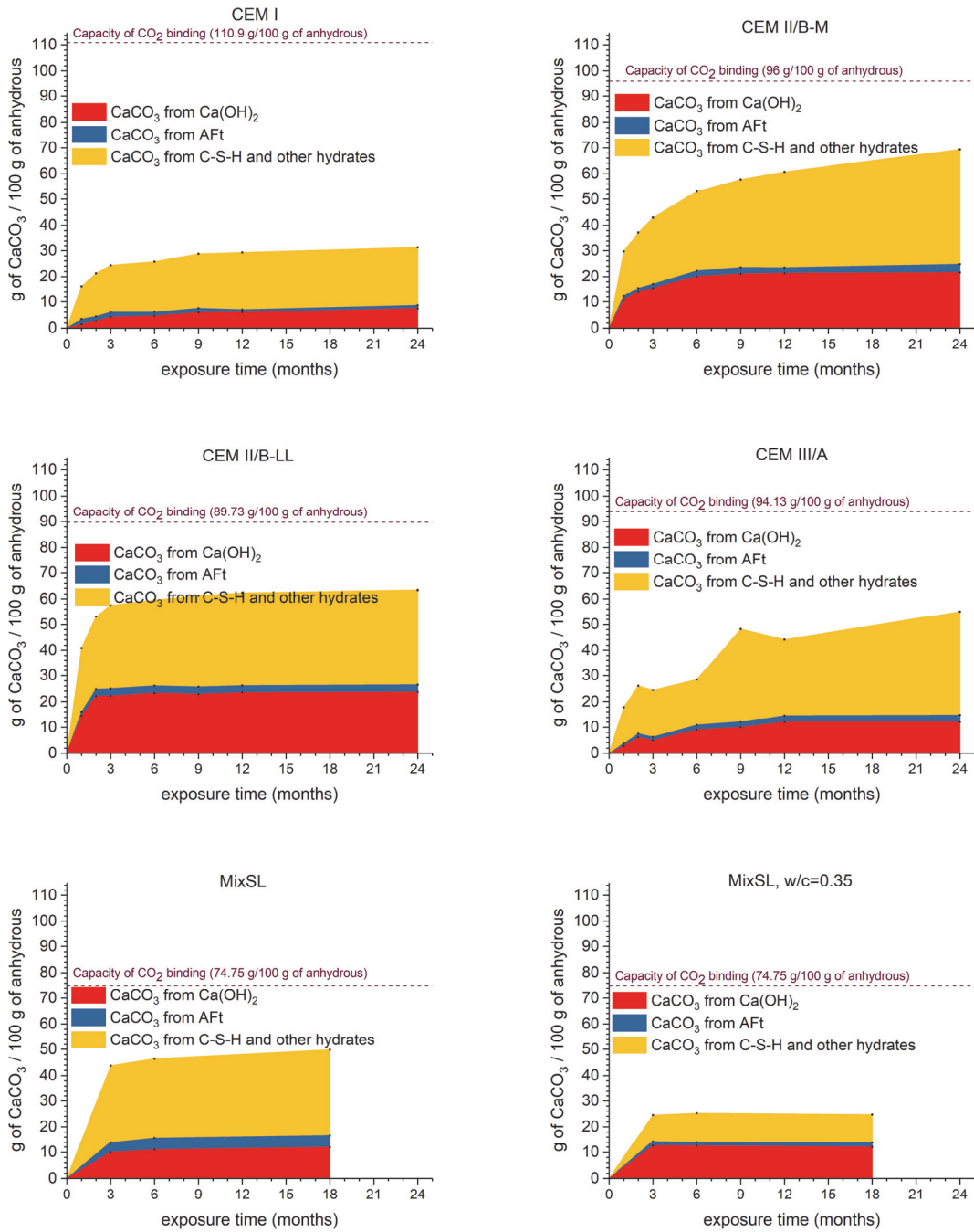


Figure 6-20. Average of the CaCO₃ origin (portlandite, ettringite, or C-S-H and other hydrates) during carbonation, coming from carbonated, non-carbonated, and reaction front regions in Imm thin disk, during 18 or 24 months of natural carbonation at 70 & RH.

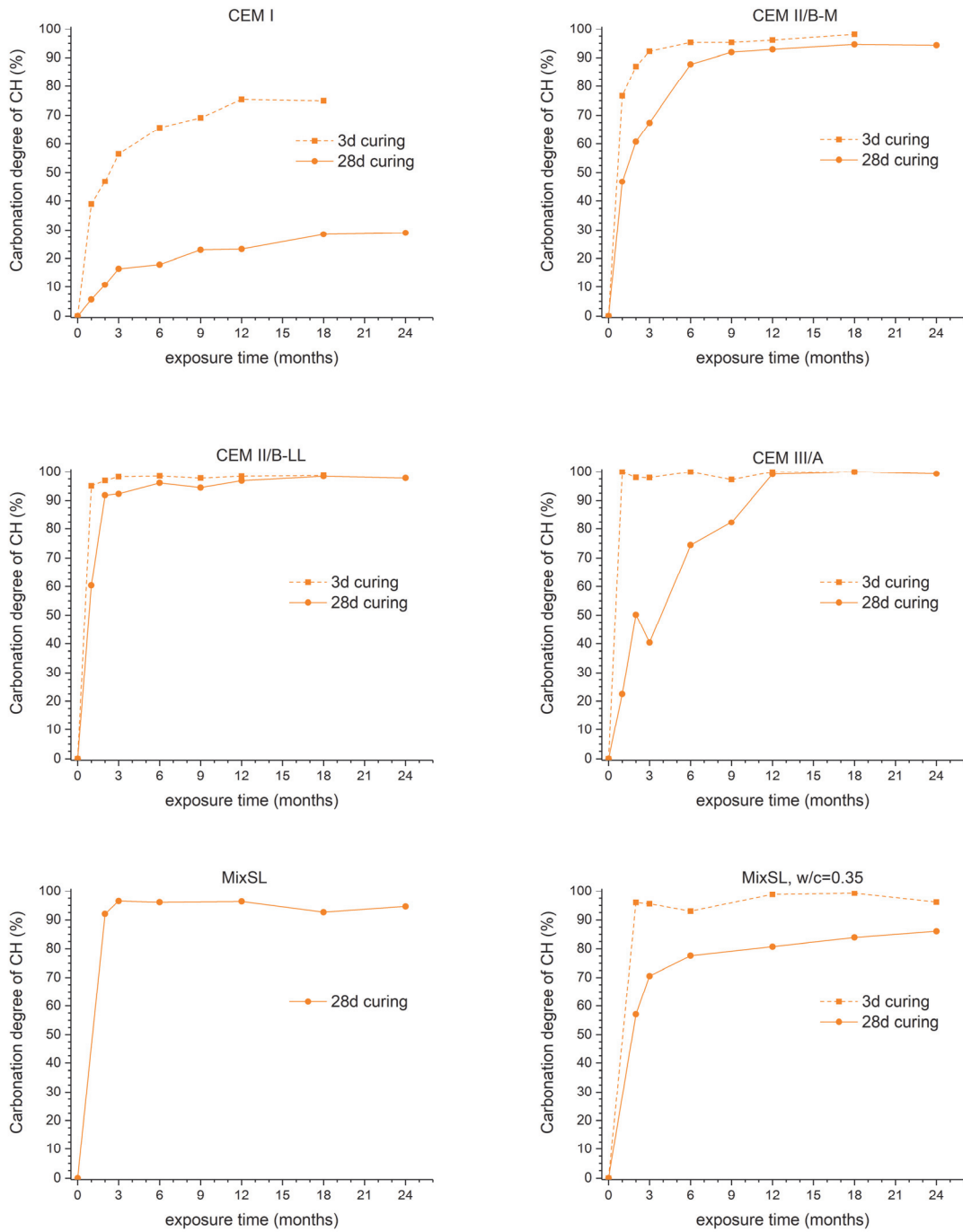


Figure 6-21. Carbonation degree of portlandite, during 2 years of exposure to carbonation at 70 % RH.

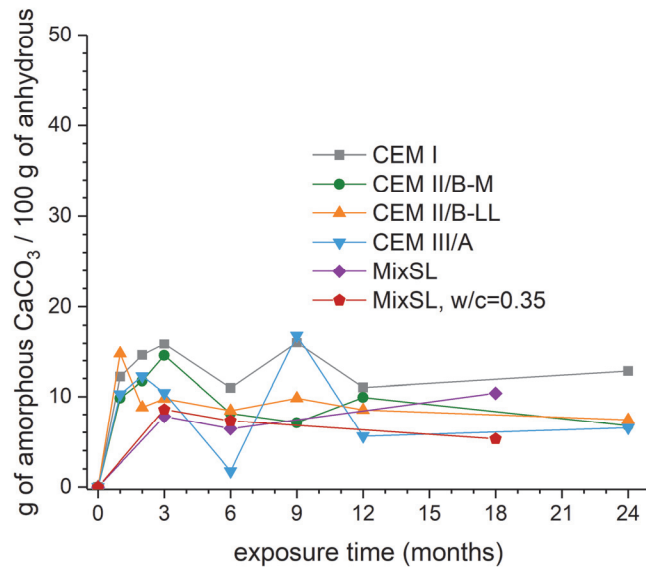


Figure 6-22. Amount of amorphous CaCO_3 for various cement mixes cured for 28 days and exposed to carbonation at RH 70% (total CaCO_3 content from TGA decreased by subtracting the crystalline CaCO_3 obtained from XRD-Rietveld).

Figure 6-21 presents the degree of the portlandite carbonation. The calculation was done by comparing the portlandite consumed by carbonation to the initial portlandite content, both obtained from XRD-Rietveld analysis. The degree of portlandite carbonation has a similar dynamic to the increase of calcite (Figure 6-12). However, we can see that calcite increases further, even after portlandite depletion, confirming the statement that calcite does not form only from portlandite, nevertheless, all $\text{Ca}(\text{OH})_2$ can contribute to CaCO_3 formation.

Figure 6-22 presents the estimated amount of amorphous calcium carbonate content. It is calculated by subtracting of the crystalline phases, obtained from XRD-Rietveld analysis, from the total CaCO_3 gained during carbonation, calculated from the TGA/DTG analysis. Amount of amorphous does not vary significantly during the exposure to carbonation, however, the contribution of the amorphous CaCO_3 into the total CaCO_3 formed during carbonation is not a negligible amount. These results show that TGA/DTG is necessary to quantify the full extent of carbonation.

6.2 Microstructure investigation using microscopy

6.2.1 Backscatter-electron images of the surface of the exposed samples

The BSE images of CEM I and CEM II/B-M exposed to different environments are shown from Figure 6-23 to Figure 6-25. The different brightness of the phases is the function of the average atomic number of the elements with which the incident electrons interact [108]. The micrographs show a clear difference between

uncarbonated and carbonated microstructure. In carbonated samples cured for 28 days, regardless of the cement type, the microstructure becomes “denser” with less observable porosity at the scale of the micrographs. However, for the CEM II/B-M cured for only 3 days before exposure to carbonation, densification was not observed via BSE images observation.

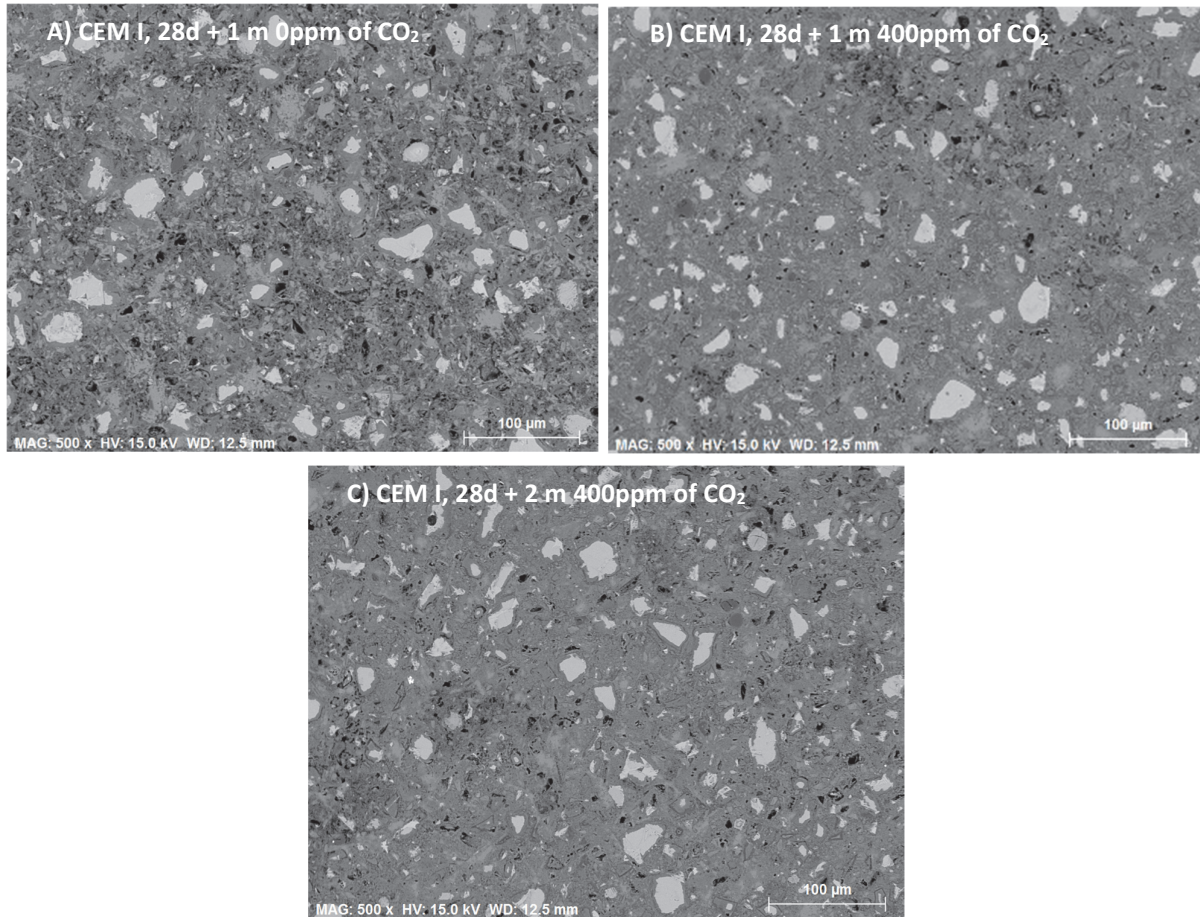


Figure 6-23. SEM-BSE images of CEM I cured for 28 days and exposed at RH 70%, A): for 1 month at CO₂-free atmosphere, B): for 1 month at 400 ppm of CO₂, C): for 2 months at 400 ppm of CO₂.

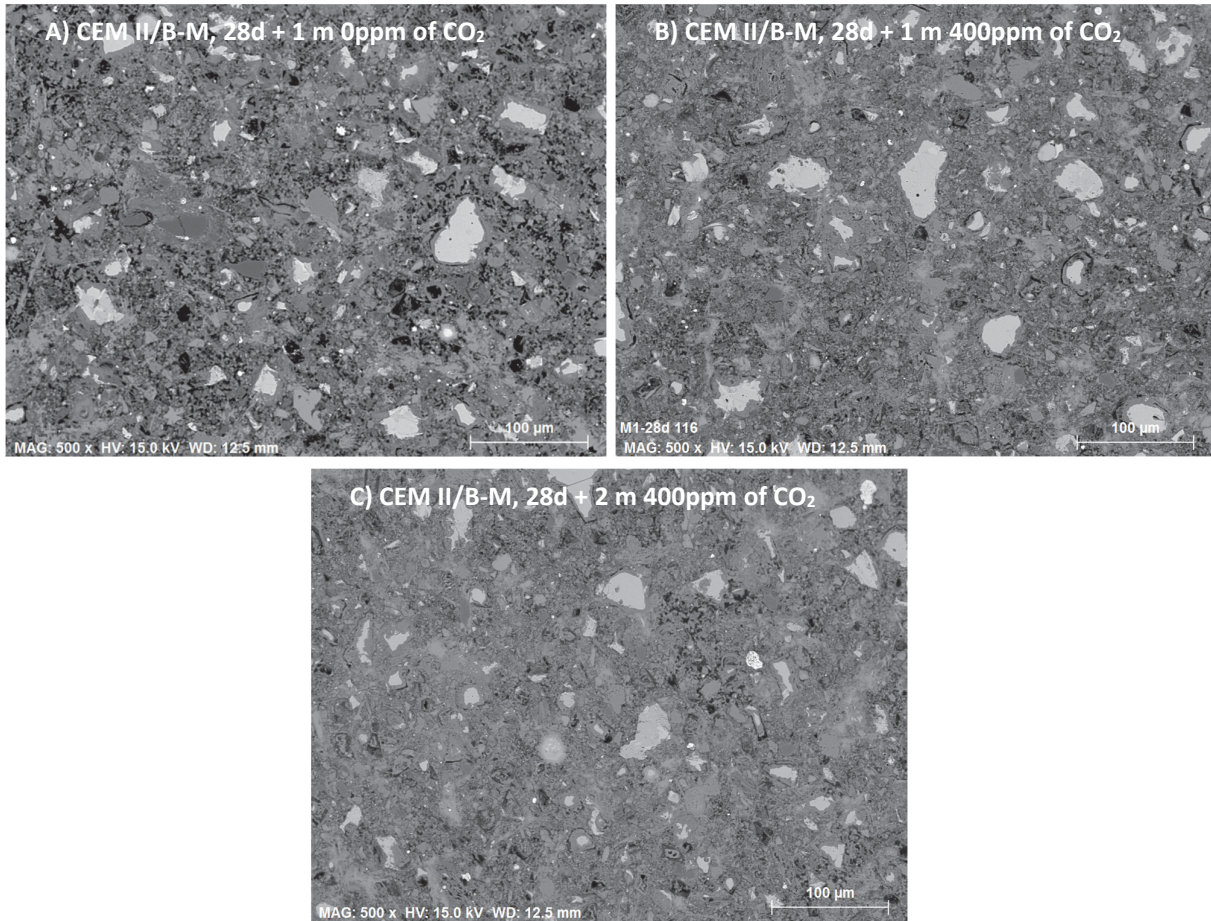


Figure 6-24. SEM-BSE images of CEM II/B-M cured for 28 days and exposed at RH 70%, A): for 1 month at CO₂-free atmosphere, B): for 1 months at 400 ppm of CO₂, C): for 2 months at 400 ppm of CO₂.

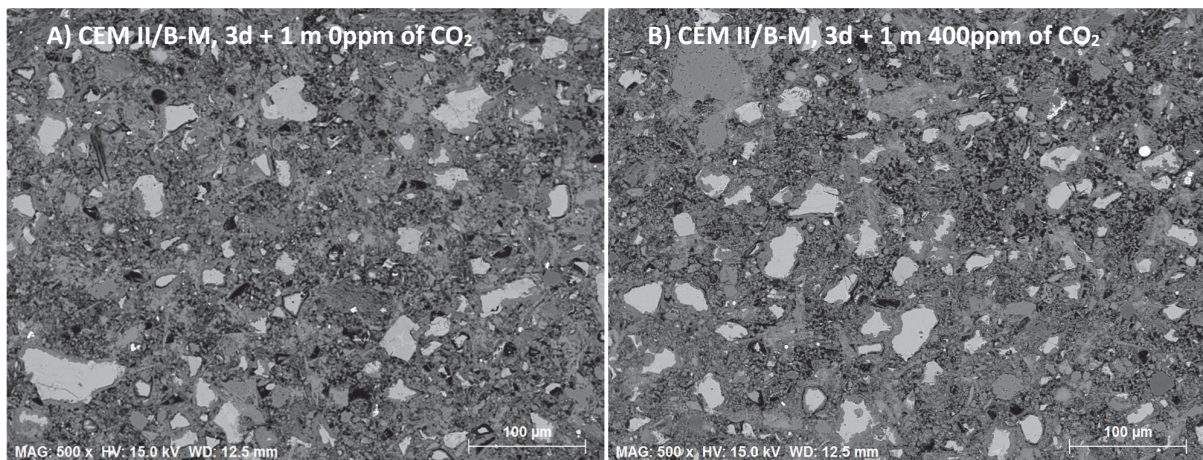


Figure 6-25. SEM-BSE images of CEM II/B-M cured for 3 days and exposed at RH 70%, A): for 1 month at CO₂-free atmosphere, B): for 1 months at 400 ppm of CO₂.

6.2.2 BSE images and EDS mapping of the cross section of the exposed samples

Figure 6-26 and Figure 6-29 also show how different are the microstructures of the cements exposed in different conditions, this time including the cross-section of the whole thickness of the sample. CEM II/B-M after 6 months of carbonation got less porous across the whole 1 mm thin sample. For CEM I, we can also see the densification, however only on the edges. This difference confirms that some of the studied samples still have all 3 zones: carbonated, non-carbonated and reaction front. The results presented for XRD and TGA are obtained from the cross-section of the sample and they are an average during two years of exposure.

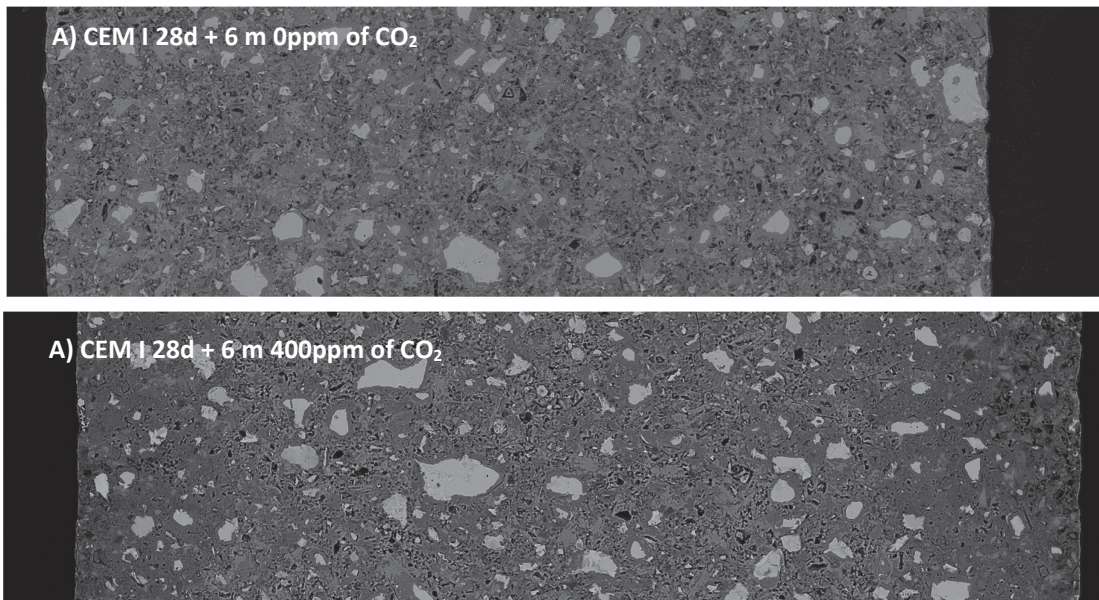


Figure 6-26. Cross section of the hydrated disk exposed to CO₂-free atmosphere (A) and to carbonation (B), at 70 % RH; CEM II/B-M cured for 28 days before exposure.

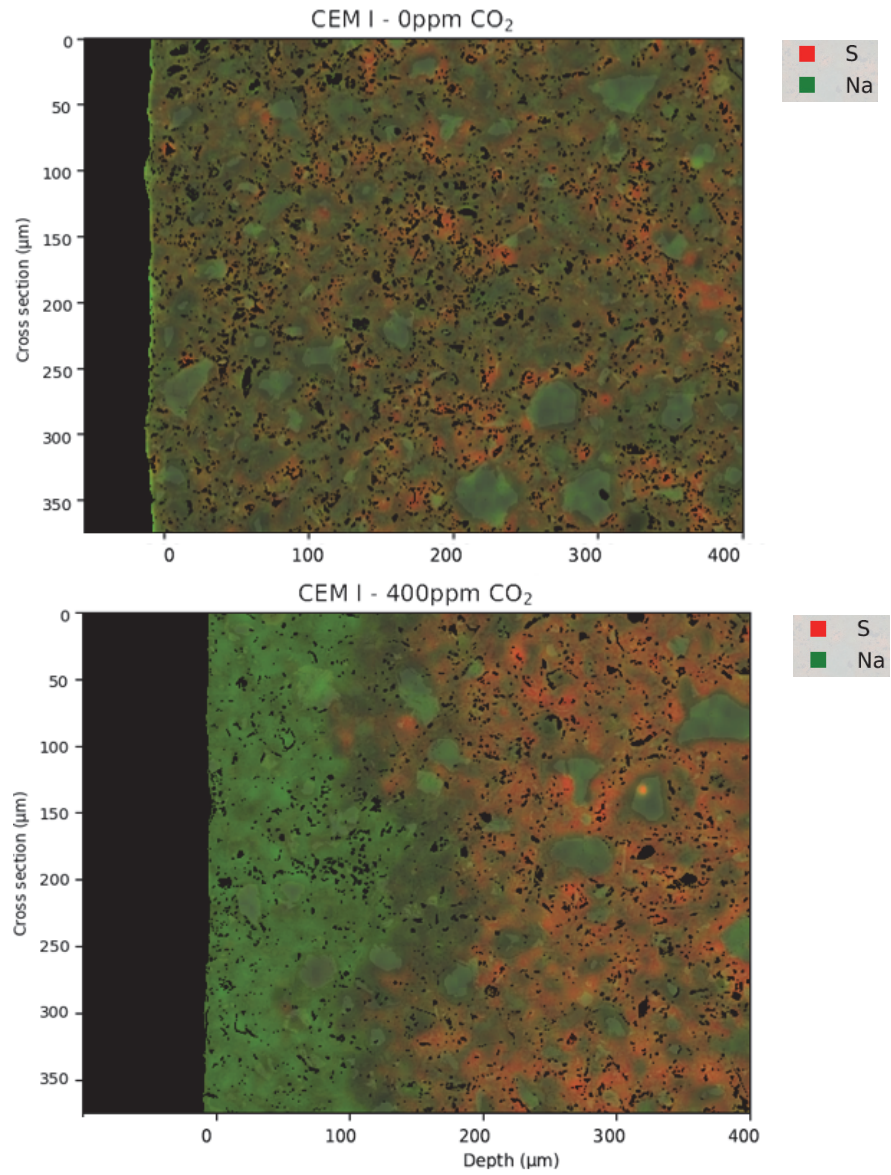


Figure 6-27. Composite map of sulphur (S) and sodium (Na) of CEM I exposed to CO₂-free atmosphere (top) and to carbonation (down), at 70 % RH.

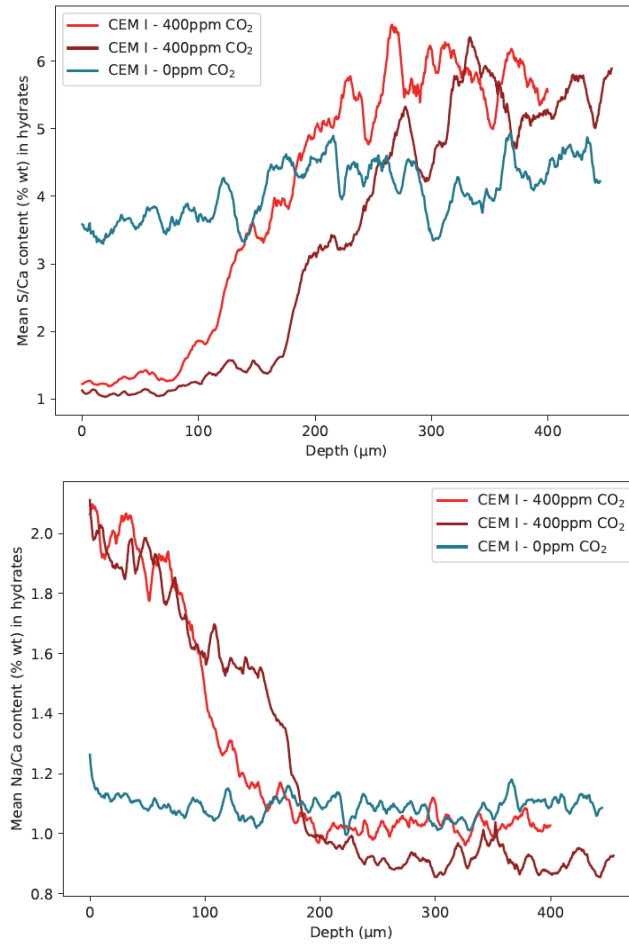


Figure 6-28. S/Ca ratio (top) and Na/Ca ratio (down) in hydrates, as a function of depth; CEM I exposed to CO₂-free atmosphere, and to carbonation at 70 % RH.

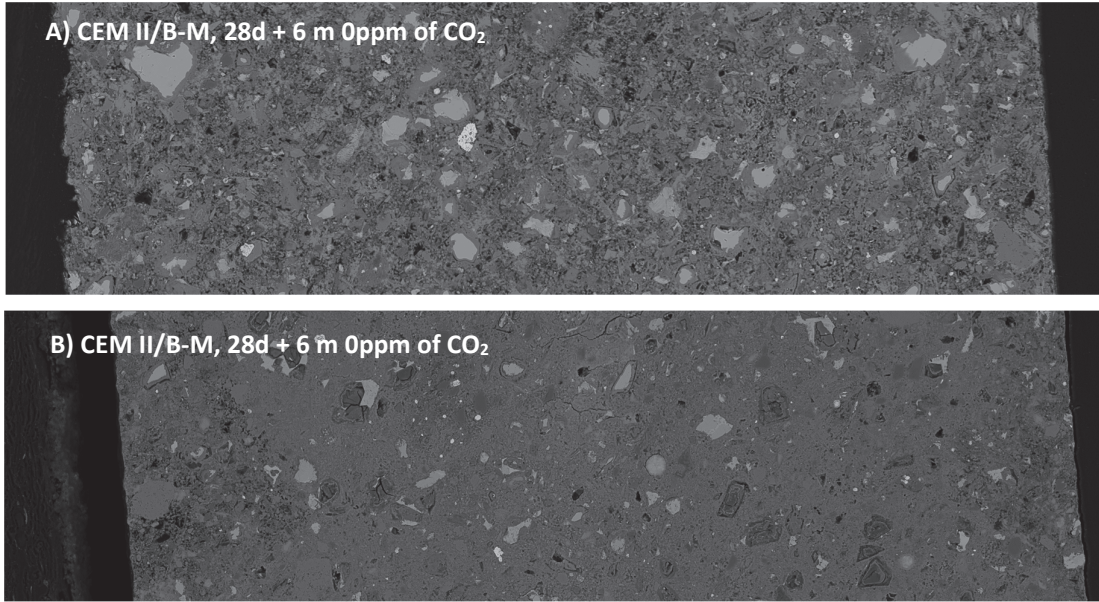


Figure 6-29. Cross section of the hydrated disk, exposed to CO₂-free atmosphere (A) and to carbonation (B), at 70 % RH; CEM II/B-M cured for 28 days before exposure.

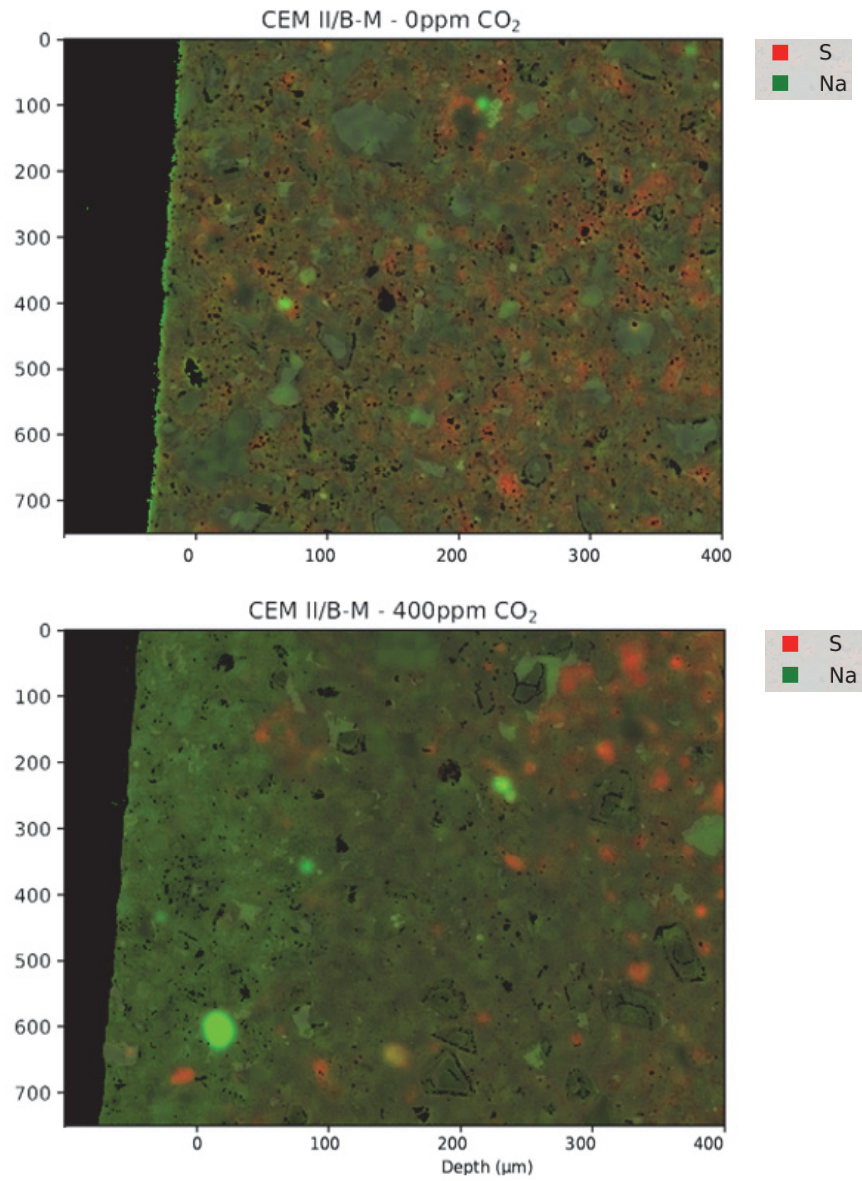


Figure 6-30. Composite map of sulphur (S) and sodium (Na) of CEM II/B-M exposed to CO₂-free atmosphere (top) and to carbonation (down), at 70 % RH.

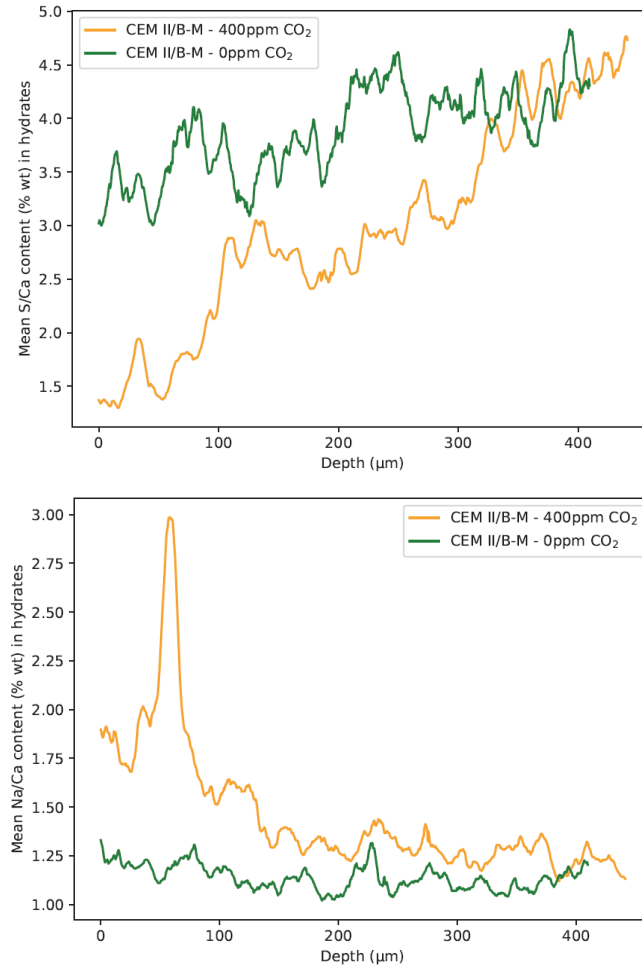


Figure 6-31. S/Ca ratio (top) and Na/Ca ratio (down) in hydrates, as a function of depth; CEM II/B-M exposed to CO₂-free atmosphere and to carbonation, at 70 % RH.

In addition to microstructure observation with BSE, EDS mapping was performed. On Figure 6-27 and Figure 6-30 composite maps are presented. The edges of the carbonated samples have a higher sodium concentration in comparison to the core, while the sulphate is depleted. These phenomena are visible especially for CEM I, where the noncarbonated and carbonated zone can be easily distinguished. On Figure 6-28 and Figure 6-31 we can see a significant difference in S/Ca and Na/Ca ration between carbonating samples and the samples exposed at CO₂-free atmosphere. It means that the sulphate gets depleted in the carbonation zone and diffuses towards the carbonation front, as it was predicted in the simulation by Georget [8] (see Figure 6-32 where it is assumed that all chemical reactions are at equilibrium). Three different layers can be observed: (i) sulphate depleted, (ii) “diffusion front”, and (iii) sulphate enriched layer. Sodium diffuses in the opposite direction as sulphate, i.e. towards the carbonated area. We can see that the sulphate and sodium ions are mobile over 100 μm. Sulphate seems to form ettringite at the carbonation front. That could contribute to the densification of the pore structure at the carbonation front due to high molar volume of ettringite, and effectively stop carbonation. However, higher resolution micrographs are needed to confirm this observation. Moreover, it was shown that

the carbonation front is sharp but tortuous. It can often lead to a wrong interpretation that carbonation does not exhibit a sharp front. It allows to reinterpret carbonation experiments and the importance of kinetics.

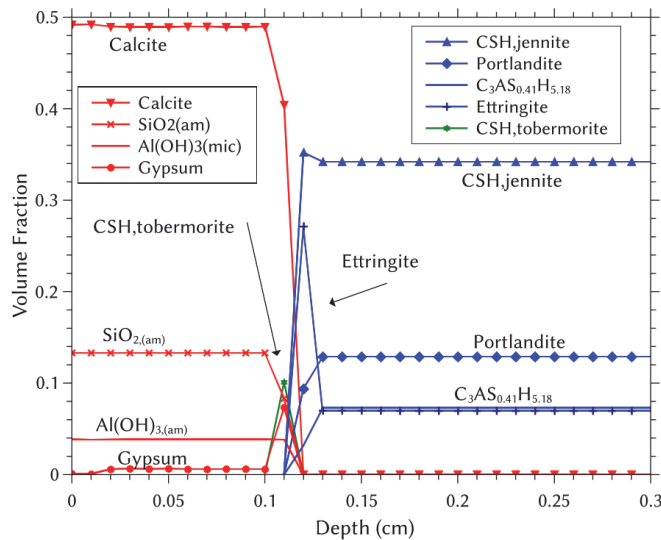


Figure 6-32. Solid phases profiles for the reference solution at 30 days [8].

6.2.3 Composition of C-S-H studied by SEM-EDS

Results of the previous sections show that the C-S-H can also carbonate, however its carbonation starts only when no more CH is available. This contradicts some experimental reports in the literature [99][42], however, it agrees with the prediction of thermodynamic modeling [41][8].

EDS point analysis was carried out on inner and outer C-S-H of surrounding cement grains. It is known that the inner C-S-H (so-called inner product) forms within the boundaries of anhydrous grain, while the outer C-S-H (called also outer product) is formed in the space originally occupied by water [109]. Both, inner and outer C-S-H are known to have similar Ca/Si ratios for well-hydrated cements [109][102].

To study the effect of the binder composition on the changes in chemical composition of C-S-H during carbonation, CEM I and CEM II/B-M were chosen. Both cements were cured for 28 days and then exposed to carbonation. Additionally, the effect of curing was examined for the blend by exposing it to carbonation already after 3 days of curing. SEM-EDS was done after curing (3 or 28 days) and after exposing to carbonation for 1 and 2 months. The experiment was executed on the polished surface of samples impregnated in epoxy. Use of the surface of the carbonating sample allowed to observe the effect of CO₂ binding relatively soon, within 2 months of exposure to natural carbonation.

Figure 6-33 presents examples of how the points were selected. Numbers from 1 to 10 are the points chosen for inner C-S-H, while the outer one is presented by numbers from 11 to 20. The procedure was repeated on 10 pictures for each system, resulting in 100 points of inner, and 100 points for outer C-S-H.

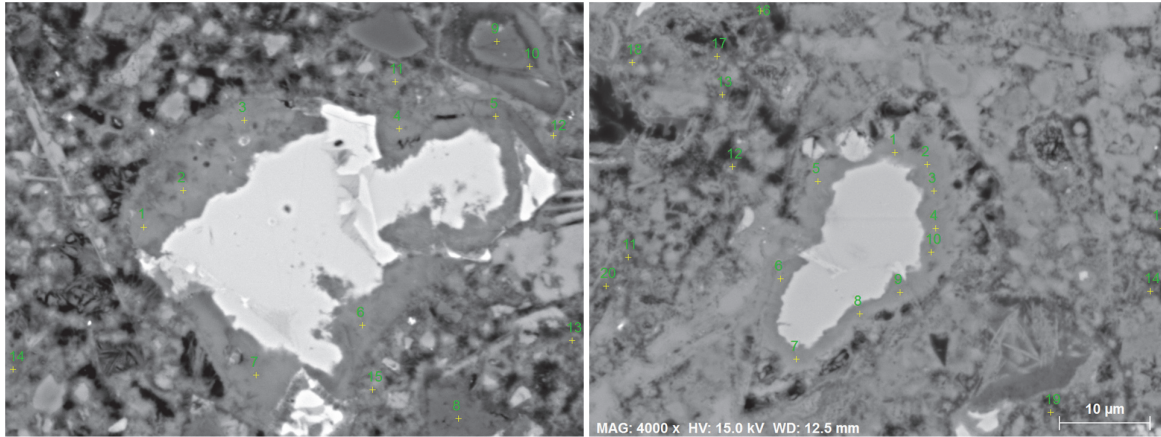


Figure 6-33. Example of selected points of inner and outer C-S-H for calculating the chemical composition of C-S-H; (CEM II/B-M, 28d curing (left) and 28d curing + 2 months of carbonation (right)).

The points obtained are visualised on the graphs from Figure 6-34 to Figure 6-36, by plotting the atomic ratio of Al/Ca and Si/Ca. The obtained plots show a cloud of points [106]. For the samples before exposure to carbonation, it was possible to acquire the atomic C-S-H composition from the edge of the cloud. Table 6-4 presents the Ca/Si ratios for all studied cements type before exposure to carbonation. The Ca/Si ratio decreases with an increase in the replacement of the clinker by SCMs, as was shown also in [110]. Due to a large degree of spread of the collected EDS points in the carbonated samples, it was not possible to report its Ca/Si. However, the analysis shows a clear difference in the elemental composition between inner and outer composition. It is due to the intermixing of calcium carbonate in the outer product. The outer C-S-H appears to be completely carbonated for all samples exposed to carbonation regardless of the curing time, binder composition or time of exposure. The same can be concluded for the inner C-S-H, with the only exception for CEM I cured for 28 days and exposed to carbonation for 1 month (Figure 6-34). In that case, carbonation caused the decalcification of only outer C-S-H, while the inner is not affected. The Ca/Si ratios seems to be the same as in the sample before exposure. However, after 2 months of exposure to carbonation, points from outer and inner C-S-H blend together, presenting the strong decalcification of the C-S-H. That is in agreement with a study done by Groves et al. [99], where it was shown that outer C-S-H carbonated more rapidly in comparison to the inner C-S-H.

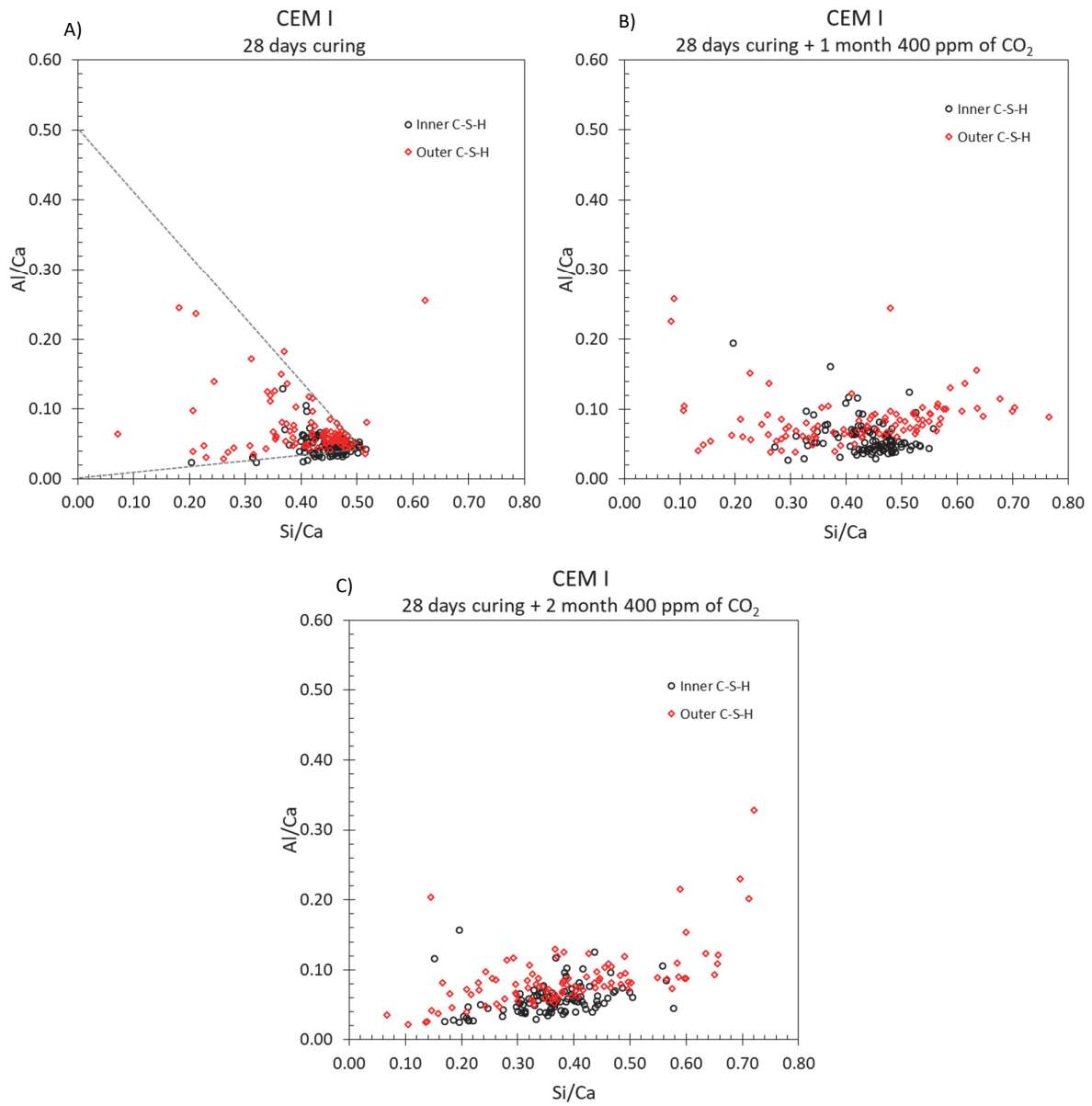


Figure 6-34. EDS point analysis of CEM I, cured for 28 days and exposed at RH 70 %, A): for 1 month at CO₂-free atmosphere, B): for 1 month at 400 ppm of CO₂, C): for 2 months at 400 ppm of CO₂.

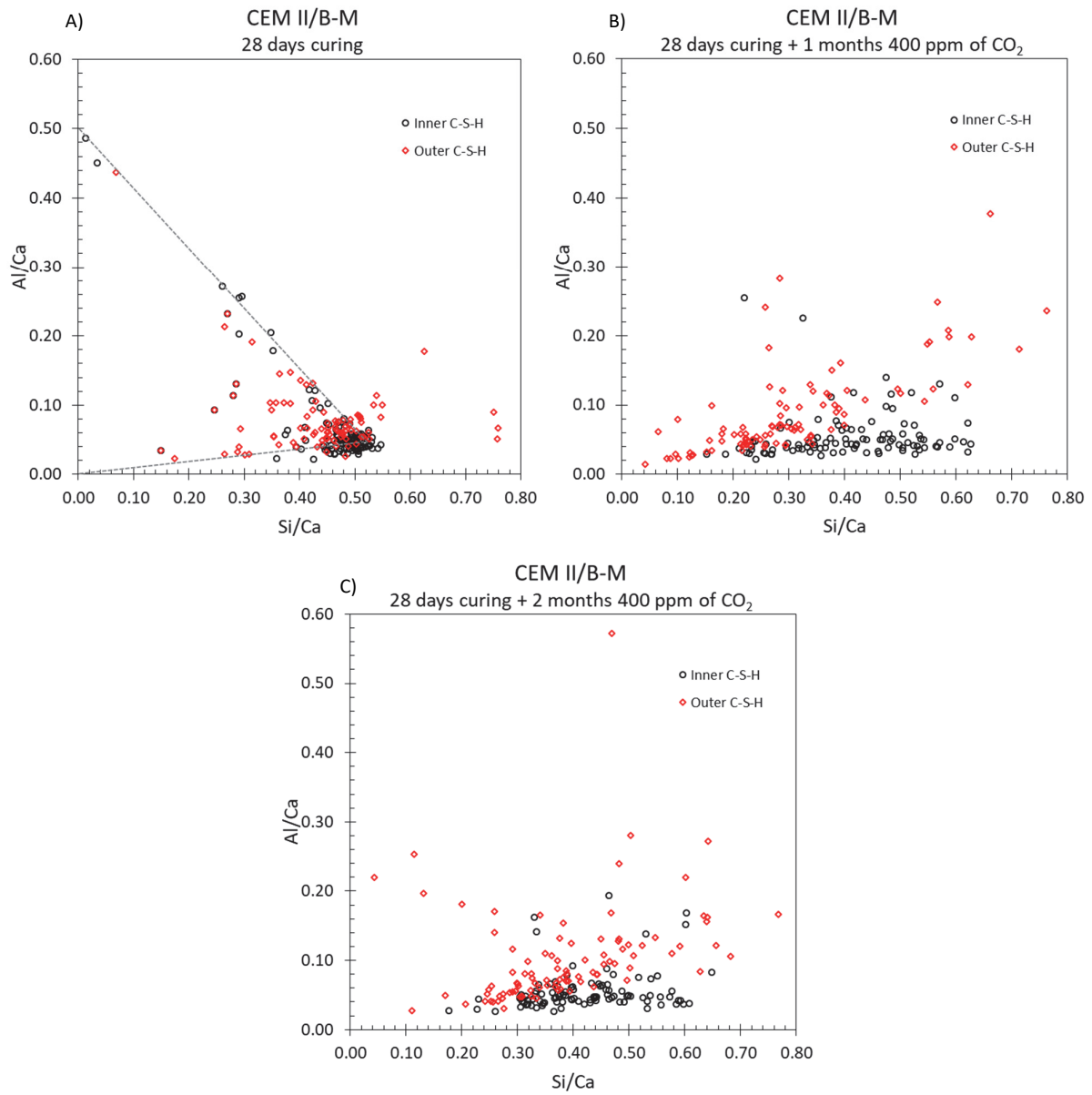


Figure 6-35. EDS point analysis of CEM II/B-M cured for 28 days and exposed at RH 70 %, A): for 1 month at CO₂-free atmosphere, B): for 1 month at 400 ppm of CO₂, C): for 2 months at 400 ppm of CO₂.

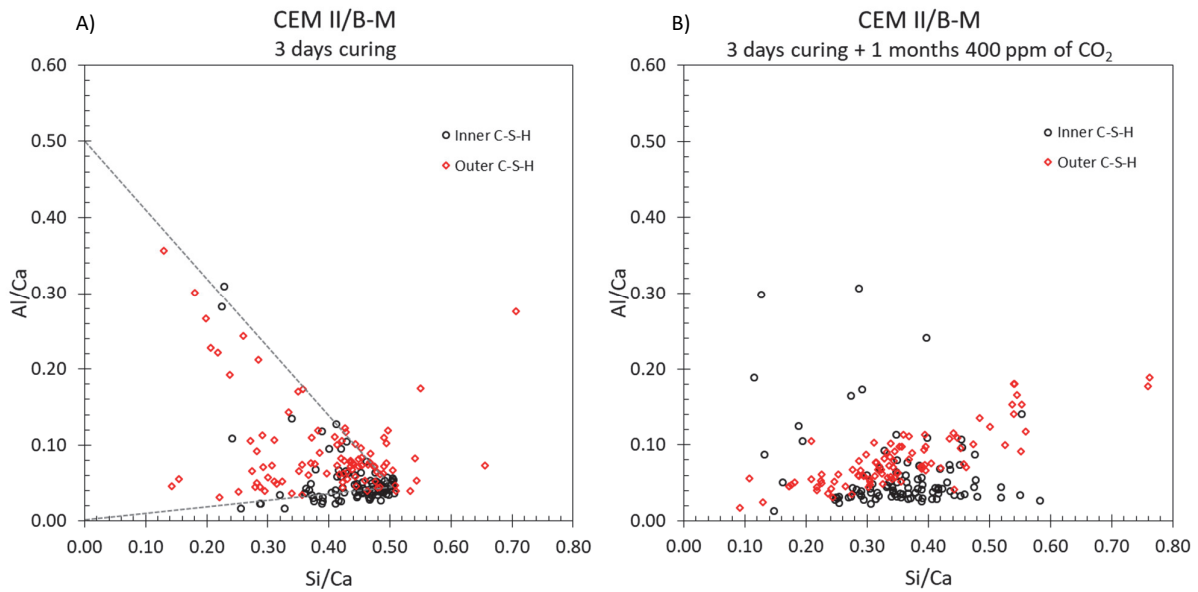


Figure 6-36. EDS point analysis of CEM II/B-M cured for 3 days and exposed at RH 70% A) for 1 month at CO_2 -free atmosphere, B) for 1 month at 400 ppm of CO_2 .

It can be noticed, that the points of the inner C-S-H relocate toward higher Si/Ca ratio, while the points of the outer C-S-H move toward higher Ca/Si ratio. It could indicate, that the inner C-S-H converts into silica gel, while the outer product indicates the presence of a calcium-rich product, most probably calcium carbonate, as observed in [110].

Table 6-4. Ca/Si ratios of the C-S-H composition (average of inner and outer C-S-H) for different cement types before exposure to carbonation.

Cement type	Ca/Si
CEM I 28d curing	1.96
CEM II/B-M 28d curing	1.89
CEM II/B-M 3d curing	1.96
CEM II/B-LL 28d curing	1.85
CEM III/A 28d curing	1.72

6.2.4 Morphology investigation using high-resolution microscopy

Figure 6-37 presents the results of using the high-resolution microscopy. The CEM II/B-M cement paste structure lost its fibrillar morphology after carbonation and became less porous. C-S-H reaction to form a silica gel appears to retain the overall morphology of the initial form of the calcium-silicate-hydrate gel [111]. The formation of the carbonate crystals filling the space causes the microstructure densification, discussed earlier in this chapter.

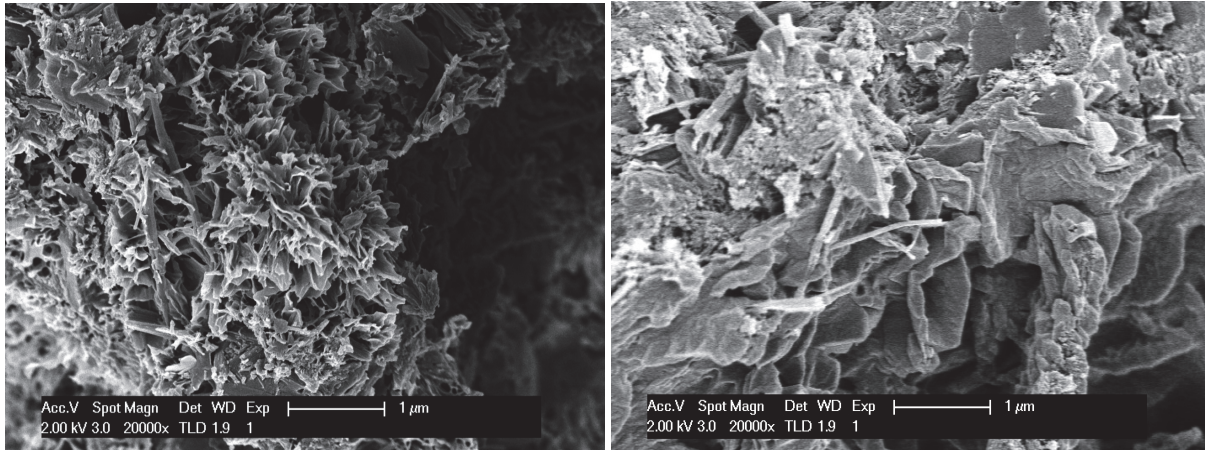


Figure 6-37. Images of CEM II/B-M cured for 3 days and exposed at 70 % RH for 12 months at CO₂-free atmosphere (left), and for 12 months at 400 ppm of CO₂ (right).

Chapter 7 Changes of the pore structure and diffusivity due to carbonation

- 7.1 Changes of the pore structure during carbonation 108
- 7.2 Gas diffusion..... 124
- 7.3 Dynamic vapor sorption (DVS)..... 132
- 7.4 Comparing the porosity changes with existing literature..... 134

This chapter discusses the influence of carbonation on the pore structure and its effect on the gas diffusion coefficient (Figure 7-1). The effect of carbonation over time on porosity and pore structure is presented. As well different definitions of “non-carbonated” cement pastes are discussed, and their relevance regarding the effect of carbonation on the pore structure was evaluated. Finally, the gas diffusion coefficients, are presented for carbonated and non-carbonated hardened cement pastes, and correlated with porosity descriptors.

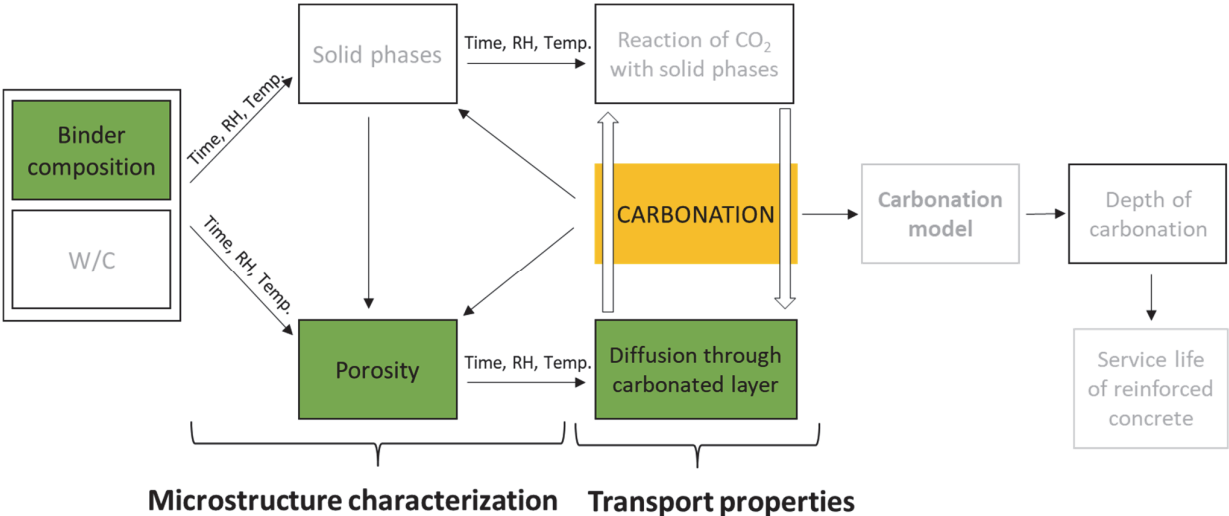


Figure 7-1. Research scope: Pore size distribution and transport properties during carbonation.

7.1 Changes of the pore structure during carbonation

The changes in the pore structure were characterised by mercury intrusion porosimetry (for details of the method see chapter 3). The pastes were prepared at $w/b=0.4$ with the exception of MixSL, where two w/c were used, 0.40 and 0.35. The paste samples were cured for 3 and 28 days before slicing and exposing them. The 1 mm thin disks were exposed to natural carbonation with CO_2 concentrations of around 400 ppm and 70 % RH. Different times of exposure were studied, starting after the first month, up to 24 months of exposure. Some systems become “fully carbonated” and the final exposure time characterises the porosity of the carbonated sample, while some still show non-carbonated regions in the core of 1 mm thick sample during using pH indicator. In that case, the pore structure is the average between the carbonated, non-carbonated and the transition zone (for example CEM I and MixSL with $w/c=0.35$, after 2 years of carbonation), as discussed in chapter 6. Reference mixes were exposed to CO_2 -free atmosphere at RH 70 %. Samples before exposure were also investigated. The porosity before the exposure is included in all graphs between Figure 7-2 and Figure 7-15.

Figure 7-2 to Figure 7-7 show how the critical radius and total porosity evolved during exposure to carbonation. We can see that for CEM I (Figure 7-2) the main changes occur during the first month of carbonation. For the sample cured for 3 days, the critical pore radius and entry pore radius are shifted towards higher values, in comparison to the sample microstructure from before exposure. Carbonation for the samples cured 28 days does not cause major differences in the critical pore radius value when compared to samples before exposure. However, the entry pore radius slightly increases.

For all carbonating samples, both, 3 and 28 days cured, the total porosity decreases significantly during carbonation, however, the rate of decrease is higher for the samples cured for a shorter time.

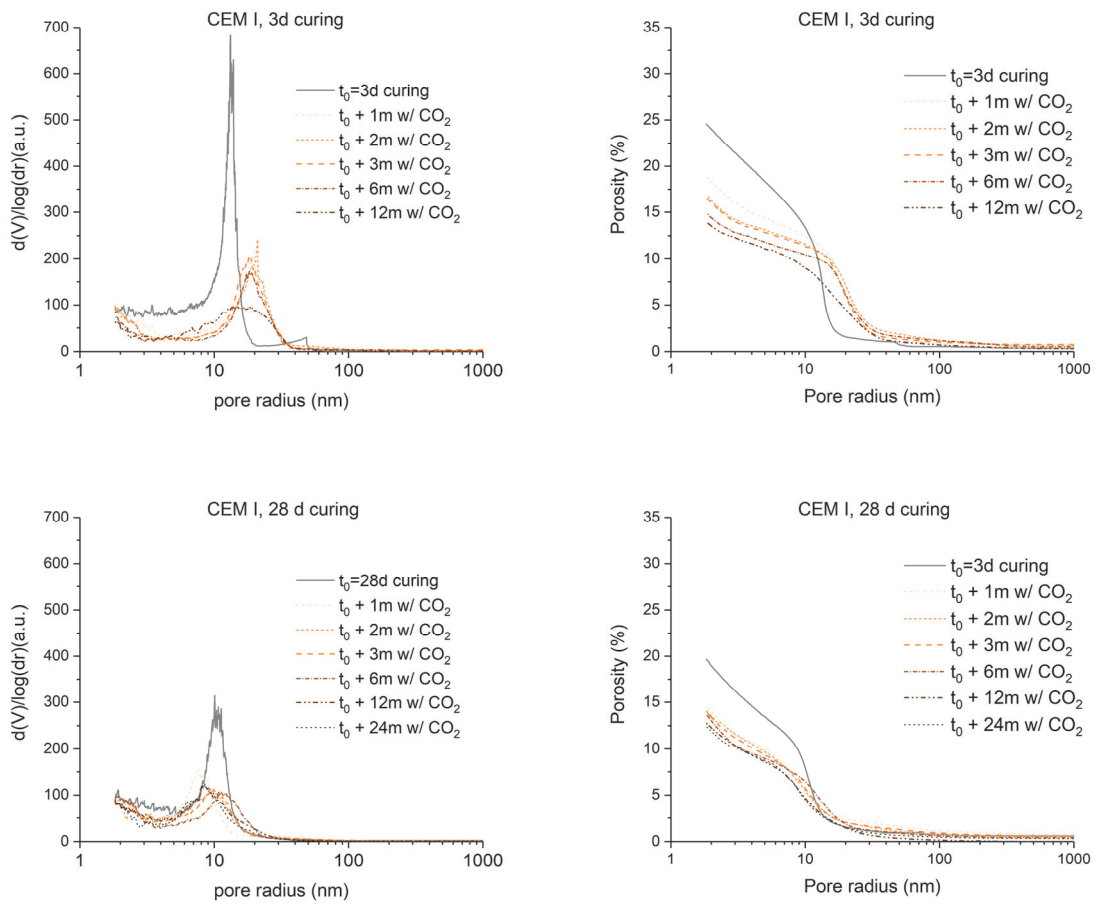


Figure 7-2. Impact of carbonation on the pore size distribution and on the total porosity for CEM I cured for 3 and 28 days, followed by exposure at 70 % RH with atmospheric CO_2 concentration.

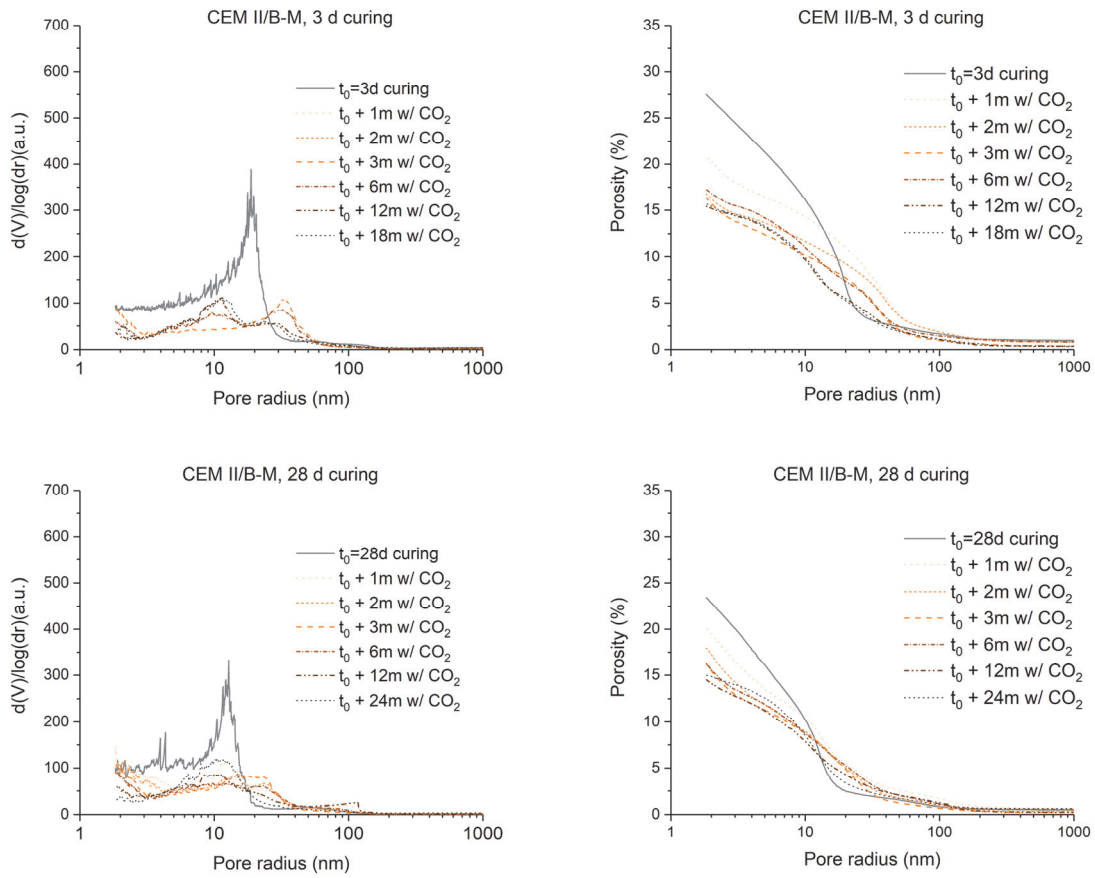


Figure 7-3. Impact of carbonation on the pore size distribution and on the total porosity for CEM II/B-M cured for 3 and 28 days, followed by exposure at 70 % RH with atmospheric CO_2 concentration.

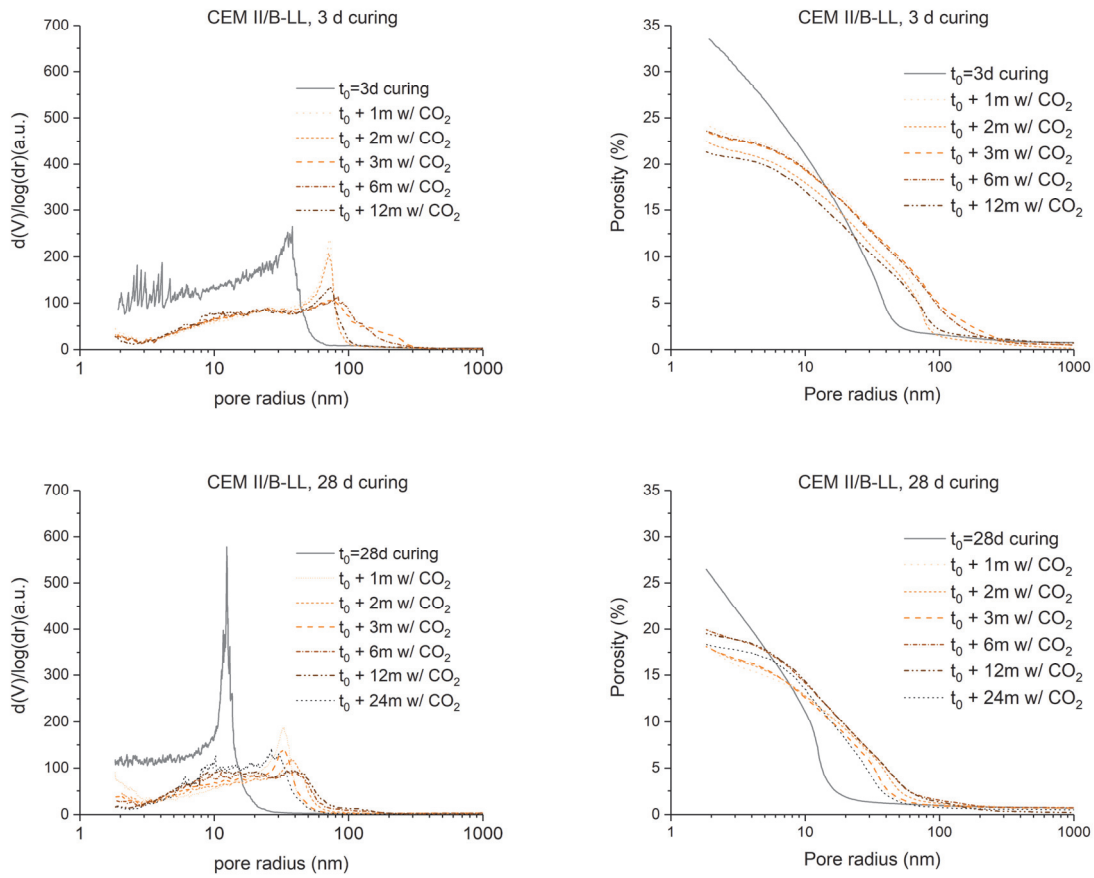


Figure 7-4. Impact of carbonation on the pore size distribution and on the total porosity for CEM II/B-LL cured for 3 and 28 days, followed by exposure at 70 % RH with atmospheric CO_2 concentration.

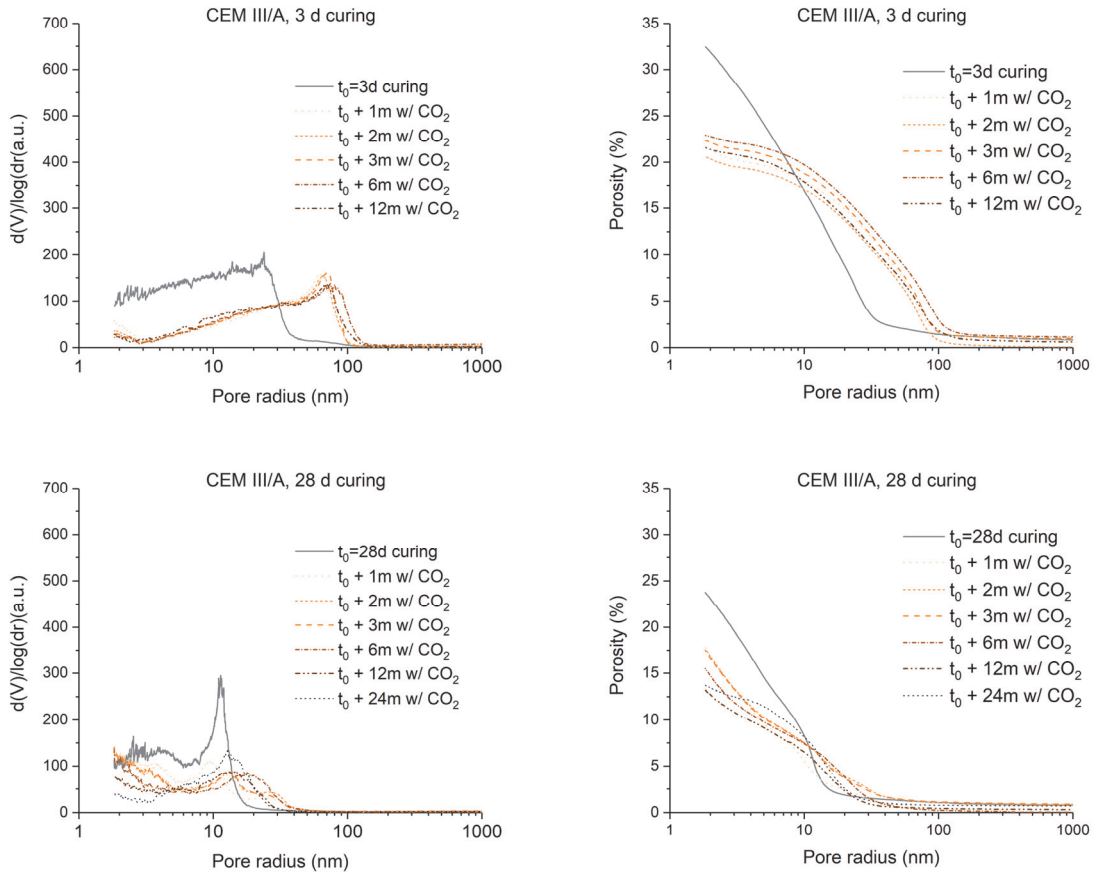


Figure 7-5. Impact of carbonation on the pore size distribution and on the total porosity for CEM III/A cured for 3 and 28 days, followed by exposure at 70 % RH with atmospheric CO_2 concentration.

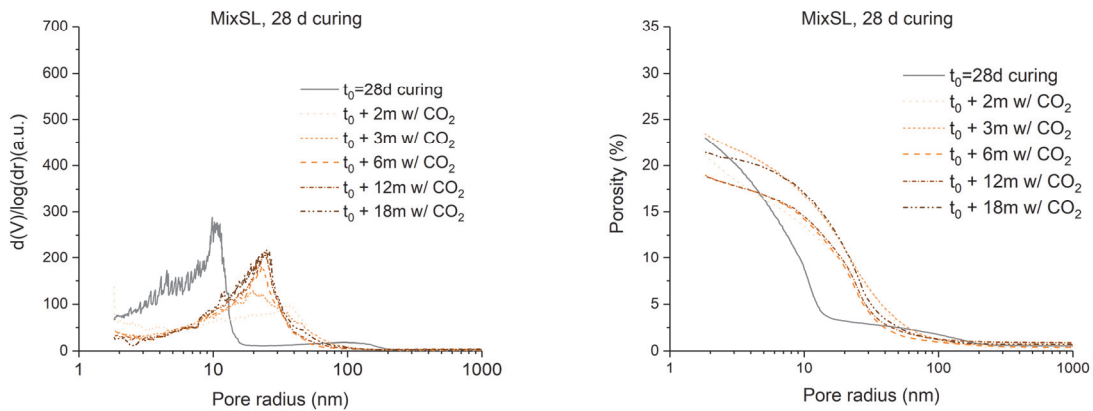


Figure 7-6. Impact of carbonation on the pore size distribution and on the total porosity for MixSL cured for 28 days, followed by exposure at 70 % RH with atmospheric CO_2 concentration.

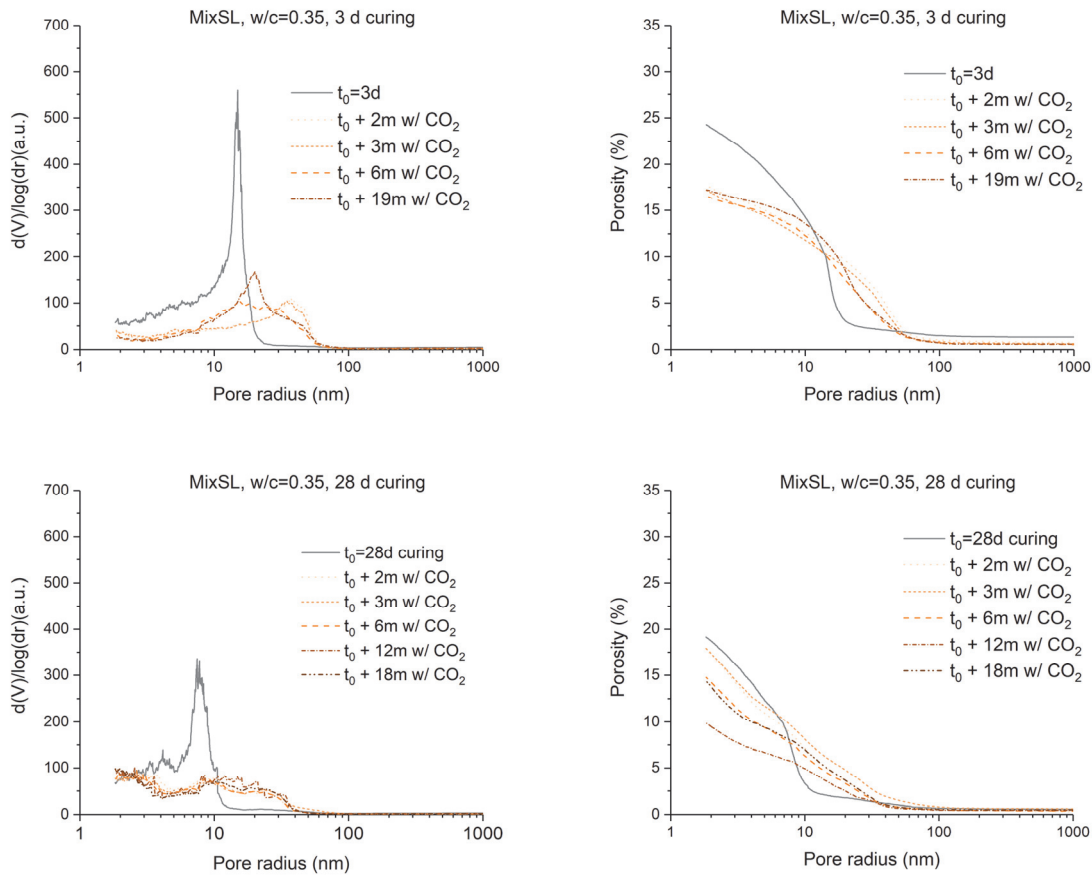


Figure 7-7. Impact of carbonation on the pore size distribution and on the total porosity for MixSL ($w/c=0.35$), cured for 3 and 28 days, followed by exposure at 70 % RH with atmospheric CO_2 concentration.

Figure 7-8 and Figure 7-9 summarise how the total porosity and the critical pore radius evolve during exposure to carbonation (table with values available in Appendix C). The point at $t=0$ refers to the pore structure before exposure (after 3 and 28 days of curing). The major drop in the total porosity takes place during the first month of carbonation. After that, the total porosity of most of the systems is stable or decreases very slightly. At the same time, the critical pore radius increases significantly after the first month of carbonation. For MixSL with $w/c=0.35$, cured for 28 days (Figure 7-7), it is rather difficult to assess the critical pore radius but we can see that a significant coarsening of the pores takes place during carbonation.

As carbonation continues the pores become finer. As an example, we can see that for CEM II/B-M cured for 3 days (Figure 7-3), the pore entry radius interval from 20 to 50 nm is decreased in favour of the interval from 7 to 20 nm. In general, the pore structure is refined if we compare the data after 1 or 2 months of carbonation with the ones after 18 or 24 months. There is a general porosity refinement during carbonation (initial months of carbonation vs the final time of exposure) for all of the cements (summary in Figure 7-8 and Figure 7-9). This phenomenon is not yet well understood. It might be related to the transformation of the calcium carbonate products with lower molar volumes into the ones with higher molar volumes, as the carbonation progresses.

As shown in chapter 6, amorphous calcium carbonate content is slightly higher at the beginning of the carbonation. Those both phenomena could be related.

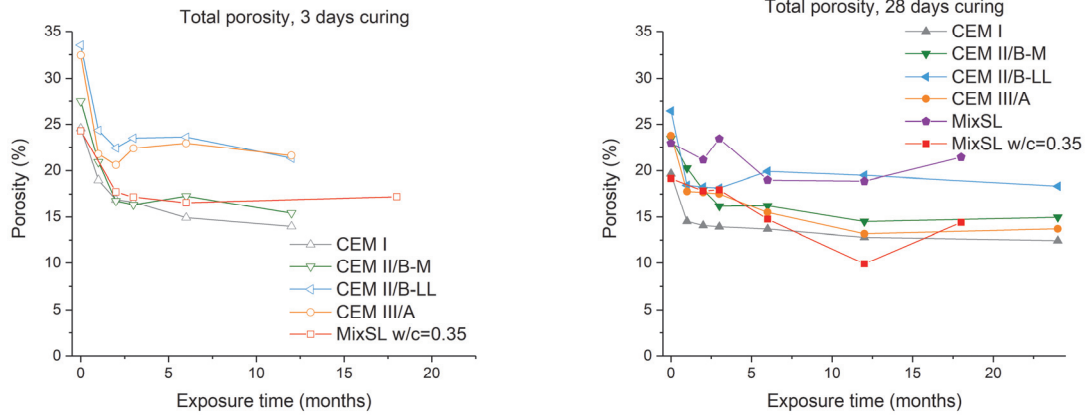


Figure 7-8. Total porosity quantification of OPC and blended cement pastes after curing for 3 and 28 days, followed by exposure to carbonation at 70 % RH.

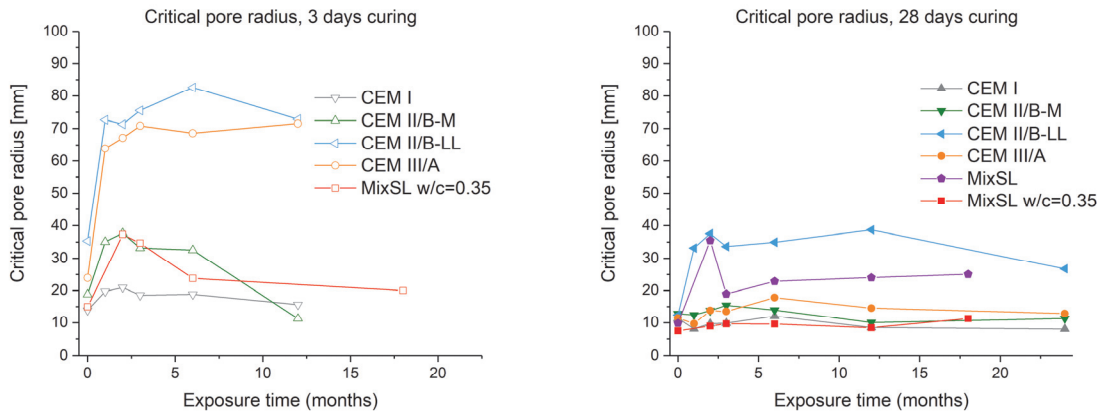


Figure 7-9. Critical pore radius quantification of OPC and blended cement pastes after curing for 3 and 28 days, followed by exposure to carbonation at 70 % RH.

So far, the comparison of the porosity was made on the samples exposed to carbonation versus the samples before exposure. In addition, the comparison of the carbonating samples with the ones exposed to CO₂-free atmosphere (70 % RH) is presented (Figure 7-10 to Figure 7-15). The total porosity also decreases during exposure to carbonation when comparing with the samples exposed to 0 ppm of CO₂. However, the critical pore radius of the carbonating samples now is lower. The exceptions are CEM III/A cured for 3 days and the systems made with MixSL (both w/c). For CEM III/A, although the total porosity decreases after carbonation, the critical pore radius and entry pore radius increase. MixSL (w/c=0.40) does not change the total porosity after carbonation but the critical and entry pore radius is shifted towards higher values. For MixSL with

$w/c=0.35$, the total porosity does not change significantly. However, its entry pore radius gets coarser, while its critical radius does not increase. This difference could be related to the substitution level, which for those mixes equals 50 %. In consequence, the portlandite content before the exposure is lower (around 10 % compared to 20 % for OPC). The full data characterizing the pore structure changes during exposure without carbon dioxide was presented in chapter 5. The values of the total porosity, critical pore radius, and entry pore radius obtained from the before exposure and at the end of the exposure time are illustrated between Figure 7-16 and Figure 7-21.

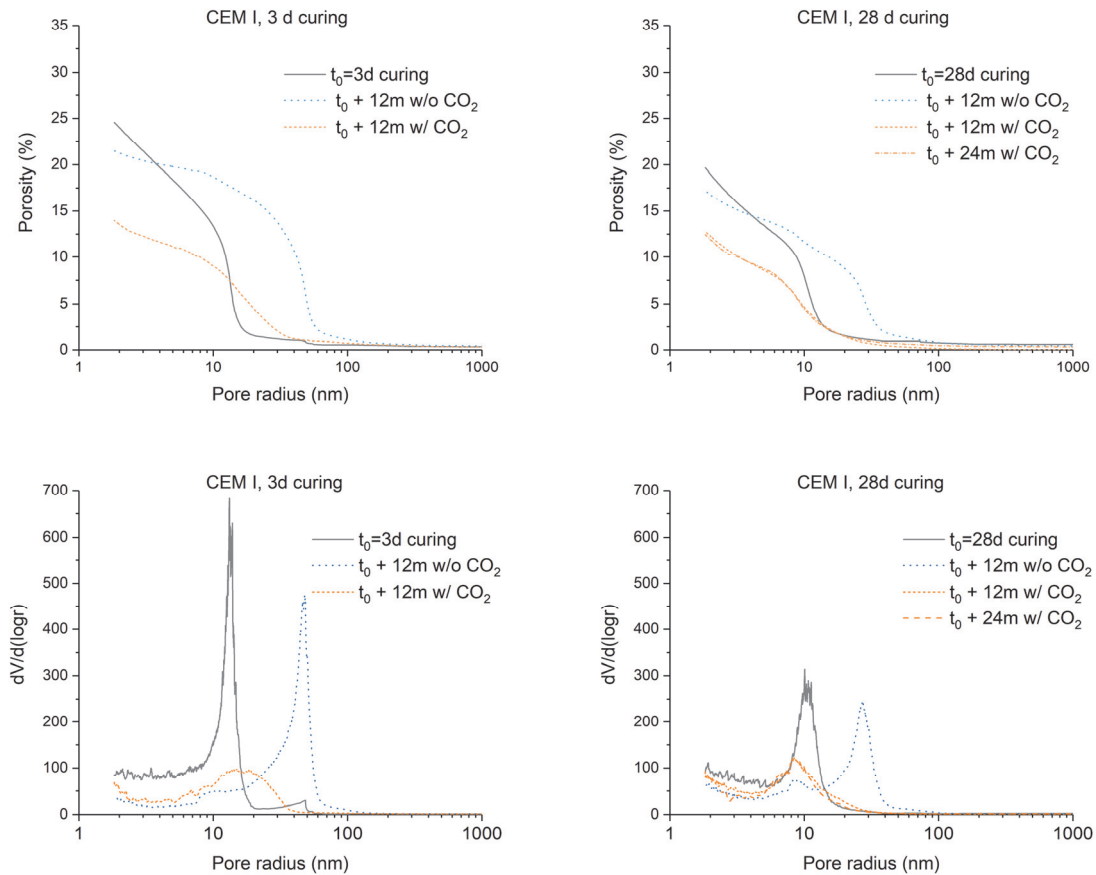


Figure 7-10. Porosity analysis of CEM I exposed to carbonation and to CO_2 -free atmosphere at 70 % RH; 3- and 28-days curing time before exposure (t_0).

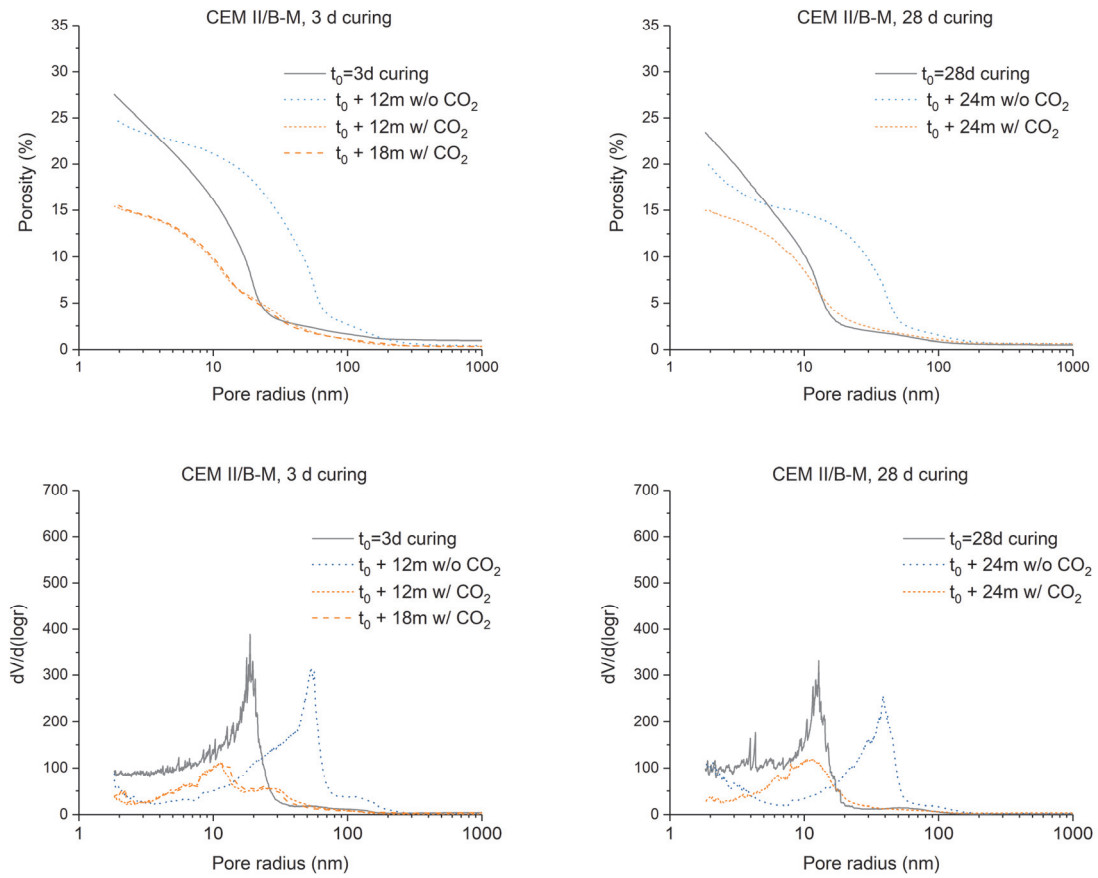


Figure 7-11. Porosity analysis of CEM II/B-M exposed to carbonation and to CO_2 -free atmosphere at 70 % RH; 3- and 28-days curing time before exposure (t_0).

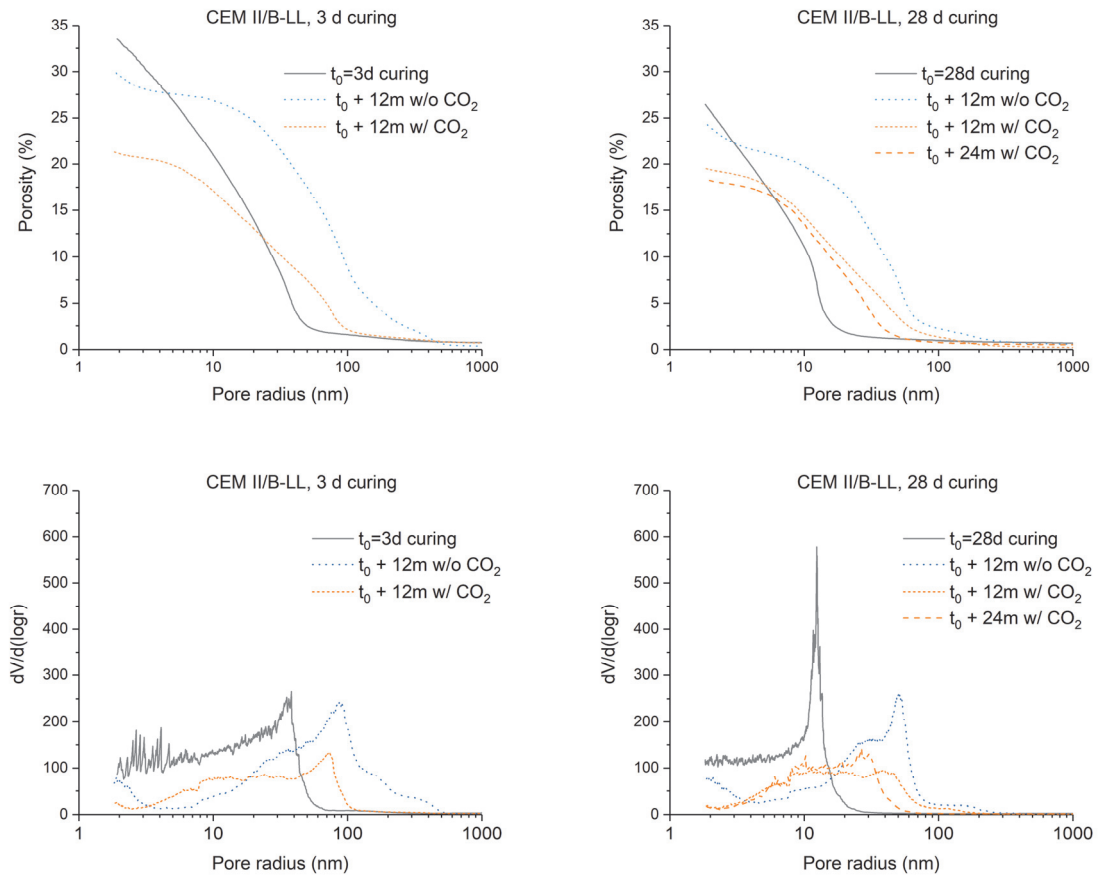


Figure 7-12. Porosity analysis of CEM II/B-LL exposed to carbonation and to CO_2 -free atmosphere at 70 % RH; 3- and 28-days curing time before exposure (t_0).

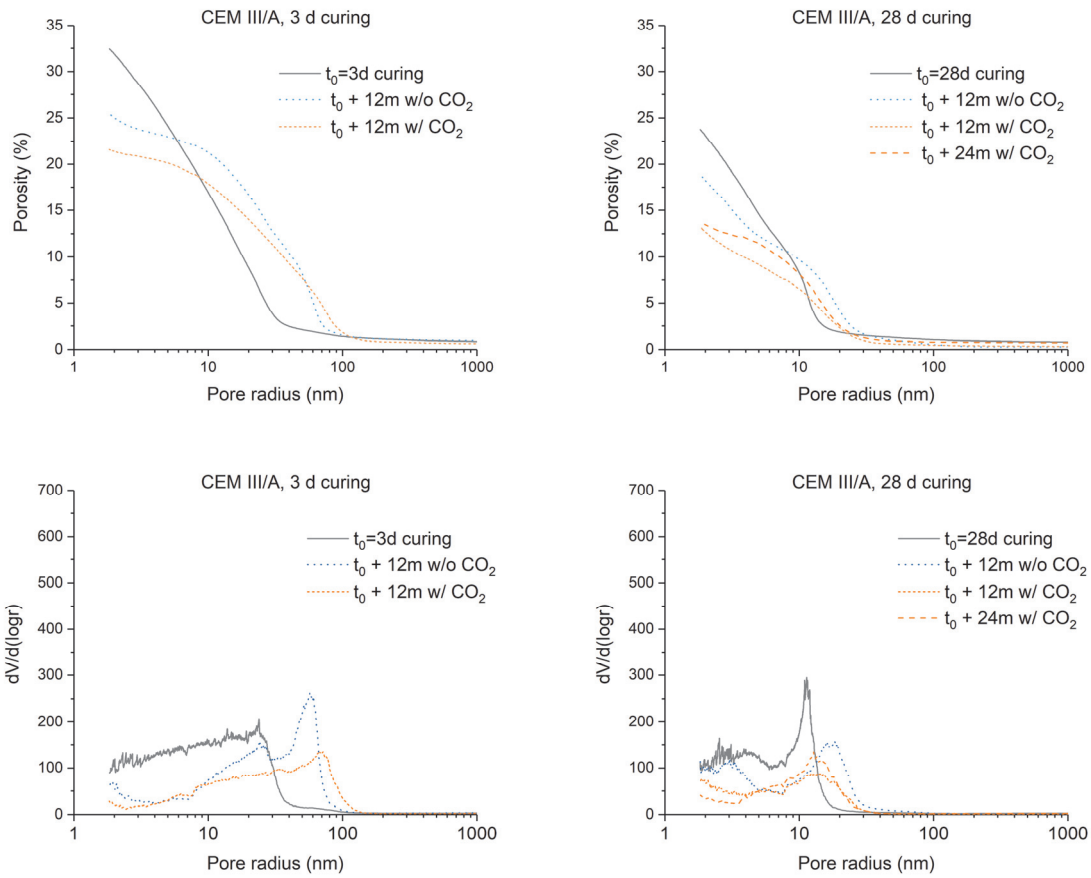


Figure 7-13. Porosity analysis of CEM III/A exposed to carbonation and to CO_2 -free atmosphere at 70 % RH; 3- and 28-days curing time before exposure (t_0).

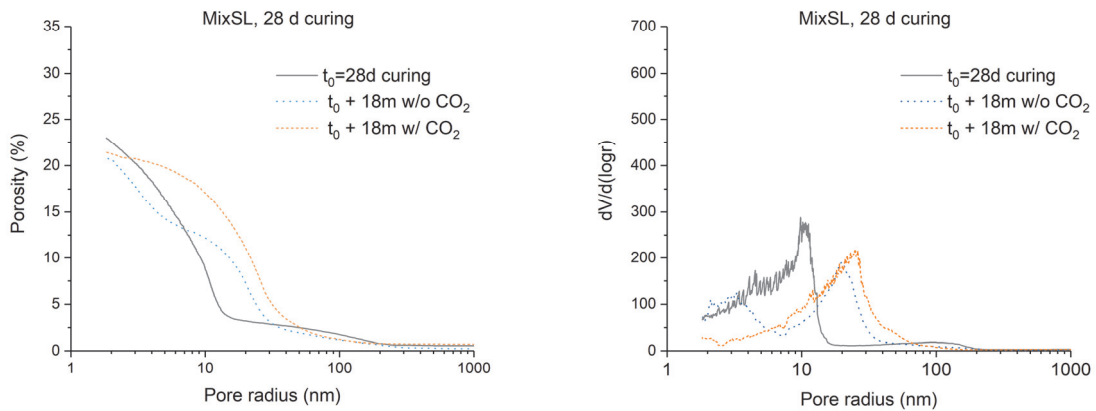


Figure 7-14. Porosity analysis of MixSL exposed to carbonation and to CO_2 -free atmosphere at 70 % RH; 28-days curing time before exposure (t_0).

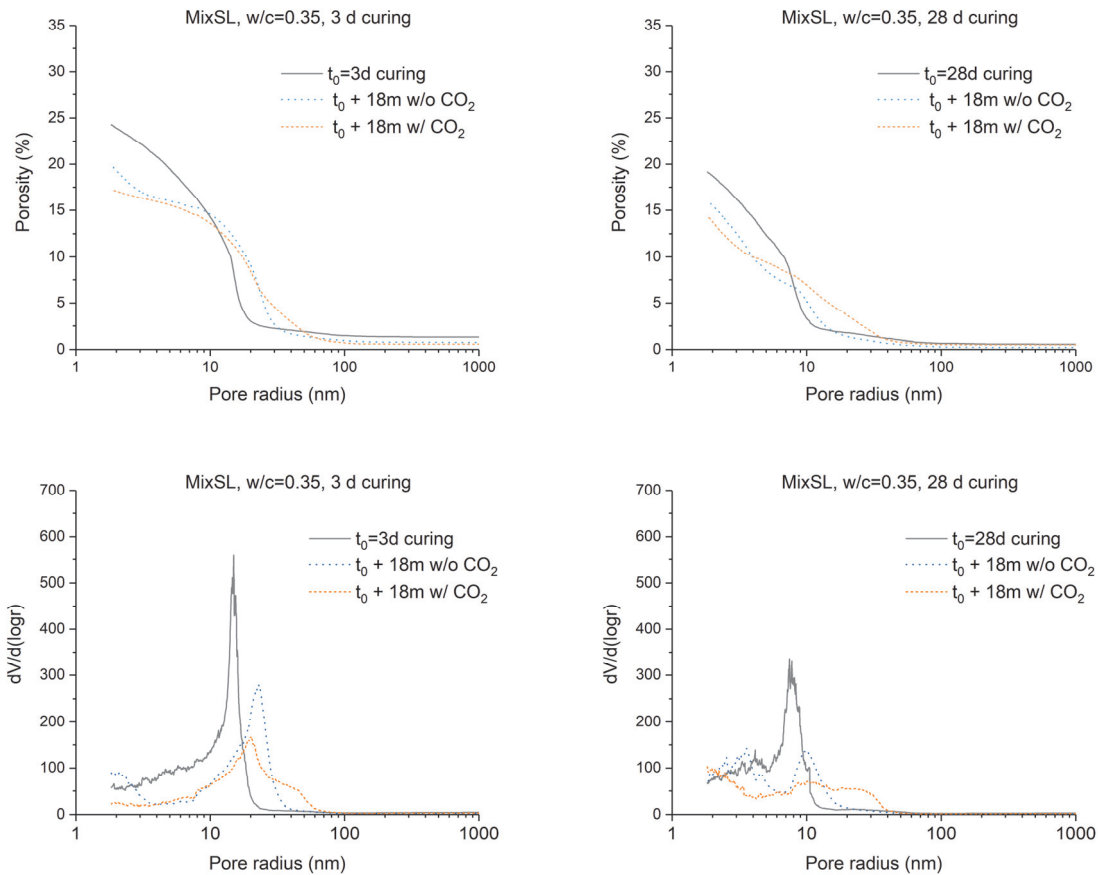


Figure 7-15. Porosity analysis of MixSL ($w/c=0.35$) exposed to carbonation and to CO_2 -free atmosphere at 70% RH; 3- and 28-days curing time before exposure (t_0).

The results show that it is not just the OPC pastes which shows a refinement of the pore structure due to carbonation. Although coarsening was observed for the blends with 50% of clinker replacement, the porosity is refined for the other blends, for which the clinker substitution level is around 30%. This indicates that the common way of comparing the pore structure of the carbonated samples with the pore structure after the end of the curing time may be misleading. Part of the coarsening observed during carbonation is the effect of the drying taking place during exposure to lower relative humidity (as discussed in chapter 5).

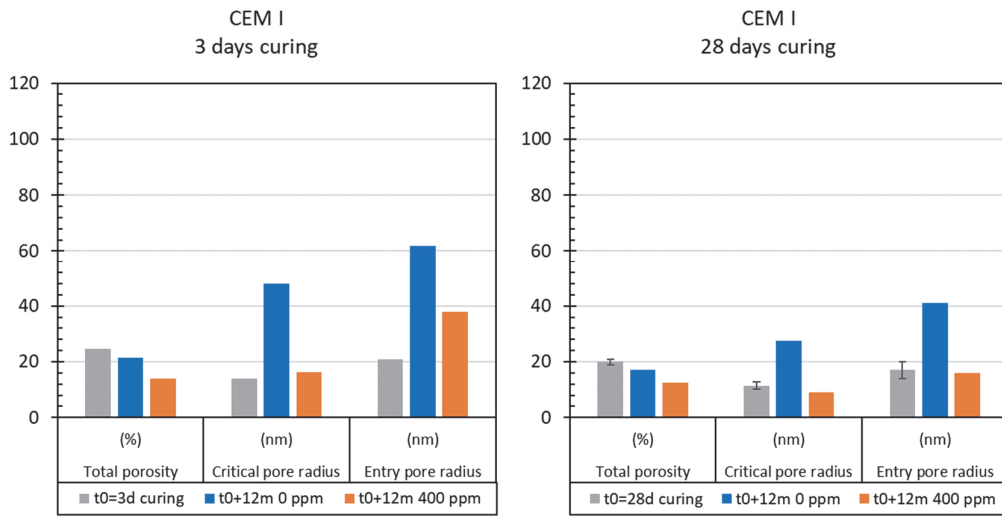


Figure 7-16. Total porosity, critical pore radius, and entry pore radius changes after carbonation in compare with two references: before exposure and exposure at CO₂-free atmosphere; CEM I cured for 3 and 28 days before exposure.

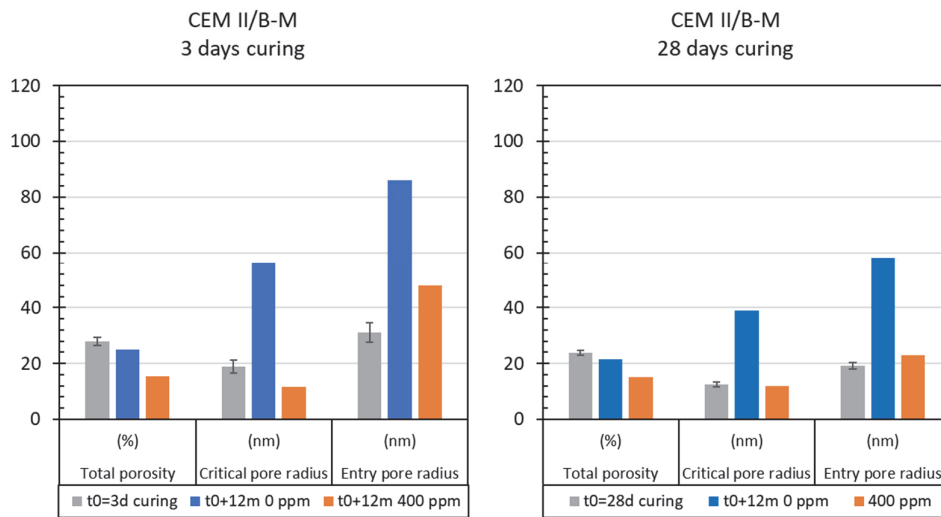


Figure 7-17. Total porosity, critical pore radius, and entry pore radius changes after carbonation in compare with two references: before exposure and exposure at CO₂-free atmosphere; CEM II/B-M cured for 3 and 28 days before exposure.

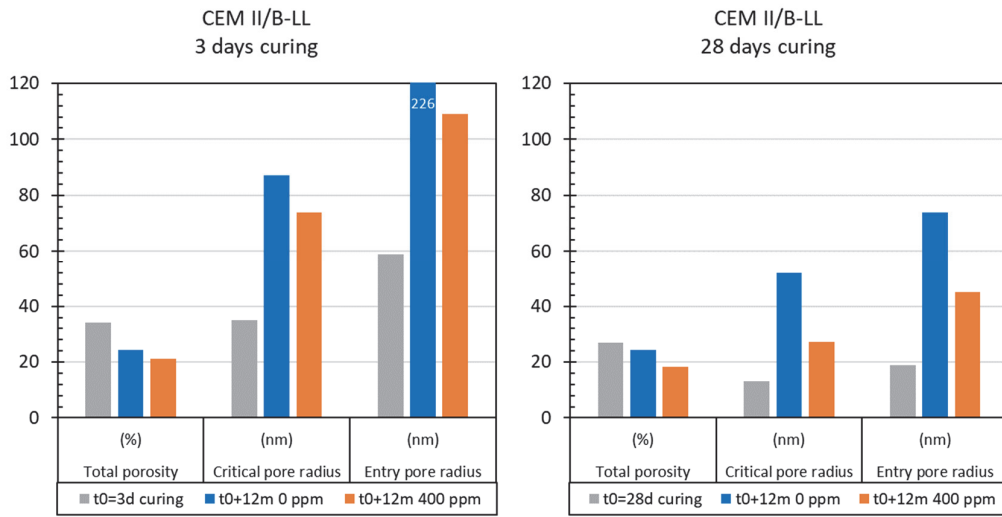


Figure 7-18. Total porosity, critical pore radius, and entry pore radius changes after carbonation in compare with two references: before exposure and exposure at CO_2 -free atmosphere; CEM II/B-LL cured for 3 and 28 days before exposure.

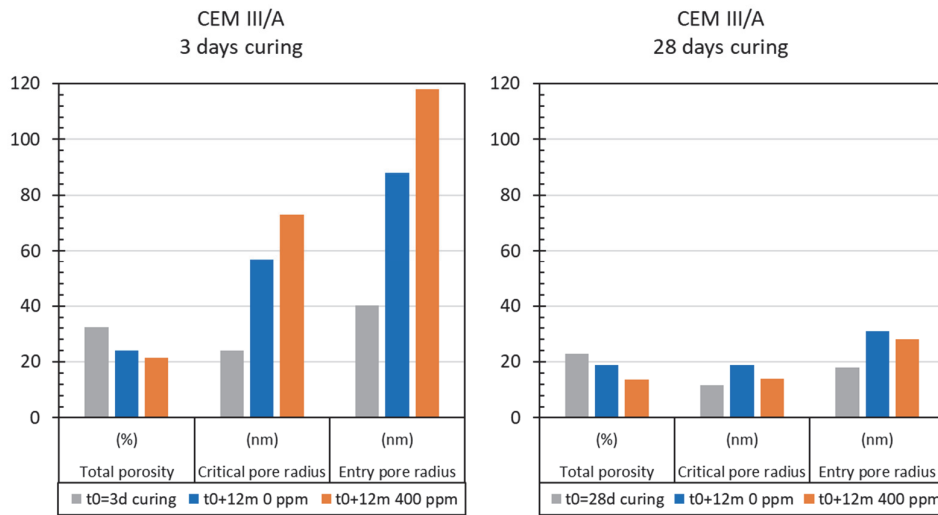


Figure 7-19. Total porosity, critical pore radius, and entry pore radius changes after carbonation in compare with two references: before exposure and exposure at CO_2 -free atmosphere; CEM III/A cured for 3 and 28 days before exposure.

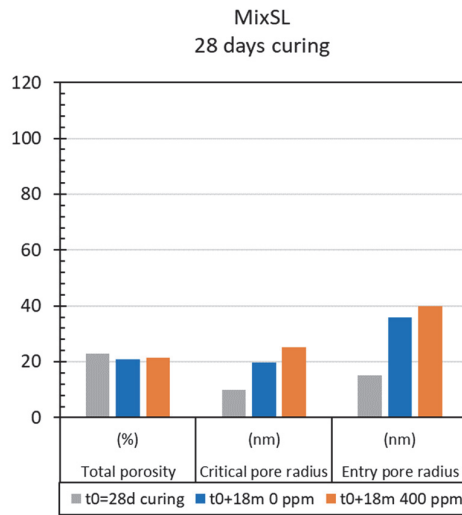


Figure 7-20. Total porosity, critical pore radius, and entry pore radius changes after carbonation in compare with two references: before exposure and exposure at CO_2 -free atmosphere; MixSL cured for 28 days before exposure.

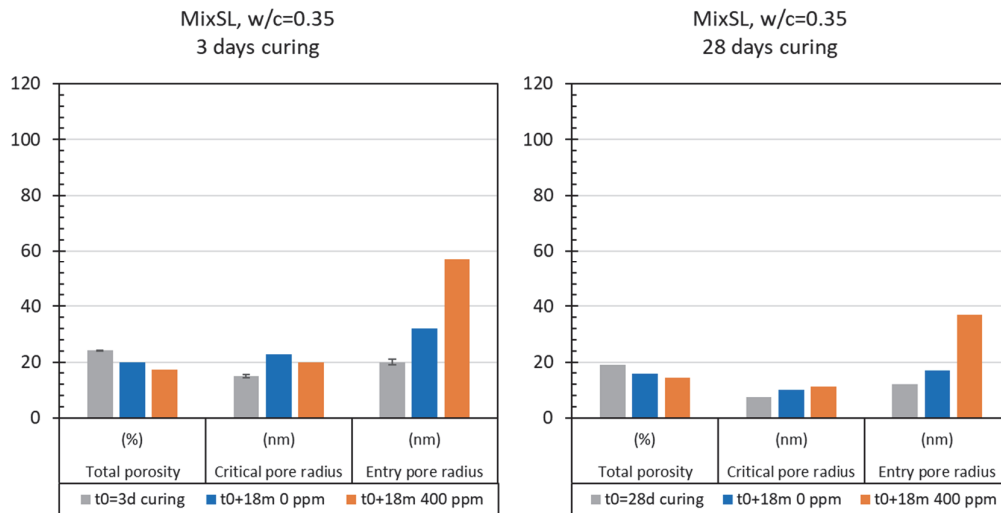






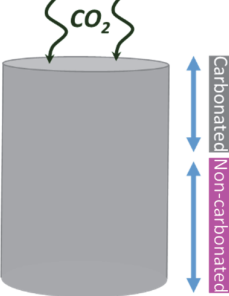
Figure 7-21. Total porosity, critical pore radius, and entry pore radius changes after carbonation in compare with two references: before exposure and exposure at CO_2 -free atmosphere; MixSL, w/c=0.35, cured for 3 and 28 days before exposure.

Coarsening of the porosity for the CEM III/A and MixSL mixes is probably due to the carbonation of other phases than calcium hydroxide, since the initial portlandite content is lower. Carbonation products have higher molar volumes than the $Ca(OH)_2$ [45][37][112]. The formation of calcite in replacement of $Ca(OH)_2$ leads to reduction of the porosity. However, when other hydrates, such as C-S-H, starts to carbonate due to portlandite depletion, there is an increase of porosity after carbonation.

The pore size distribution of the samples exposed to the atmosphere without CO₂, does not seem to have stabilised (Chapter 5). Nevertheless, the final conclusion, that the pore structure of the CEM I, CEM II/B-M and CEM II/B-LL is refined after carbonation when comparing with CO₂-free exposure would not change, as long as the critical pore radius keeps increasing or stabilises.

Figure 7-22 shows the porosity distribution for OPC and 3 blended cements at different exposure environments: before exposure, after additional curing, exposed at CO₂-free atmosphere, exposure to carbonation, and non-carbonated zone from the core of carbonating paste cylinders. The preparation of different reference types is presented in Table 7-1. In Table 7-2 we can see how big impact can have the selected reference when the effect of carbonation is evaluated. If we choose the non-carbonated sample as the one from before exposure to carbonation or after additional curing (to ensure mature microstructure) then the obtained results lead to the conclusions that carbonation causes coarsening of the porosity. However, if the non-carbonated sample was the one which was exposed at CO₂-free atmosphere or the one from uncarbonated zone of carbonating sample – then the refinement of porosity is observed. The porosity distribution curves of the samples exposed to CO₂-free atmosphere, and the one from the uncarbonated zone of the sample exposed to carbonation, are remarkably close. They indicate that this is a true physical phenomenon and not just an effect of the sample geometry.

Table 7-1. Different types of reference samples compared with carbonated sample.

t ₀ =28d curing	90d curing	t ₀ + curing 12 w/o CO ₂	t ₀ + curing 12 w/ CO ₂	t ₀ + curing 30 w/ CO ₂ (non-carbonated zone from carbonating cylinder)
 RH > 95 % for 28 days	 RH > 95 % for 90 days	 0 ppm of CO ₂ 70 % RH	 400 ppm of CO ₂ 70 % RH	 400 ppm of CO ₂ 70 % RH

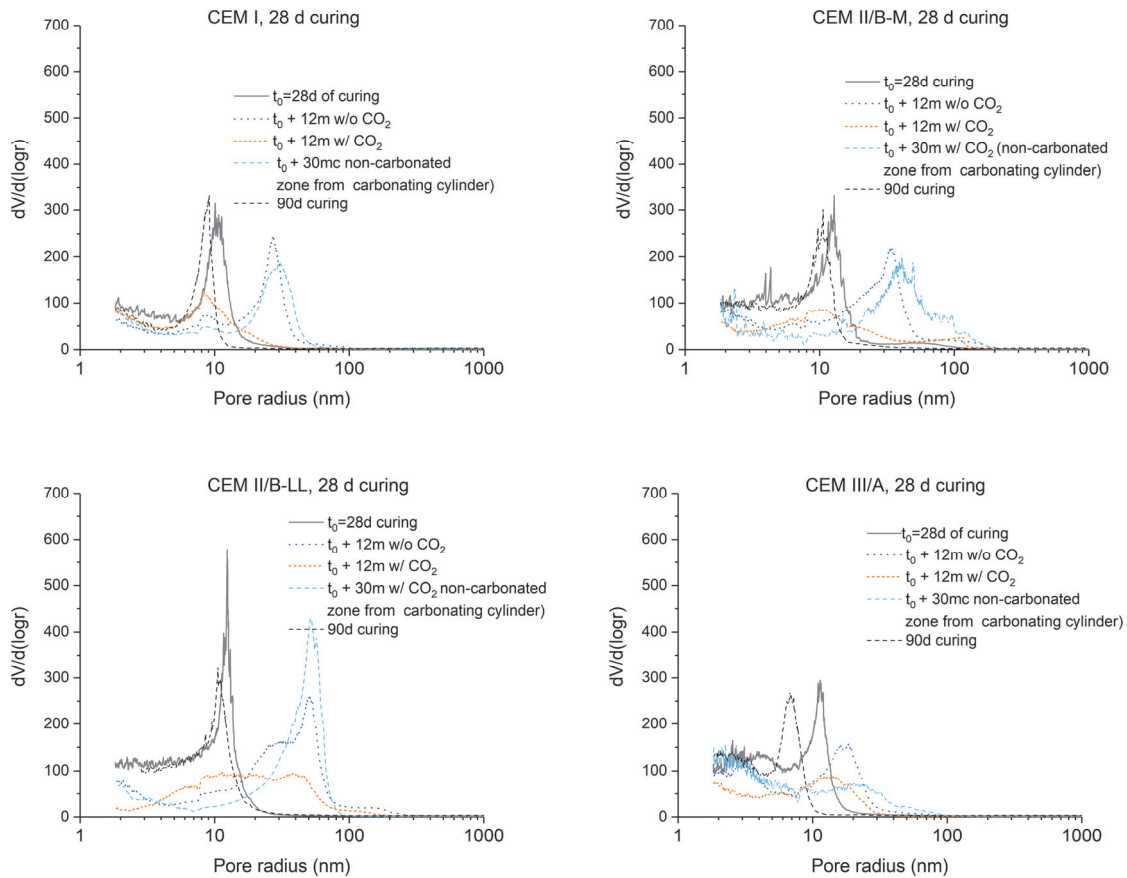


Figure 7-22. Porosity distribution after carbonation vs before exposure vs elongated curing (90 days) vs exposure at CO_2 -free atmosphere vs non-carbonated zone of a cylinder exposed to carbonation.

Coupled effect of drying and exposure to CO_2 can overestimate the effect of carbonation. The work presented separates those phenomena. Next part of this chapter presents how the changes caused by carbonation affect the transport of the oxygen through the different microstructures.

7.2 Gas diffusion

It was shown that the correlation between the reaction front and the gas diffusion coefficient of the uncarbonated concrete is very poor ([10]). As the diffusion coefficient changes after carbonation, it is impossible to obtain a good carbonation model based on the diffusion parameters of non-carbonated concrete. The modifications of the microstructure due to carbonation causes changes in the diffusion properties. In this part, the influence of carbonation on gas diffusion is presented. Oxygen gas was chosen to perform this experiment due to its neutral effect on the hydrated cement paste microstructure, as well as safety reasons.

The evolution of the oxygen concentration in the nitrogen chamber was performed on the partially saturated samples (70 % RH). That data was used to back-calculate the diffusion coefficient. More details about the set-up and the experimental procedure are described in chapter 3 “Materials and methods”.

Gas diffusion properties were studied on the samples exposed for 18 or 24 months to CO₂-free atmosphere, and to natural carbonation, both at 70 % RH, after 3 or 28 days of curing. The results obtained show that the disks made with CEM I, CEM II/B-M, and CEM II/B-LL followed by exposure at CO₂-free atmosphere have a higher diffusion coefficient than the carbonated ones. It links well with the porosity data obtained from MIP (see from Figure 7-10 to Figure 7-12). Table 7-2 shows the values of diffusion coefficient for the studied systems. Each figure is an average value obtained by carrying out the diffusion test on 2 or 3 different samples. The duplicates showed good repeatability of the experiment (Table 7-3).

Table 7-2. Diffusion coefficient as a function of cement type, curing time and exposure conditions.

Cement type	Curing time before exposure (days)	CO ₂ concentration at 70 % RH	Diffusion coefficient (D _e)	Standard deviation
			(cm ² /s)	
CEM I	3	0 ppm	20.50·10 ⁻⁵	2.96·10 ⁻⁵
		400 ppm	0.36·10 ⁻⁵	0.03·10 ⁻⁵
	28	0 ppm	5.58·10 ⁻⁵	0.30·10 ⁻⁵
		400 ppm	0.22·10 ⁻⁵	0.03·10 ⁻⁵
CEM II/B-M	3	0 ppm	49.60·10 ⁻⁵	1.89·10 ⁻⁵
		400 ppm	3.51·10 ⁻⁵	0.68·10 ⁻⁵
	28	0 ppm	20.80·10 ⁻⁵	0.73·10 ⁻⁵
		400 ppm	6.05·10 ⁻⁵	0.15·10 ⁻⁵
CEM II/B-LL	3	0 ppm	114.00·10 ⁻⁵	10.51·10 ⁻⁵
		400 ppm	62.90·10 ⁻⁵	3.25·10 ⁻⁵
	28	0 ppm	54.10·10 ⁻⁵	0.43·10 ⁻⁵
		400 ppm	35.90·10 ⁻⁵	2.12·10 ⁻⁵
CEM III/A	3	0 ppm	34.40·10 ⁻⁵	1.01·10 ⁻⁵
		400 ppm	67.50·10 ⁻⁵	0.75·10 ⁻⁵
	28	0 ppm	1.49·10 ⁻⁵	0.21·10 ⁻⁵
		400 ppm	4.63·10 ⁻⁵	0.07·10 ⁻⁵
MixSL	28	0 ppm	5.29·10 ⁻⁵	0.78·10 ⁻⁵
		400 ppm	37.90·10 ⁻⁵	2.90·10 ⁻⁵
MixSL w/c=0.35	3	0 ppm	9.62·10 ⁻⁵	0.83·10 ⁻⁵
		400 ppm	31.30·10 ⁻⁵	1.47·10 ⁻⁵
	28	0 ppm	0.40·10 ⁻⁵	0.06·10 ⁻⁵
		400 ppm	0.85·10 ⁻⁵	0.04·10 ⁻⁵

Table 7-3. Example of repeatability of the test; standard deviation evaluated after testing 3 different samples of the same system.

Sample and exposure type	Number of samples tested	Diffusion coefficient (D_e)	Standard deviation
		(cm ² /s)	
CEM II/B-M, 28d curing 24 months at 400 ppm of CO ₂	Sample #1	5.86·10 ⁻⁵	0.15·10 ⁻⁵
	Sample #2	5.95·10 ⁻⁵	
	Sample #3	6.24·10 ⁻⁵	
CEM II/B-LL, 3d curing 24 months at 0 ppm of CO ₂	Sample #1	109·10 ⁻⁵	10.51·10 ⁻⁵
	Sample #2	126·10 ⁻⁵	
	Sample #3	106·10 ⁻⁵	

Figure 7-23 shows the relation of different porosity properties to diffusion coefficient (D_e) for the samples which were 3 days cured before exposure to carbonation. We can see that D_e decreases with the decrease of the total porosity for most of the cements. Exceptions are CEM III/A (with 50 % replacement by slag), and MixSL with $w/c=0.35$ (with 50 % replacement by a mixture of burnt oil shale, limestone, and slag). For those mixes, D_e increased after carbonation, although total porosity is decreasing. A further comparison was made with the critical pore radius. For CEM III/A the critical radius increased after carbonation, what could explain the increase in the D_e , however, the critical pore radius for MixSL ($w/c=0.35$) slightly decreases. Finally, D_e was compared with the entry pore size. This parameter seems to explain the increase of the diffusion coefficient after carbonation. Moreover, for all other systems entry pore radius decrease after carbonation as well as the diffusion coefficient.

The situation looks to be a bit more complicated for systems cured for 28 days (Figure 7-24). For CEM III/A and MixSL with $w/c=0.35$ the diffusion coefficient barely changes after carbonation despite the entry pore radius is increasing. On the other hand, for MixSL ($w/c=0.40$) in spite of there being only a minor increase in the entry pore radius after carbonation, the diffusion coefficient changes significantly.

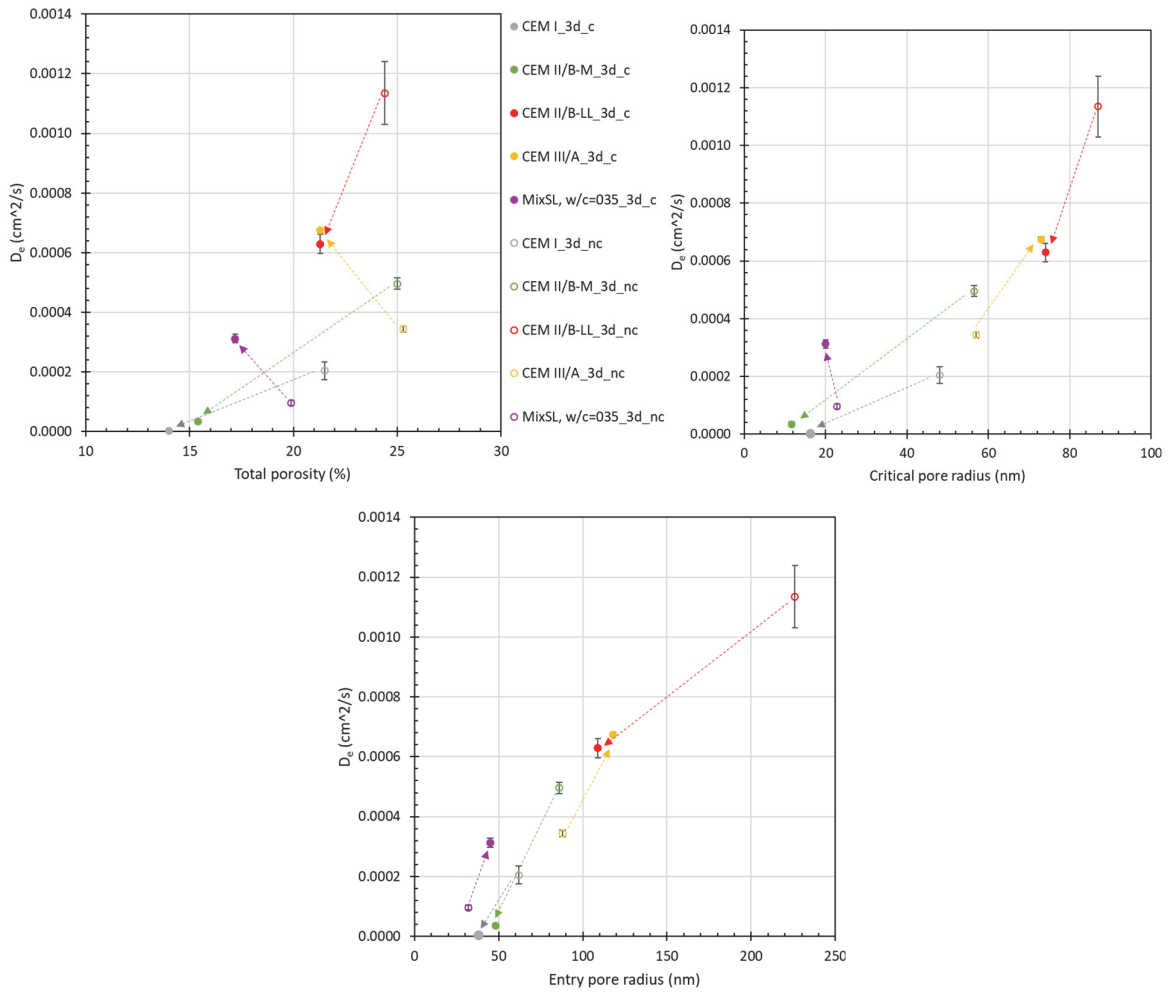


Figure 7-23. Correlation of the total porosity, the critical pore radius, and the entry pore radius with diffusion coefficient for carbonated and non-carbonated samples cured for 3 days before carbonation.

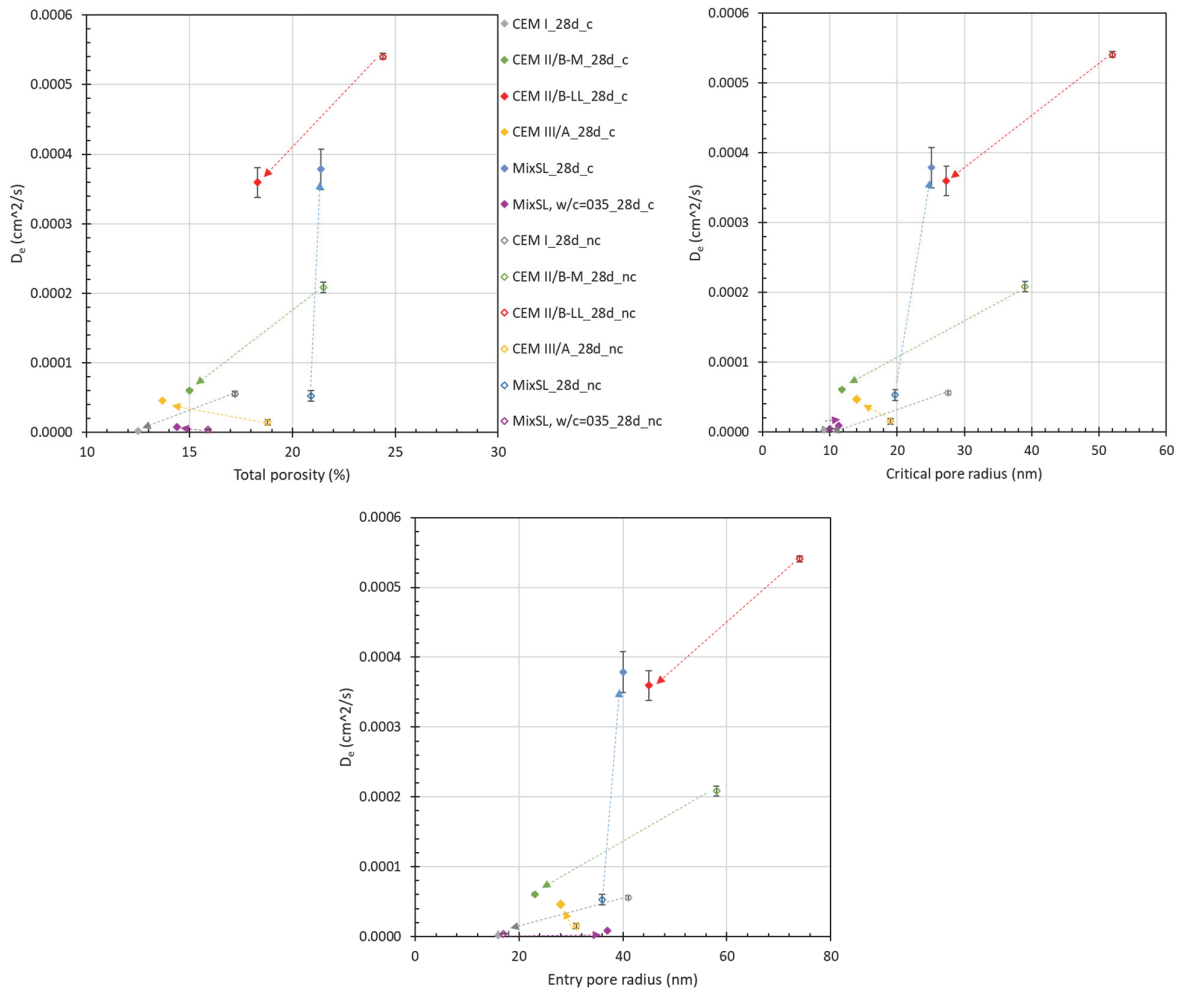


Figure 7-24. Correlation of the total porosity, the critical pore radius, and the entry pore radius with diffusion coefficient for carbonated and non-carbonated samples cured for 28 days before carbonation.

All measured diffusion coefficients, regardless of curing time, are presented together as a function of the total porosity, the critical pore radius, and the entry pore radius (see from Figure 7-25 to Figure 7-27). Overall, the diffusion coefficient seems to correlate well with the critical pore radius and the entry pore radius (R^2 equal 0.82 and 0.85 respectively). No obvious correlation is observed between the diffusion coefficient and the total porosity. In addition to the linear scale, a perspective of the diffusion coefficient in the logarithmic scale is presented, to allow comparison of the diffusion coefficient with existing literature.

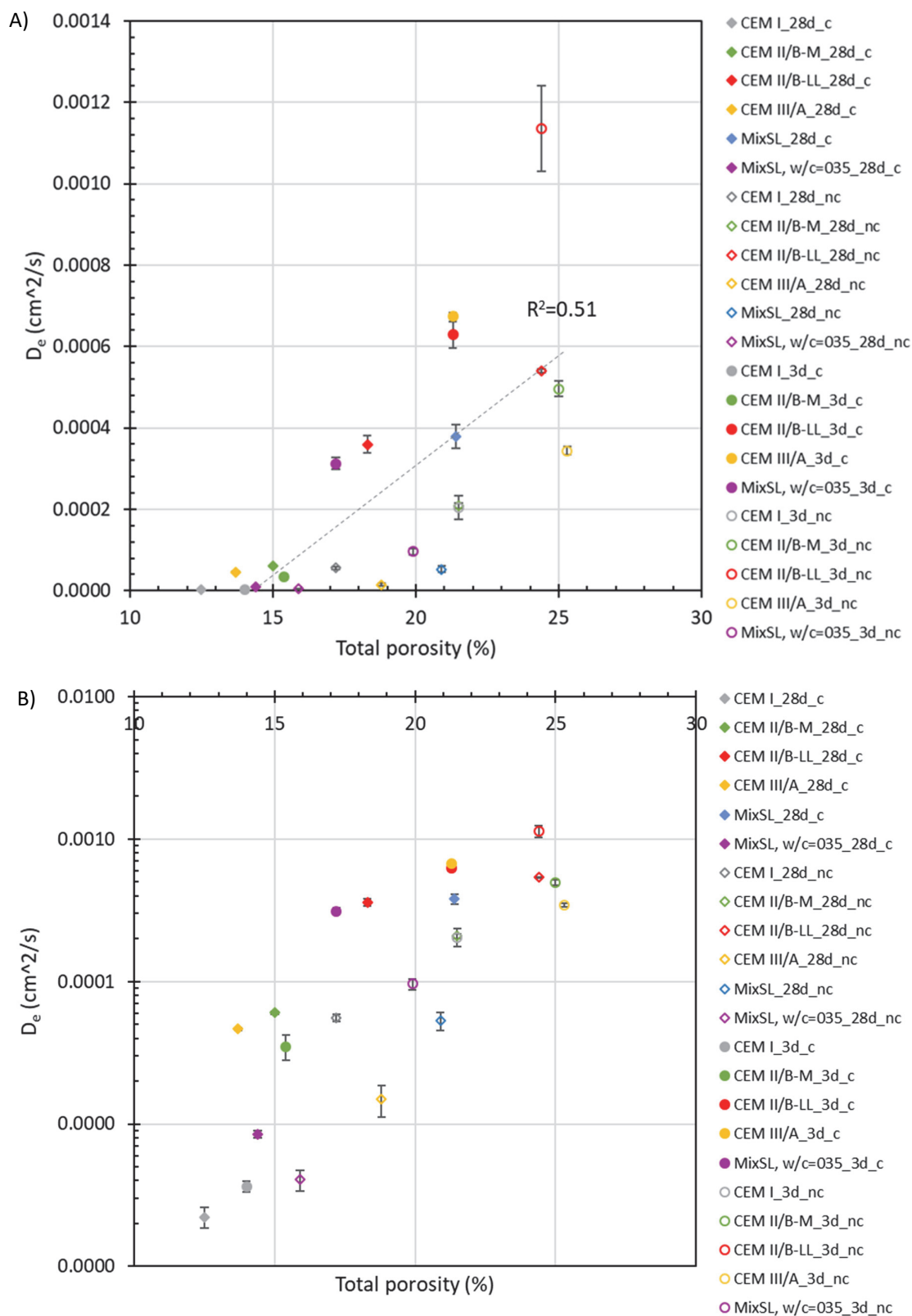


Figure 7-25. Correlation of the diffusion coefficient with the total porosity obtained from MIP; A): linear scale, $R^2=0.51$, B): logarithmic scale.

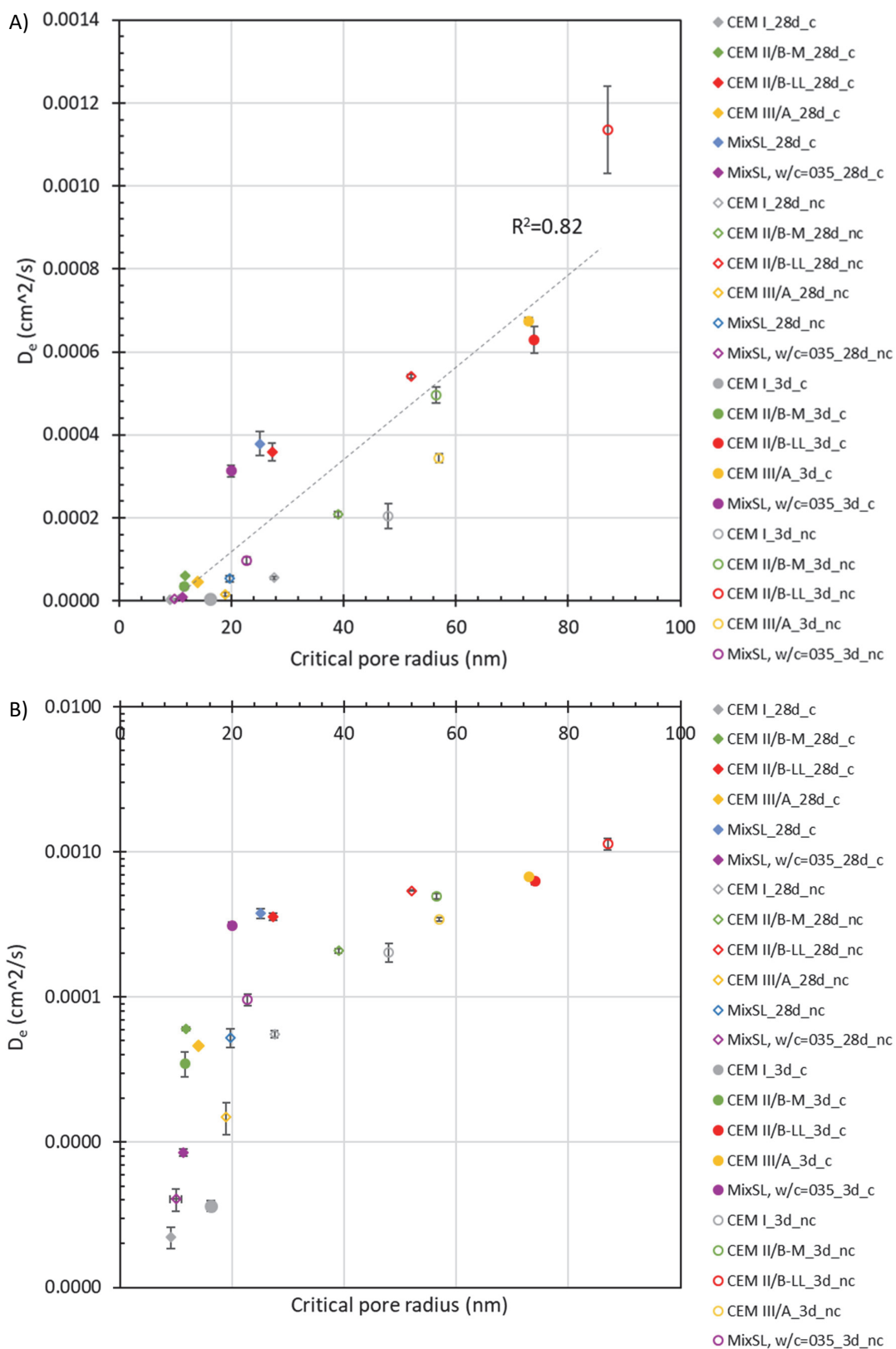


Figure 7-26. Correlation of the diffusion coefficient with the critical pore radius obtained from MIP; A): linear scale, $R^2=0.82$, B): logarithmic scale.

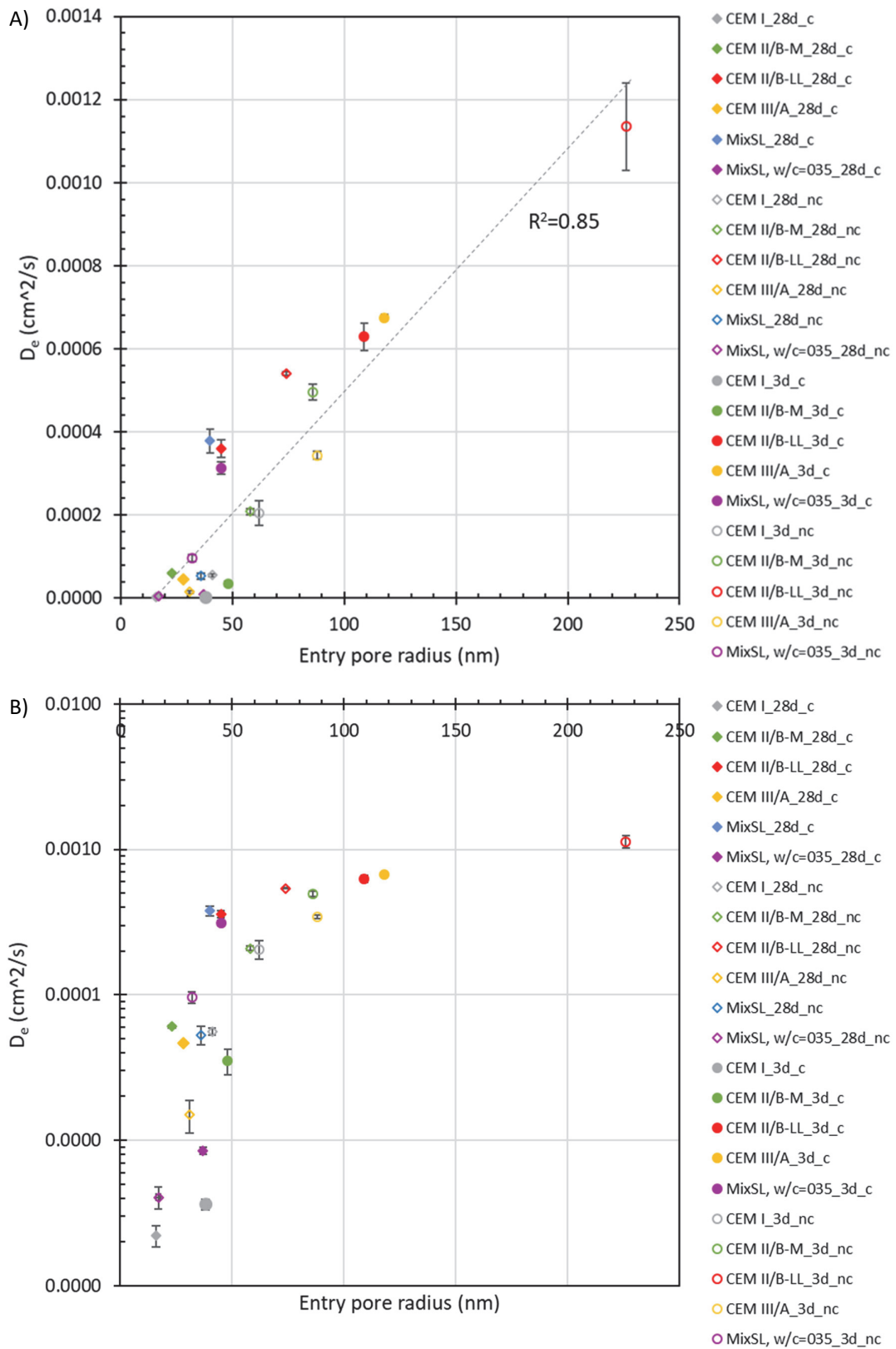


Figure 7-27. Correlation of the diffusion coefficient with the entry pore size obtained from MIP; A): linear scale, $R^2=0.85$, B): logarithmic scale.

It has to be emphasized that all diffusion coefficients data were obtained on partially saturated samples, whereas the MIP data were performed on the samples dried by solvent exchange. It has to be kept in mind that some of the pores in 70 % RH are partially or completely saturated. That is why the correlation of the diffusion coefficient with porosity parameters can be distorted. Information about saturated porosity would ensure the more coherent link between diffusion coefficient and porosity characteristic. For that reason, dynamic vapor sorption experiment was performed. Results are presented in the following section.

7.3 Dynamic vapor sorption (DVS)

To model carbonation, it is essential to link the diffusion coefficient versus porosity and water content in carbonated and non-carbonated samples. To obtain the water content as a function of different relative humidities DVS experiment was performed [56].

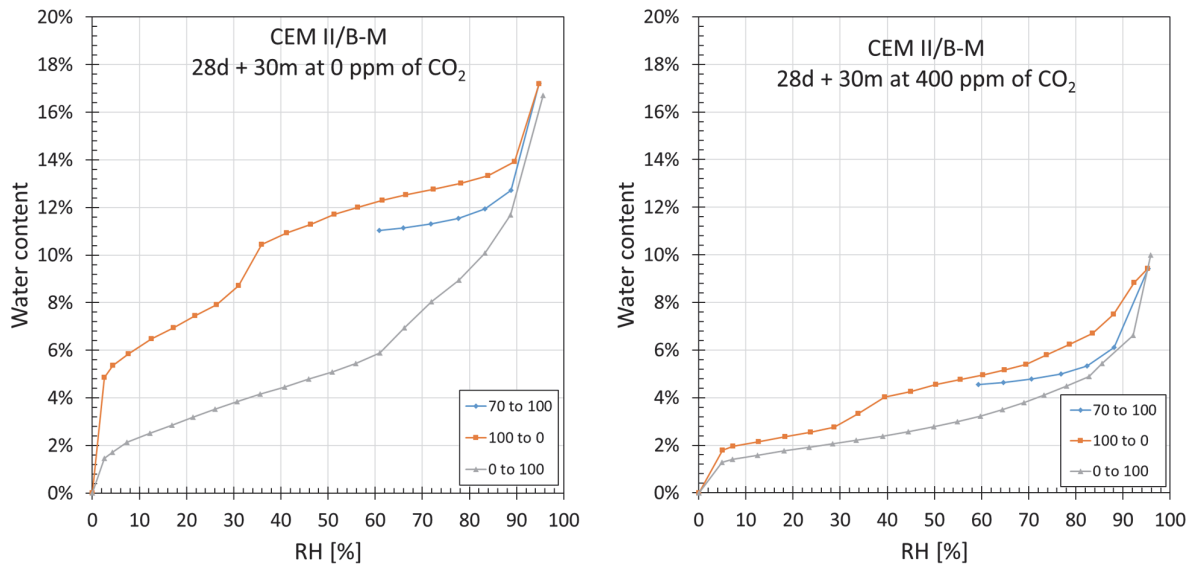


Figure 7-28. DVS of the CEM II/B-M, exposed to CO₂-free atmosphere (left) and to carbonation (right), at 70 % RH for 30 months after 28 days of curing.

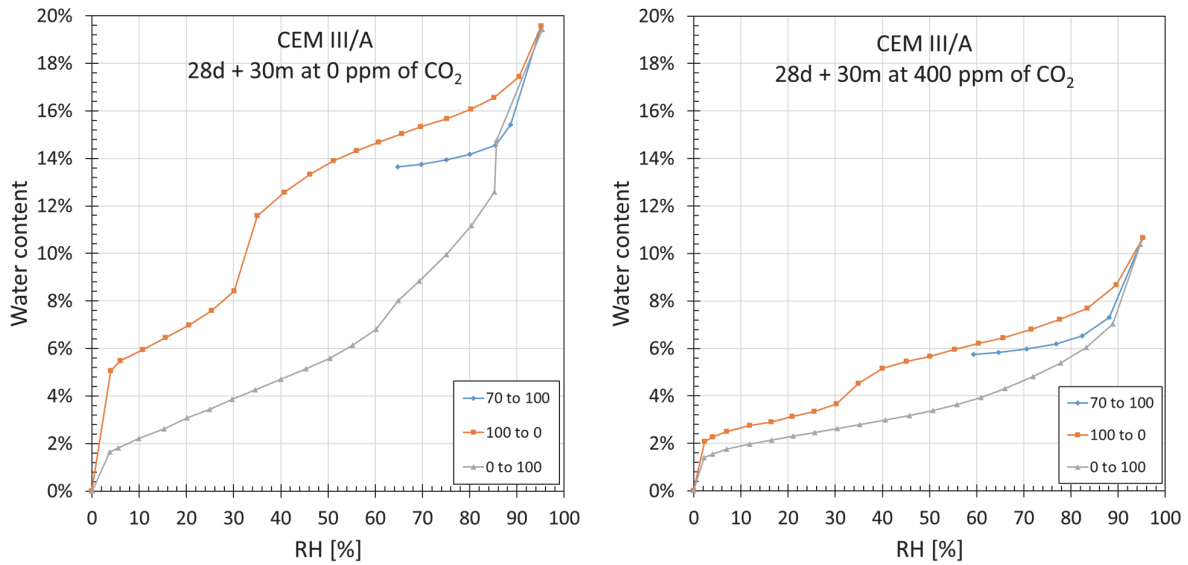


Figure 7-29. DVS of the CEM III/A, exposed to CO₂-free atmosphere (left) and to carbonation (right), at 70 % RH for 30 months after 28 days of curing.

Two blended cement systems were chosen to perform dynamic vapor sorption experiment. CEM II/B-M and CEM III/A cured for 28 days followed the exposure to carbonation at CO₂-free atmosphere. The RH for both exposure conditions was maintained at 70 %. After 30 months of exposure the samples were removed from the exposure environment, and without any pre-drying powdered sample was placed in the DVS chamber. The saturation from 70 % up to 100 % RH was done in the DVS equipment. Then, desorption until dry mass at 0 % RH was executed, to finally follow the adsorption up to 100 % RH.

We can see that, for both cement types, the water content of the carbonated sample is clearly lower than the water content of the samples exposed into the environment without CO₂. That is consistent with the lower total porosity measured by MIP presented at the beginning of this chapter. The lower water content for carbonated samples was observed along all RH range. The altering of the isotherms is a consequence of the pore size distribution modification. There is also an important decrease observed in the desorption curves between 40 % RH and 30 % RH which for DVS corresponds to the final loss of liquid water from C-S-H [113]. Moreover, the hysteresis between desorption and adsorption is much smaller for carbonated samples.

Unfortunately, due to a problem with calibration of the machine, the results for the moment can only be used qualitatively. Some missing data about the water content from the sensitive range between 95 % and 100 % RH are substantial, therefore current results do not allow for good normalization. Contrary to the results reported recently by Auroy [7], our sorption curves show much higher sensitivity in this RH range. Obtaining the desorption curve from 100 % RH is a promising perspective, as it would allow computing the saturated porosity, which would relate the pore size distribution to the effective diffusion coefficient.

7.4 Comparing the porosity changes with existing literature

Most of the existing literature shows that carbonation causes refinement of the porosity for OPC, yet it results in coarsening of the porosity for blended cements [114]. Litvan and Meyer [49] studied carbonation effect in 20 years old concrete from field exposure for CEM I and CEM III. They found that carbonation led to refinement of the CEM I, whereas coarser pores were affected for CEM III. A similar observation was concluded by Bier [83]. The study of Morandau [115] showed that carbonation causes a reduction in porosity for CEM I, whereas mixes with fly ash coarsened the porosity after carbonation. Auroy et al. [7] show porosity distribution for four different cements (see figure 11 in [7]). All mixes were made with w/c of 0.4 however curing was 3 months longer than in current study (in compare with 28 days cured systems). Refinement of porosity was reported for CEM I, and a blend with slag and fly ash, whereas for two other blends (slag blend and low pH blend) coarsening was observed after carbonation. Critical pore radius for CEM I decreased from 11 nm to 6 nm after carbonation. For slag blend, where coarsening was observed, critical pore radius increases from 10 to 18 nm. On the other hand, from Figure 5-3 (chapter 5) we can see that drying causes an increase of the critical pore radius from 11 nm to 28 nm for CEM I, and from 12 nm to 19 nm for slag blend. The competition between the two effects will depend on many aspects, for instance, w/c, curing time, cement composition or exposure conditions. However, the change induced by carbonation and by drying is in the same range. Therefore, the coarsening due to drying cannot be neglected.

Some of the past studies tried to decouple the effect of carbonation from drying. However, for different researchers, “non-carbonated” samples were obtained differently. Some took a reference after a long curing time, to ensure full hydration [7]. In that case, the changes in porosity attributed only to carbonation might be partially an effect of exposure in lower RH (70 %). Although the samples before exposure to carbonation test were equilibrated until reaching a stable mass, it does not ensure reaching a stable porosity. As shown in Figure 7-30, the exposure does not change the mass (values between 1 month and 6 months of exposure) and we know from Figure 5-2 and Figure 5-3, that at the same time the porosity is significantly altered. Although samples are only 1 mm thin, they show a significant difference in porosity distribution during 12 months of exposure. Moreover, the porosity distribution of the thin disk, and the porosity examined in the non-carbonated zone of the cylinder exposed to carbonation are remarkably close. They indicate that this is a true physical phenomenon and not just an effect of the sample geometry. Some researchers report unchanged porosity during exposure in lower RH, however, the specimen for testing was taken 27-30 mm away from the surface [114]. Drying most probably has not reached that depth in the given time period (16 weeks). In other studies, a non-carbonated specimen was also extracted from the core of the carbonating specimen [116]. In those cases, drying effect is not deconvoluted from carbonation.

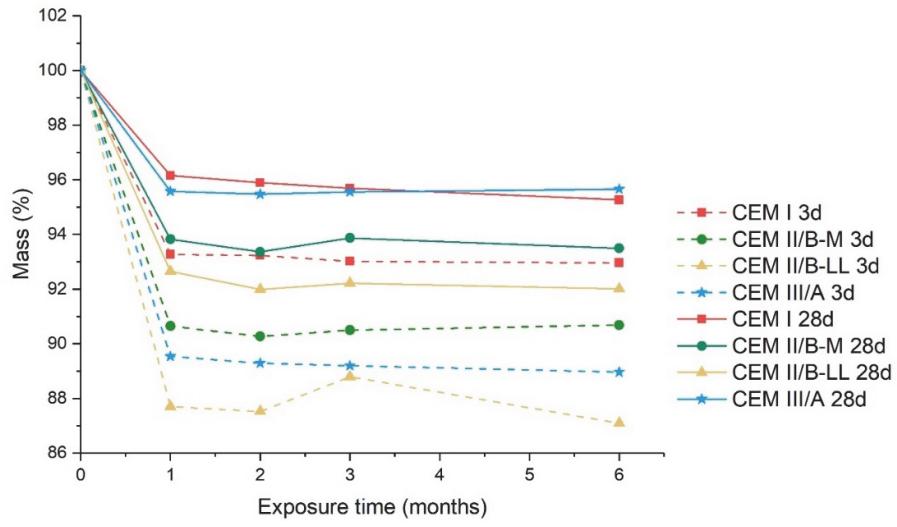


Figure 7-30. Mass dependence during 6 months exposure at 70 % RH in CO₂-free atmosphere for all studied cements.

Chapter 8 Conclusions and perspectives

Many processes impact the rate of carbonation and therefore impact how the microstructure of cement paste is modified due to carbonation. These changes in turn affect the transport properties of carbon dioxide through this microstructure. This work focused on the investigation of the changes that happen due to carbonation in OPC and in low carbon binders during carbonation. The results obtained in this work help to better understand the reactive transport process of carbonation, and to advance the field of carbonation modeling, which in a global perspective will contribute to a more accurate prediction of the service life of real concrete structures.

The results presented in chapter 4 show how carbonation resistance is influenced by the design of the concrete, including binder composition, water to cement ratio, curing time before exposure, and by exposure conditions itself, particularly relative humidity which plays a big role. The case study performed in accelerated condition questions the carbonation tests where the concentration of CO_2 is increased. Although accelerated tests are the most widely used approaches due to their relatively short duration, we must be aware that such tests can change the mechanism of carbonation. These modifications impact the changes in microstructure, which governs transport properties in the concrete exposed to atmospheric CO_2 .

In the existing carbonation literature many different approaches are used to prepare reference samples that can lead to incorrectly interpret the effect of carbonation. Most past research studies into the effect of carbonation on porosity neglected the effect of relative humidity alone on the porosity changes, and they attribute the findings only to carbonation. This has resulted in some contradictory conclusions. This study sheds a new light on the problem of overestimating the effect of carbonation on the microstructure of the cementitious material and shows the importance of subtracting the effect of the drying during carbonation to describe the effect of carbonation on microstructure. Moreover, it is remarkable that the porosity distribution of the thin disk exposed to CO_2 -free atmosphere at 70 % RH, and the one examined in the non-carbonated zone of the sample exposed to carbonation are in the same range. They indicate that this is a real physical phenomenon and not just an effect of the sample geometry. It means that the use of the thin disk is representative of real conditions taking place on the non-carbonated side of the carbonation front. Furthermore, studying the microstructure of the hydrates exposed in an environment with lower relative humidity in the absence of CO_2 using high-resolution microscopy confirmed, that the coarsening effect observed by MIP is not only a distorted result of overestimating the big pore size (often attributed to the interpretation of the method) but a real phenomenon.

Changes to the phase assemblage during exposure to carbonation were intensively studied in chapter 6. In addition to the calculation of the contribution of the individual hydrates dissolution to calcium carbonate precipitation, the degree of carbonation for different binders was also presented. Moreover, results on carbonation resistance obtained on the new type of ternary blend with the clinker-substitution level of 50 %, reached by using limestone, burnt oil shale, and slag, show promising performance against carbonation. Therefore, they can effectively contribute to the decrease of CO₂ emission during cement production and they can make the concrete an even more environmentally friendly material.

Most of the systems studied here showed that portlandite can be completely depleted. Therefore, our results led to the argument against the theory that the hindered dissolution of Ca(OH)₂ can be explained by the diffusion barrier, which proposes that a dense coating forms around partially reacted Ca(OH)₂ limits accessibility to portlandite [37][36][99][46]. It is a proposed explanation to the common observation that after a period of a relatively rapid consumption of portlandite, its carbonation rate is significantly reduced [40], and other hydrates, such as C-S-H or ettringite starts to carbonate in spite portlandite is still in the system.

For two systems studied here (CEM I and MixSL with w/c=0.35, cured 28 days) our quantitative results of phase assemblage show that portlandite does not deplete completely, and carbonation seems stopped in the time scale of the experiment. Three possible scenarios related with thermodynamic limitation could explain the stability of portlandite in our carbonated materials: (i) lack of space for calcite to precipitate, (ii) not enough CO₂ has diffused to the reaction front, (iii) preferential diffusion paths, leading to inhomogeneous carbonation. The results obtained here support the lack of space theory, which could be explained by the refinement of the porosity during carbonation. When the pore structure gets refined, the calcium concentration required for calcite precipitation becomes higher and higher. It means that at some point portlandite becomes more stable than the calcite and, the carbonation is effectively stopped (as well illustrated in Figure 6-13 in chapter 6). When the portlandite is stable then the other hydrates (i.e. ettringite) will also be stable (as seen in our quantitative analysis). If a diffusion barrier would exist, then those phases would dissolve further to maintain the alkalinity of the pore solution to keep a high pH. Therefore, the statement of formation of the thin layer around the portlandite crystals inhibiting its dissolution [99][36][46] might have to be rediscussed and often stated conclusions that all phases tend to carbonate simultaneously [24][28][42] might not be a good interpretation of the carbonation reaction. Moreover, it was shown that the carbonation front is sharp but tortuous. It can often lead to a wrong interpretation that carbonation does not exhibit a sharp front. It allows to reinterpret carbonation experiments and the importance of kinetics.

The fact that the local equilibrium during carbonation seems to be respected is quite important for the carbonation models:

- The portlandite needs to be consumed before further changes can happen.

- No diffusion-barrier mechanism (caused by forming a dense layer around portlandite grains prohibiting its dissolution) takes place if portlandite is still present, which will control pH and calcium of the pore solution.
- Dissolution of ettringite and unreacted clinker phase is possible, but after the portlandite is depleted.
- Including CaO from unreacted clinker in $\text{CaO}_{\text{reactive}}$ is the correct approach, since it will participate in the carbonation reaction.
- If the lack of space theory is correct, then the thermodynamic models need to be linked to the evolution of the pore size distribution.

Finally, it was shown how important it is to characterize the transport properties in the carbonated materials. Results on gas diffusion obtained by using a new approach of thin paste samples in the diffusion cell showed how drastically diffusion coefficient can change for carbonated materials. This data is extremely important for carbonation models. They also show that changes in the diffusion parameters during carbonation are very sensitive to different binders composition. Much data published on diffusion properties were characterized on non-carbonated samples. All those results are important but they become less relevant for durability assessment, due to disregarding the fact that concrete structures are exposed to carbonation and their microstructure change due to the presence of carbon dioxide in the atmosphere.

The quantitative analysis helped to create a new set of data for reactive transport models built by combining chemistry, microstructure, and a transport module. Our studies demonstrated that the focus on the paste scale does provide real advantages in the study of the real-world problems concerning the durability issues in concrete.

In general, studies on carbonation should be focused on better understanding of the phases that are formed upon natural carbonation. It will help to decide the accelerated tests compatible with natural conditions. This compatibility will allow the extrapolation of the accelerated tests to natural conditions.

The diffusion coefficients measured in this study were correlated with the porosity distribution obtained from MIP analysis. This method gives us a first approximation about the dependence of transport properties on diffusion properties. However, complementary data on saturated porosity is needed to better correlate the changes of the diffusion properties with porosity properties. DVS seems to be a promising method to complete the missing information about the saturated porosity and to give a full picture of the data needed to assess the carbonation resistance in various cement types. Alternatively, the use of ^1H NMR could also be a useful method, that could help to characterize changes in the saturated porosity after carbonation.

Studying the carbonated microstructure with high-resolution microscopy highlighted the problem of the porosity coarsening due to exposure at lower relative humidity. The use of high-resolution microscopy could only provide a semi-quantitative analysis. Use of another method, giving a full 3D information about pore

structure in the cement microstructure, could help to fully understand the coarsening phenomenon and verify our theory about C-S-H diverging due to conservation in lower relative humidity.

The finding about higher sulphate concentration at the carbonation front confirms the thermodynamic prediction which is quite remarkable. Verifying if the sulphate precipitate as an ettringite phase could help to better understand if it contributes to decreasing the porosity. Use of microscopy setting with higher resolution would be a first assessment of the correctness of this theory.

Overall, the results obtained advance the understanding of carbonation mechanism. They show important aspects which should be considered in carbonation modeling, such as:

- Precipitation of different calcium polymorphs, which influence the space filling during carbonation, that finally have an influence on porosity and diffusion properties
- Characterization of the diffusion properties in carbonated cement paste, as the diffusion of CO_2 is through the carbonated layer and the reaction front.
- Understanding the diffusion of the sulphate into the carbonation front, which might contribute to porosity clogging.
- “Lack of space” theory, that could help to understand the influence of the porosity refinement on stopping of the carbonation progress.

Implementing those findings in carbonation models can improve the prediction of the long-term durability of daily used concrete structures. The profit will be to make the cement and concrete even more sustainable and more environmentally friendly material.

Appendix A

Composition of C-S-H

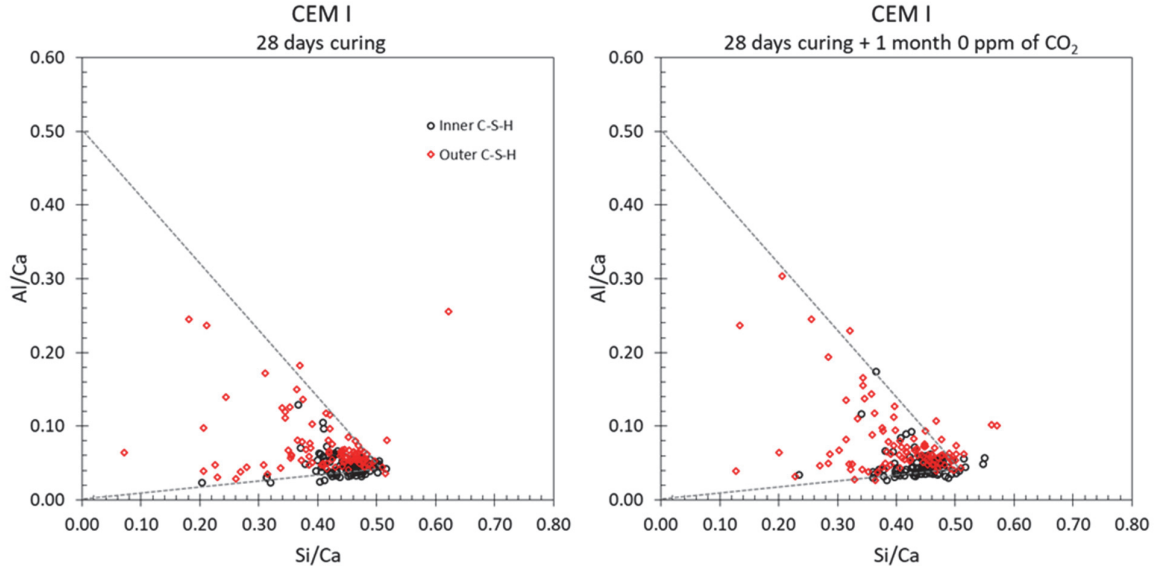


Figure A-8-1. C-S-H composition studied by SEM-EDS for CEM I cured for 28 days (A) and then exposed at 70 % RH in CO₂-free atmosphere for 1 month (B).

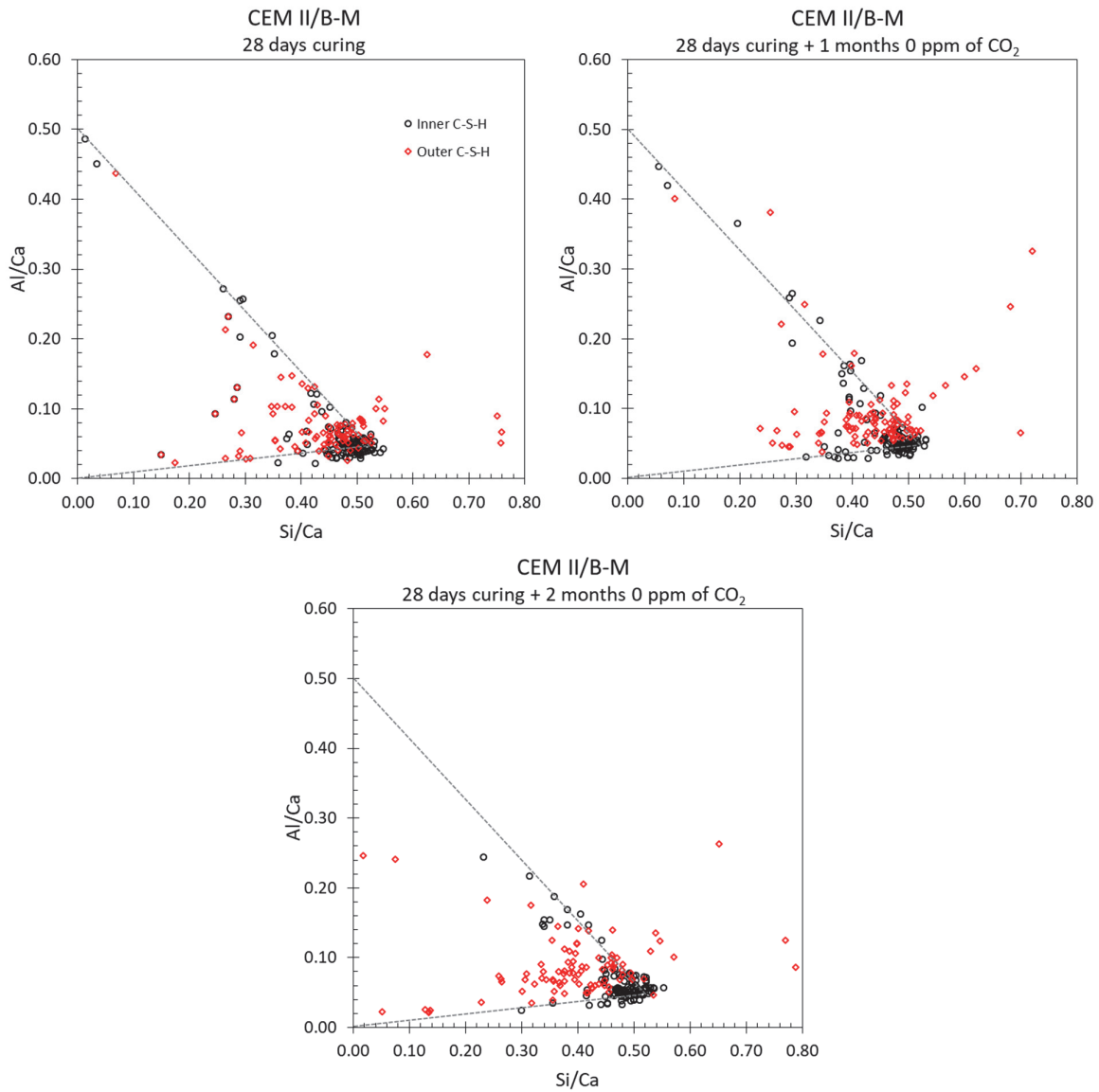


Figure A-8-2. C-S-H composition studied by SEM-EDS for CEM II/B-M cured for 28 days (A) and then exposed at 70 % RH in CO₂-free atmosphere for 1 month (B) and 2 months (C).

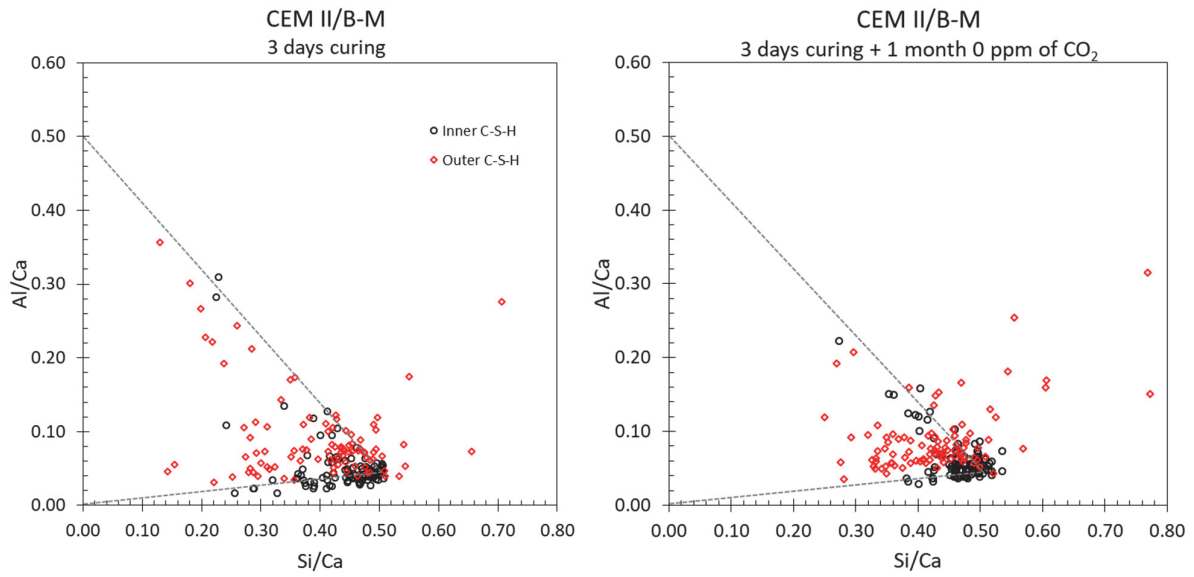


Figure A-8-3. C-S-H composition studied by SEM-EDS for CEM II/B-M cured for 3 days (A) and then exposed at 70 % RH in CO₂-free atmosphere for 1 month (B).

Appendix B

XRD diffractograms during exposure to carbonation

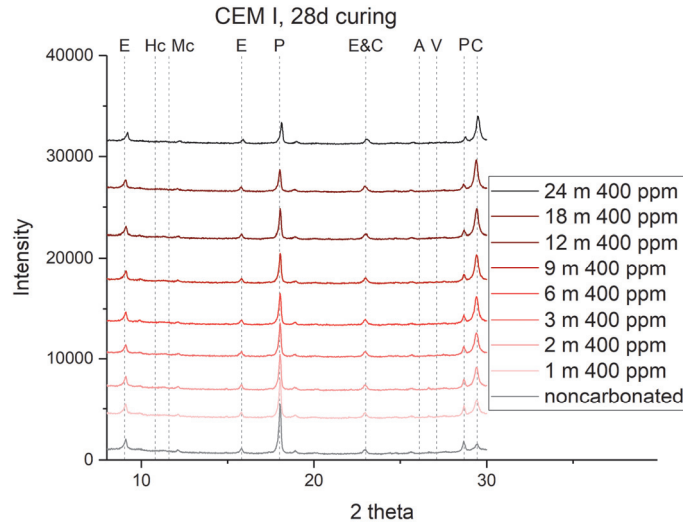


Figure B-1. XRD plots of CEM I during 2 years of exposure to natural carbonation after 28 days of curing; E-ettringite, Hc-hemicarboaluminate, Mc-monocarboaluminate, P-portlandite, A-Aragonite, V-vaterite, C-calcite.

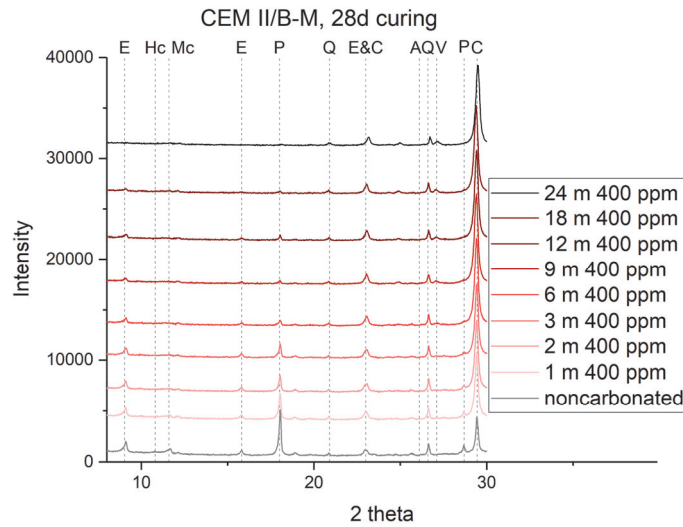


Figure B-2. XRD plots of CEM II/B-M during 2 years of exposure to natural carbonation after 28 days of curing; E-ettringite, Hc-hemicarboaluminate, Mc-monocarboaluminate, P-portlandite, A-Aragonite, V-vaterite, C-calcite.

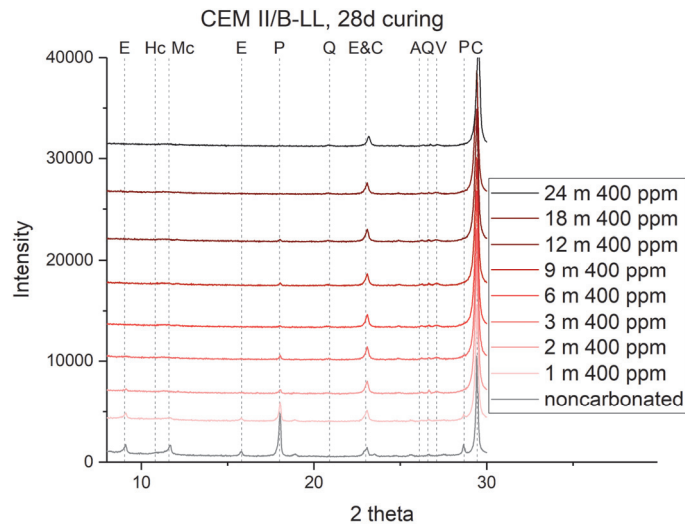


Figure B-3. XRD plots of CEM II/B-LL during 2 years of exposure to natural carbonation after 28 days of curing; E-ettringite, Hc-hemicarboaluminate, Mc-monocarboaluminate, P-portlandite, A-Aragonite, V-vaterite, C-calcite.

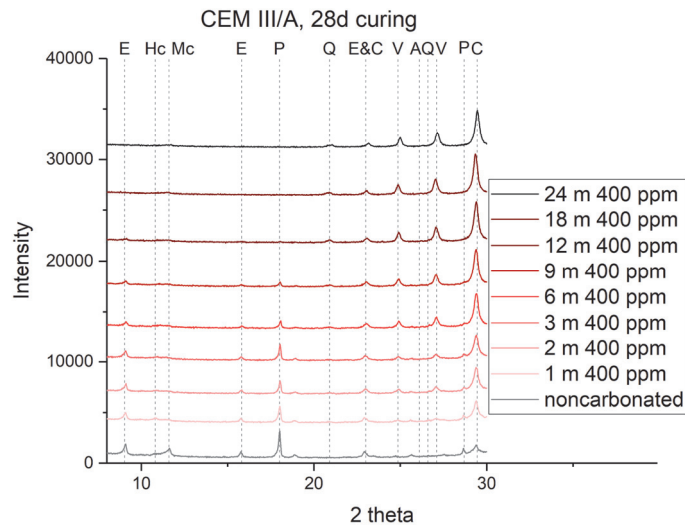


Figure B-4. XRD plots of CEM III/A during 2 years of exposure to natural carbonation after 28 days of curing; E-ettringite, Hc-hemicarboaluminate, Mc-monocarboaluminate, P-portlandite, A-Aragonite, V-vaterite, C-calcite.

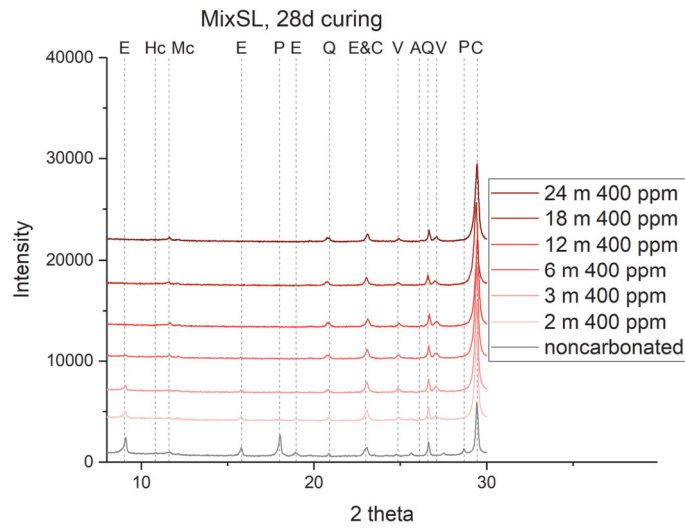


Figure B-5. XRD plots of MixSL during 2 years of exposure to natural carbonation after 28 days of curing; E-ettringite, Hc-hemicarboaluminate, Mc-monocarboaluminate, P-portlandite, A-Aragonite, V-vaterite, C-calcite.

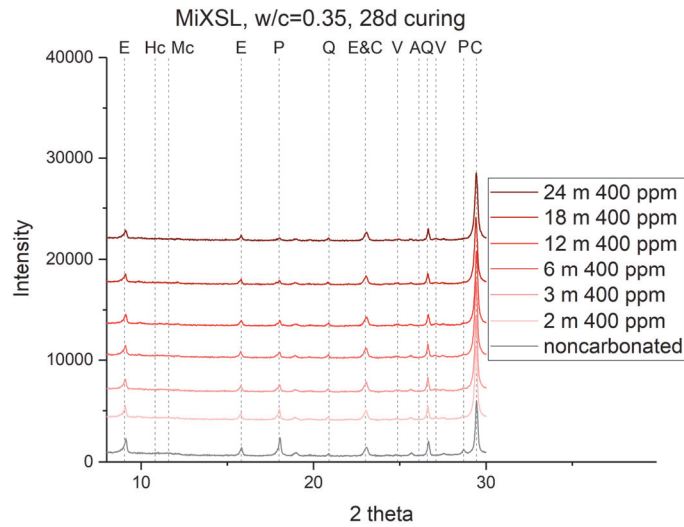


Figure B-6. XRD plots of MixSL, w/c=0.35 during 2 years of exposure to natural carbonation after 28 days of curing; E-ettringite, Hc-hemicarboaluminate, Mc-monocarboaluminate, P-portlandite, A-Aragonite, V-vaterite, C-calcite.

Appendix C

Porosity characteristics during exposure to carbonation

Table C-1. Total porosity, critical pore radius and entry pore radius changes due to exposure to carbonation in a function of cement type and curing time.

Cement type	Curing time before exposure (days)	CO ₂ concentration at 70 % RH	Total porosity (%)	Critical pore radius (μm)	Entry pore radius (μm)
CEM I	3	t ₀ =3d curing	24.56	13.9	21.26
		t ₀ + 12m 0 ppm	21.5	48	62
		t ₀ + 12m 400 ppm	14	16.2	38
	28	t ₀ =28d curing	19.7	11.3	17
		t ₀ + 12m 0 ppm	17.2	27.6	41
		t ₀ + 24m 400 ppm	12.5	9.1	16
CEM II/B-M	3	t ₀ =3d curing	27.5	18.8	31
		t ₀ + 12m 0 ppm	25	56.5	86
		t ₀ + 12m 400 ppm	15.4	11.6	48
	28	t ₀ =28d curing	23.5	12.8	19
		t ₀ + 24m 0 ppm	21.5	39	58
		t ₀ + 24m 400 ppm	15	11.8	23
CEM II/B-LL	3	t ₀ =3d curing	33.5	35.3	58
		t ₀ + 12m 0 ppm	24.4	87	226
		t ₀ + 12m 400 ppm	21.3	74	109
	28	t ₀ =28d curing	26.4	12.4	19
		t ₀ + 12m 0 ppm	24.4	52	74
		t ₀ + 12m 400 ppm	18.3	40.1	45
CEM III/A	3	t ₀ =3d curing	24.1	23.9	40.8
		t ₀ + 12m 0 ppm	25.3	57	88
		t ₀ + 12m 400 ppm	21.6	73	118
	28	t ₀ =28d curing	23.8	11.4	17.5
		t ₀ + 12m 0 ppm	18.8	19	31
		t ₀ + 12m 400 ppm	13.7	13.1	28
MixSL	28	t ₀ =28d curing	22.9	9.8	15
		t ₀ + 18m 0 ppm	20.9	19.7	36
		t ₀ + 18m 400 ppm	21.4	25.1	40
MixSL w/c=0.35	3	t ₀ =3d curing	24.3	15.0	20
		0 ppm	19.9	22.8	32
		400 ppm	17.2	20	45
	28	t ₀ =28d curing	19.2	7.5	12
		0 ppm	15.9	9.9	17
		400 ppm	14.4	11.3	37

Appendix D Code for obtaining the diffusion coefficient

```
#Copyright (c) 2018, 2019 Fabien Georget <fabien.georget@epfl.ch>, EPFL
#All rights reserved.
#
#Redistribution and use in source and binary forms, with or without
#modification, are permitted provided that the following conditions are met:
#
#1. Redistributions of source code must retain the above copyright notice, this
#list of conditions and the following disclaimer.
#
#2. Redistributions in binary form must reproduce the above copyright notice,
#this list of conditions and the following disclaimer in the documentation
#and/or other materials provided with the distribution.
#
#3. Neither the name of the copyright holder nor the names of its contributors
#may be used to endorse or promote products derived from this software without
#specific prior written permission.
#
# THIS SOFTWARE IS PROVIDED BY THE COPYRIGHT HOLDERS AND CONTRIBUTORS "AS IS"
# AND ANY EXPRESS OR IMPLIED WARRANTIES, INCLUDING, BUT NOT LIMITED TO, THE
# IMPLIED WARRANTIES OF MERCHANTABILITY AND FITNESS FOR A PARTICULAR PURPOSE
# ARE DISCLAIMED. IN NO EVENT SHALL THE COPYRIGHT HOLDER OR CONTRIBUTORS BE
# LIABLE FOR ANY DIRECT, INDIRECT, INCIDENTAL, SPECIAL, EXEMPLARY, OR
# CONSEQUENTIAL DAMAGES (INCLUDING, BUT NOT LIMITED TO, PROCUREMENT OF
# SUBSTITUTE GOODS OR SERVICES; LOSS OF USE, DATA, OR PROFITS; OR BUSINESS
# INTERRUPTION) HOWEVER CAUSED AND ON ANY THEORY OF LIABILITY, WHETHER IN
# CONTRACT, STRICT LIABILITY, OR TORT (INCLUDING NEGLIGENCE OR OTHERWISE)
# ARISING IN ANY WAY OUT OF THE USE OF THIS SOFTWARE, EVEN IF ADVISED OF THE
# POSSIBILITY OF SUCH DAMAGE.

"""Module to analyse O2 diffusion cell results.

Usage:
>>> geometry = get_default_geometry()
>>> # change geometry if needed
>>> fit_experiment(<filename.csv>, geometry, calib=None, verbose=True)

<filename.csv> is a csv file with the experimental data:
- 2 columns separated by comma or semi-colon
- 1st: time (h), 2nd: O2 in N2 content (%)
- 1 line of header

If calib (scalar) is provided, the data is normalized with respect to that value.
"""

import numpy as np
import matplotlib.pyplot as plt
import scipy.optimize as sco
import scipy.signal as ssi

def get_default_geometry():
    """Return the default EPFL-LMC cell geometry"""
    data = {
        "thickness_sample": 0.1, # cm
        "length_chamber": 8.167, # cm
        "c_ext": 21.0, # ambient O2 in N2
        "diameter_sample": 3.0, #cm
        "diameter_chamber": 3.0 #cm
    }

    return data

def get_lafarge_geometry():
    """Return the default LCR (LafargeHolcim) geometry"""
    data = {
```

```

        "thickness_sample": 0.1, # cm
        "length_chamber": 9.0, # cm
        "c_ext": 21.0, # ambient O2 in N2
        "diameter_sample": 3.0, #cm
        "diameter_chamber": 4.0 #cm
    }

    return data

def get_new_setup_geometry():
    """Return the default EPFL-LMC cell geometry"""
    return get_default_geometry()

def get_geometry(setup, thickness):
    """Return a geometry by name

    :param setup: name of the setup
    :param thickness: thickness of the sample
    """
    if setup=="new_epfl_setup":
        data=dict(get_new_setup_geometry())
        data["thickness_sample"]=thickness
        return data
    elif setup=="lafarge_setup":
        data=dict(get_lafarge_geometry())
        data["thickness_sample"]=thickness
        return data
    else:
        raise ValueError("Unknown setup: {}".format(setup))

def get_func_diffusion(c0, geometry):
    """Analytical solution to the diffusion equation through the sample"""
    dx_s_dx_c = geometry["thickness_sample"]*geometry["length_chamber"]
    ratio_d_square = (geometry["diameter_sample"]/geometry["diameter_chamber"])**2
    c_ext = geometry["c_ext"]

    def diffusion(xts,diffusion_sample):
        ys=[c0]
        for i in range(1, len(xts)):
            dt = xts[i]-xts[i-1]
            factor = dt*float(diffusion_sample)*ratio_d_square/(dx_s_dx_c)
            y = 1.0/float((1.0+factor))* (ys[i-1]+factor*c_ext)
            ys.append(y)
        return ys
    return diffusion

def extract_from_csv(filename, c_ext, calib=None, remove_bad_data=True):
    """Obtain the experimental data from the CSV.

    :param filename: csv file
    :param c_ext: O2 in air
    :param calib: (float) O2 in air as read by the sensor
    :param remove_bad_data: if true, filter bad data (nan, and anomalous peaks)
    """
    try:
        exp_data = np.genfromtxt(filename, delimiter=";", skip_header=1, usecols=(0,1))
    except ValueError:
        exp_data = np.genfromtxt(filename, delimiter=";", skip_header=1, usecols=(0,1))

    if remove_bad_data:
        exp_data = exp_data[~np.isnan(exp_data[:,1]),:]
        peaks, other = ssi.find_peaks(exp_data[:,1], 1, distance=100, prominence=0.1)
        w, inter, ips1, ipsr = ssi.peak_widths(exp_data[:,1], peaks, rel_height=1)
        index_to_removes = []
        for ind,peak in enumerate(peaks):

```



```

        index_to_removes.extend(np.arange(max(int(peak-w[ind]),0),
min(int(peak+w[ind]),len(exp_data)-1),1))
        exp_data=exp_data[[i for i in range(len(exp_data[:,0])) if i not in index_to_re-
moves],:]

    exp_data[:,0] -= exp_data[0, 0] # start at t = 0
    exp_data[:,0] *= 3600          # transform time unit : h -> s

    if calib is None:
        calib = exp_data[-1, 1]

    exp_data[:,1] *= c_ext/calib # normalize data

    if exp_data[0,0] != 0.0:
        exp_data[:,0] -= exp_data[0,0]

    return exp_data

def fit_experiment(filename,geometry,calib=None,verbose=True,remove_bad_data=True):
    """Back calculate the diffusion coefficient from an experiment given a
    geometry.

    :param filename: csv file containing the data
    :param geometry: geometry of the cell and the sample
    :param calib: O2 in N2 as read by the sensor (if None, read from the last value)
    :param verbose: if True, plot the experimetnal datapoints and the fit
    :param remove_bad_data: if True, remove NaN and anomalous peaks in data

    """
    exp_data = extract_from_csv(filename, geometry["c_ext"], calib, remove_bad_data=re-
move_bad_data)
    xts = exp_data[:,0]
    ys = exp_data[:,1]

    func = get_func_diffusion(ys[0],geometry)
    popt, pcov = sco.curve_fit(func,xts,ys,p0=1e-4)

    De = popt[0]
    perr = np.sqrt(pcov[0])[0]
    if verbose:
        print("Analysis for {0}: \n - De = {1:.3e} cm^2/s\n - perr = {2:.3e}".for-
mat(filename, popt[0], perr))

    fitted_ys = func(xts, popt[0])

    if verbose:
        plt.plot(xts/3600, ys, ".", label=filename)
        plt.plot(xts/3600, fitted_ys, "-", label="fit")
        plt.xlabel("time (h)")
        plt.ylabel("O2 in N2 (%)")
        plt.legend()

    return ((De, perr), (xts/3600, ys, fitted_ys))

```

Link for the online version:

<https://bitbucket.org/specmicp/nonsteadydiffusiocell/src/964fdac47b714f176be7a2a87c6274dac3fcb683?at=master>

References

1. Metz, B., Davidson, O., de Coninck, H., Loos, M. & Meyer, L. *IPCC Special Report on Carbon Dioxide Capture and Storage*. IPCC (2005).
2. European standards. En 197-1. 1–29 (2000).
3. Scrivener, K., John, V. & Gartner, E. Eco-efficient cements: Potential economically viable solutions for a low-CO₂ cement-based materials industry. (2016).
4. Papadakis, V. G., Fardis, M. N. & Vayenas, C. G. Effect of composition, environmental factors and cement-lime mortar coating on concrete carbonation. *Mater. Struct.* **25**, 293–304 (1992).
5. Neville, A. M. *Properties of Concrete*. *Journal of General Microbiology* **Fourth**, (1996).
6. Steefel, C., And, K. M.-R. in M. & 1996, U. Approaches to modeling of reactive transport in porous media. *GeoScienceWorld*
7. Auroy, M. *et al.* Impact of carbonation on unsaturated water transport properties of cement-based materials. *Cem. Concr. Res.* **74**, 44–58 (2015).
8. Georget, F., Prévost, J. H. & Huet, B. Impact of the microstructure model on coupled simulation of drying and accelerated carbonation. *Cem. Concr. Res.* **104**, 1–12 (2018).
9. Antoni, M. Investigation of cement substitution by blends of calcined clays and limestone. (2013).
10. Harrison, T. A., Jones, M. R., Newlands, M. D., Kandasami, S. & Khanna, G. Experience of using the prTS 12390-12 accelerated carbonation test to assess the relative performance of concrete. *Mag. Concr. Res.* **64**, 737–747 (2012).
11. Boumaaza Huet G Pham P Turcry A At-Mokhtar C Gehlen, M. B. A new test method to determine the gaseous oxygen diffusion coefficient of cement pastes as a function of hydration duration, microstructure, and relative humidity. *Mater. Struct.* **51:51**, (2018).
12. J. Hilger. in *Oil shale* 347–355 (2003).
13. Stefanoni, M. The corrosion of steel in near-neutral porous media - Corrosion rate in carbonated concrete. (2018).
14. Plummer, L. N. & Busenberg, E. The solubilities of calcite, aragonite and vaterite in CO₂-H₂O solutions between 0 and 90°C, and an evaluation of the aqueous model for the system CaCO₃-CO₂-H₂O. *Geochim. Cosmochim. Acta* **46**, 1011–1040 (1982).
15. Morandea, A., Morandea, A. & Morandea, A. Carbonatation atmosphérique des systèmes cimentaires à faible teneur en portlandite To cite this version : par Carbonatation atmosphérique des systèmes cimentaires à faible teneur en portlandite. (2014).
16. Saetta, A. V., Schrefler, B. A. & Vitaliani, R. V. The carbonation of concrete and the mechanism of moisture, heat and carbon dioxide flow through porous materials. *Cem. Concr. Res.* **23**, 761–772 (1993).
17. Houst, Y. F. The role of moisture in the carbonation of cementitious materials. *Int. J. Restor. Build. Monum.* **2**, 49–66 (1996).
18. Houst, Y. F., Houst, Y. F., Wittmann, F. H. & Wittmann, F. H. Depth profiles of carbonates formed during natural carbonation. *Cem. Concr. Res.* **32**, 1923–1930 (2002).
19. Johannesson, B. & Utgenannt, P. Microstructural changes caused by carbonation of cement mortar. *Cem. Concr. Res.* **31**, 925–931 (2001).
20. Emeritus, T. & Taylor, H. F. W. Cement chemistry. *Cem. Concr. Compos.* **20**, 335 (1998).
21. Glasser, F. P., Marchand, J. & Samson, E. Durability of concrete - Degradation phenomena involving detrimental chemical reactions. *Cem. Concr. Res.* **38**, 226–246 (2008).

22. Antoni, M., Rossen, J., Martirena, F. & Scrivener, K. Cement substitution by a combination of metakaolin and limestone. *Cem. Concr. Res.* **42**, 1579–1589 (2012).
23. Bier, T. Influence of type of cement and curing on carbonation progress and pore structure of hydrated cement paste. *Mater. Res. Soc. Symp.* (1987).
24. Groves, G. W., Rodway, D. I. & Richardson, I. G. The carbonation of hardened cement pastes. *Adv. Cem. Res.* **3**, 117–125 (1990).
25. Black, L. *et al.* Structural features of C-S-H(I) and its carbonation in air-A Raman spectroscopic study. Part II: Carbonated phases. *J. Am. Ceram. Soc.* **90**, 908–917 (2007).
26. Black, L., Garbev, K. & Gee, I. Surface carbonation of synthetic C-S-H samples: A comparison between fresh and aged C-S-H using X-ray photoelectron spectroscopy. *Cem. Concr. Res.* **38**, 745–750 (2008).
27. Morales-Florez, V., Findling, N. & Brunet, F. Changes on the nanostructure of cementitious calcium silicate hydrates (C–S–H) induced by aqueous carbonation. *J. Mater. Sci.* **47**, 764–771 (2012).
28. Villain, G., Thiery, M. & Platret, G. Measurement methods of carbonation profiles in concrete: Thermogravimetry, chemical analysis and gammadensimetry. *Cem. Concr. Res.* **37**, 1182–1192 (2007).
29. Šauman, Z. Carbonization of porous concrete and its main binding components. *Cem. Concr. Res.* **1**, 645–662 (1971).
30. Georget, F., Prévost, J. H. & Vanderbei, R. J. A speciation solver for cement paste modeling and the semismooth Newton method. *Cem. Concr. Res.* **68**, 139–147 (2015).
31. Gabrisová, A., Havlica, J. & Sahu, S. Stability of calcium sulphoaluminate hydrates in water solutions with various pH values. *Cem. Concr. Res.* **21**, 1023–1027 (1991).
32. Nishikawa, T., Suzuki, K., Ito, S., Sato, K. & Takebe, T. Decomposition of synthesized ettringite by carbonation. *Cem. Concr. Res.* **22**, 6–14 (1992).
33. Xiantuo, C., Ruizhen, Z. & Xiaorong, C. Kinetic study of ettringite carbonation reaction. *Cem. Concr. Res.* **24**, 1383–1389 (1994).
34. Zhou, Q. & Glasser, F. P. Kinetics and mechanism of the carbonation of ettringite. *Adv. Cem. Res.* **12**, 131–136 (2000).
35. Castellote Lorenzo Fernandez AE Carmen Andrade AE Cruz Alonso, M. A. Chemical changes and phase analysis of OPC pastes carbonated at different CO₂ concentrations. (2008).
36. Groves, G. W., Brough, A., Richardson, I. G. & Dobson, C. M. Progressive Changes in the Structure of Hardened C3S Cement Pastes due to Carbonation. *J. Am. Ceram. Soc.* **74**, 2891–2896 (1991).
37. Thiery, M., Villain, G., Dangla, P. & Platret, G. Investigation of the carbonation front shape on cementitious materials: Effects of the chemical kinetics. *Cem. Concr. Res.* **37**, 1047–1058 (2007).
38. Galan, I., Glasser, F. P., Baza, D. & Andrade, C. Assessment of the protective effect of carbonation on portlandite crystals. *Cem. Concr. Res.* **74**, 68–77 (2015).
39. Hidalgo, A. *et al.* Microstructural changes induced in Portland cement-based materials due to natural and supercritical carbonation. *J. Mater. Sci.* **43**, 3101–3111 (2008).
40. Dunster, A. M. An investigation of the carbonation of cement paste using trimethylsilylation. *Adv. Cem. Res.* **2**, 99–106 (1989).
41. Shi, Z. *et al.* Experimental studies and thermodynamic modeling of the carbonation of Portland cement, metakaolin and limestone mortars. *Cem. Concr. Res.* **88**, 60–72 (2016).
42. Morandau, A., Thiéry, M. & Dangla, P. Investigation of the carbonation mechanism of CH and C-S-H in terms of kinetics, microstructure changes and moisture properties. *Cem. Concr. Res.* **56**, 153–170 (2014).

43. Leemann, A., Nygaard, P., Kaufmann, J. & Loser, R. Relation between carbonation resistance, mix design and exposure of mortar and concrete. *Cem. Concr. Compos.* **62**, 33–43 (2015).
44. Leemann Fabrizio Moro, A. Carbonation of concrete: the role of CO₂ concentration, relative humidity and CO₂ buffer capacity. *Mater. Struct.* **50:30**, (2017).
45. Balonis, M. & Glasser, F. P. The density of cement phases. *Cem. Concr. Res.* **39**, 733–739 (2009).
46. Šavija, B. & Luković, M. Carbonation of cement paste: Understanding, challenges, and opportunities. *Constr. Build. Mater.* **117**, 285–301 (2016).
47. Houst, Y. F. Microstructural changes of hydrated cement paste due to carbonation. *Int. J. Restor. Build. Monum.* **2**, 49–66 (1996).
48. Houst, Y. & Wittmann, F. Influence of porosity and water content on the diffusivity of CO₂ and O₂ through hydrated cement paste. *Cem. Concr. Res.* **24**, 1165–1176 (1994).
49. Litvan, G. G. & Meyer, A. Carbonation of granulated blast furnace slag cement concrete during twenty years of field exposure. *Proc. 2nd Int. Conf. Fly, Ash, Silica Fume, Slag, Nat. Pozzolans Concr.* **N91**, 1445–1462 (1986).
50. Ngala, V. & Page, C. Effects of carbonation on pore structure and diffusional properties of hydrated cement pastes. *Cem. Concr. Res.* **27**, 995–1007 (1997).
51. Claisse, P. A. in *Transport Properties of Concrete* 1–16 (2014).
52. Fick, A. On Liquid Diffusion. *Philos. Mag. Ser. 4* **10**, 30–39 (1855).
53. Nilsson, L. & Fridh, K. *Division of Building Materials CO₂-cycle in cement and concrete Part 1 : Examination of a previous NIC-project Part 2 : Further literature study on mechanisms / models.* (2009).
54. Mason, E. & Malinauskas, A. Gas transport in porous media: the dusty-gas model. (1983).
55. Rimmelé, G., Barlet-Gouédard, V., Porcherie, O., Goffé, B. & Brunet, F. Heterogeneous porosity distribution in Portland cement exposed to CO₂-rich fluids. *Cem. Concr. Res.* **38**, 1038–1048 (2008).
56. Johannesson, È. & Utgenannt, P. Microstructural changes caused by carbonation of cement mortar. **31**, 925–931 (2001).
57. Kurdowski, W. in *Cement and Concrete Chemistry* 533–583 (2014).
58. Bertolini, L., Elsener, B., Pedferri, P. & Polder, R. P. in *Corrosion of Steel in Concrete: Prevention, Diagnosis, Repair* 249–269 (2005).
59. Papadakis, V. G., Vayenas, C. G. & Fardis, M. N. Experimental investigation and mathematical modeling of the concrete carbonation problem. *Chem. Eng. Sci.* **46**, 1333–1338 (1991).
60. Kropp, T. A. B. J. & Hilsdorf, H. K. Formation of Silica gel During Carbonation of Cementitious Systems Containing Slag Cements. *Spec. Publ.* **114**, 1413–1428 (1989).
61. Bary, B. & Sellier, A. Coupled moisture—carbon dioxide—calcium transfer model for carbonation of concrete. *Cem. Concr. Res.* **34**, 1859–1872 (2004).
62. Saetta, A. V. & Vitaliani, R. V. Experimental investigation and numerical modeling of carbonation process in reinforced concrete structures: Part I: Theoretical formulation. *Cem. Concr. Res.* **34**, 571–579 (2004).
63. Song, H. W., Kwon, S. J., Byun, K. J. & Park, C. K. Predicting carbonation in early-aged cracked concrete. *Cem. Concr. Res.* **36**, 979–989 (2006).
64. Georget, F., Prévost, J. H. & Huet, B. Impact of the microstructure model on coupled simulation of drying and accelerated carbonation. *Cem. Concr. Res.* **104**, 1–12 (2018).
65. Georget, F. A Reactive Transport Simulator for Cement Pastes. (2017).

66. Georget, F., Prévost, J. H. & Huet, B. A reactive transport simulator for variable porosity problems. *Comput. Geosci.* **21**, 95–116 (2017).
67. Durdziński, P. T. Hydration of multi-component cements containing cement clinker, slag, calcareous fly ash and limestone. (2016). EPFL-THESIS-6834
68. Scrivener, K., Snellings, R. & Lothenbach, B. *A practical guide to microstructural analysis of cementitious materials*. (2016).
69. Mota Gassó, B. Impact of alkali salts on the kinetics and microstructural development of cementitious systems. (EPFL, 2015). EPFL-THESIS-6763
70. Rossen, J. E. Composition and morphology of C-A-S-H in pastes of alite and cement blended with supplementary cementitious materials. (2014). EPFL-THESIS-6294
71. Berodier, E., Bizzozero, J. & Muller, A. *Mercury intrusion porosimetry*. (2016).
72. Cook, R. A. & Hover, K. C. Experiments on the contact angle between mercury and hardened cement paste. *Cem. Concr. Res.* **21**, 1165–1175 (1991).
73. Papadakis, V. G., Vayenas, C. G. & Fardis, M. N. Fundamental Modeling and Experimental Investigation of Concrete Carbonation. *ACI Mater. J.* **88**, 363–373 (1991).
74. Papadakis, V., Fardis, M., Journal, C. V.-M. & 1992, undefined. Hydration and carbonation of pozzolanic cements. *concrete.org*
75. Bertolini, L., Elsener, B., Pedferri, P. & Redaelli, E. *Corrosion of steel in concrete: prevention, diagnosis, repair*. (2013).
76. Russell, D., Basheer, P., G. R.-P. of the & 2001, U. Effect of relative humidity and air permeability on prediction of the rate of carbonation of concrete. *researchgate.net*
77. Khunthongkeaw, J., Tangtermsirikul, S. & Leelawat, T. A study on carbonation depth prediction for fly ash concrete. *Constr. Build. Mater.* **20**, 744–753 (2006).
78. Sakata, K. A study on moisture diffusion in drying and drying shrinkage of concrete. *Cem. Concr. Res.* **13**, 216–224 (1983).
79. Leemann, A., Nygaard, P., Kaufmann, J. & Loser, R. Relation between carbonation resistance, mix design and exposure of mortar and concrete. *Cem. Concr. Compos.* **62**, 33–43 (2015).
80. Fattuhi, N. I. Concrete carbonation as influenced by curing regime. *Cem. Concr. Res.* **18**, 426–430 (1988).
81. Patel, R. G., Killoh, D. C., Parrott, L. J. & Gutteridge, W. Influence of curing at different relative humidities upon compound reactions and porosity in Portland cement paste. *Mater. Struct. Constr.* **21**, 192–197 (1988).
82. Hermida, G., Moranville, M. & Flatt, R. J. The Role of Paste Volume on Performance of Concrete. *Spec. Publ.* **261**, 201–214 (2009).
83. Bier, T. Influence of type cement and curing on carbonation progress and pore structure of hydrated cement pastes. *MRD Online Proc. Libr. Arch.* **85**, (1986).
84. Spears, R. The 80 percent solution to inadequate curing problems. *Concr. Int.* 15–18 (1983).
85. Sakata, K. A study on moisture diffusion in drying and drying shrinkage of concrete. *Cem. Concr. Res.* **13**, 216–224 (1983).
86. Parrot, J. Novel methods of processing cement gel to examine and control microstructure and properties. *R. Soc.* **310**, 155–166 (1983).
87. Powers, T., Copeland, L., Hayes, J. & Mann, H. Permeability of Portland cement paste. *J. Proc.* **51**, 285–298 (1954).

88. Patel, R., Parrott, L., Martin, J. & Killoh, D. Gradients of microstructure and diffusion properties in cement paste caused by drying. *Cem. Concr. Res.* **15**, 343–356 (1985).
89. Sellevold, D. & Bager, E. Ice formation in hardened cement paste, Part II - Drying and resaturation on room temperature cured pastes. *Cem. Concr. Res.* **16**, 835–844 (1986).
90. Patel, R., Killoh, D., Parrott, L. & Gutteridge. Influence of curing at different relative humidities upon compound reactions and porosity in Portland cement paste. *Mater. Struct. Constr.* **21**, 192–197 (1988).
91. Scrivener, K. L., John, V. M. & Gartner, E. M. *Eco-efficient cements: Potential economically viable solutions for a low-CO₂ cement-based materials industry.* (2016).
92. Richardson, I. G. Tobermorite/jennite- and tobermorite/calcium hydroxide-based models for the structure of C-S-H: applicability to hardened pastes of tricalcium silicate, β -dicalcium silicate, Portland cement, and blends of Portland cement with blast-furnace slag, metakaol. *Cem. Concr. Res.* **34**, 1733–1777 (2004).
93. Diamond, S. Mercury porosimetry: An inappropriate method for the measurement of pore size distributions in cement-based materials. *Cem. Concr. Res.* **30**, 1517–1525 (2000).
94. Beaudoin, J. J. Porosity measurement of some hydrated cementitious systems by high pressure mercury intrusion-microstructural limitations. *Cem. Concr. Res.* **9**, 771–781 (1979).
95. Karen Scrivener, Ruben Snellings, B. L. *A Practical Guide to Microstructural Analysis of Cementitious Materials - Google Books.* (First Spon Press, Boca Raton, 2016).
96. Renaudin, G., Filinchuk, Y., Neubauer, J. & Goetz-Neunhoeffler, F. A comparative structural study of wet and dried ettringite. *Cem. Concr. Res.* **40**, 370–375 (2010).
97. Barlos, K. *et al.* Carbonation in 36 year old, in-situ concrete. *Tetrahedron Lett.* **30**, 3943–3946 (1989).
98. Rahman, A. A. & Glasser, F. P. Comparative studies of the carbonation of hydrated cements. *Adv. Cem. Res.* **2**, 49–54 (1989).
99. Groves, G. W., Rodway, D. I. & Richardson, I. G. The carbonation of hardened cement pastes. *Adv. Cem. Res.* **3**, 117–125 (1990).
100. Georget, F., Prévost, J. H. & Huet, B. Impact of the microstructure model on coupled simulation of drying and accelerated carbonation. (2017).
101. Brečević, L. & Nielsen, A. E. Solubility of amorphous calcium carbonate. *J. Cryst. Growth* **98**, 504–510 (1989).
102. Kocaba, V. Development and evaluation of methods to follow microstructural development of cementitious systems including slags. (2009). EPFL-THESIS-4523
103. Herterich, J. Microstructure and Phase Assemblage of Low-Clinker Cements during Early Stages of Carbonation. (2017).
104. Sauman, Z. Carbonation of porous concrete and its main binding components. *Cem. Concr. Res.* **1**, 645–662 (1971).
105. Ogino, T., Suzuki, T. & Sawada, K. The formation and transformation mechanism of calcium carbonate in water. *Geochim. Cosmochim. Acta* **51**, 2757–2767 (1987).
106. Durdziński, P. T. Hydration of multi-component cements containing cement clinker, slag, calcareous fly ash and limestone. (2016). EPFL-THESIS-6834
107. Matsushita, F., Aono, Y. & Shibata, S. Carbonation degree of autoclaved aerated concrete. *Cem. Concr. Res.* **30**, 1741–1745 (2000).
108. Rossen, J. E. & Scrivener, K. L. Optimization of SEM-EDS to determine the C–A–S–H composition in matured cement paste samples. *Mater. Charact.* **123**, 294–306 (2017).
109. Richardson, I. G. & Groves, G. W. Microstructure and microanalysis of hardened ordinary Portland cement

- pastes. *J. Mater. Sci.* **28**, 265–277 (1993).
110. Shah, V., Scrivener, K., Bhattacharjee, B. & Bishnoi, S. Changes in microstructure characteristics of cement paste on carbonation. *Cem. Concr. Res.* **109**, 184–197 (2018).
 111. Groves, G. W., Rodway, D. I. & Richardson, I. G. The carbonation of hardened cement pastes. *Adv. Cem. Res.* **3**, 117–125 (1990).
 112. Glasser, F. P., Marchand, J. & Samson, E. Durability of concrete — Degradation phenomena involving detrimental chemical reactions. [j.cemconres.2007.09.015](https://doi.org/10.1016/j.cemconres.2007.09.015)
 113. Muller, A. C. A. Characterization of porosity & C-S-H in cement pastes by ¹H NMR. (2014). EPFL-THESIS-6339
 114. Morandau, A., Thiéry, M. & Dangla, P. Investigation of the carbonation mechanism of CH and C-S-H in terms of kinetics, microstructure changes and moisture properties. *Cem. Concr. Res.* **56**, 153–170 (2014).
 115. Morandau, A., Thiéry, M. & Dangla, P. Impact of accelerated carbonation on OPC cement paste blended with fly ash. *Cem. Concr. Res.* **67**, 226–236 (2015).
 116. Leemann, A., Nygaard, P., Kaufmann, J. & Loser, R. Relation between carbonation resistance, mix design and exposure of mortar and concrete. *Cem. Concr. Compos.* **62**, 33–43 (2015).

Curriculum Vitae



Route du Bois 19
CH-1024 Ecublens
Switzerland
+41 79872 47 29
wiojasoja@gmail.com
[Wioletta-Soja](#)



Education

- 2015 – 2019:** **École Polytechnique Fédérale de Lausanne (EPFL), Switzerland**
PhD in Materials Science
Doctoral program: Materials Science and Engineering
Laboratory of Construction Materials;
Doctoral thesis: “Carbonation of low carbon binders”
- 2012 – 2013:** **AGH University of Science and Technology in Cracow, Poland**
Master of Science in Chemical Technology
Faculty of Material Science and Ceramics; Department of Building Materials Technology
- 2012 – 2013:** **Empa, Swiss Federal Laboratories for Materials Science and Technology, Duebendorf, Switzerland**
Department of High-Performance Ceramics
Master Thesis: “Forcespinning of magnesium spinel-based ceramic fibres”
- 2008 – 2012:** **AGH University of Science and Technology in Cracow, Poland**
Bachelor of Engineering in Chemical Technology
Faculty of Material Science and Ceramics

Professional experience

- 2015 – 2019:** **École Polytechnique Fédérale de Lausanne (EPFL), Switzerland**
Research assistant
Teaching activities (laboratories for master students, lecturer during LC3 Doctoral School 2018 and 2019); Person in charge of Mercury Intrusion Perimetry (training for new users)
- 2013:** **University of Rostock, Germany**
Laboratory assistant, Institute of Physics
2-month IAESTE Internship (International Association for the Exchange of Students for Technical Experience)
- 2011:** **CEMEX, Chelm, Poland**
Quality department
2-month internship, practical training in industrial technologies
Technological process of production of clinker and cement; internal organization structure and testing methods

Technical skills

Experimental and characterisation techniques:

Mercury intrusion porosimetry (MIP),	Gas diffusion,
Dynamic vapour sorption (DVS),	Mechanical tests
Thermogravimetric analysis (TGA),	Mortar/concrete preparation
X-ray diffraction (XRD),	Phenolphthalein test
Scanning electron microscopy (SEM)	Isothermal calorimetry,
Energy dispersive analysis (EDS),	Polishing

IT: OriginPro, X'Pert HighScore, Plus Windows, Microsoft Office

Languages

Polish:	Mother tongue
English:	Fluent spoken and written (C1)
German:	Good spoken (B2), intermediate written (B1)
Language stays:	German: 2-month stay in Rostock, Germany, 2013 (intensive course at "Study in Germany" School); 1 year at "Migros Klubschule", Zurich, Switzerland, 2014; English: 4-month stay in Mallow, Ireland, 2009 and 2010

Volunteering Experience**2014: Au-Pair program, Zurich Switzerland**

1-year stay with a Swiss family sharing their language, culture, lifestyle, and tradition; childcare experience; German classes

2010 – 2013: IAESTE AGH Cracow (The International Association for the Exchange of Students for Technical Experience)

Responsible for the promotion of the organization; acquisition of new internship offers for foreign students; ability to work cooperatively as a team member in a group setting

Interests

Art and music:	Photography, drawing, choir member
Sport:	Climbing indoor and outdoor, hiking, skiing, roller skating, cycling (to work)
Environment:	Participation in challenges: <i>Act for Change (2018)</i> , <i>Bike to Work (2015-2018)</i>
Other:	Travelling, dancing (Tango, Lindy-hop)

Personal details

Nationality:	Polish
Date of birth:	19.03.1989
Driving licence:	category B

Publications

Conference Proceedings:

W. Soja, F. Avet, H. Maraghechi, K. Scrivener "Investigation of the carbonation profiles of Limestone Calcined Clay Cement (LC3)" 35th Cement and Concrete Science Conference in Aberdeen, 2016,

W. Soja, F. Avet, H. Maraghechi, P. Durdziński, K. Scrivener "Evolution of microstructure and phase assemblage in blended cement pastes exposed to natural carbonation" XIV International Conference on Durability of Building Materials and Components, DBMC, Ghent, 2017

W. Soja, H. Maraghechi, K. Scrivener "Microstructural and Phase Assemblage Changes in Naturally Carbonated Cement Paste with Supplementary Cementitious Materials (SCMs)", International Conference on Advances in Construction Materials and Systems", Chennai, 2017

W. Soja H. Maraghechi, F. Georget, K. Scrivener "Changes of Microstructure and Diffusivity in Blended Cement Paste Exposed to Natural Carbonation", International Conference on Concrete Repair, Rehabilitation and Retrofitting, Cape Town, 2018

Journal Articles:

W. Soja, F. Georget H. Maraghechi, K. Scrivener, "Evolution of microstructural changes in cement paste during environmental drying in the absence of carbon dioxide" (in preparation)

W. Soja, F. Georget, K. Scrivener, "Effect of Microstructure Changes after Carbonation on Diffusivity in Cement Paste made with Low Carbon Binders" (in preparation)

F. Georget, W. Soja, K. Scrivener, "Natural tracers for carbonation: long-range sulphate and sodium diffusion in carbonated cements paste observed by SEM-EDS" (in preparation)

